Multi-periodic and random mode of Atmospheric Pressure Plasma Jets and their interactions with liquid and biological target

Hang Yang

INSTITUT POLYTECHNIQUE DE PARIS

NNT : 2023IPPAX012

Thèse de doctorat

Multi-periodic and random mode of Atmospheric Pressure Plasma Jets and their interactions with liquid and biological targets

Thèse de doctorat de l'Institut Polytechnique de Paris
préparée à l'École Polytechnique

École doctorale n°626 l'Institut Polytechnique de Paris (ED IP Paris)
Spécialité de doctorat: Optique, laser et plasma

Thèse présentée et soutenue à Palaiseau, 02/03/2023, par

Hang Yang

Composition du Jury :

Anne Bourdon Directrice de recherche, École polytechnique (– LPP)	Présidente
Eric Robert Directeur de recherche, Université d'Orléans (– GREMI)	Rapporteur
James Walsh Professor, University of York	Rapporteur
Joao Santos-Sousa Chargé de recherche, Université paris Saclay (–LPGP)	Examinateur
Angelo Pierangelo Ingénieure de recherche, École polytechnique (– LPICM)	Examinateur
Antoine Rousseau Directeur de recherche, École polytechnique (– LPP)	Directeur de thèse

Abstract

Atmospheric Pressure Plasma Jets (APPJ) have been intensively studied and have numerous applications in plasma medicine such as wound healing or tumor reduction. In this thesis, three main features of APPJ are investigated: i) multi-periodic and random modes of propagation and the role of surface charges; ii) the interaction between the APPJ and liquid targets; iii) the modification of inert skin samples after plasma treatment.

A helium APPJ driven by 15~18 kHz sinusoidal voltage ignites multi-periodic self-triggered mode or random mode depending on the applied voltage, driven frequency, and inter-electrode gap distance. Most of the observed multi-periodic bullets operate every 2 or 3 sinusoidal periods. Such bullets show similarities with pulsed operating mode, having a jitter of smaller than 100 ns. The presence of an outer grounded electrode ring is a key parameter permitting the ignition of multiperiodic bullets; it also enhances the propagation length up to 8 times. Fast imaging reveals that 2-3 self-triggered discharges occur in the gap region prior to ignition of the bullet in both positive or negative polarities; this leads to an accumulation of charges beneath the ground electrode, locally enhancing the electric field. Time-resolved optical emission spectra at different locations and voltages show that most of the OH emission comes from the glow-like discharge in the gap region after the plasma bullet formation.

When interacting with a water target, the propagation of this APPJ shows similar multi-periodic modes and random modes. The H_2O_2 production rate is measured in water and it is concluded that the H_2O_2 is mostly produced inside the APPJ from the impurities disorbed from the gas tube's inner wall.

Defrost pig skin is treated by the APPJ and analyzed by full-field Mueller polarimetric imaging (MPI). It is shown to modify the linear phase retardance and the total depolarization for higher plasma power and/or longer treatment duration. According to control groups, tissue alterations are primarily caused by the local heating concomitant to plasma-skin interaction above 0.5W/45 ℃. This study aims to show that full-field MPI is suitable for fast and without-contact detection of skin microstructure modifications induced by plasma treatment.

Keywords: APPJ, multi-periodic plasma, self-trigger, RONS, MPI, plasma medicine

Résumé

Le Jet de Plasma à Pression Atmosphérique (APPJ) est un type de source de plasma qui génère un Plasma Non-Thermique (NTP) à l'intérieur des capillaires. Ces dernières années, il a été largement étudié en raison de son grand potentiel pour des applications dans les domaines biomédicaux tels que la guérison des plaies, la dermatologie, le traitement du cancer, etc. Les plasmas générés dans les APPJ peuvent se propager sur de longues distances dans le tube capillaire ou se propager dans l'air ambiant et interagir avec une surface. Le NTP peut produire une abondance d'espèces réactives de l'oxygène et de l'azote (RONS), qui sont connues pour avoir des effets multiples sur les tissus vivants en fonction du type de RONS et de la dose, comme l'inactivation des bactéries, l'induction de la mort cellulaire ou la promotion de la cicatrisation des plaies.

Au cours des dernières années, notre équipe s'est consacrée à l'étude de la promotion de la cicatrisation des plaies par traitement avec des APPJ à l'hélium entraînés par une tension alternative. Du côté de la physique, l'objectif de cette thèse est d'étudier les aspects fondamentaux de l'APPJ, y compris l'influence des conditions de fonctionnement sur son allumage et sa propagation, ainsi que son interaction avec des cibles liquides ou des modèles de peau inerte.

De nombreux chercheurs ont signalé les comportements non linéaires des décharges à barrière diélectrique et des jets de plasma, tels que la formation de motifs, de stries, de turbulences, etc. L'un des phénomènes non linéaires qui attirent beaucoup l'attention est le chaos et la multiplication de périodes de la décharge dans les jets de plasma alimtenté en CA. Les caractéristiques du plasma peuvent présenter un mode aléatoire ou une périodicité en fonction des conditions de fonctionnement. Cela a été attribué à l'effet de mémoire bien connu du plasma qui est considéré comme étant causé par les charges résiduelles. Cependant, il n'est pas clair si les charges résiduelles de surface ou volumétriques jouent un rôle majeur. Bien que certains chercheurs pensent que les charges de surface influencent la périodicité du plasma, d'autres montrent que les densités d'électrons de départ influencent l'intensité et la longueur des décharges. Dans le cas de l'APPJ, seuls quelques travaux ont été consacrés au lien entre l'allumage dans la région de l'espace et le lancement de balles de plasma multi-périodiques. Dans cette thèse, nous discuterons du rôle des charges résiduelles de surface et volumétriques en caractérisant un APPJ à l'hélium alimenté par une tension sinusoïdale de 15 à 18 kHz. Un APPJ à l'hélium alimenté par une tension sinusoïdale de 15 à 18 kHz allume un mode auto-déclenché multi-périodique ou aléatoire en fonction de la tension appliquée, de la fréquence d'entraînement et de la distance entre les électrodes. La plupart des balles multi-périodiques observées fonctionnent toutes les 2 ou 3 périodes sinusoïdales. De telles balles présentent des similitudes avec le mode de fonctionnement pulsé, avec une gigue inférieure à 100 ns. La présence d'une bague d'électrode extérieure mise à la terre est un paramètre clé permettant l'allumage de balles multi-périodiques ; elle augmente également la longueur de propagation

jusqu'à 8 fois. L'imagerie rapide révèle que 2 à 3 décharges auto-déclenchées se produisent dans la région de l'espace avant l'allumage de la balle dans les polarités positives ou négatives ; cela conduit à une accumulation de charges sous l'électrode de terre, renforçant localement le champ électrique. Les spectres d'émission optique résolus dans le temps à différents endroits et tensions montrent que la plupart de l'émission de OH provient de la décharge de type lueur dans la région de l'espace après la formation de la balle de plasma.

Les RONS sont formés dans l'APPJ via des réactions complexes. Comme l'effet des RONS sur les tissus vivants dépend de la dose, de nombreuses tentatives ont été faites pour manipuler le taux de production de RONS par l'APPJ. Par exemple, les mécanismes de formation de H_2O_2 dans l'APPJ ont suscité des discussions parmi les chercheurs. Il est proposé dans la littérature que H_2O_2 est formé à l'interface plasma-liquide, dans le plasma en vrac à l'intérieur du capillaire, ou par photolyse UV, etc. Dans cette thèse, nous caractérisons le taux de production de H_2O_2 par un jet d'hélium à 10 kHz entraîné par une tension alternative en interaction avec de l'eau et étudions les mécanismes de H_2O_2 par une étude paramétrique et une spectroscopie d'émission optique. Lorsqu'il interagit avec une cible d'eau, la propagation de cet APPJ montre des modes multi-périodiques similaires et des modes aléatoires. Le taux de production de H_2O_2 est mesuré dans l'eau et il est conclu que le H_2O_2 est principalement produit à l'intérieur de l'APPJ à partir des impuretés désorbées de la paroi interne du tube de gaz.

NTP appliquée en dermatologie est utilisée avec différentes puissances et provoque différents effets sur la peau, tels que la réparation de plaies avec une puissance relativement faible et l'induction de la mort des tumeurs avec une puissance relativement élevée. En fonction de la dose de traitement NTP, des modifications microstructurales sont induites sur la peau par les plasmas. Dans la littérature, la plupart des études sont consacrées à l'effet biologique des NTP sur les tissus vivants et le rôle des RONS ainsi que d'autres effets du plasma tels que le champ électrique ou le transfert de chaleur sont considérés. Dans cette thèse, nous utilisons un seul jet plasma à l'hélium piloté par une tension CA de 10 kHz pour traiter des échantillons de peau de porc inerte afin d'étudier les changements physico-chimiques à court terme. L'effet sur la microstructure des échantillons de peau est évalué en utilisant l'imagerie polarimétrique Mueller à champ complet (MPI) qui est un outil rapide et non invasif pour diagnostiquer les changements de microstructure de la peau. Les paramètres MPI tels que la retardance linéaire et la dépolarisation totale de la zone de peau traitée sont modifiés en fonction de la puissance du plasma. Dans des conditions NTP douces et à une température de 35°C qui est souvent requise pour la guérison des plaies, aucun paramètre MPI n'est modifié. Les modifications apparaissent à partir de 45°C (0,5 W) et augmentent continuellement jusqu'à 73°C (1,5 W). Une telle NTP de haute puissance est souvent utilisée pour induire la mort des tumeurs. En utilisant une approche paramétrique où les échantillons de peau sont traités par la chaleur seule ou H_2O_2 seule, nous avons pu attribuer une partie de ces modifications au chauffage de l'échantillon de peau et à la dénaturation des fibres de collagène. En revanche, le traitement chimique à l'aide de H_2O_2 ne montre aucun effet sur les propriétés polarimétriques. Sur des

échantillons de peau inerte, une si petite quantité d'espèces chimiques ne devrait probablement pas induire de changement dans la microstructure de la peau.

Mots-clés : APPJ, plasma multi-périodique, auto-déclenchement, RONS, MPI, plasma médecine

Acknowledgements

I would first like to thank Fondation de l'École Polytechnique for granting my 40-month Ph.D.

I would like to express my sincere gratitude to my supervisor Professor Antoine Rousseau from LPP of École Polytechnique. He has provided great support and guidance in my work while giving me maximum flexibility and autonomy. This has been important for me to acquire my independence as a young researcher. He has been a responsible supervisor and a good friend to me.

I would like to thank Dr. Angelo Pireangelo from LPICM of École Polytechnique for working with us on the Muller polarimetric imaging experiments and writing the corresponding paper.

I would also like to thank Professor Julien Fuchs from LULI of École Polytechnique for working with us on the observation with the streak camera.

I would like to express my appreciation to my colleagues, Dr. Océane Blaise, Louis Sauge, Dr. Joseph Youssef, and former colleagues Dr. Bo Liu, Dr. Xianjie Wang, Dr. Bruno Honnorat, and Dr. Constance Duchesne, for helping and supporting my work and for being my good friends.

I would like to send my appreciation to my friends, Yaoyuan Miao, Dr. Yanting Han, and Dr. Xiaolong Zhang. Our friendship has helped me through the anxiety and loneliness of life in France.

I sincerely thank all the members of LPP, all the researchers, and the administration team, for providing all kinds of help and support over the past three years.

I would like to express my gratitude to my family for their love and support from China.

Contents

General introduction

Atmospheric Pressure Plasma Jet (APPJ) is a type of plasma source that generates Non-thermal Plasma (NTP) inside capillaries. In recent years, it has been intensively studied due to its great potential for applications in biomedical fields such as wound healing, dermatology, cancer treatment, etc. Plasmas generated in APPJs can propagate over long distances in the capillary tube or propagate into the ambient air and interact with a surface. NTP can produce abundant Reactive Oxygen and Nitrogen Species (RONS), which are known to have multiple effects on living tissues depending on the type of RONS and dose, like inactivating bacteria, inducing cell death, or promoting wound repair.

In the past several years, our team has been dedicated to studying the promotion of wound healing via treatment with helium APPJs driven by AC voltage. On the physics side, the aim of my thesis is to study the fundamental aspects of the APPJ, including the influence of operating conditions on its ignition and propagation, and its interaction with liquid or inert skin model targets.

Numerous researchers reported the nonlinear behaviors of dielectric barrier discharges and plasma jets, such as the formation of patterns, striation, turbulance, etc. One of the nonlinear phenomena that attract much attention is the chaos and period multiplication of discharge in AC-driven plasma jets. The characteristics of the plasma can exhibit randomness or periodicity depending on the operating conditions. It has been attributed to the well-known memory effect of plasma which is considered to be caused by the residual charges. However, it is unclear whether the surface residual charges or the volumetric residual charges play a major role. Although some researchers believe that the surface charges influence the periodicity of plasma, some other researchers show that the seed electron densities influence the intensity and length of discharges. In the case of APPJ, only a few works have been dedicated to the link between ignition in the gap region and launching multiperiodic plasma bullets. In this thesis, we will discuss the role of surface and volumetric residual charges by characterizing a 10~18 kHz AC-driven helium APPJ in random and multi-periodic modes. Multiple diagnostic methods, including ICCD (intensified charge-coupled device) imaging, steak cameras, optical emission spectroscopy (OES), electrical diagnostic methods, etc. are combined.

RONS are formed in the APPJ via complex reactions. As the effect of RONS on living tissues are dose-dependent, many attempts have been made to manipulate the production rate of RONS by APPJs. For example, the mechanisms of H_2O_2 formation in APPJ have raised discussion among researchers. It is proposed in literature that H_2O_2 is formed in the plasma-liquid interface, in the bulk plasma inside the capillary, or by UV photolysis, etc. In this thesis, we characterize the H_2O_2 production rate by a 10 kHz AC-driven helium jet interacting with water and study the mechanisms of H_2O_2 through parametric study and optical emission spectroscopy.

NTP applicated in dermatology are operated with different power and caused different effect on the skin, such as wound repair with relatively low power and inducing tumor death with

relatively high power. Depending on the dose of NTP treatment, microstructural modifications are induced on the skin treatment by plasmas. In literature, most studies are dedicated to the biological effect of NTPs on living tissues and the role of RONS as well as others plasma effects such as electric field or heat transfer are considered. In this thesis, we use a single helium APPJ driven by a 10 kHz AC voltage to treat *inert* pig skin samples to investigate short-term physical-chemistry changes. The effect on the microstructure of skin samples is evaluated using Mueller Polarimetric Imaging (MPI) which is a non-invasive, fast tool to diagnose the microstructure change of skin. The role of plasma heating and RONS is addressed through comparative studies with control groups.

The structure of the thesis is shown below.

Chapter 1 provides a literature review of the topics studied in this thesis. A brief introduction to Non-Thermal Plasma (NTP) and Atmospheric Pressure Plasma Jet (APPJ) is made. The random and multi-periodic modes of plasma ignition are introduced with a special focus on the role of surface and volumetric residual charges. The possible mechanisms of the H_2O_2 formation in APPJs are summarized. The principle of Mueller Polarimetric Imaging is introduced. The microstructural modification caused by NTP is summarized.

Chapter 2 summarizes the instruments, experiment setups, experiment methods, and data treatment methods that are used in this thesis. It includes electrical and optical diagnostics methods for plasma, like fast imaging with ICCD cameras, optical emission spectroscopy; measurement of liquid phase long-live RONS concentrations; MPI measurement, etc.

Chapter 3 investigates the random and multiperiodic modes of plasma ignition in APPJ. A helium APPJ with a needle-like electrode driven by 15~18 kHz sinusoidal voltage ignites multi-periodic self-triggered mode or random mode depending on the applied voltage, driven frequency, and inter-electrode gap distance. Most of the observed multi-periodic bullets operate every 2 or 3 sinusoidal periods with a small jitter of less than 100 ns. The change of surface residual charge due to the presence of an outer grounded electrode ring is a key parameter permitting the ignition of multiperiodic bullets. Time and space resolved optical emission spectroscopy is performed to understand the mechanism of plasma bullet formation. A comparative study is performed using a DC pulsed APPJ to reveal the role of instantaneous applied voltage and the role of the ground electrode.

Chapter 4 investigates the plasma bullets in random mode with a 5 mm inter-electrode gap distance. Multiple consecutive plasma bullets are observed. Long random plasma bullets are ignited after short periodic plasma bullets. The velocity of random long bullets is measured statistically.

Chapter 5 studies the interaction of a similar APPJ with a water target. An external ring-like powered electrode is used to avoid arc formation between the electrode and the target. The

effect of the water target on the plasma propagation is visualized with the ICCD camera. The production of H_2O_2 is characterized and the origin of H_2O_2 production is discussed.

Chapter 6 studies the microstructure modification caused by an APPJ on defrost *inert* pig skin samples. The Mueller matrix of the pig samples is measured after the plasma treatment to evaluate the change in microstructure.

At the end of this thesis, the main outcome is summarized and the future perspectives are pointed out.

Most of my three years of research is done at Laboratoire de Physique des Plasma (LPP), École Polytechnique. The measurement with streak camera is finished in collaboration with Pr. Julien Fuchs at LULI, École Polytechnique; the measurement of MPI introduced in chapter 6 is performed in collaboration with Dr. Angelo Pierangelo at LPICM, École Polytechnique.

Chapter 1. State of the art

This chapter provides a scientific background of the topics studied in the present thesis.

Section 1.1 introduces some basic concepts about non-thermal plasma and its important applications, especially in biomedical fields.

Section 1.2 introduces the physics of Atmospheric Pressure Plasma Jet (APPJ), with a special focus on the periodic and random ignition of the plasma.

Section 1.3 introduces the production of Reactive Oxygen and Nitrogen Species (RONS) in liquid by APPJs, with a special focus on the production mechanisms of H_2O_2.

Section 1.4 introduces the Mueller Polarimetric Imaging as a new fast non-invasive tool to detect the microstructural modification to the skin caused by NTP treatment.

Section 1.5 makes a summary of the chapter.

1.1 General context of plasma

1.1.1 Basic concepts of plasma

Plasma, as a state of matter, is an ionized gas in which the long-range electric and magnetic fields dominate its behavior. The density of positive and negative charges in plasma is close, so the plasma exhibits quasi-neutrality.

Depending on the thermodynamic equilibrium state, plasma can be classified into high-temperature plasma and low-temperature plasma [1].

In a high-temperature plasma (HTP), the free electrons and charged heavy species like ions are in thermal equilibrium state, and the temperature is higher than 10^7 K. Typical high-temperature plasma includes the matters in stars like the sun; magnetic confined plasma in Tokamak, etc.

Low-temperature plasma (LTP) can be divided into thermal and non-thermal plasmas (NTP). In thermal plasmas, the electrons and ions are in thermal equilibrium state and the temperature is about 10^4 K. Atmospheric pressure arc plasmas and plasma torches are considered as thermal plasmas. In NTP, the electrons and ions are not in thermal equilibrium state. The temperature of the heavy species remains close to room temperature, while the temperature of electrons can be up to several electron volts. Common non-thermal plasmas include glow discharge, Dielectric Barrier Discharge (DBD), RF discharge, Atmospheric Pressure Plasma Jet (APPJ), etc. The classification of plasma is shown in Table 1.1.

Table 1.1 Classification of Plasmas [1].

Low-Temperature Plasma (LTP)		High-Temperature Plasma (HTP)
Thermal Plasma	Non-Thermal Plasma (NTP)	
$T_e \approx T_i \approx T \leq 2\times10^4$ K	$T_i \approx T \approx$ 300-1000 K $T_e \approx$ 1-10 eV	$T_e \approx T_i \geq 10^7$ K
e.g. Arc Plasma at normal pressure	e.g. Low pressure glow discharge, DBD, corona discharge, APPJ	e.g. Fusion Plasmas

With atmospheric pressure, due to high particle density and high collision rate, electric discharge plasmas easily transform into thermal plasmas like arcs if the discharge current is not limited. Some techniques have been used by researchers to generate atmospheric pressure non-thermal plasmas, and dielectric barrier discharge (DBD) is one of the most frequently used NTP. In this case, a dielectric barrier is present between the two electrodes, which prevents continuous strong discharge current.

1.1.2 Application of non-thermal plasma in medicine

In the past decades, the applications of atmospheric pressure NTP have developed in numerous fields, including material science [2], environmental protection [3], agriculture [4], chemical engineering [5], medicine [6], etc. The abundant reactive species are found to have a significant effect on biological cells, which inspires researchers to develop numerous applications of NTP in biomedical fields.

In 1996, Laroussi *et al.* reported using atmospheric pressure glow discharge generated by low-frequency RF voltage to inactivate bacteria [7]. Compared to traditional sterilization methods like heating, UV radiation, and chemical solutions, NTP can sterilize the infected medium with high efficiency and without damaging the medium itself, which is important in the sterilization of some medical tools, food, live tissues, etc. NTP plasma treatment is also proven to be efficient in removing biofilms [8,9], which are difficult to be eradicated due to their high resistance to antimicrobial treatment [10]. The mechanisms of NTP effects are considered to include long-lifetime and short-lifetime reactive species, electric field, UV radiation, etching effects, etc [11,12].

The sterilization effect of NTP makes it a promising tool for treating skin diseases. It has been used to treat psoriasis, atopic dermatitis, pruritus, etc [13]. Some medical devices have been developed, certificated, and applied to clinics to treat the skin of patients, like PlasmaDerm® [14], and the kINPen [15]. One of the most exciting applications of NTP in dermatology is the healing of chronic wounds, which are also called non-healing wounds. They are difficult to heal due to the infection of resistant bacteria or biofilms. Typical chronic wounds include venous and arterial ulcers, diabetic ulcers, pressure ulcers, etc. Other than the significant advantage in bacteria inactivation of NTP, the reactive chemical species produced by NTP have been proven to trigger different signaling pathways in cells that help would healing. Arjunan *et al.* showed that the reactive oxygen species created by non-thermal DBD induces fibroblast growth factor-2(FGF-2) release which improves angiogenesis [16]. Duchesne *et al.* proved that cold atmospheric pressure plasma increases the levels of endogenous NO in endothelial cells, which stimulates important pro-angiogenic VEGFA/VEGFR2 signaling *in vitro* [17]. They also provide evidence that CAP activates defense mechanisms of macrophages [18].

NTP has also been used to treat varieties of tumors, like glioma tumors, lung cancer, brain tumors, pancreatic tumors, etc [19,20]. NTP treatment is shown to significantly reduce the amount of cancer cells and tumor size. Experiments showed that the effect of NTP on tumors is highly dependent on plasma dose. The mechanism of anti-tumor effect of NTP is unclear. RONS is considered by many researchers to be responsible for causing the tumor cell death.

However, Honnorat *et al.* reported that the hyperthermia effect may be produced by NTP depending on operating conditions and should also be considered [21].

1.2 Atmospheric Pressure Plasma jet (APPJ)

Atmospheric Pressure Plasma Jets, known as APPJs, ignite and propagate in small dielectric tubes. The dielectric tube is usually fed with noble gas such as helium or argon. The cold atmospheric pressure plasma generated by an APPJ can propagate over a long distance, ranging from several centimeters to up to 1 meter. Thus, APPJ is a convenient tool to transfer the abundant reactive species to the surface to be treated, which makes plasma jet one of the most studied and used types of plasma in biomedical fields.

The physics of APPJ has been widely investigated. In 2005, Teschke *et al*. first observed the plasma propagation in APPJ with fast imaging in nanosecond scale, and showed that the plasmas in APPJ are a series of ionization front propagating in the dielectric capillary [22]. Figure 1.1 shows the light emission of their plasma jet with an exposure time of 100 ns. The shape of ionization front is similar to a bullet, so it was given the name "plasma bullet" [22,23]. For simplicity, in the rest of this manuscript, the term "plasma bullet" will be used to refer to the ionization front where the intensity of visible light emission is the highest.

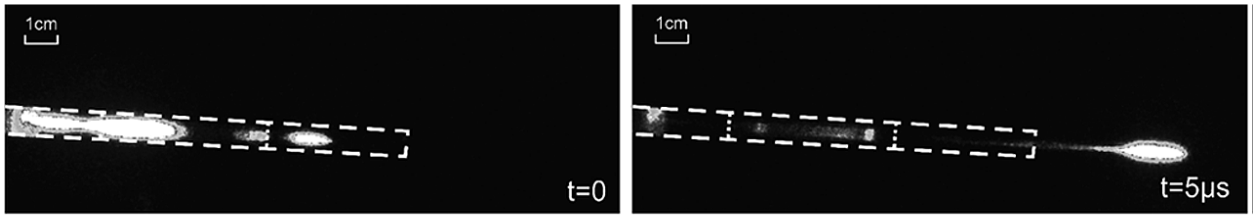

Figure 1.1 Image of plasma bullet propagating (a)inside the dielectric tube and (b)in ambient air with 100 ns exposure time [22].

However, the word "plasma bullet" is misleading, as it implies that the ionization front is a distinct plasma cloud. Many researches show that the ionization degree of gas between the plasma bullet and electrode is as high as in the plasma bullet although the light emission is much lower. Thus, the plasma bullet is in fact electrically connect to the electrode via this ionized channel. Shashurin *et al.* measured the electric potential of the plasma bullet and found no significant voltage drop along the tube [24]. Sretenović *et al.* measured the electric field and estimated the electron density, showing that the electron density in the plasma channel is about 10^{11} cm^{-3} [25].

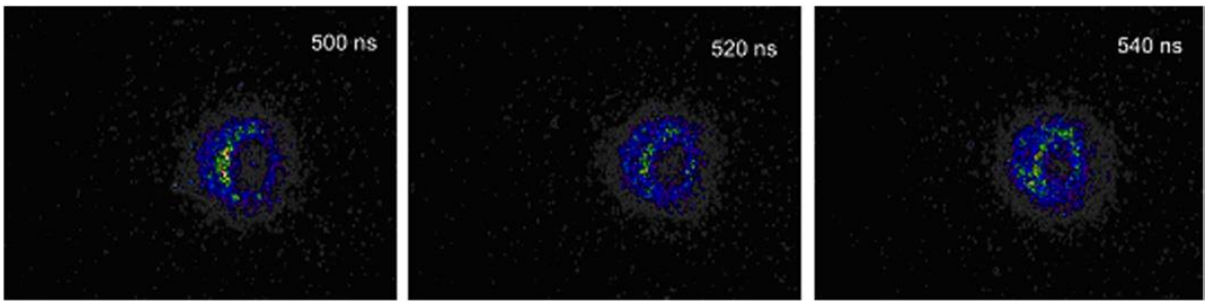

Figure 1.2 On-axis photographs of the plasma bullets in helium illustrating their donut shape [26].

The plasma bullet is considered as a surface discharge whose propagation is guided by the capillary inner surface. While propagating in the tube with a diameter of more than about 500 μm, in the axial direction, the plasma bullet has a "donut" shape, as shown in figure 1.2. The donut shape plasma bullet has been widely reported [27–29]. Simulation results shows that the highest electric field and electron density appears close to the capillary inner surface instead of the center [30,31]. Figure 1.3 shows the simulated radial profile of electron density in the streamer channel in a 0.4 cm diameter tube at different axial positions, showing that the maximum value appears between the center and surface, and that the electron density at the center is much lower [30]. However, further studies show that the radial profile of the plasma bullets depend on the capillary wall permittivity, capillary diameter, electrode geometry, etc [28,32–34]. For example, Jansky *et al.* reported that the plasma is homogenous in radial direction if the tube radius is 100 μm [33].

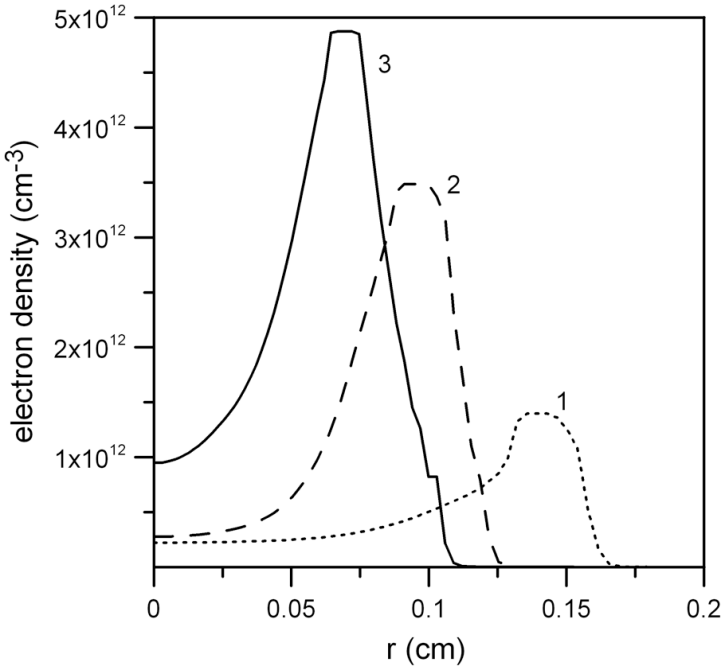

Figure 1.3 Simulated radial profiles of electron density in the streamer channel at the axial positions x = 0.5 (1), 1.0 (2) and 1.5 (3) cm. The helium flow rate is 2.8 l/min in a tube with 0.2 cm radius.[30]

1.2.1 Plasma jet configurations and applications

In the past few decades, researchers designed many types of plasma jet for different purposes.

The powered electrodes used in APPJ can be classified to pin electrodes and ring electrodes. Pin electrode is usually a metal electrode with small curvature radius and is inserted into the capillary. It can also be a thin metal tube so that it can be used to inject the gas at the same time. Some example of APPJ using pin electrode is shown in figure 1.4. The advantage of a pin electrode is the high electric field near the tip due to the small curvature radius. Plasma can be ignited with a relatively small voltage. However, when treating a target, between the electrode and target, a conductive column could be formed without any dielectric layer to limit the current, so the plasma risks to transform to arc. In this case, plasma jets with pin electrodes are not the best for biomedical applications due to safety issues [35]. The risk of forming arc can be avoided by a thin dielectric layer coating on the electrode surface.

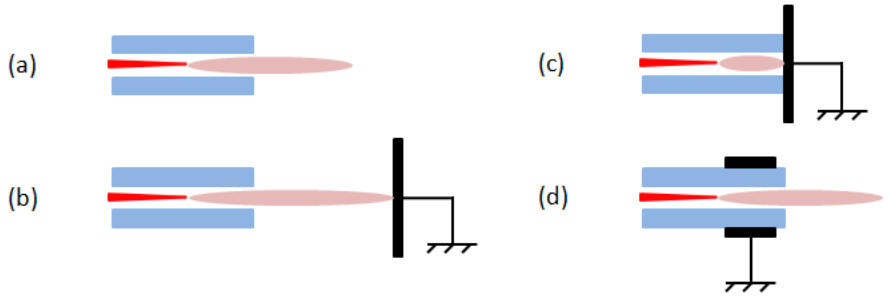

Figure 1.4 Typical APPJ configuration with internal needle-like powered electrodes.

Ring electrode is usually a ring shape metal wrapped around the capillary outer surface. Some examples are shown in figure 1.5. The presence of the dielectric layer between the discharge channel and electrode prevents the formation of arcs. Due to the distance between the electrode and the gas, the electric field in the capillary generated by the electrode is smaller compared to the electric field generated by a pin electrode, thus higher applied voltage is needed to ignite the plasma jet. However, due to the memory effect, which will be discussed later, the voltage required to maintain the discharge is lower than the ignition voltage [36].

A ring-shape ground electrode is commonly used on the plasma jets, like shown in figure 1.4(d) and figure 1.5(b). It forms a DBD gap region, which is considered to enhance the electric field in the inter-electrode gap region. In this case the propagation length is increased and the ignition voltage is decreased.

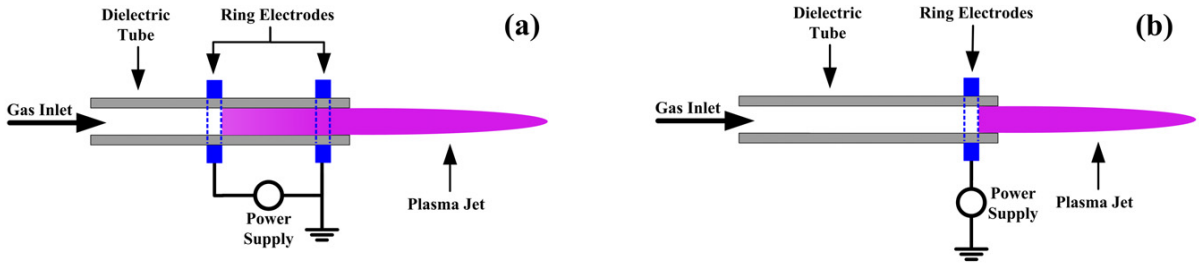

Figure 1.5 Typical APPJ configurations with external ring-like powered electrodes.[23]

1.2.2 Plasma jet propagation important parameters: frequency, voltage, flow rate

Other than the geometry of the electrode, the propagation of plasma jet is influenced by many parameters. In this section, we will discuss the influence of voltage waveform, voltage amplitude, voltage frequency, gas flow rate, and capillary diameter.

The most common power supply used for plasma jets is DC pulsed power supply and AC sinusoidal power supply. AC sinusoidal power supply is widely used in plasma jet applications. It ignites plasma bullets during both the positive and negative half cycle. Depending on the voltage and frequency, more than one plasma bullet can be ignited in every half cycle. Mussard *et al.* reported that multiple plasma bullets are ignited in one half-cycle in an APPJ powered by 600 Hz sinusoidal voltage, and the propagation length of these plasma bullets increases consecutively [37]. Under some conditions, the ignition of plasma bullets is unstable, i.e. the jitter of ignition time in every cycle is significant compared to the voltage period [38–43]. DC pulsed voltage is widely used in many researches of plasma jets. The voltage rises fast at the beginning of the voltage pulse, which helps ignite plasma bullets stably. Another advantage of DC voltage is the adjustable duty cycle and pulse width, which allows the scientists to study the effect of time between two discharges.

1.2.3 Memory effect: volume charges vs surface charges.

Memory effect means that the ignition and propagation of a discharge are influenced by the residual charges left by the former discharges. A discharge can create an ionized column with charged particles and metastable species, whose density decreases over time, and will influence the next discharge. A discharge can also deposit charges on the dielectric surface, which changes the electric field and influence the next discharge. In this section, we will discuss how the volumetric residual charges and the surface residual charges affect the discharges.

Volumetric residual charges

After one discharge, the electrons and ions recombine and the electron density decreases exponentially. Figure 1.6 shows two examples of electron density evolution in a helium APPJ

as a function of time. Schans *et al.* measured the electron density in an N_2 APPJ, showing that the electron density decayed by 3 order of magnitude 60 μs after the discharge [44]. Both studies shown in Figure 1.6 show that the decay rate of electron density depends on the operation conditions, like the input power, flow rate and pulse width.

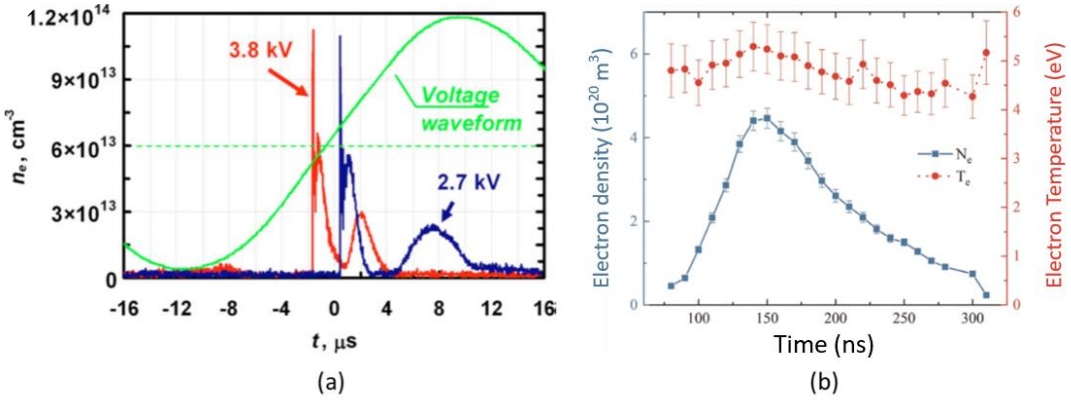

Figure 1.6 (a) shows the electron density evolution of an AC-driven helium plasma jet in several microseconds [45]. (b) shows the electron density evolution of a helium plasma jet (pin-to-plane) driven by 8 kV pulsed voltage in a few hundred nanoseconds and was recently measured with Thomson scattering method [46].

The electrons that exist before a discharge are called seed electrons. The seed electrons density is influenced by the voltage frequency, and duty cycle in case of pulsed discharges. Other than the electron left by the previous discharges, the sources of the seed electron also include the fast electron detachment from the accumulated O_2^- ions, pre-ionization by atmospheric radon [47].

Wu *et al.* investigated the effect of seed electron on plasma bullet propagation by changing the pulse repetition frequency, and reported that plasma bullets appear random with frequency lower than 0.2 kHz, which corresponds to n_{seed} of 10^5 cm^{-3} according to simulation [48]. Nijdam *et al.* show that the discharge propagation is likely to follow the path of the previous discharge propagation which has an electron density of more than 5×10^{11} cm^{-3} in 133 mbar argon gas [49]. However, the streamer cannot propagate into a region with too high electron density like 10^{13} cm^{-3} in atmospheric-pressure room-temperature air [49,50]. The velocity of streamer or plasma bullets are investigated with different seed electron densities, and the results show that the propagation velocity is independent to the seed electron density below 10^{10} cm^{-3} [51–53]. Ning *et al.* also proposed that the relatively long-lifetime metastable species can reduce the ionization threshold and promote the discharge by Penning ionization [39,54,55].

Surface residual charges.

The surface charge deposition has been intensively investigated in DBD. When a discharge propagates to a dielectric surface, charges are accumulated on the surface and form an electric field with a direction opposite to the applied electric field. The voltage formed by the surface

charges can be called the memory voltage. Thus, the gap voltage which ignites the plasma is equal to the sum of the memory voltage and the applied voltage. Figure 1.7 shows the time evolution of the voltage and discharge current of an argon DBD [56]. When a discharge is ignited, the memory voltage changes polarity, and the gap voltage decreases. This also explains why the applied voltage is usually low when a breakdown happens. The memory voltage decreases the gap voltage after breakdown, causing the disappearance of discharge, and increases the gap voltage before breakdown when the applied voltage polarity reverses. As a result, once the plasma is ignited, the applied voltage needed to sustain the plasma is lower than the applied voltage needed to create the plasma [57].

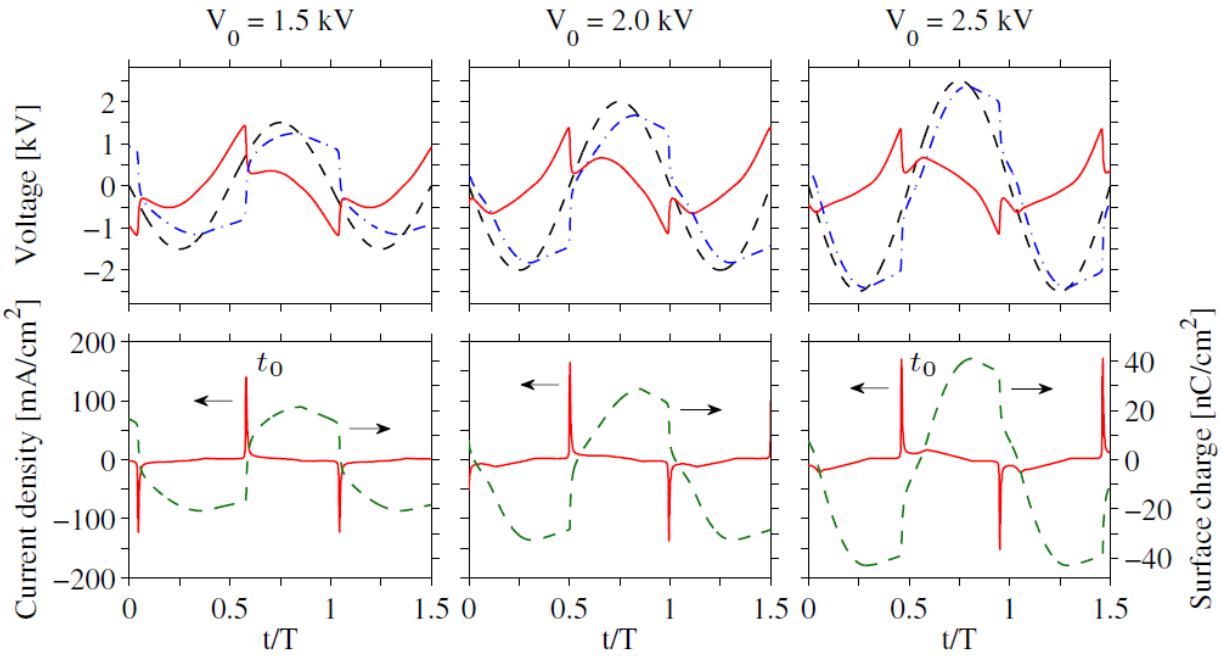

Figure 1.7. Top: Temporal variation of applied voltage (black), gap voltage (red) and memory voltage (blue) with different applied voltages. Bottom: corresponding temporal variation of current density (red) and surface charge density (green). The results are measured in an asymmetric argon DBD with an electrode gap of 1.5 mm and a dielectric layer thickness of 0.5 mm [56].

The lifetime of the surface charges depends on the gas composition, dielectric material [58], etc. In general, it is considered to be much longer than the life time of volumetric residual charges. The memory voltage shown in figure 1.7 decreases very little between two discharges, or even increases due to the continuous small current of the discharge column. Brandenburg *et al.* reported that after switching off a nitrogen atmospheric pressure DBD, within 14 hours, the voltage needed to re-ignited the plasma is lower than the voltage needed for the first ignition [36]. Robert *et al.* investigated a plasma jet powered by negative pulse voltage, and reported that the length of plasma propagation decreases while frequency increases from 1 to 75 Hz, and become constant after 100 Hz [59], which implies that the influence of residual charges last for about 20 ms. Robert suggests that the surface charge of the same polarity shield the electric potential, thus reduce the propagation length. Mussard *et al.* reported that in a 600 Hz

AC-driven helium APPJ, when a positive plasma bullet propagated from a positively charged region to a negatively charged region, the light intensity and propagation velocity are increased due to the electric field caused by the surface discharges [37]. This result implies that the surface charges in a helium APPJ made of glass can sustain more than 1 ms.

1.2.4 Periodic vs random plasma jet

Numerous researches reported the nonlinear behaviors of the DBD and plasma jets, like the formation of patterns, striation, discharge modes, turbulence, etc [36,60–62]. One of the phenomena that attract much attention is the chaos and period multiplication of discharge in plasma jets driven by AC voltage. In chaotic mode, the parameters of plasma like discharge current, light intensity, velocity, etc. exhibit random features. While in periodic mode, the plasma parameters can be the same in every AC cycle, or exhibits a periodic evolution, whose period is an integer multiple of the voltage period.

Qi *et al*. did one of the earliest investigations of multi-periodic behavior in plasma jets. They reported that the discharge current amplitude evolution can have a period of 8P or 9P or exhibits randomness, depending on the frequency and voltage[63]. P here represents the period of applied voltage, and this denotation will be used in the rest of this manuscript. Walsh *et al.* reported similar behavior of discharge current in a ring-to-plate plasma jet exhibiting 1P, 2P and 3P [38]. Liu *et al.* reported periodic and chaotic modes in a pin-to-ring plasma jet while treating a water target [40]. However, the research mentioned above focused only on the phenomenological description of the multi-periodic behavior using electrical diagnostic methods. The ignition and propagation of the discharges in different periods of the nP modes were not compared, and the mechanism remains unclear. Schweigert *et al.* [43]used a pin-to-ring plasma jet to treat a target, and found the touching-target current exhibited multi-periodic behavior. They explained that the ionized gas created by a strong discharge reduced the propagation of the next discharge, as plasma is shown to be unable to penetrate to regions with too high electron density [50]. They further validated their assumption using 2D fluid model simulations. However, optical diagnostic was not used to observe the ignition and propagation process, thus it is questionable to use the same model for discharge process in different periods, and their explanation did not include surface charges which should play an important role in the plasma ignition phase.

More work on spatial and temporal self-organization behaviors has been done in DBDs, and the role of surface charges has been addressed. Berneker *et al.* investigated a DBD in Neon at 100 torr and found that the discharge filaments form a honeycomb structure [64]. Their group pointed out the important role of the surface charges in forming these spatial discharge patterns [61]. Célestin *et al.* show how the surface charges deposited upon the dielectric plate modify the spatial organization of microdischarges in a pin-to-plate AC DBD [65]. Chirokov *et al.* investigated the 2D distribution of a micro DBD, and proposed that the deposited surface

charges facilitate the new avalanches and result in the formation of localized streamers [66]. Meanwhile, some works also pointed out the role of volumetric residual charges on the ignition and propagation of DBDs [50,67]. Temporal chaotic behaviors of NTP are first reported by Cheung *et al.*, who found period-doubling bifurcation and chaos in a low-pressure argon discharge [68]. Want *et al.* were the first to report period multiplication and chaos in a 1D fluid mode of an atmospheric pressure parallel plate DBD [69]. They pointed out that a strong discharge creates high surface charge accumulation, and leads to a following weak discharge of opposite polarity. Similar methods were later used to find more temporal patterns of DBD [70,71]. Dai *et al*. later reported period multiplication of atmospheric pressure DBD experimentally [72].

However, most of these experiments used parallel plate DBD. In a plasma jet, the surface charge deposition is not only near the electrode, but also along the dielectric surface of plasma propagation route. Thus, it is unclear whether we can use the same model to explain the multi-periodic discharge in plasma jets, and the role of surface deposited charges and volumetric residual charges remains to be investigated.

APPJ has been intensively investigated due to its potential application in medical fields. Depending on the operating conditions such as frequency, voltage, gas flow rate, etc., the ignition of plasma in APPJs can exhibit periodic or random characteristics. This is attributed to the memory effect linked to the presence of volumic or surface residual charges between two consecutive discharges.

1.3 Plasma jet chemistry

Due to the important role of plasma-created Reactive Oxygen and Nitrogen Species (RONS) in biological applications, the chemistry of plasma interacting with ambient air and liquid has gained increasing attention. This section summarizes the works on the production of RONS, its effect in plasma medicine, and the mechanism of RONS production.

1.3.1 ROS and RNS and effect on living tissues

Reactive Oxygen Species(ROS) created by plasma mainly include O_3, H_2O_2, and short-life species like OH• radicals, O•, etc. The short-life species only have a lifetime of milliseconds [73], and will reacts with each other or other species to form stable species like H_2, O_2, O_3, H_2O, H_2O_2, etc.

Using plasma to produce ozone dates back to one hundred years ago. It is well-known for its efficiency in bacteria efficiency. However, it is harmful to human health at concentrations of ppm level.

The biological effect of H_2O_2 has been intensively studied in the past ten years. High concentration of H_2O_2 causes oxidative damage to cells and leads to cell death [74,75], which is considered to be useful in NTP cancer therapy. H_2O_2 is also produced in human cells. Low-concentration H_2O_2 is known as a signaling molecule which plays an important role in regulating metabolism, phosphatase activity and gene transcription in cytoplasm [75]. It is also found to be an important mediator of wound healing process and initiates inflammatory process [76].

Most of the short-life species transform to long-life species in submicroseconds to milliseconds time scale, so it is difficult to study their effect. However, many experiments show that Plasma Activated Water(PAW) treatment has less effect than direct plasma treatment on biological tissues, which implies that the short-life species also play an important role [77]. Van der Paal *et al.* investigated the interaction of plasma generated OH• with a model which is an approximation of the upper layer of the skin, showing that it eventually leads to the degradation of the skin barrier function and enhancement of the drug delivery through skin barrier [78]. Pan *et al.* used a plasma jet for teeth whitening, and reveal that OH radical enhanced the bleaching effect [79].

Reactive nitrogen species are mainly formed in gas phase while interacting with ambient air. Nitrogen oxides like NO and NO_2 are created in gas phase, and eventually form acids, like nitrite (NO_2^-) and nitrate(NO_3^-). RNS can also be oxidized by ROS, forming HNO_3, NOOH, NOO^-, etc.

Some RNS is known to have an important effect on cells. For example, NO is known to improve angiogenesis in tissue repair model [80] and promote tissue and burn wound repair[81,82]. NO_2^- also has many therapeutic applications [83]. NO_2^- can decompose and exhibits strong antimicrobial effects [9]. On the other hand, it can also release NO in an acidic environment, acting as a storage of NO [84].

1.3.2 Plasma parameters influencing RONS production

To manipulate the RONS production of plasma jets for medical applications, numerous researches were conducted.

Electrical parameters

The electrical parameters directly influence the discharge properties, thus influence the RONS production. According to published works, type of power supply (ac or dc pulsed), applied voltage and frequency are reported to have an impact on RONS production of APPJ.

Uchida *et al*. compared the H_2O_2 and NO_2^- production of He 5 kHz APPJ and an Ar RF APPJ, the results show that H_2O_2 is the dominant species in low-frequency He jet, while NO_2^- is the dominant species in high-frequency Ar jet [85]. While if using the same frequency (30 kHz), Ogawa *et al.* found that Argon APPJ is slightly more efficient in producing H_2O_2 than NO_2^-. Baek *et al.* investigated the effects of electrical parameters and gas flow rate on RONS production of a He APPJ driven by a pulsed bipolar source [86]. The results show that the increase of applied voltage and pulse frequency lead to the increases of OH• and NO in gas phase and liquid phase. Omran *et al.* showed that increasing frequency in kHz range leads to a more uniform distribution of plasma on the water surface, therefore more air can mix with the plasma plume and cause more RONS production [87].

Gas Parameters

The RONS production is also influenced by gas parameters, including the injected gas composition, gas flow rate, and gap distance. While treating liquid targets, the gas flow rate and gap distance will influence the mixing of injected gas with ambient gas as well as the water evaporated from the target, thus changing the gas composition in the plasma plume. For example, Yagi *et al.* measured the humidity and OH radical density in the plasma plume treating water using LIF method, and the results show that when the flow rate increases from 0.05 slm to 0.3 slm, the humidity and OH• radical density both decrease in the plasma plume [88]. Baek *et al.* reported that when varying the flow rate from 0.5~4 slm, the RONS production is maximum when the flow rate is around 2 slm [86].

The target distance (the distance between the APPJ outlet and the target) influences the plasma power delivered to the water surface and the mixing with ambient air in the plasma plume. When the target distance is small, the plasma power delivered to the liquid is strong, but the N_2, O_2 and H_2O impurities in the plasma plume are small; if the gap distance is big, the plasma power delivered to the liquid becomes weak, but the impurities in the plasma plume are high. Oh *et al.* reported that the production of RONS is maximum when the gap distance is about 30 mm [89]. However, Uchida *et al.* reported that the RONS production in water monotonically decreases with the increase of gap distance, and no maximum point is found[90]. This agrees with the results obtained by Ghimire *et al.* using an Ar plasma jet with 24 kHz frequency [91].

The gas composition can be influenced not only by the flow rate and gap distance. Researchers also try to add H_2O, N_2 or O_2 impurities to the He or Ar gas injected to the plasma jet. Li et al. reported that the OH• production efficiency gradually decreases while air percentage in helium increase from 0 to 2%; at the same time, ozone production efficiency increases; a small increase of O_2 percentage from 0 to 0.1% drastically decrease the NO production efficiency by 90% or 99% or more depending on electrical parameters [92]. Gorbanev *et al.* increased the relative humidity of helium gas, and found that the H_2O_2 and OH• concentrations increase with the humidity, and 0.5% of O_2 will decrease the H_2O_2 production in the case of high humidity [93].

In summary, the production of RONS by plasma jet is influenced by many parameters, including the electrical parameters which influence the discharge properties, and the gas parameters which mainly influence the gas composition. High impurities provide particles for the formation of the plasma jet, but too high impurities are toxic for plasma generation. Therefore, it is possible to manipulate the production of RONS by changing these parameters, but due to the complex interaction of many parameters, it is important to characterize the influence of these parameters on RONS production for each plasma jet design.

1.3.3 Production of H_2O_2

As the effect of RONS on living tissues are usually highly dose-dependent, it is important to quantitatively control the production rate of RONS. Thus, researchers made much effort to understand the formation mechanisms of RONS.

H_2O_2 can be formed in gas phase and diffuse to the liquid, or be formed directly in liquid phase via direct plasma-liquid interaction. Experiments are conducted to clarify the pathway of H_2O_2 formation in plasma liquid interaction, but different conclusions were drawn by different groups.

Gorbanev *et al.* investigated the origin of some reactive species in water created by an AC-driven helium APPJ using isotope labeling, spin-trapping and electron paramagnetic resonance (EPR)[93]. The results suggest the liquid phase H_2O_2 delivered to the sample is almost exclusively created in gas phase from species in the plasma tube. Hefny *et al.* found the H_2O_2 produced in water by a helium APPJ is correlated to the humidity of helium, which implies that the H_2O_2 is mainly formed in the plasma tube if there are water impurities in discharge gas [94].

On the contrary, He *et al.* used Dimethyl sulfoxide as a scavenger of hydroxyl (OH) radicals to investigate the contribution of dissolved OH• radicals to the H_2O_2 in a DC pulsed Argon APPJ, and the result indicates that with both positive and negative discharges, the H_2O_2 formed in liquid mainly results from the combination of OH• radicals at the liquid surface, while to dissolution of gaseous H_2O_2 and plasma-induced ultraviolet radiation has no contribution[95]. Chen *et al.* compared three pathways of H_2O_2 formation in water treated by helium DC voltage, and concluded that the OH• combination at the water surface is dominant compared to the dissolution of gaseous H_2O_2 and electrolysis [96].

Meanwhile, the origin of OH• radical formation has been investigated. Gorbanev *et al.* concluded that OH_{aq} radicals are mainly formed in gas phase in the gap region between the tube nozzle and water surface [93]. Attri *et al.* investigated the generation mechanism of OH• radical in biosolution treated by an argon APPJ, and concluded that the plasma-initiated UV photolysis continuously generate OH• species [97]. This is contradictory to the conclusion of He *et al.* about UV photolysis makes no contribution to H_2O_2 formation, with the assumption that the main source of H_2O_2 is OH•.

In conclusion, the origin of H_2O_2 formed in liquid by plasma jet treatment is unclear, as different results were reported by different groups. It is possible that the origin of H_2O_2 is related to the different designs of the plasma jet, like tube and electrode geometry, gas, voltage waveform and frequency, etc., and needs to be characterized for each plasma jet [85].

APPJ can produce abundant RONS, which is known to have an important effect on the metabolism of living tissues. The production efficiency of RONS by APPJ is influenced by many parameters like the type of high voltage waveform, the gas flow rate, and the gas composition, etc. In particular, the production mechanisms of H_2O_2 are intensively discussed and different conclusions were reported. It is unclear whether the H_2O_2 is formed in the bulk plasma or on the plasma-liquid interface.

1.4 Mueller Polarimetric Imaging as a tool to diagnose the effect of plasma on pig skin

1.4.1 Principle of Mueller Polarimetric Imaging

The polarization state of light can change due to the interaction between light and mediums, including process of scattering, birefringence and dichroic absorption. When polarized light propagates thought a medium, the more it is scattered, the more it loses polarization. Polarization imaging measured the change of polarization due to interaction with mediums, which is determined by the microstructure of the mediums.

1.4.2 MPI parameters and skin microstructures

For a light in three-dimensional space, the intensity and polarization state together can be described by 4 parameters that are linearly independent. The number of combinations of the 4 parameters are infinite. Stokes vector is a 4×1 column vector grouping a combination of 4 parameters, which are four measurable light intensities. It is a commonly used method to describe the polarization state. The definition of Stokes vector is equation(1.16).

$$\boldsymbol{S} = \begin{bmatrix} I \\ Q \\ U \\ V \end{bmatrix} = \begin{bmatrix} I_H + I_V \\ I_H - I_V \\ I_{45°} - I_{-45°} \\ I_R - I_L \end{bmatrix} \tag{1.1}$$

Where I, Q, U, V are the four components of the Stokes vector. I represents the total intensity of the light. It is often normalized to 1; Q, U and V are normalized accordingly. Naturally, I is

equal to the sum of the intensity of the two light components that are linearly polarized in horizontal direction (I_H) and vertical direction (I_V). Q represents the difference of light intensity I_H and I_V; U represents the intensity difference of the two light components that are linearly polarized in 45° direction($I_{45°}$) and -45°direction($I_{-45°}$); V represents the intensity difference of the two light components that are circularly polarized in right-handed (I_R)direction and left-handed direction (I_L). Naturally we have equation (1.16)

$$I = I_H + I_V = I_{45°} + I_{-45°} = I_R + I_L \tag{1.2}$$

So, equation (1.1) can also be written as equation(1.16)

$$\boldsymbol{S} = \begin{bmatrix} I_H + I_V \\ I_H - I_V \\ 2I_{45°} - (I_H + I_V) \\ 2I_R - (I_H + I_V) \end{bmatrix} \tag{1.3}$$

Definition of Mueller matrix

When a beam of light is reflected on the surface of medium, the Stokes vector of the incident light S changes to the Stokes vector of the reflected light S′. The transformation from S to S′ is a linear transformation, which can be expressed as a 4×4 matrix, which is called Mueller matrix, as equation (1.16)

$$\boldsymbol{S} = \boldsymbol{M}\boldsymbol{S}' \tag{1.4}$$

Where **M** represents the Mueller matrix.

Decomposition of Mueller matrix

In this study, the Mueller Matrix Polar Decomposition (MMPD) is used to analyze the Mueller matrix of the sample. Lu-Chipman algorithm[98] is applied for to decompose the Mueller matrix to the product of three matrices: depolarizer $\mathbf{M_\Delta}$, retarder $\mathbf{M_R}$ and deattenuator $\mathbf{M_D}$, as in equation (1.16)

$$\boldsymbol{M} = \boldsymbol{M_\Delta M_R M_D} \tag{1.5}$$

To decompose the Mueller matrix, it is first normalized with M_{11}:

$$\boldsymbol{M} = M_{11} \begin{bmatrix} 1 & M_{12}/M_{11} & M_{13}/M_{11} & M_{14}/M_{11} \\ M_{21}/M_{11} & M_{22}/M_{11} & M_{23}/M_{11} & M_{24}/M_{11} \\ M_{31}/M_{11} & M_{32}/M_{11} & M_{33}/M_{11} & M_{34}/M_{11} \\ M_{41}/M_{11} & M_{42}/M_{11} & M_{43}/M_{11} & M_{44}/M_{11} \end{bmatrix} = M_{11} \begin{bmatrix} 1 & \boldsymbol{D^T} \\ \boldsymbol{P} & \boldsymbol{m} \end{bmatrix} \tag{1.6}$$

Where **m** is a 3×3 matrix which is the lower right part of **M**. Define $\mathbf{M_\Delta}$, $\mathbf{M_R}$, and $\mathbf{M_D}$ as equation(1.7)~(1.9).

$$\boldsymbol{M_\Delta} = \begin{bmatrix} 1 & \boldsymbol{0^T} \\ \boldsymbol{P_\Delta} & \boldsymbol{m_\Delta} \end{bmatrix} \tag{1.7}$$

$$\boldsymbol{M_R} = \begin{bmatrix} 1 & \boldsymbol{0^T} \\ \boldsymbol{0} & \boldsymbol{m_R} \end{bmatrix} \tag{1.8}$$

$$\boldsymbol{M_D} = \begin{bmatrix} 1 & \mathbf{D^T} \\ \mathbf{D} & \boldsymbol{m_D} \end{bmatrix} \tag{1.9}$$

$\mathbf{m_D}$ is expressed by (1.10), where $\mathbf{I}$ is a 3×3 unit matrix.

$$\boldsymbol{m_D} = \sqrt{1-\boldsymbol{D}^2}\mathbf{I} + \left(1-\sqrt{1-\boldsymbol{D}^2}\right)\boldsymbol{D}\boldsymbol{D}^T \tag{1.10}$$

Thus, $\mathbf{m_\Delta}$, $\mathbf{P_\Delta}$ and $\mathbf{m_R}$ needs to be solved. Define a Mueller Matrix $\mathbf{M'}$ as equation(1.11):

$$\boldsymbol{M'} = \boldsymbol{M}\boldsymbol{M_D^{-1}} = \boldsymbol{M_\Delta}\boldsymbol{M_R} = \begin{bmatrix} 1 & \boldsymbol{0^T} \\ \boldsymbol{P_\Delta} & \boldsymbol{m_\Delta}\boldsymbol{m_R} \end{bmatrix} = \begin{bmatrix} 1 & \boldsymbol{0^T} \\ \boldsymbol{P_\Delta} & \boldsymbol{m'} \end{bmatrix} \tag{1.11}$$

Thus, $\mathbf{m_\Delta}$ can be obtained by equation(1.12)

$$\begin{aligned} \boldsymbol{m_\Delta} = \pm\left[\boldsymbol{m'}(\boldsymbol{m'})^T + \left(\sqrt{\lambda_1\lambda_2}+\sqrt{\lambda_2\lambda_3}+\sqrt{\lambda_3\lambda_1}\right)\mathbf{I}\right]^{-1} \\ \times\left[\left(\sqrt{\lambda_1}+\sqrt{\lambda_2}+\sqrt{\lambda_3}\right)\boldsymbol{m'}(\boldsymbol{m'})^T + \sqrt{\lambda_1\lambda_2\lambda_3}\mathbf{I}\right] \end{aligned} \tag{1.12}$$

The sign of $\mathbf{m_\Delta}$ follows the sign of the determinant of $\mathbf{m'}$. λ_1, λ_2 and λ_3 are the eigen values of the matrix $\mathbf{m'}(\mathbf{m'})^T$.

$\mathbf{P_\Delta}$ is obtained by equation (1.16).

$$\boldsymbol{P_\Delta} = \frac{\boldsymbol{P}-\boldsymbol{m}\boldsymbol{D}}{1-\boldsymbol{D}^2} \tag{1.13}$$

Now that $\mathbf{M_\Delta}$ is obtained, $\mathbf{M_R}$ can be calculated according to equation (1.11).

With $\mathbf{M_\Delta}$, the total depolarization parameter Δ is defined as equation

$$\Delta = 1 - \frac{|tr(\boldsymbol{M_\Delta})-1|}{3}\ (0 \le \Delta \le 1) \tag{1.14}$$

With the retarder matrix, the total retardance R is defined as equation(1.16)

$$R = \arccos\left[\frac{\mathrm{tr}(\boldsymbol{M}_R)}{2}-1\right] = R_L + R_C \tag{1.15}$$

Where R_L and R_C are the linear retardance and the circular retardance, respectively. In this study, R_L is analyzed. It is calculated with equation (1.16) [99].

$$R_L = \arccos\left[\sqrt{(M_{R22}+M_{R33})^2+(M_{R32}+M_{R23})^2}-1\right] \tag{1.16}$$

Interpretation of Mueller matrix parameters

The polarization degree of a light beam is defined as the ratio of the intensity of its fully polarized component to the its total light intensity. Total depolarization Δ is equal to the change of polarization degree when a light beam is refracted on a medium. The change of polarization

is caused by the birefringence effect and the optical rotation of the medium. It is related to the surface topography and the microstructure of the medium. The change of total depolarization is caused by the random scattering effect when a light interacts with a media.

The linear retardance R_L is the linear phase shift between the ordinary ray and extraordinary ray which are formed after a light interacts with a birefringent media. In biological tissues, the linear retardance is caused by the fibrous structures which are most collagen fibers.

1.4.3 NTP effect on skin microstructures

Several complex biological processes appear when NTP (Non-Thermal Plasma) interacts with skin tissue. The investigation of these processes opened the way to a new promising multidisciplinary research field in dermatology. Indeed, NTP can help to heal skin wounds such as burns and incisional wounds [17,77,100], cure skin diseases such as psoriasis [101], pruritus [102], and atopic dermatitis [103]. In clinical and preclinical trials, NTP treatment appeared to favor wound healing at low power or shorter treatment time. Indeed, NTP exhibits both antibacterial activity [104] and pro-healing effects with the stimulation of cell motility [77,105], as well as improved extracellular matrix deposition and angiogenesis in wounds [17,106].

At higher power, NTP treatment induces cell death, exhibits anti-tumoral properties [107–109], and helps blood coagulation in wounds [110,111]. These effects can also be associated with the modification and damage in the skin's extracellular matrix induced by the NTP treatment [112,113]. However, the leading causes behind such microstructural modifications are still unclear. They may be due to the RONS but also to the increase of the skin temperature depending on the plasma treatment conditions. In particular, thermal effects can play a crucial role in NTP treatment's microstructural changes induced on the skin. Indeed, the experiments of Chernets *et al.* [114] showed that the temperature at the center of B16-F10 tumor in C57BL/6 mice is approximately 27°C higher than the average tissue temperature. The observed increase in the local temperature was associated with macroscopically visible tissue damage just after plasma exposure [114]. These macroscopic tissue changes are due to microscopic alterations that remain very difficult to characterize and quantify.

Changes in tissue microstructure, sometimes unobservable on intensity-based images or with the naked eye, can be clearly detected by Mueller polarimetric imaging (MPI). This technique has received increasing interest in the last few years. In particular, its ability to provide a comprehensive polarimetric characterization of biological tissues at various penetration depths, using different wavelengths in the visible spectral range, is of tremendous interest for biomedical applications [115,116]. The great advantage of this technique is that it can be implemented with a wide field of view to analyze large areas (up to several cm^2) while providing information concerning the tissue microstructure, impossible to obtain with conventional intensity-based imaging. In addition, this non-invasive diagnostic tool does not

require tissue contact or chemical reagents. For all these reasons, the number of biomedical applications of MPI has grown considerably in the last few years. In particular, this technique appears as a promising tool to improve cancer detection on a wide variety of biological tissues such as cervix [117–121], colon [122–124], rectum [125], intestine [126], and skin [127,128]. Recently, it has been used to characterize the photo-damaging process in mouse skin and evaluate the effectiveness of sunscreens developed to prevent skin aging and disease generated by daily UVR exposure [129]. Finally, the development of Mueller polarimetric endoscopic systems can improve the detection of pathologies on the surface of internal organs [130,131].

Mueller polarimetric imaging (MPI) can be a fast, non-invasive, without-contact method to detect modification of living tissue structures such as the productio of collagen or the presence of cancer cells. MPI has been used for the detection of the tissue microstructure change on cervix, colon, rectum, etc. We will first time use this diagnostic to investigate physical changes of inert skin tissues model exposed to Non-thermal Plasma.

1.5 Summary

Non-Thermal Plasma (NTP) created by electrical discharges have electrons and heavy species in non-equilibrium state. The electron temperature in NTP is typically several electron-volts while the gas temperature can be close to the room temperature. NTP is widely investigated due to its potential in applications in medical fields such as sterilization, wound healing, tumor treatment, etc.

Atmospheric Pressure Plasma Jet (APPJ) is a type of plasma source that generates NTP in a dielectric capillary flown with noble gases such as helium and argon. The ignition and propation of plasma bullets in APPJ depends on operating conditions including the geometry of APPJ, the applied voltage, the gas flow rate, etc. under different operating conditions, the plasma bullets in AC-driven APPJs can exhibit random or periodic behaviors, which is attributed to the memory effect caused by residual charges. However, it is unclear whether the role of surface residual charges or volumetric residual charges is more important.

APPJ can produce abundant Reactive Oxygen and Nitrogen Species (RONS) which play important roles in biomedical process. The production of RONS is influenced by the operating conditions of APPJs. H_2O_2 is one of the long-live Reactive Oxygen Species produced by APPJ. The mechanisms of H_2O_2 formation in liquid by APPJ reported by different groups are different, including formation is gas phase, formation in plasma-liquid interface, and formation in bulk water by photolysis,etc.

NTP applicated in dermatology are operated with different power and caused different effect on the skin. Microstructural modifications are observed to be induced on skin due to NTP

treatment. Mueller Polarimetric Imaging (MPI) provide a fast, non-invasive method to diagnose such modifications.

Chapter 2. Material and methods

2.1 Plasma source and diagnostic methods

2.1.1 Plasma source

The plasma jet is built to study the propagation of plasma in APPJ. The plasma is generated in a capillary made of glass(pyrex). The inner diameter and outer diameter are 1 mm and 4.2 mm, respectively. The total length of the capillary is 15 cm. The gas inlet of the glass capillary is connected to a nylon gas tube via a connecter which is manufactured with a 3d printer. The material of the 3d printed connecter is PLA(Polylactic acid).

The discharge gas is pure helium (Airliquid Alphagas 1 Helium). The impurities in the gas bottle include H_2O (< 3 ppm) and O_2(< 2 ppm) according to the labeling. However, more impurities are present in the discharge gas due to molecule desorption on the inner surface of the gas tube and glass capillary. The impurities in the discharge gas are analyzed and will be introduced in section 2.3.

For the pin-to-ring configuration shown in figure 2.1, the powered electrode is a needle made of stainless-steel. It is inserted into the capillary through the 3d-printed connecter. It a has 0.3 mm diameter, and the curvature radius of the tip is ~200 μm. The ground electrode is made of copper tape wrapped on the outer surface of the glass capillary. The width of the ground electrode is 3 mm. In this thesis, the interelectrode gap distance is varied from 5 mm to 40 mm.

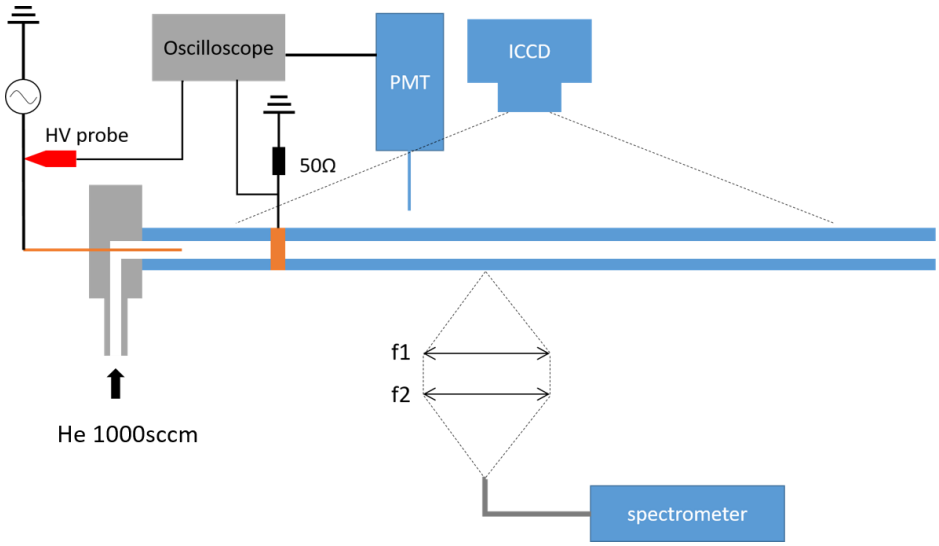

Figure 2.1 Schematic of the APPJ and diagnostic methods that are used.

Two power supplies were used. The AC power supply (Coronalab CPT-2000K) provides a sinusoidal voltage. The frequency ranges from 9 kHz to 18 kHz. However, while the frequency is in the range of 11 kHz~13 kHz, the voltage is unstable due to resonance with the plasma source. The maximum voltage provided depends on the frequency. For example, when f = 16 kHz, the maximum peak-to-peak voltage(V_{PP}) is 10 kV with a relative standard deviation of ~0.6%.

The DC power supply (Eagle Harbor Technologies, NSP-120-20-P-500-L) provides positive voltage pulses. The frequency ranges from single pulses to 10 kHz. Pulse width ranges from 50 ns to 550 ns. The maximum voltage is 8 kV. The rise time of the voltage pulse is ~100 ns. An example of the voltage pulse is shown in figure 2.2(b).

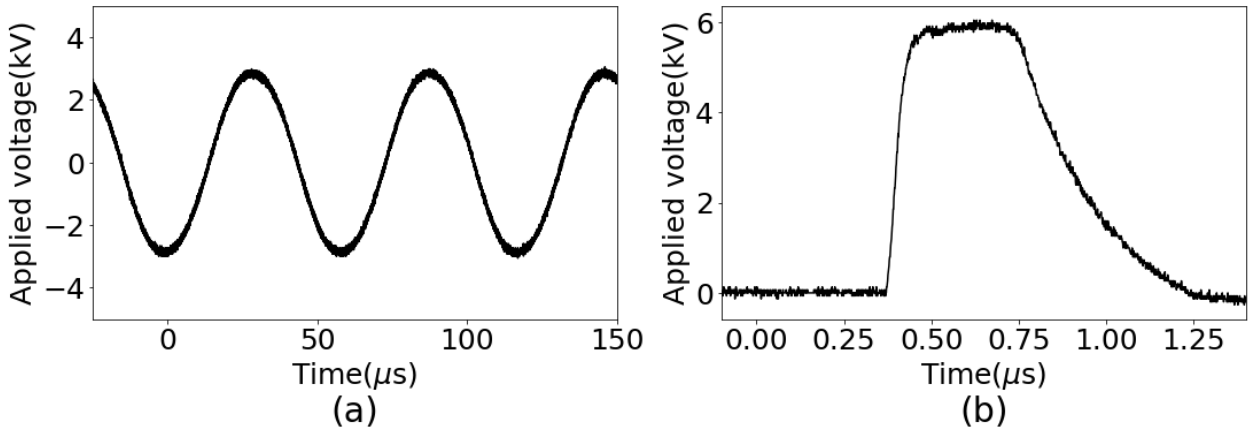

Figure 2.2 (a) The waveform of the voltage provided by the AC power supply. (b) The waveform of the voltage provided by the DC pulsed power supply.

The plasma source for the treatment of the water target is shown in Figure 2.3. It is similar to the jet shown in Figure 2.1, but the inner pin electrode is replaced with an external ring-like electrode with a width of 8 mm. The target is 15 ml of distilled water contained in a plastic petri dish with a diameter of 15 mm. A ground electrode made with aluminum tape is attached to the bottom of the petri dish. A 10 nF capacitor is connected between the bottom aluminum electrode and the ground. The voltage on the capacitor is measured for measuring the charges deposited to the water target and for calculating the power transferred to the water target.

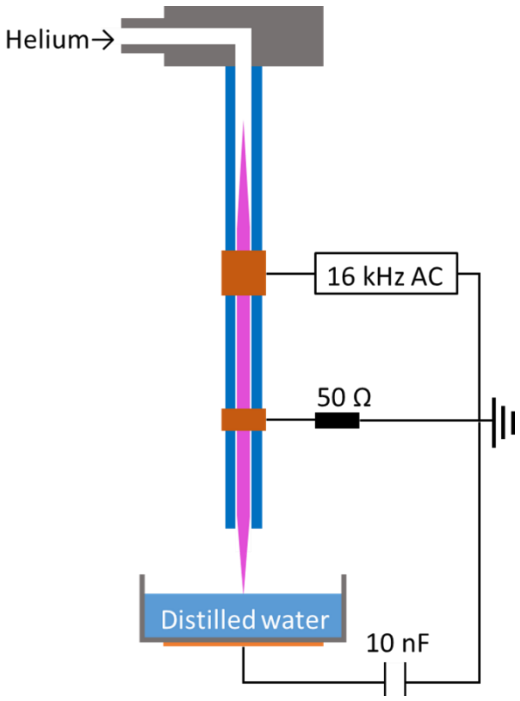

Figure 2.3 The APPJ used for treating water. An 8 mm wide external ring-like powered electrode and a 3mm wide ground electrode is used. The distance between the powered electrode and the ring-like ground electrode is 30 ~ 40 mm.

2.1.2 Electrical diagnostics

The voltage signals are monitored by passive probes PP08(×10 attenuation) and a high-voltage probe (Teledyne Lecroy PPE 20 kV). The signals are recorded and displayed on a digital oscilloscope (Teledyne Lecroy Waverunner 625Zi, bandpass=2.5 GHz).

The discharge current is monitored by a 50 Ω resistor between the ring electrode and the ground. Figure 2.4(a) shows an example of the discharge current of an AC-driven plasma jet. The current peaks are only detected when the plasma propagates to the ground electrode. Figure 2.4(b) shows the discharge current driven by a DC pulse. Due to the short rise time, the DC pulse causes a significant displacement current which needs to be subtracted. The displacement current at a certain applied voltage is measured by switching off the helium gas flow while maintaining the voltage. In this case, the plasma ignition and discharge current disappear, and the signal measured by the oscilloscope is saved as the displacement current and is subtracted from the plasma-on signal.

The amount of charges carried by the plasma is also measured. In this case, we use a 10 nF capacitor to replace the resistor used for current monitoring. The voltage change caused by the displacement current is significant both in AC and DC cases and needs to be subtracted using the same method as subtracting the displacement current from the discharge current. The

plasma charges the capacitor and causes a voltage step, thus the amount of charges ΔQ carried by the plasma is calculated by equation (2.1)

$$\Delta Q = c\Delta U \tag{2.1}$$

Where c is the capacitance and ΔU is the voltage change. An example of the charge Q on the capacitor is shown in figure 2.5.

The voltage on the capacitor can also be used to calculate the plasma power. The average power $\bar{P}$ during one oscilloscope acquisition is calculated according to

$$\bar{P} = \frac{1}{t_{aqui}} \int_{t_0}^{t_0+t_{aqui}} U_a(t) \frac{dQ(t)}{dt} dt \tag{2.2}$$

Where t_{aqui} is the acquisition time of one oscilloscope measurement, U_a is the applied voltage. According to equations (2.1) and (2.2), we have

$$\bar{P} = \frac{1}{t_{aqui}} \int_{t_0}^{t_0+t_{aqui}} U_a(t) \frac{dU_c(t)c}{dt} dt = \frac{c}{t_{aqui}} \int_{t_0}^{t_0+t_{aqui}} U_a(t) dU_c(t) \tag{2.3}$$

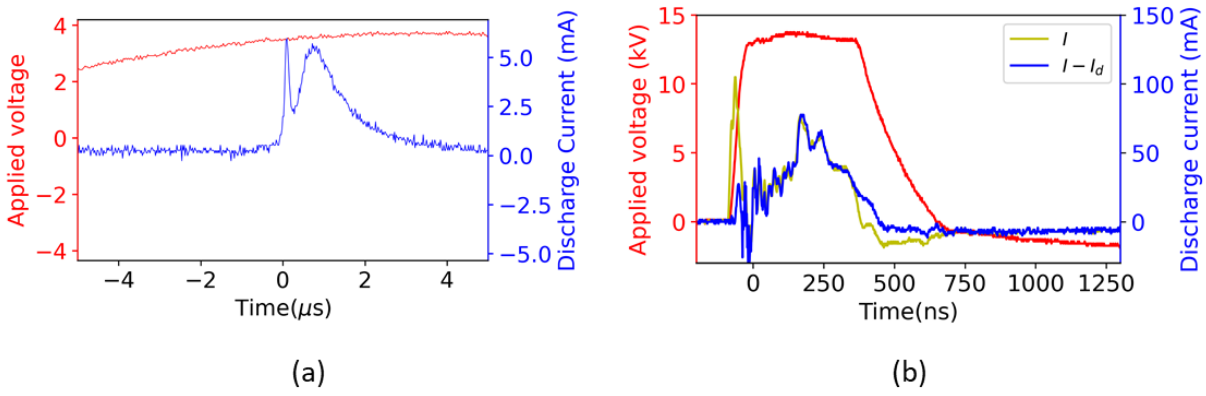

Figure 2.4 Discharge current and applied voltage of the (a) AC-driven APPJ (b) DC-pulsed APPJ. In (b), the measured current I is shown in yellow and the current after subtracting the displacement current I_d is shown in blue.

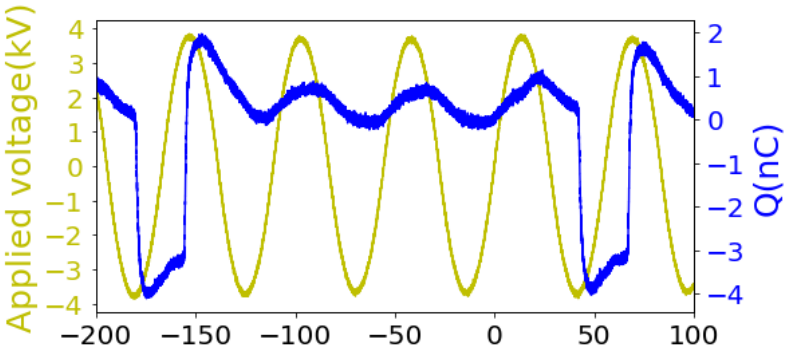

Figure 2.5: Example of the charges measured by the capacitor according to Q=CU (blue curve). The capacitance is 10 nF. V_{pp} = 7.9 kV. The voltage on the capacitor caused by the displacement current is subtracted.

$\bar{P}$ is calculated for every acquisition using the built-in functions of the oscilloscope and is then averaged over all the acquisitions.

2.1.3 Optical diagnostics

Photon multiplier tube

Plastic optical fibers are used to detect the light emitted by the plasma. Optical fibers are fixed using a 3d-printed holder and are perpendicular to the axis of the capillary. The tip of the optical fiber is directly in contact with the surface of the glass capillary.

The light signal is transmitted to a photomultiplier tube (PMT) (Hamamatsu R928, electron transit time of 22ns). The PMT is powered by d DC power supply(Hamamatsu c9525-03) providing -800V DC voltage. The output voltage is monitored by the oscilloscope using 50 Ω coupling.

ICCD imaging

The propagation dynamics of the APPJ are observed by fast imaging recorded with an ICCD camera(Andor iStar). The minimum gate width of the ICCD camera is 20 ns. The camera is triggered by the TTL signal which is output from the oscilloscope when the oscilloscope is triggered by the acquired signal. The internal delay between the triggering of the oscilloscope and the opening of the ICCD gate is 200 ns.

For each photo, the background is recorded with the same gate width and environmental light but without plasma. The background is subtracted from the plasma photos using Matlab.

Optical emission spectroscopy (OES)

The spectrum of the plasma emission is acquired using optical emission spectroscopy. The photons of the plasma emission are acquired with a quartz optical fiber. The effective wavelength of the optical fiber is 200 nm~1000 nm. The tip of the optical fiber is metal, thus placing the optical fiber too close to the capillary will cause a strong perturbation to the plasma propagation. Therefore, two convex lenses are used to collect the plasma-emitted photons, as shown in figure 2.6. The focus length of the two convex lenses is 60 mm and 80 mm. The discharge channel and the optical fiber entrance are placed at the focus plane of the convex lenses. Two spectrometers were used for optical emission spectroscopy.

Spectrometer OceanOptics Maya 2000 pro is used for long-exposure time spectrum. Each acquisition scans the wavelength from 200 nm to 1100 nm with an integration time of 100 ms. The resolution of this spectrometer is 0.5 nm.

Time-resolved OES is performed with another spectrometer. The monochromator(Shamrock 303i, Andor Technology) has 3 gratings. In this work, the grating of 600 grooves/mm is chosen. The dispersed light is guided to an Andor iStar ICCD camera, similar to the one used for space imaging. This spectrometer can be externally triggered by the TTL signal output by the oscilloscope. The minimum gate width of each acquisition is 20 ns. The background spectrum is recorded with the same gate width and environmental light but without plasma, and is subtracted from the plasma spectrum.

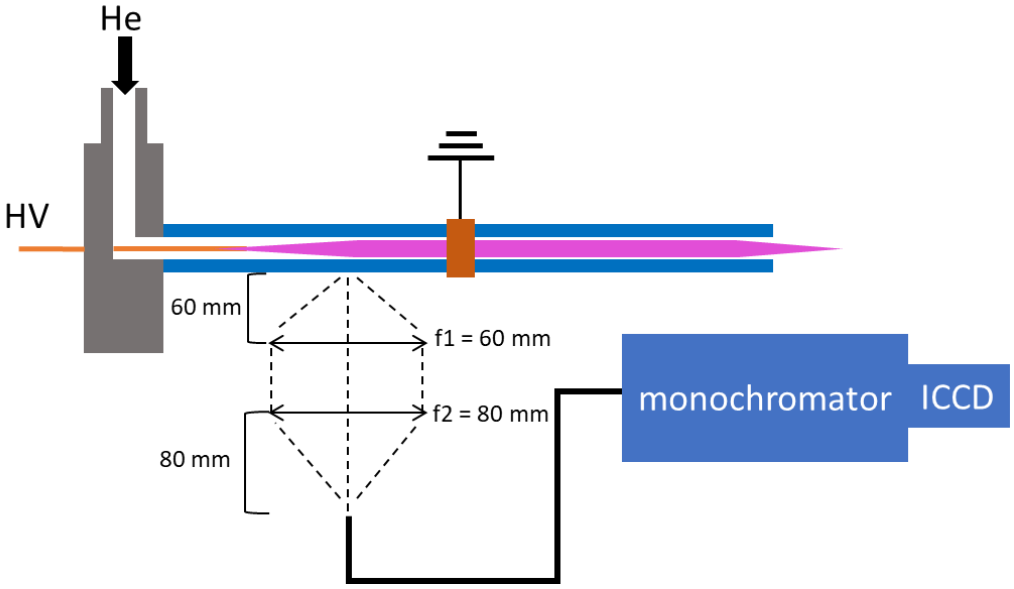

Figure 2.6 The configuration of the optical emission spectroscopy (OES).

2.2 Measurement of plasma produced aqueous species

The major long-lifetime species produced by APPJ treating water include H_2O_{2aq}, NO_2^-, and NO_3^-. Previous experiments show that the ratio between the concentration of NO_2^- and NO_3^- is almost constant, so only the concentrations of H_2O_{2aq} and NO_2^- are measured with photometric methods.

The plasma-activated water is diluted and put into disposable PMMA cuvettes (10 mm optical path). A chemical compound solution is added to the cuvette to form a colored solution. Then the absorbance of the solution in the cuvette is measured by a photometer (Secomam Uviline 9100) with a certain wavelength. According to Beer-Lambert law, the absorbance is linear to the concentration of the colored species. Therefore, the concentration of H_2O_{2aq} and NO_2^- can be calculated according to the calibration curves obtained using standard H_2O_{2aq} and NO_2^- solutions.

2.2.1 Measurement of NO_2^-

The NO_2^- concentration is measured with Griess reagent(Sigma-Aldrich G4410). The NO_2^- detection working range is 0.45~65 μmolar. In an acidic medium, NO_2^- reacts with the Griess' Reagent (Sigma Aldrich-035553) and forms a pink-colored azo compound. 800 μL diluted PAW is mixed with 800 μL Griess' Reagent. The dilution of PAW is adjusted so that the NO_2^- concentration is in the range of calibration. The mixed solution is incubated for 15 minutes. Then the absorbance is measured at 540 nm.

The NO_2^- concentration calibration is performed using $NaNO_2$ solutions diluted from standard 0.1 M $NaNO_2$ solution (Sigma-Aldrich 72586). The standard solution is diluted to 0.5~50 μmolar. 3 samples of each solution are made, and each sample is measured 3 times. The calibration curve is shown in figure 2.7.

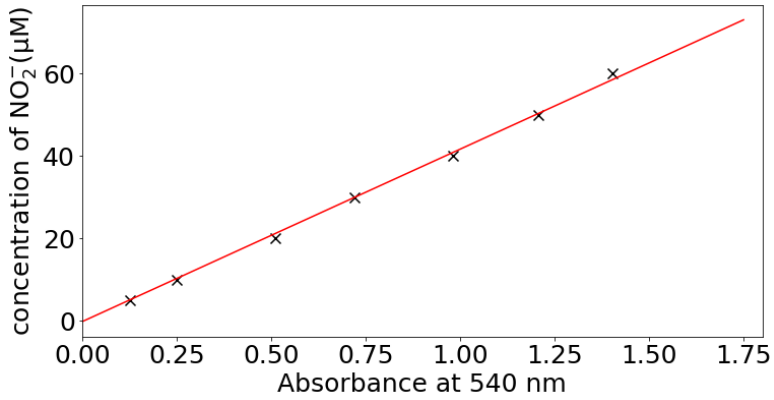

Figure 2.7 Calibration curve of the NO_2^- measurement

Linear fitting shows that the absorbance at 540 nm is linear with the concentration of NO_2^- as in equation (2.4)

$$c(NO_2^-) = 41.83a - 0.134 \qquad (2.4)$$

Where $c(NO_2^-)$ is the NO_2^- concentration in micromolar, and a is the absorbance measured at 540 nm.

2.2.2 Measurement of H_2O_2

The H_2O_2 concentration is measured with a commercial H_2O_2 test kit(Sigma-Aldrich 1.18789). The H_2O_2 detection working range is 0.03~6 mg/l. The test kit contains two reagents which contain Copper (II) ion and 2,9-dimethyl-1,10-phenanthroline (DMP). H_2O_{2aq} reduces Cu(II)-DMP and forms $Cu(DMP)_2^+$ with a 1-1 stoichiometry, which is an orange-colored complex that is determined photometrically. 800 μL diluted PAW is mixed with 50 μL of reagent I and 50 μL of reagent II. The dilution of PAW is adjusted so that the H_2O_2 concentration is in the range of calibration. The mixed solution is incubated for 10 minutes. Then the absorbance is measured at 340 nm.

The H_2O_2 concentration calibration is performed using H_2O_2 solutions diluted from standard 3% H_2O_2 solution (Sigma-Aldrich 88597). The standard solution is diluted to 1~200 μmolar. 3 samples of each solution are made, and each sample is measured 3 times. The calibration curve is shown in figure 2.8.

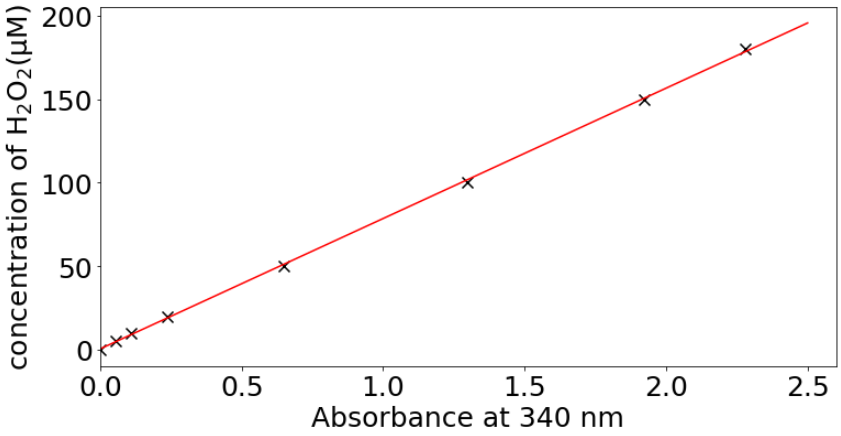

Figure 2.8 calibration curve of H_2O_2 measurement

Linear fitting shows that the absorbance at 340 nm is linear with the concentration of H_2O_2 with equation (2.5)

$$c(H_2O_2) = 78.08a + 0.512 \quad (2.5)$$

Where $c(H_2O_2)$ is the H_2O_2 concentration in micromolar, and a is the absorbance measured at 340 nm.

2.3 Characterization of the discharge gas impurities

The impurities of helium gas are indicated on the gas bottle. It is indicated that the main impurities are H_2O < 3 ppm, and O_2 < 2 ppm. However, we found in experiments that the impurities indicated on the gas bottle is not enough for producing the amount of reactive species that we measured. Thus, the amount of impurities in the gas flow is measured with a mass spectrometer.

Figure 2.9 shows the configuration of the mass spectrometer measuring the gas composition flowing out of the glass capillary. A 1 m long gas tube is connected to the outlet of the APPJ to introduce the helium gas into the ambient air. A T connector is used 20 cm downstream of the APPJ outlet to connect to the sampling orifice of the MS via a 20 cm gas tube. The APPJ is not powered so there is no discharge.

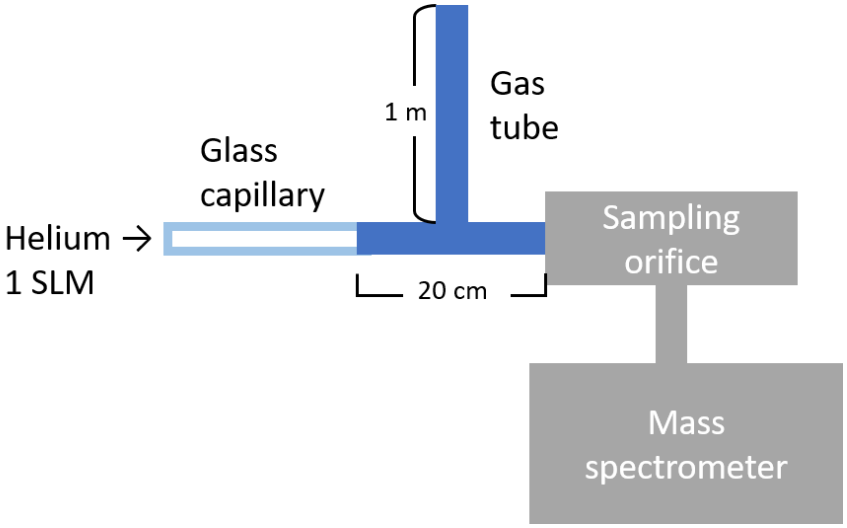

Figure 2.9. Schematic of the experimental setup of the mass spectrometer measuring the impurities inside the APPJ. The APPJ is not powered so there is no discharge.

First, the background signal of the MS is acquired by pumping the system to a pressure of 1.2×10^{-8} mbar without sampling. Then pure helium gas with a flow rate of 1 SLM is flown in the APPJ. The sampling orifice is adjusted until the pressure is 1.0×10^{-6} mbar. Thirdly, 1% of dry air is injected into the helium gas flow. The pressure of the vacuum system is maintained constant.

The mass spectrum of "pure" helium and helium +1% air is shown in Figure 2.10. When the mixture of dry air is not added, the main impurities have a relative mass of 17 u, 18 u, 28 u, 30 u, 32 u, and 44 u, which correspond to OH, H_2O, N_2, CO, O_2, and CO_2, respectively. The OH should come from the ionization of H_2O molecules by the filaments of the mass spectrometer.

When 1% of air is added to the gas composition, a significant increase in the signal amplitude is observed at the relative mass of 14 u, 16 u, 28 u, 30 u, and 32 u, corresponding to N, O, N_2, NO, and O_2. The increased signals result from the added air composition. The signal at the relative mass of 17 u, 18 u, and 44 u is not increased due to the air mixture, therefore H_2O and CO_2 should exist in the discharge gas as impurities in this work.

The impurities in the system may come from the leakage from ambient air or desorption from the inner walls of the gas tube. However, the H_2O ratio in the air is much less than the ratio of N_2 and O_2, so the leakage should not make H_2O the dominant impurity.

As the composition of the dry air is known, the mass spectrum of He with 1% air can be used to calibrate the response of the mass spectrometer. It is difficult to have a gas with known humidity, so we assume a flat transmission function, i.e. the ratio between the ion flux current and the amount of substance at the relative mass of 18 u is the same as 28 u:

$$\frac{I(18\,u)}{n(18\,u)} = \frac{I(28\,u)}{n(28\,u)} \tag{2.6}$$

Where *I* is the ion flux and the *n* stands for the amount of substance.

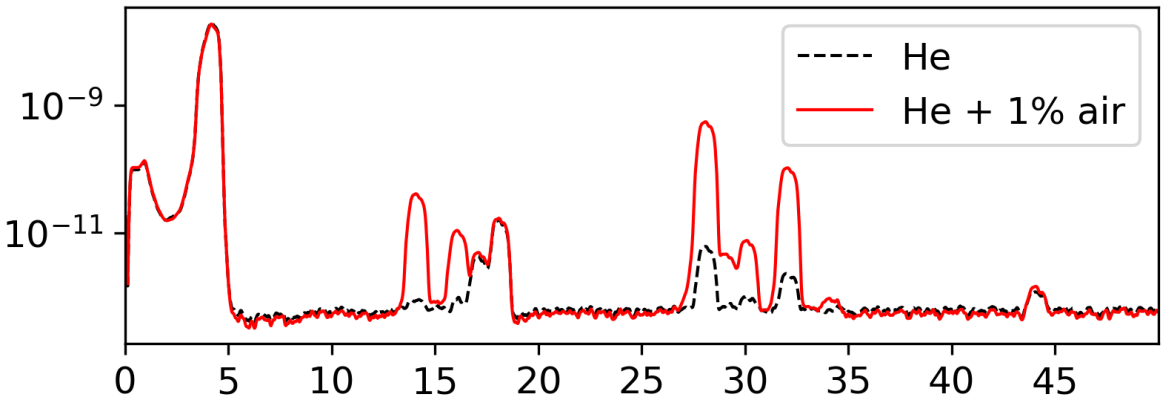

Figure 2.10 The mass spectrum (ion current) of the helium gas(black dash line) and helium with 1% dry air after flushing the tube for about 2 hours

The calculated concentrations of impurities in the discharge gas are shown in Table 2.1. The result is obtained by flushing the gas tube with helium for about 2 hours. The main impurity is water with a concentration of 256 ppm, which is equal to 1.15×10^4 nmol per liter of gas. Thus, the H_2O_2 production mainly comes from these impurities. Also, the N_2 and O_2 impurities are not negligible.

The time evolution of the humidity while flushing the tube with helium is shown in Figure 2.11. The humidity is almost stable after 1 hour. Thus, for ensuring the reproducibility of experiment results, all the experiments using APPJ in this thesis are performed after flushing the tube with helium for at least 1.5 hours.

Table 2.1. The estimated concentrations of impurities in the discharge gas caused by leakage and molecule desorption from the tube's inner wall.

Impurity	H_2O	N_2	O_2	CO_2
Estimated concentration(ppm)	256	95	50	21

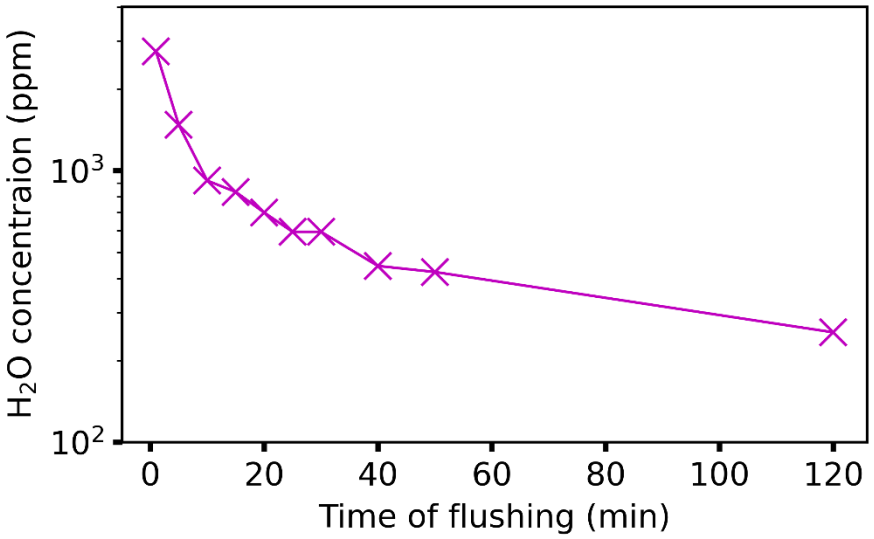

Figure 2.11 Time evolution of the humidity in the discharge gas measured by the mass spectrometer while flushing the gas tube for two hours.

2.4 *Ex vivo* pig skin treatments

2.4.1 Sample preparation

The ex-vivo experiments were carried out on skin samples obtained from a pig (Large White, female, 8 weeks old, about 40 kg, source M. Raphael LIMOSIN 15 rue Huillet 02500 Neuvemaison) on January 21st 2021. The pig skin was cut into small square samples of approximately 1.5 cm × 1.5 cm and the hair is shaved with an animal clipper. The skin samples are placed in a sealed box and stored in a refrigerator at -20°C. The experiments have been carried out between February 2021 and March 2022.

Before the treatment, the pig skin samples are first taken out of the fridge and put into 1X PBS solution for ~ 20 min to restore the skin temperature to room temperature and restore the moisture lost due to the conservation.

The mass of the pig skin changes due to water uptake/loss during the sample preparation and treatment. The mass is measured with an analytical balance (Denver Instrument SI-64.1) with a precision of 0.1mg.

2.4.2 Plasma treatment

The plasma jet used to treat the pig skin is an improved version of the APPJ that has been described in the thesis of Dr. Bruno Honnorat and Dr. Bo Liu. The APPJ used in previous studies is 3d-printed with PLA. However, the power of plasma generated by this plasma jet

seems unstable. A sudden increase of the plasma power is sometimes observed and results in filamentary-like plasma and high gas temperature, which causes damage to the skin surface. This is possibly due to the roughness of the 3d-printed capillary inner surface which can cause a local high electric field. The new configuration used in this report is shown in Figure 2.12. The distance between the powered electrode and the outlet of the capillary is 4 cm. Pure Helium gas is injected into the capillary with a 1 SLM flow rate. The high voltage electrode is a 1 cm wide copper tape wrapped around the capillary outer surface, and is powered by a power supply providing 10 kHz sinusoidal voltage. The pig skin sample is placed in a glass petri dish. The distance between the capillary outlet and the skin surface is 5 mm. An aluminum electrode is attached to the bottom of the petri dish. A 1 nF capacitor is connected between the aluminum electrode and the ground. The voltage over the capacitor is measured by the oscilloscope and the power deposited on the target is calculated according to equation (2.3).

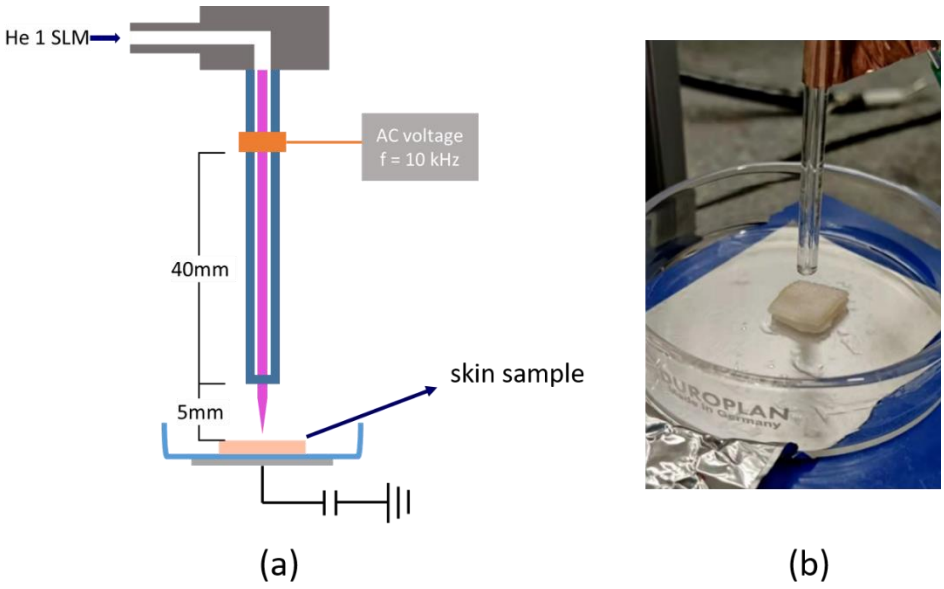

Figure 2.12 (a) shows the schematic of the APPJ used to treat the pig skin. (b) is a photo showing the jet and the skin sample.

When the plasma plume contacts the pig skin surface, the plasma propagates along the surface, creating a plasma irradiation spot which is a circular area with approximately 2 mm diameter. The plasma causes a temperature increase in the plasma irradiation area. The temperature is measured with an infrared camera. An example of a 2d temperature image on the skin surface during 1 W plasma treatment is shown in figure 2.13. The maximum temperature appears at the center of the plasma irradiation area.

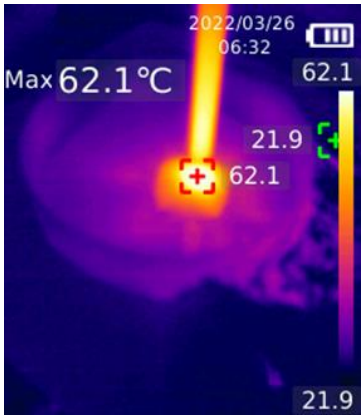

Figure 2.13 Temperature distribution in the skin surface during plasma treatment with a power of 1 W. The image is acquired after about 2 minutes treatment.

Before the plasma treatment, the pig skin samples are first taken out of the fridge and put into 1X PBS solution for ~ 20 min to restore the skin temperature to room temperature and restore the moisture lost due to the conservation. The skin sample is put into an icebox and transported to the room for Mueller Polarimetric Imaging (MPI) within 5 min walking distance. Then the Mueller matrix of the skin sample is measured and is considered as the control. After the measurement, the skin sample is taken back into the icebox to the room for plasma treatment. Mueller matrix imaging is performed again after the treatment.

2.4.3 Heating treatment

To evaluate the heating effect of plasma on pig skin samples, pig skins are heated with a beam of white light.

The light is provided by a halogen light source (Olympus CLH-CS). Two convex lenses are used to converge the light beam and form a bright spot on the skin sample surface as shown in Figure 2.14(a). By replacing the skin sample with a CCD camera (Stingray F-080 with Sony ICX204), the light intensity is measured. Figure 2.14(b) shows the normalized light intensity along an axis that crosses the center of the light spot. The FWHM is about 2 mm, which is close to the diameter of the plasma-treated zone. The temperature of the skin during treatment is monitored with the infrared camera and is adjusted by changing the light intensity of the light source.

After treatment, MPI is performed and the result is compared with plasma treatment with the same temperature.

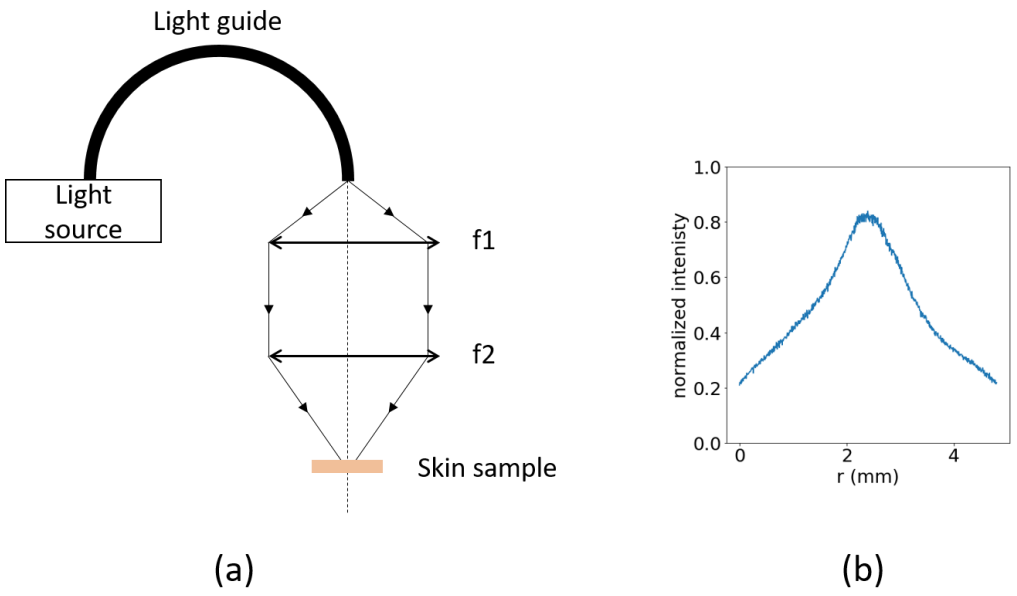

Figure 2.14 (a) shows the experimental setup of heating the skin sample with a beam of light focused by two convex lenses. (b) shows the normalized light intensity on the skin surface measured by a CCD camera.

2.4.4 ROS treatment

The main long-lifetime ROS in plasma-treated liquid is H_2O_2. To evaluate the effect of H_2O_2 on the skin sample, a droplet of H_2O_2 solution is used to treat the skin sample.

A droplet of H_2O_2 solution is put at the center of the prepared skin sample surface. The amount of H_2O_2 in this droplet is the same as the amount of H_2O_2 produced by the plasma jet with 1 W power during 4 min treatment, which is determined with the experiment method introduced in section 2.2.2.

The H_2O_2 solution droplet is removed from the skin sample surface after 4 min or 1 h, then MPI is performed.

2.5 Mueller Matrix Imaging

2.5.1 Principle of measurement

The MPI used in this study is a backscattering configuration, as shown in figure 2.15. The measurement system consists of a Neon light source, a polarization state generator (PSG), a polarization state analyzer (PSA), and a charge-coupled device (CCD) camera(f080b Allied Vision, 512×386 pixels). A zoom lens placed in front of the CCD camera enables adjusting the field of view to the sample size. In particular, a field of view of 5x4 cm^2 was considered for the

experiments performed in this study. The actual measured resolution of the imaging system was about 150 μm/pixel. The polarimetric images were acquired at 550 nm with a spectral bandwidth of 40 nm.

The LED light source (Olympus CLH-CS) provides an incoherent white light. The PSG is constructed by a linear polarizer and two tunable ferroelectric liquid crystals (LC) working as a quarter-wave plate with fixed retardation [132,133]. It alternatively modulates the incident light into 4 polarization states which are linearly independent. Then, by grouping the 4×1 stokes vector of the 4 polarization states, the polarization state of the incident light is noted as a 4×4 matrix $\boldsymbol{W}$ as in equation(1.16)

$$\boldsymbol{W} = [\boldsymbol{S_1}\ \boldsymbol{S_2}\ \boldsymbol{S_3}\ \boldsymbol{S_4}] \tag{2.7}$$

Where $\boldsymbol{S_i}$ (i = 1 ~ 4)is the Stokes vectors of the 4 polarization states of the PSG. The light is reflected by the skin sample. Similarly, the polarization state of the reflected light is noted as $\boldsymbol{W'}$. According to the definition of Mueller Matrix, we have equation (2.8)

$$\boldsymbol{W'} = [\boldsymbol{S_1'}\ \boldsymbol{S_2'}\ \boldsymbol{S_3'}\ \boldsymbol{S_4'}] = \boldsymbol{MW} \tag{2.8}$$

Where $\boldsymbol{M}$ is the 4×4 Mueller Matrix of the skin sample.

The reflected light propagates through the PSA. The polarizer in PSA provides four linearly independent polarizations, whose polarization direction is denoted with unit vectors $\boldsymbol{S_j^a}$(j = 1 ~ 4). Thus the polarization of the PSA is described by $\boldsymbol{A}$ given by equation (2.9).

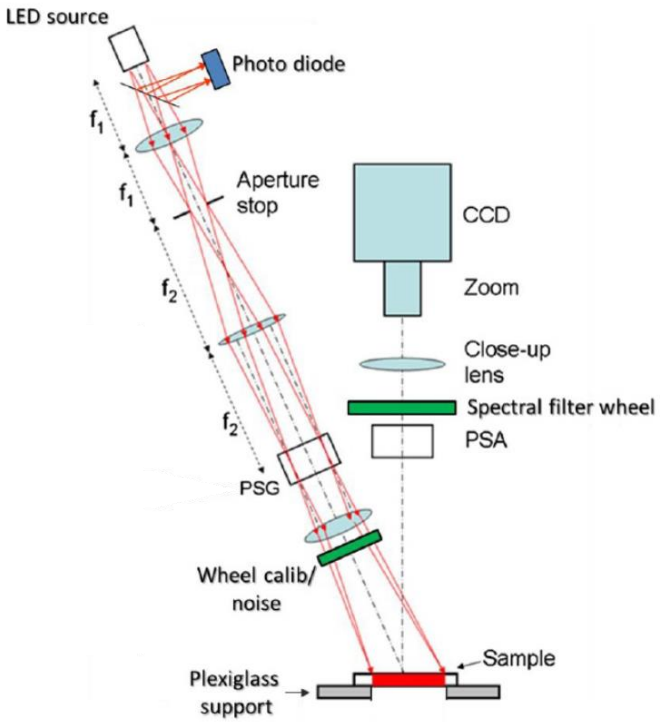

Figure 2.15: Schematic of the Mueller Polarimetric Imaging system.[134]

$$\boldsymbol{A} = [\boldsymbol{S_1^a}\ \boldsymbol{S_2^a}\ \boldsymbol{S_3^a}\ \boldsymbol{S_4^a}] \tag{2.9}$$

When a linearly polarized light with polarization state $\boldsymbol{S_i'}$ propagate through a polarization analyzer with polarization state $\boldsymbol{S_j^a}$, the intensity of the light after PSA is given by the inner product of $\boldsymbol{S_i'}$ and $\boldsymbol{S_i^a}$, or represented as the matrix product of 1×4 matrix $\boldsymbol{S_j^{aT}}$ and 4×1 matrix $\boldsymbol{S_i'}$, as equation (2.10).

$$B_{ij} = \boldsymbol{S_i'} \cdot \boldsymbol{S_j^a} = \boldsymbol{S_j^{aT}} \boldsymbol{S_i'} \tag{2.10}$$

The 4 polarization states $\boldsymbol{S_i'}$ of PSG and 4 directions of PSA $\boldsymbol{S_j^a}$ make 16 combinations, so light with 16 different polarization states alternatively propagates to the CCD camera. So the CCD camera gives 16 intensities which can be written as a 4×4 matrix $\boldsymbol{B}$ which is given by the matrix product of $\boldsymbol{A^T}$ and $\boldsymbol{W'}$, as in equation (2.11)

$$\boldsymbol{B} = \begin{bmatrix} B_{11}\ B_{12}\ B_{13}\ B_{14} \\ B_{21}\ B_{22}\ B_{23}\ B_{24} \\ B_{31}\ B_{32}\ B_{33}\ B_{34} \\ B_{41}\ B_{42}\ B_{43}\ B_{44} \end{bmatrix} = \begin{bmatrix} \boldsymbol{S_1^{aT}} \\ \boldsymbol{S_2^{aT}} \\ \boldsymbol{S_3^{aT}} \\ \boldsymbol{S_4^{aT}} \end{bmatrix} [\boldsymbol{S_1'}\ \boldsymbol{S_2'}\ \boldsymbol{S_3'}\ \boldsymbol{S_4'}] = \boldsymbol{A^T W'} \tag{2.11}$$

Combining equation (2.8) and equation (2.11), the Muller Matrix of the sample can be given by equation (2.12).

$$\boldsymbol{M} = (\boldsymbol{A^T})^{-1} \boldsymbol{B W^{-1}} \tag{2.12}$$

The main polarimetric properties of the sample were obtained from M using the Lu-Chipman decomposition [98]. This decomposition allows expressing M using the following expression:

$$\boldsymbol{M} = \boldsymbol{M_\Delta M_R M_D} \tag{2.13}$$

where M_Δ, M_R and M_D are the Mueller matrices of a depolarizer, a birefringent medium, and a diattenuator, respectively. The most relevant polarimetric properties for the skin are the total depolarization (Δ) and the linear phase retardance (LR). The parameter Δ quantifies the ability of the sample to depolarize both linear and circular polarization states. It is defined as:

$$\Delta = 1 - \frac{|a| + |b| + |c|}{3} \tag{2.14}$$

where the coefficients a, b and c are the eigenvalues of $\mathbf{M}_\Delta$. In Eq. (4), $\Delta = 0$ for a non-depolarizing sample and $\Delta = 1$ for a pure depolarizing sample.

The parameter LR quantifies the difference in optical phase shifts between two main orthogonal polarization eigenstates. It is defined as:

$$LR=\arccos\left(\frac{tr(\mathbf{M}_R)}{2}-1\right) \quad (2.15)$$

where $tr(\mathbf{M}_R)$ is the trace of $\mathbf{M}_R$. In general, LR varies between 0° and 180° for biological tissues.

A Matlab program developed by Dr. Junha Park and Jérémy Vizet from LPICM is used to decompose **M**. The components of **M**, including M11, LR and Δ are calculated according to equation (2.13(2.15).

2.5.2 Protocol of MPI

A calibration is required to calculate the Muller Matrix of the skin sample. The calibration is done by acquiring the Mueller matrix of a metallic plate with a rough surface. A metallic plate is placed slightly away from the focus plane to make the image of the metallic plate homogeneous. The calibration is based on the procedure of Eigenvalues Calibration Method(ECM)[135].

After calibration, the skin sample to be measured is placed on a microscope slide, and the focus plane is adjusted to the surface of the skin sample. Note that it is important to place the skin sample on an optically transparent substrate, as the reflection significantly influences the measurement.

The exposure time is adjusted so that the signal obtained by the camera is maximum but non-saturated. Then the acquisition is performed 16 times and averaged.

2.5.3 Methods of Statistics

Statistical analysis was performed using Prism software (GraphPad Software, San Diego, CA). The measured value for mass, linear phase retardance, and/or total depolarization, was compared between two groups with a parametric paired t-test.

A one-way parametric ANOVA (Analysis of Variance) was used to compare more than two groups. The analysis was corrected for multiple comparisons using Dunett's statistical hypothesis test.

Each test provided a *p*-value that allowed the statistical significance of the results to be assessed. The null hypothesis is rejected if $p < 0.05$. It means that the difference between the two groups should be considered statistically significant. In particular, the *p*-values obtained in this study were indicated as "*", "**", and "***", if they were lower than 0.05, 0.01, and 0.001, respectively. If $p > 0.05$, the null hypothesis cannot be rejected. It means that the difference between the two groups should be considered statistically non-significant (denoted as "ns" in the following text).

Chapter 3. Multi-periodic self-trigger plasma

As introduced in chapter 1, the ignition of plasma bullets in APPJs can be random or periodic depending on the operating condition. The surface residual charges or volumetric residual charges are considered to be the main factor that influences the periodicity of plasma ignition. Random plasma can cause difficulties in the observation of plasma. On the other hand, the transition between random and periodic plasma causes a sudden change in the characteristics of plasma, which raises difficulties in controlling of APPJs for applications.

In this chapter, we observe the plasma ignition and propagation of an APPJ that exhibits multi-periodic and random modes, and try to reveal the role of surface charges in the multi-periodic self-trigger plasma ignition. Although an APPJ with an external ring-like powered electrode is the most commonly used for medical applications, such configuration causes both upstream and downstream plasmas which influence each other, and will be introduced in chapter 5. For simplicity, let us start with an APPJ with a needle-like internal powered electrode, as shown in Figure 3.1, which has also been introduced in chapter 2. In this configuration, plasmas only ignite from the pin and propagate downstream. The distance between the tip of the powered electrode and the capillary outlet is approximately 17 cm. Helium with a flow rate of 1 SLM is injected into the capillary. For most of the experiments in this chapter, an AC power supply is used, with a frequency from 9 kHz to 12 kHz or from 14 kHz to 18 kHz. When the frequency is 12~14 kHz, the voltage is strongly fluctuating due to resonances. Some comparison study is also performed using a DC-pulse power supply which provides positive pulses. The frequency ranges from single pulses to 10 kHz.

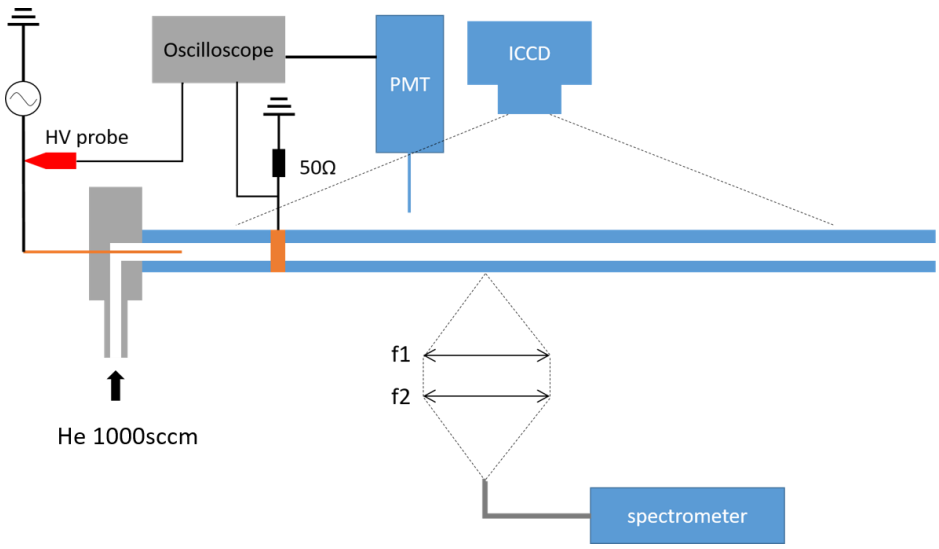

Figure 3.1 Experimental setup of the APPJ used in this chapter. The distance between the pin and the ring-like ground electrode is 20 ~ 40 mm. The distance from the pin to the capillary outlet is 17 cm. The helium flow rate is 1000 sccm. A PMT, an ICCD camera and a spectrometer are combined for the optical diagnostics of the plasma.

Multiple diagnostic methods are combined to observe the ignition and propagation of the discharges, and the focus is made on the plasmas in the inter-electrode gap region.

The structure of this chapter is described below:

Section 3.1 describes the multi-periodic and random ignition of the plasma bullet generated by AC voltage. The inter-electrode gap distance, applied voltage, and frequency is found to influence the multi-periodic modes.

Section 3.2 shows the propagation of plasma in the gap region. Multiples ionization waves are found to ignite before the formation of the plasma bullets. The role of surface-deposited charges in the formation of multi-periodic plasma bullets is pointed out.

Section 3.3 shows the propagation velocity of plasma bullets are similar in different multi-periodic modes.

Section 3.4 shows the time-integrated, time-resolved, and space-resolved optical emission spectrum of the plasma. The intensities of helium emission are similar in different conditions, while the intensities of OH band emission vary in time and space.

Section 3.5 makes a general conclusion of this chapter.

3.1 Periodic plasma in single electrode configuration

To highlight the role of the ground electrode, let us first investigate the configuration with a single powered electrode without a ground electrode. The discharge light signal is acquired by an optical fiber located 10 mm downstream from the HV tip. An example of waveforms of applied voltage and light signal is shown in Figure 3.2.

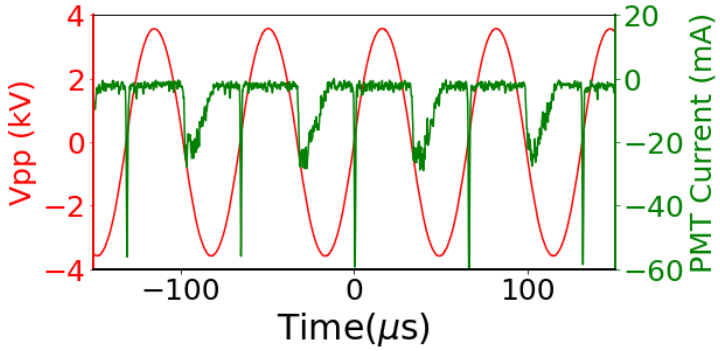

Figure 3.2. Applied voltage(red) and PMT signal (green) at 10 mm downstream from the HV tip. V_{pp} = 7 kV, f = 16 kHz. The discharge is generated in a plasma jet with only a powered pin electrode and no ground

The emission light signal and ICCD imaging (not shown) show that the positive discharge is a streamer-like discharge with most of the light emission localized at the ionization front, but the negative discharge is a glow-like discharge with a long tail. The applied instant voltage of the plasma ignition is close to 0. Statistical study over more than 10000 counts shows that the light pulse in positive half cycles has a jitter of ~100 ns, less than 0.2% of the actual period (V_{pp}=6 kV and f=16 kHz) and much less than the actual propagation time of the ionization front (more than 5 µs). Hence, the plasma can be considered self-triggered. When varying the applied voltage from 3 kV to 12 kV and frequency from 10 kHz to 18 kHz, the jitter of the light emission pulse remains small compared to the voltage period. However, the propagation length of the discharge is 5 cm maximum with 12 kV voltage.

Generally, with a needle-like powered electrode without a ground electrode, periodic plasmas are generated with low light intensity and short propagation length. The breakdown happens while the applied voltage is close to 0 V.

3.2 Multi-periodic self-trigger plasma with an external ring-like ground electrode

In many studies, a ground electrode is added on the capillary outer surface near the powered electrode, forming a DBD gap region to enhance the discharges. To enhance the electric field in the gap region, a short gap distance of around a few mm is often used [40,41]. Such

configuration leads to multiple random discharges in one voltage cycle and will be described in Chapter 4. In the present work, the gap distance is increased to 25~40 mm, and multi-periodic plasma ignition is ignited under certain operating conditions. The propagation length is also significantly increased.

3.2.1 Periodic multiplication observed when a ring-like grounded electrode is added

In this section, the role of an external ring grounded electrode is investigated. The distance between the HV electrode and the ground electrode ranges from 25 to 40 mm and is called the gap in the following. In the present work, discharges in the gap region (between high voltage and ground electrodes) are ignited in every cycle, but only a fraction of these discharges can propagate beyond the ground electrode. For the sake of clarity, in the following, the word "bullet" refers to ionization waves propagating outside the gap region. The plasma bullets in this APPJ exhibit periodic or random behavior depending on the applied voltage amplitude, applied voltage frequency, and gap distance. Figure 3.3 shows the discharge current and PMT signal with 4 different applied voltages; the PMT signal is acquired by an optical fiber at 2 mm downstream of the ground electrode; the gap distance is equal to 30 mm and the applied voltage frequency is 17 kHz. In Figure 3.3(a), where the applied voltage is 5.88 kV, in every 3 periods (3P), a negative discharge is ignited first and is then followed by a positive discharge. The amplitudes of the discharge current of positive or negative discharges measured at the ground electrode are identical. In this condition, the ignition of bullets is periodic with a period of 3P, where P is the period of the applied voltage. Such denotation will be used in the rest of this report. In Figure 3.3(b), the voltage is increased to 5.95 kV, the plasma exhibits random behavior. But there is always at most one bullet in each positive or negative cycle. In Figure 3.3(c), the applied voltage is 6 kV, and the plasma ignition is periodic with a period of 2P (one bullet every 2 periods). When the voltage continues to increase to 8 kV, as shown in Figure 3.3 (d), the discharge is random. In some conditions, multiple random discharges may happen in one positive or negative cycle as shown in Figure 3.3(d): the waveform of the discharge current is superposed with many spikes, which is possibly due to many micro discharges in the gap region. It is also worth pointing out that the amplitude of light intensity detected via the PMT is larger in the case of periodic discharges in Figure 3.3(a) and (c) than in the case of random discharges in Figure 3.3(b) and (d).

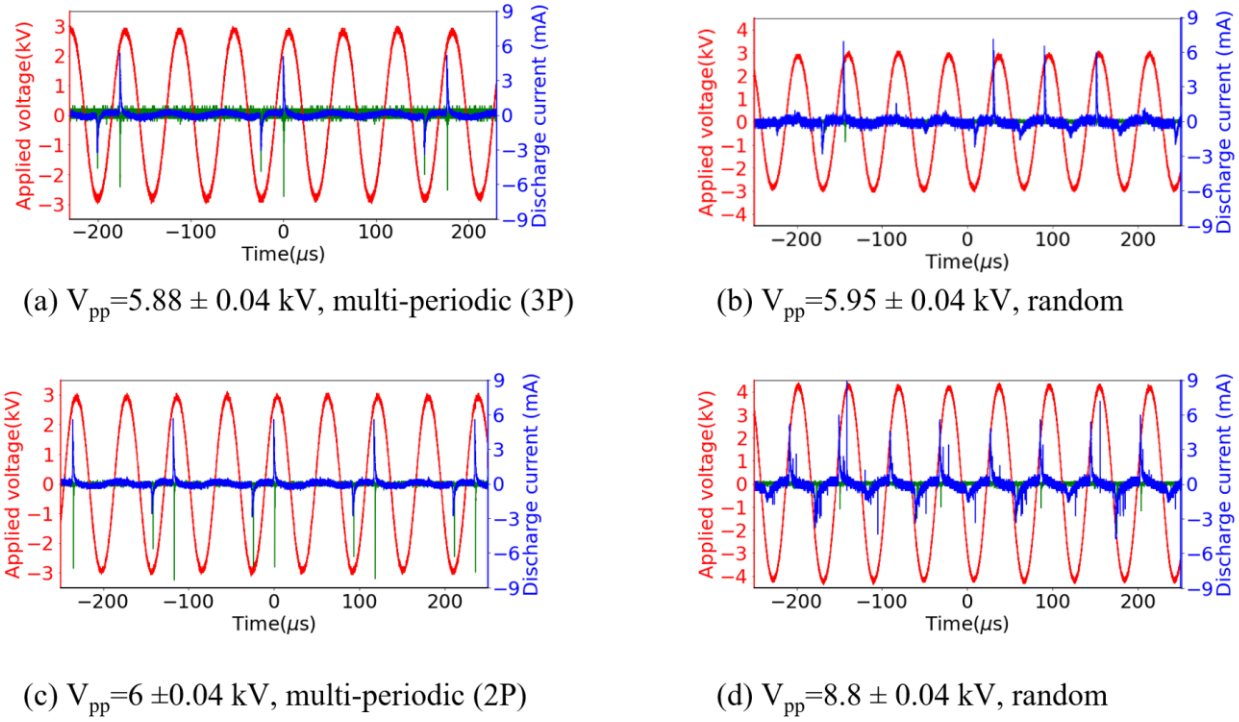

Figure 3.3. Examples of waveforms of applied voltage (red curve), discharge current (blue curve), and PMT signal (green curve, acquired at 2 mm downstream of the ground electrode) in four conditions. (a) V_{pp}=5.88 ± 0.04 kV. The long discharge is observed every 3 cycles. (b) V_{pp}=5.95 ± 0.04 kV. The discharge is random. And at most one discharge is observed in each cycle. (c) V_{pp}=6±0.04 kV. The long discharge is observed every 2 cycles. (d) The discharge is random and multiple discharges can be observed in one cycle.

It is also observed that the plasma bullets in periodic mode propagate longer than in the random mode. The propagation length of the jet for gap distances of 25 mm, 30 mm, and 40 mm and the length of a jet with no ground electrode are plotted in Figure 3.4 as a function of the applied voltage. The applied voltage frequency is fixed at 17 kHz, and the length 0 of the y-axis corresponds to the HV tip. First, when there is no ground electrode, the propagation length increases quasi-linearly with the applied voltage. Second, the presence of a grounded electrode leads to a dramatic increase in the discharge propagation length if the applied voltage exceeds a critical value V_{crit}. The critical voltage V_{crit} corresponds to the voltage for which the plasma is long enough to reach the ground electrode and V_{crit} depends on the gap distance. For example, in the case of a 30 mm gap region (red curve in Figure 3.4), once the plasma length reached 30 mm with a voltage equal to or higher than 5.75 kV, the discharge enters periodic modes with a period of 3P or 2P, corresponding to Figure 3.3(a) and (c) respectively; the propagation length extends from 30 mm to around 140 mm abruptly. We will show in the following that in such multi-periodic modes 2P and 3P, all bullets are highly reproducible in terms of velocities and length.

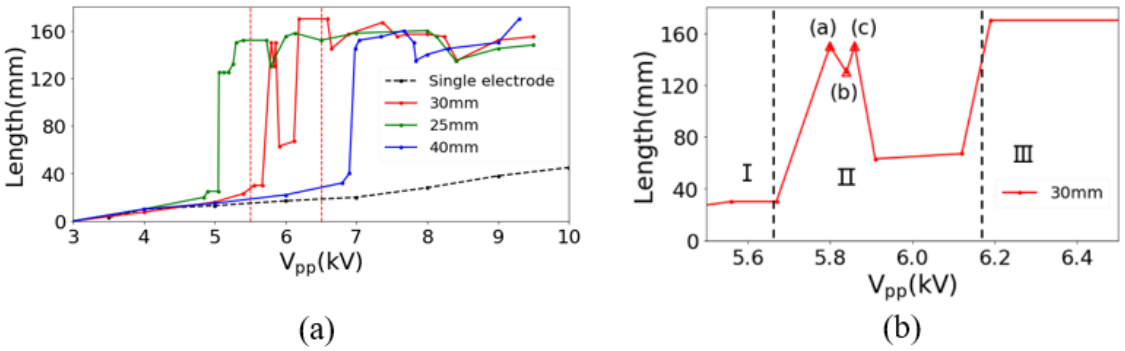

Figure 3.4. (a) shows the propagation length of discharges as a function of the applied voltage with 25 mm, 30 mm, or 40 mm gap (colored solid lines) or with a single high voltage tip (black dash line). The driving frequency is 17 kHz. (b) shows the zoom of the region between the vertical red dash lines in (a). The points a, b, and c correspond to figure(a), (b), and (c) in Figure 3.3.

For most plasma jets, applied voltage, waveform, and frequency are the key factors that influence the length of the plasma. Usually, the plasma propagates further with higher applied voltage, which is consistent with our results without a ground electrode shown in Figure 3.4.

However, when a grounded electrode is present, like in region II of Figure 3.4(b), it is shown that a voltage increase leads to a decrease in the plasma length to about 60 mm. In this condition, plasma bullets are formed in every cycle (1P mode), but their length is reduced. 1P mode has different propagation dynamics with nP mode when ($n \geq 2$), and is stable in much smaller range of conditions, so it is excluded from the discussion of this report. In region III in Figure 3.4(b), plasma bullets are also formed every cycle, but the length is alternatively long and short and long plasma bullets can propagate to 160 mm. After region III, the discharge ignition is random, corresponding to Figure 3.3 (d). Although the applied voltage and plasma power increase, the plasma length reaches a steady state. In the transition state between two different multi-periodic modes, the plasma ignition is random, corresponding to Figure 3.3 (b).

Figure 3.4 also shows plasma length for gap distances of 25 mm and 40 mm, as a function of the applied voltage. The trend is similar to the case of a gap equal to 30 mm described above. The minimum voltage required for the plasma to bridge the gap and reach the grounded electrode increases with the gap length. It equals 5 kV, 5.5 kV, and 6.8 kV for gap widths of 25 mm, 30 mm, and 40 mm respectively. Also, the gap length does not seem to have any influence on the maximum propagation length. The strong increase in the jet length is clearly linked to the periodic discharge and the presence of the ground electrode.

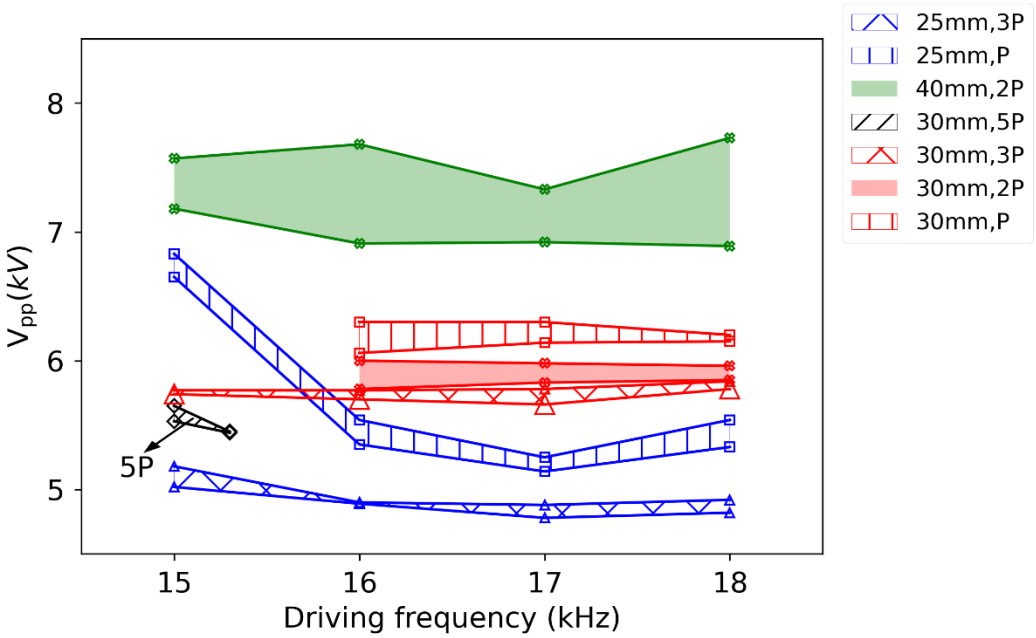

Figure 3.5. Mapping of the dynamic behavior by varying the applied voltage and driving frequency with a gap distance of 25 mm, 30 mm, and 40 mm. The colored region represents the periodic plasma, like Figure 3.3(a) and (c). "nP" denotes the period of the ignition of long discharge where "P" stands for the period of the applied voltage. Plasma is random between the colored region, like shown in Figure 3.3(b) and (d)

The periodic system shows dependency on several parameters, including applied voltage frequency, applied voltage amplitude, and the geometry of the jet. In this report, we investigated the influence of voltage, frequency, and gap distance on the periodic system. With each fixed gap distance, the discharge is periodic within a range of applied voltage and frequency, so this range can be shown with an area in a 2D voltage-frequency figure. Such mapping is repeated with gap distances equal to 25 mm, 30 mm, and 40 mm, and the results are shown in Figure 3.5, where the mapping of 25 mm, 30 mm, and 40 mm gap distance conditions are shown with blue, red, and green areas, respectively. Depending upon the condition, the plasma is periodic or multiperiodic in a limited range of 20~500 V. As the frequency increases, the voltage required for the periodic system decreases slightly. The gap distance has a significant influence on plasma behavior. With a larger gap distance, it requires a higher voltage to reach the same periodicity as 2P or 3P. Under certain conditions, the multi-periodic mode cannot be achieved by varying the applied voltage. For example, with a 15 kHz frequency and 30 mm gap distance, 2P and 1P modes are not possible. A possible explanation is that the voltage range where 1P or 2P multiperiodic mode can be observed is extremely limited at 15 kHz, and is smaller than voltage fluctuations. Hence, in practice, a stable multiperiodic domain is not observed at 15 kHz. The gas composition may also influence the voltage limit of the periodic system. For example, the 5p mode with a 30 mm gap distance can only be observed for about 10 min. This is probably because the plasma decreases the gas impurities by desorbing the molecules on the tube's inner surface. In fact, the voltage required

for certain np modes continues to decrease by about 200 V during the first hour of the plasma operation.

Walsh *et al.* plotted a map of dynamic behaviors by varying the applied voltage and the gas flow rate [38]. Similarly, as the voltage increases, the discharges change from 3P region to 2P and 1P regions. Qi *et al* also plotted similar mapping with driving frequency and applied voltage as parameters but the results show an opposite trend to ours: as the driving frequency increases, the voltage of periodic regions increases [41]. This difference may be due to the fact in their jet, the ground electrode is wrapped around the needle electrode and thus there is no gap region.

With the presence of a ring-like ground electrode with a gap distance of 20~40 mm, plasma bullets can be ignited in random mode or multi-periodic mode. In a so-called "nP" multi-periodic mode, a negative bullet followed by a positive bullet is ignited every n AC cycle. The formation of nP mode or random mode depends on the applied voltage, driving frequency, and the gap distance.

3.2.2 Self-triggered multiple gap discharges promote multi-periodic plasma bullets

Before the formation of a plasma bullet, multiple ionization waves are observed in the gap region in this work and the literature. Ning *et al* showed the 2 consecutive gap discharges with a streak camera and measured the velocity of each discharge[39]. Chen *et al* focused on the second gap discharge in a He-APPJ with CF_4 mixtures and concluded that the second discharge is promoted by the species generated by the first gap discharge[136]. To understand the formation mechanism of the multi-periodic plasma bullets seen in section 3.1, it is necessary to investigate the gap discharges.

The gap discharges before multi-periodic plasma bullets are similar to the self-triggered DBD discharges reported by Wang *et al* [69]. It is assumed that the self-organization of gap discharges is due to the periodic variation of the accumulated charges in the gap region. The multi-periodic gap discharges make possible the monitoring of the plasma bullet formation and propagation process using fast ICCD camera imaging. In this section, we studied the propagation of discharges in 3P mode. The gap distance is 30 mm and the driving frequency is fixed at 17 kHz.

Figure 3.6 shows the zoomed discharge current and PMT signal of the negative and positive plasma bullets. For both positive and negative plasma bullets, the discharge current has two peaks. The first and the second current peaks have a time difference of ~1 μs, and correspond to the ignition of plasma bullet and the formation of a glow-like discharge in the gap region, respectively. The PMT signal is acquired in the middle of the 30 mm gap region. For the negative bullets shown in Figure 3.6, a light signal is detected about 0.6 μs before the current peak, and a second stronger light peak is detected about 1 μs after the first light peak. We will

show with ICCD imaging that the two light peaks correspond to the backward propagating discharges and the glow-like discharge in the gap region.

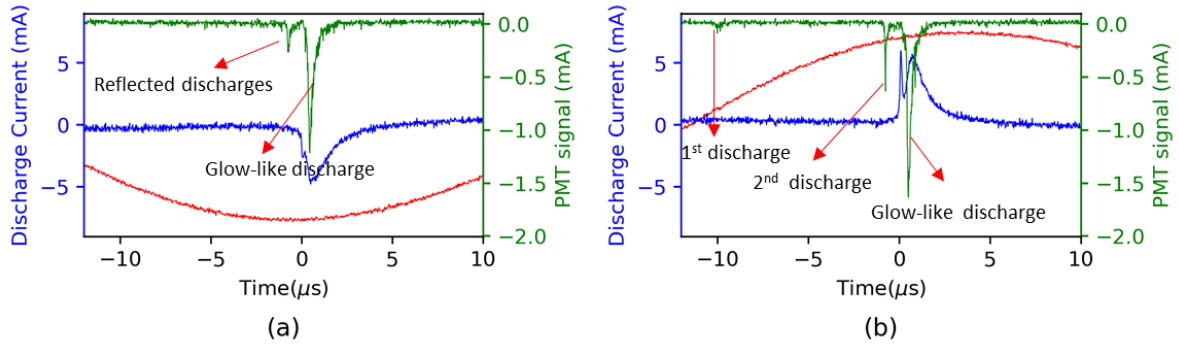

Figure 3.6 Discharge current (blue), PMT signal (green), and applied voltage (red) of (a) a negative plasma bullet and (b) a positive plasma bullet. The applied voltage is 6 kV with a frequency of 17 kHz. The PMT signal is acquired at the middle of the 30 mm gap region.

The ICCD camera is triggered by the discharge current peak and delayed 3 cycles to record the photo of the next bullet; the jitter is less than 200 ns. Similar results are also seen in the case of 2P mode. Figure 3.7 shows the propagation of negative bullets. Each photo is accumulated 100 times. The gap distance is 30 mm. The applied voltage is 6 kV. The driving frequency is 17 kHz. The high voltage tip is at the upper edge of the image and the orange area represents the ground electrode. The white dashed lines represent the outer edge of the capillary. The corresponding discharge current is shown above the ICCD photos in Figure 3.7. The discharge current peak is composed of two superposed peaks, and the time 0 is defined as the maximum of the first peak. Figure 3.7 (a) shows the discharge dynamic within about 16 μs with an exposure time of 1 μs for each photo, and Figure 3.7 (b) shows the discharge dynamic within 2.5 μs with an exposure time of 200 ns for each photo. The light intensity is shown in log scale to improve the contrast.

Before the negative bullet clearly starts, a multiple-ionization process occurs in the gap region. A weak gap discharge starts more than 10 μs before the formation of a bullet. It continuously emits light through the whole ionized channel. Due to its weak light intensity, it is not observed by the PMT so it is not shown in Figure 3.6(a). When it reaches the ground electrode, it is reflected and then propagates upstream. After the reflection, the ionization wave becomes faster and brighter, until at ~0.2 μs it stops at the ground electrode. The reflected ionization waves correspond to the first PMT signal peak in Figure 3.6(a). At 0.8 μs, the negative plasma bullet is observed to ignite at the ground electrode. It can propagate over 10 cm with a velocity of 20 km/s. A glow-like discharge is generated in the gap region and induced a light emission which is almost spatially uniform through the whole inter-electrode gap region for about 0.5 μs. This glow-like discharge corresponds to the second PMT signal peak in Figure 3.6(a).

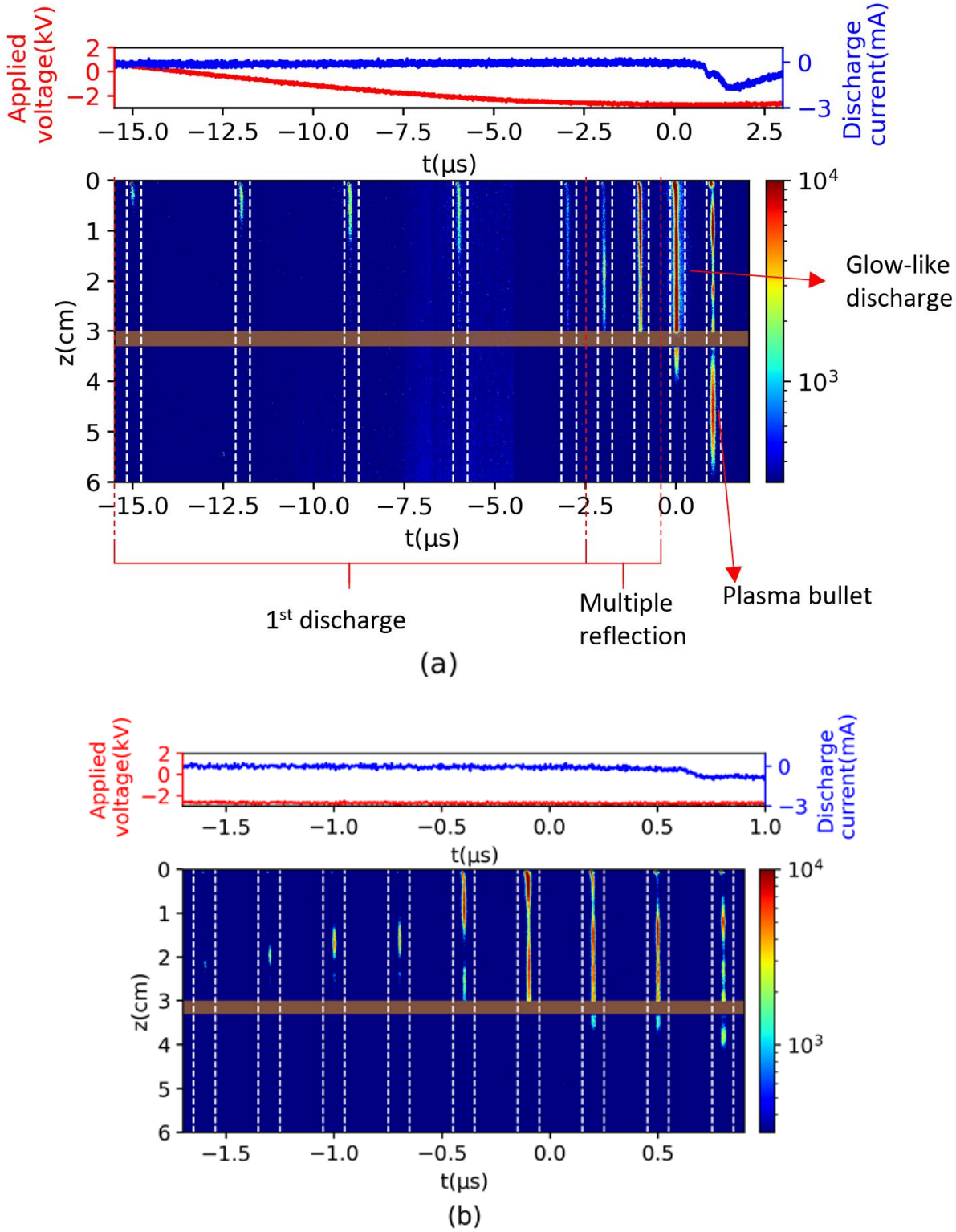

Figure 3.7. Waveform and ICCD photos of the propagation dynamics of the negative bullet in different time scales. Each photo is accumulated 100 times. The gap distance is 30 mm. The applied voltage is 6 kV. The driving frequency is 17 kHz. The high voltage tip is at the upper edge of the image and the orange area represents the ground electrode. The white dashed lines represent the outer edge of the capillary. (a) shows the propagation in a time range of 16 μs with an exposure time of 1 μs for each

photo. (b) shows the propagation in a time range of 2.5 μs with an exposure time of 200 ns for each photo. Light intensity is shown in log scale. Note that the intensity of the first 4 photos of figure (a) is doubled to ensure readability.

In all reported configurations, a positive bullet starts during the positive cycle right after the negative bullet described above. The propagation of the positive discharge is shown in Figure 3.8(a) and (b) in two different time scales. A weak gap discharge is observed to initiate at -15 μs. It propagates for 2 cm maximum and disappears at about -10 μs. It induced the first PMT signal peak observed in Figure 3.6(b). Between -4~-1 μs, a second gap discharge is formed and propagates from the HV tip to the ground electrode. It starts with weak emission intensity and a small velocity of about 10 km/s, but it is significantly enhanced when it approaches the ground electrode at -0.5 μs. However, this gap discharge stops at the ground electrode. It induced the second PMT signal peak observed in Figure 3.6(b). At −1 μs, most of the gap region emits light, perhaps due to a second ionization front traveling across the gap. At 0 μs, the positive bullet is clearly seen passing through the grounded electrode and can propagate over 10 cm at the velocity of 30 km/s. Similar to the negative cycle, a glow-like discharge is induced in the gap region, which corresponds to the third PMT signal peak in Figure 3.6(b). Interestingly, the discharge processes before the build-up of the actual plasma bullets are not observed when the ring ground electrode is removed evidencing the crucial role of the ground electrode in the generation of multi-periodic bullets.

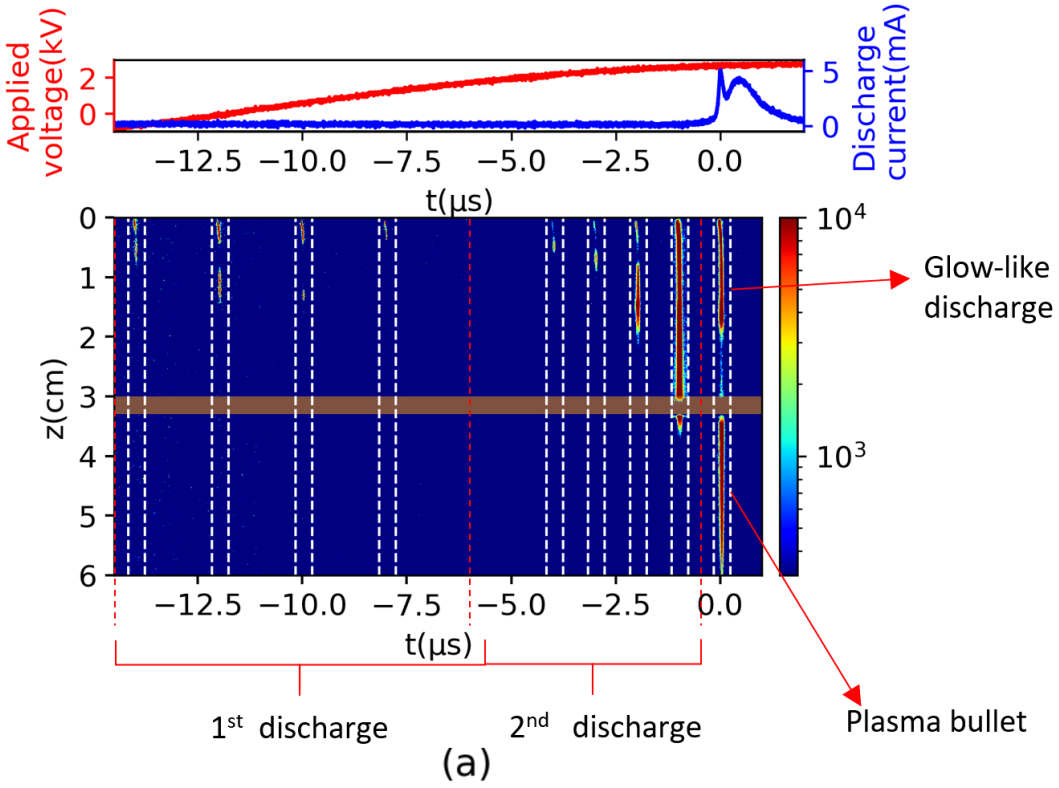

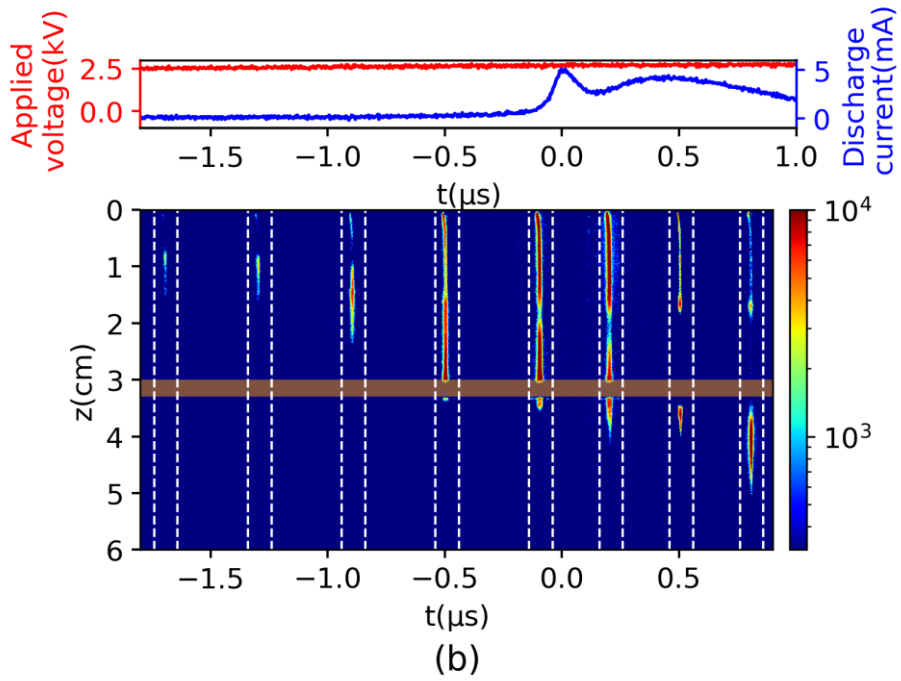

Figure 3.8. Waveform and ICCD photos of the propagation dynamics of the positive bullet in different time scales. The experiment conditions are the same as in Figure 3.7. (a) shows the propagation in a time range of 14 μs with an exposure time of 1 μs for each photo. The intensities of the first 4 photos are much weaker than the others, so the contrast is increased by a factor of 10. (b) shows the propagation in a time range of 2.5 μs with an exposure time of 200 ns for each photo. Light intensity is shown in log scale. Note that the intensity of the first 4 photos of figure (a) is increased by a factor of 5 to ensure readability.

Figure 3.7 and Figure 3.8 clearly show the link between self-triggered gap discharges and multi-periodic plasma bullets formation.

In the HV cycles without plasma bullet formation, some short discharges are also observed in the gap. Figure 3.9 shows the ignition time and length of the discharges in 5P, 3P, and 2P modes. The position of the bars represents the ignition time of a discharge, and the length of the bars represents the propagation length of discharges. Note that the 5P mode is only stable for about 15 min, then it disappears because the plasma changes the gas impurities by desorbing the molecules on the tube's inner surface.

It is clear that the long plasma bullets i.e. discharge longer than 10 cm in sequence B, are ignited with a higher voltage than the short discharges. By comparing Figure 3.9(a) (b) and (c), the evolution of plasma can be summarized as the repetition of discharge sequences A and B. Sequence A is a sequence of 5 discharges during two ac periods, like in Figure 3.9(b) from 100 μs to 200 μs. Sequence B is a sequence of two gap discharges during one ac period, like in Figure 3.9(b) from 40 μs to 100 μs. In 2P mode, only sequence A happens. In nP(n>2) mode, discharge sequence B happens n-1 times between two sequence A. Figure 3.9 evidences that

short gap discharges similar to DBDs occur between bullets. These gap discharges (e.g. ii and iii) happen both in sequences A and B.

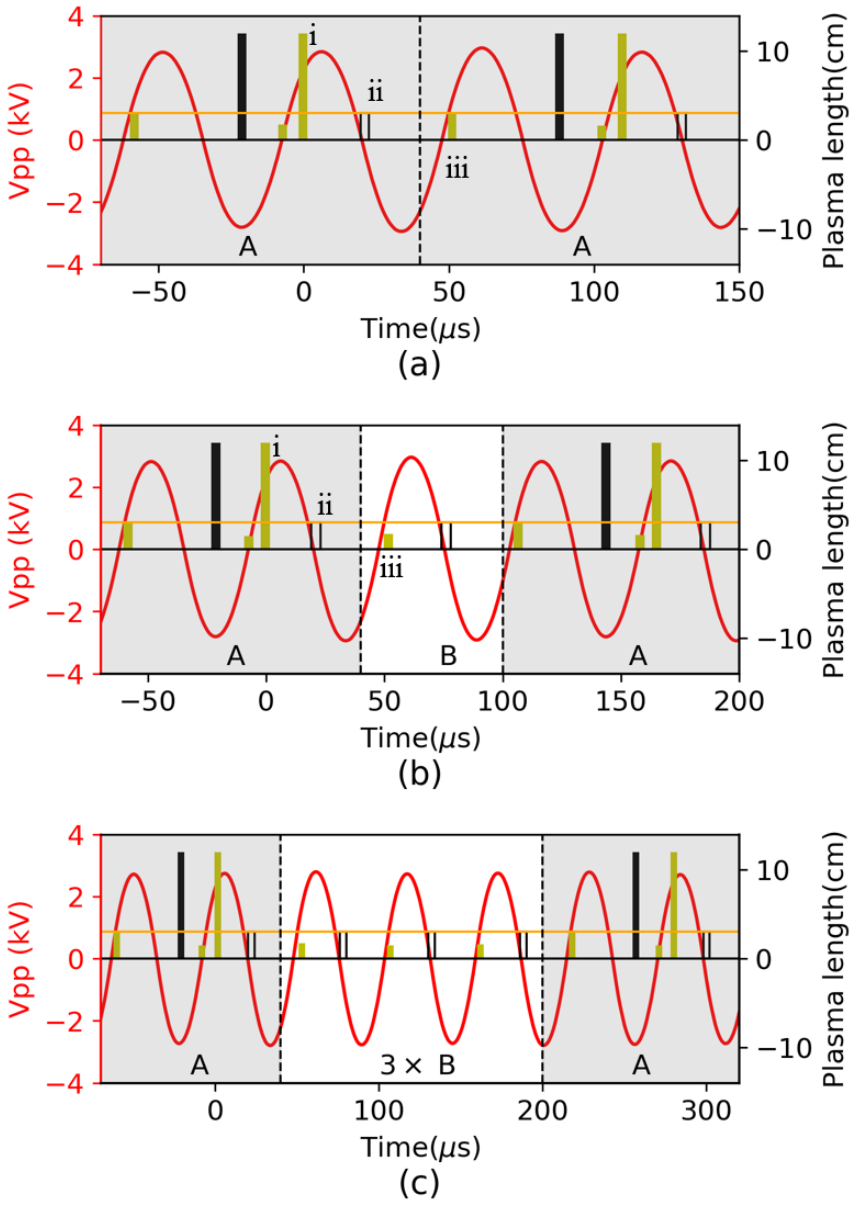

Figure 3.9. Ignition time and propagation length of discharges in (a) 2P, (b) 3P, and (c) 5P mode. The position of the bars represents the ignition time of a discharge, and the length of the bars represents the propagation length of discharges. The yellow bars represent the positive discharges that are streamer-like. The black hollow bars represent the glow-like negative discharges. The black-filled bars represent the negative bullets. The grey and white background colors separate sequence A and sequence B.

In an “nP” (n≥2) multi-periodic mode, short gap discharges are observed before the formation of plasma bullets. In the case of negative plasma bullets, these short gap discharges propagate back and forth in the gap region; in the case of positive plasma bullets, there are two gap

discharges that propagate downstream. For both negative and positive plasma bullets, a glow-like discharge is formed in the gap region after the plasma bullets.

3.2.3 Discussion: different mechanism of gap discharges and plasma bullets

The DBD ignition dynamics in the gap region shown in Figure 3.7 and Figure 3.8, and the discharge ignition time and length shown in Figure 3.9 reveals different mechanisms of long plasma bullets and short gap discharges in multi-periodic plasma jet. To understand the mechanism of the multi-periodic modes, it is necessary to focus on the inter-electrode DBD.

Many works show the important role of surface charge in self-organized DBDs with spatial or temporal patterns. Célestin *et al* show how the surface charge deposited upon the dielectric plate modifies the spatial organization of microdischarges in a pin-to-plate AC DBD [65]. Berneker *et al.* point out the important role of surface charges on the formation of discharges with honeycomb structure in a DBD in Neon at 100 torr and 1 mm gap [64]. Chirokov *et al.* investigated the 2D distribution of a micro DBD and proposed that the deposited surface charges facilitate the new avalanches and result in the formation of localized streamers [66]. Alternatively, some works also pointed out the role of volumetric residual charges on the ignition and propagation of DBDs [50,67]. However, the time between the first discharge of sequence A and the previous discharge is more than 30 μs. Some experimental measurements show that the electron density after a plasma bullet decays drastically in several microseconds [45,137]. In contrast, the lifetime of surface charges can be up to hours [36]. Thus, we assume that the role of volumetric charge is negligible in the working frequency range of this work, and in the present work, we consider that the propagation process is mainly influenced by the surface charges.

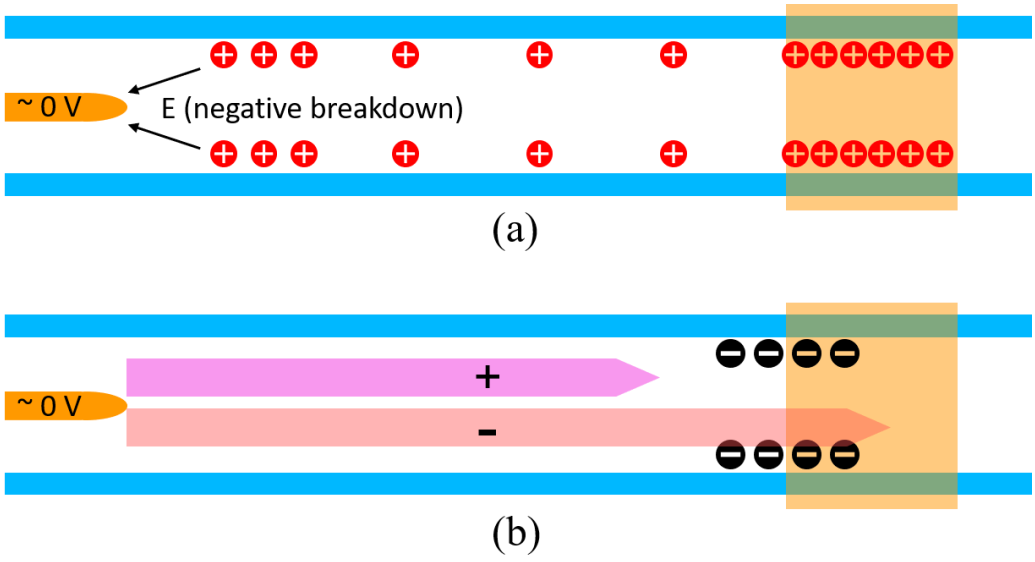

Figure 3.10 A schematic view of the role of gap discharges and deposited charges after a positive plasma bullet and before a negative one. (a) shows the surface charge before the breakdown ii shown in Figure 3.9. (b) shows the net negative surface charge accumulation due to the different propagation lengths of positive and negative gap discharges during sequence B.

The time of breakdown is significantly influenced by the surface charges. For example, during the increase of the applied high voltage, a large amount of positive surface charges is accumulated along the inner surface, after a positive plasma bullet (discharge i in Figure 3.9(a) and (b)). When the applied high voltage decreases, these positive surface charges enhance the electric field near the pin electrode, as shown in Figure 3.10(a). As a result, the negative breakdown happens when the applied voltage is close to 0 (like discharge ii in Figure 3.9). In the present study, the short gap discharges always correspond to the absolute value of instant breakdown voltage from 0 to 500 V, while the long plasma bullets are always ignited when the absolute value of instant applied voltage is higher than 2.5 kV. We assume that the propagation length is dominated by the instant breakdown voltage, and the instant breakdown voltage is shifted because of the evolution of surface deposited charges near the pin electrode. The instant voltage can affect the propagation of the ionization front because the ionization front is electrically connected to the powered electrode[24]. A similar effect has also been reported by Kim *et al*, who reported that in the irregular discharges of an APPJ, a discharge with higher instant voltage has increased optical intensity [42].

The discharge evolution after sequence A depends on the propagation length of the following gap discharge (like gap discharge iii in Figure 3.9(a) and (b)). When gap discharge iii is long enough to bridge the gap region (like discharge iii in Figure 3.9(a)), it transfers some positive surface charge to the ground electrode region; these surface charges can then trigger the reflection process of negative discharge shown in Figure 3.7. However, the multiple reflection process and formation of negative bullets are very little studied and the mechanism remains unclear. If V_{pp} is not high enough, the gap discharge iii is shorter than the gap distance (like discharge iii in Figure 3.9(b)), the negative bullet cannot be generated, and the sequence B happens until a sufficient amount of surface charges has been built-up.

As demonstrated in Figure 3.10(b), during sequence B, the negative gap discharge is longer than the positive gap discharge, thus a small amount of negative surface charges is accumulated near the ring electrode, and slightly decrease the electric potential and attracts the following positive discharge. Sequence B may repeat several times until one positive gap discharge can bridge the gap region and trigger sequence A.

To summarize, we consider that the multiperiodic mode occurs because the plasma jet transfers between two processes: In sequence A, a positive gap discharge that can bridge the gap region triggers the following plasma bullets; if V_{pp} is not high enough, sequence B is necessary to relaunch sequence A; in sequence B, negative surface charges accumulation enables the positive gap discharge which triggers sequence A.

The explanation to the phenomenon only applied to the "nP" multiperiodic modes with $n \geq 2$. Further research is required for understanding the transition between the 1P mode and random modes.

3.2.4 Charge accumulation beneath the ground electrode enhances the propagation length

In Figure 3.7 and Figure 3.8, ICCD imaging shows that the ionization wave slows down at the gap electrode for about 500 ns before launching the bullet. However, the stop and reignition process is not clear in distinct ICCD photos with a time resolution of 200 ns. To confirm the stop and reignition process, an optical fiber is placed 2 mm downstream of the ground electrode so that the light signal is acquired by the PMT, as shown in Figure 3.11(a). Figure 3.11(b) shows the acquired PMT signal (green curve) of the positive plasma bullet and the applied voltage (red curve). A small light peak is observed ~500 ns before the strong light peak. The PMT signal confirms that the plasma stops at the ground electrode and then forms the plasma bullet.

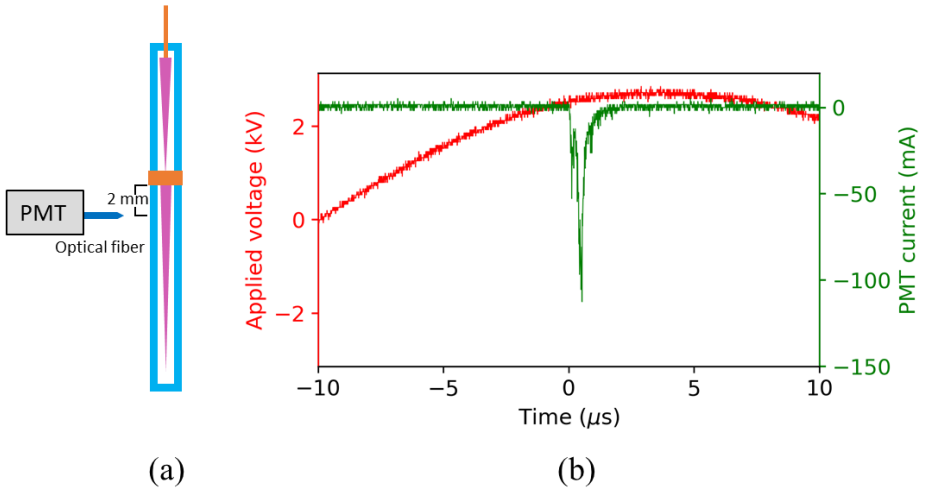

Figure 3.11. (a) shows the experiment condition where an optical fiber is placed 2 mm downstream of the ground electrode. (b) shows the applied voltage (red curve) and the signal of the PMT (green curve) acquired at the position shown in (a).

The formation of plasma bullets in the vicinity of the ground electrode has been reported by Jiang *et al* [138,139]. When a gap discharge reaches the ground electrode, it slows down or even stops due to the potential drop and charge accumulated by the previous gap discharge with opposite polarity. When the residual deposited charges are compensated, the charges are accumulated beneath the ground electrode and create a potential that increases abruptly. This fast-rising potential is similar to a pulsed power supply and can ignite a plasma bullet about 1 μs after the gap discharge reaches the ground electrode. Jiang et al. called the plasma jet generated by the accumulated charges an “overflow” jet. The jet had the characteristics of a pulsed discharge although driven by a sinusoidal high voltage and was suitable for biomedical applications such as sterilization[140]. The generation threshold voltage and propagation length of an overflow jet are influenced by the width of the ground electrode. In the present work, the width of the ground electrode is only 3 mm, thus accumulated charges beneath the ground electrode are localized in a small region, which allows the formation of a local high

electric field and bright plasma bullets with lower applied voltage compared to the article of Jiang et al[139].

To evaluate the potential created by the accumulated charges beneath the ground electrode after the gap discharge reached the ground electrode and before the plasma bullet is ignited, we calculated the electric field by solving Poisson equations with COMSOL. Note that this numeric simulation is based only on an electrostatic model without a volumetric space charge field. Poisson equation is solved in a 2d axisymmetric configuration shown in Figure 3.12(a).

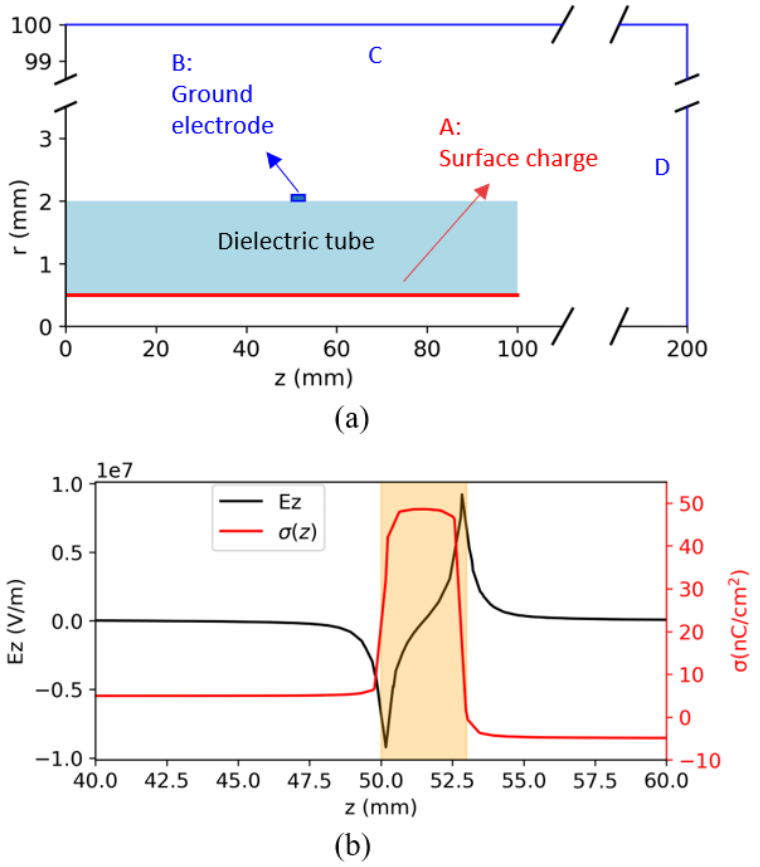

Figure 3.12. (a) shows that simulation configuration and boundary conditions. (b) shows the hypothesis of surface charge distribution below the ground electrode, and the orange rectangle represents the ground electrode. In (b), the surface charge density on boundary A near the ground electrode is shown in the red curve. The calculated z component of the electric field in the capillary at 0.1 mm to the inner surface is shown in the black curve. The orange rectangle represents the ground electrode.

The boundary A represents the capillary inner surface beneath the ground electrode and has a surface charge density of σ(z). When z<50 mm, we assume $\sigma(z)=\sigma_{gap}$ due to the gap discharge propagation. When z>53 mm, the surface charge deposition σ(z) is due to the plasma bullet in the previous negative plasma bullet and is assumed to be $\sigma(z)= -\sigma_{gap}$. Boundary B represents the ring-shaped ground electrode. Boundaries C and D represent the extremity of the simulation area which is set to be grounded.

The value of accumulated surface charge density beneath the ground electrode (50 mm<z<53 mm) is estimated from experimental measurement. The 50 Ω resistance shown in Figure 3.1 is replaced by a 1 nF capacitor C_m. When the discharge is initiated at the ground electrode, the voltage increase U_g across the C_m capacitor is measured. The surface charge density σ beneath the ground electrode is estimated as equation (1.1):

$$\sigma(50mm < z < 53mm) = \frac{C_m \, \Delta U_g}{\pi d_{jet} l_g} \tag{3.1}$$

Where d_{jet} is the inner diameter of the glass capillary equal to 1 mm, and l_g is the length of the ground electrode equal to 3 mm. This is a rough estimation assuming that most of the charges measured using the capacitor C_m are located in the immediate vicinity of the ground electrode. Typically, the value of σ is 50 nC/cm^2 with a ± 10% variation from one bullet to another.

In the gap and downstream of the ground electrode region, the value of deposited charges σ_{gap} is estimated from published numerical simulations as an estimation. For example, Jansky *et al.* show by simulation that the surface charge density deposited by a plasma bullet ranges from 0 to 10 nC/cm^2, depending on the dielectric material [141]. In our simulation, we assume σ_{gap}=5 nC/cm^2. So the surface charge deposition on boundary A along the z-axis is shown in Figure 3.12(b).

The potential can be calculated by solving Poisson equations. Considering the ring shape of the plasma bullets, we deduce the z-component of the electric field close to the inner surface (r=0.4 mm) and the results are shown in Figure 3.12(b), where the downstream is the positive direction. It is shown that the accumulated charges create an electric field as high as 10^7 V/m, which is similar to the electric field at the high voltage tip if the potential of the tip is 2.2 kV. Varying the value of σ_{gap} in the range of 0~10 nC/cm^2 has negligible influence on the electric field.

The ground electrode region can store more surface residual charges than other regions of the inner wall. When the second gap discharge propagates to the ground electrode, the ionization stops due to the residual surface charges. When a sufficient amount of surface charges are accumulated in the ground electrode region, it is shown by solving the Poisson equation that these charges create an electric field as high as 10^7 V/m, which is possibly responsible for the ignition of plasma bullets in the downstream area.

3.3 Measurement of plasma velocity in different multi-periodic modes

Since plasma behaviors are non-linear with the operation conditions, it is important to compare the characterization of plasma in different multi-periodic modes. In this section, the propagation in 2P and 3P modes are compared.

The propagation velocity of positive and negative bullets outside the gap region is measured with one optical fiber connected to PMT. This optical fiber is placed at different positions along the glass capillary, and at each position, the time difference between the PMT signal and discharge current peak is measured. Then the average velocity between the two positions can be deduced. The velocity measured in different conditions is shown in Figure 3.13. The position x=0 represents the inner edge (close to the high voltage electrode) of the ground electrode. It is remarkable that the trend of the bullets velocities does not seem to depend on the gap or 2P vs 3P. Generally, the plasma after the ground electrode starts with a velocity of 10~20 km/s. It accelerates to its maximum velocity after about 15 mm of propagation, which is higher than the initial speed by a factor of 2, approximately. Then the velocity decreases linearly with the distance. Figure 3.13(a) shows that the velocity of positive discharges in different periodic modes has a maximum difference of about 20%. The maximum velocity is observed in the discharges in a jet with a 30 mm gap distance in 3P mode, showing that the velocity is not directly linked to the amplitude of driven voltage. Figure 3.13(b) shows that the velocity of negative discharge is significantly slower that the positive discharges, which has been reported in other experiments [142]. It can be explained by the higher electric field in positive discharges than in negative discharges, which has been reported in numerical and experimental research [31].

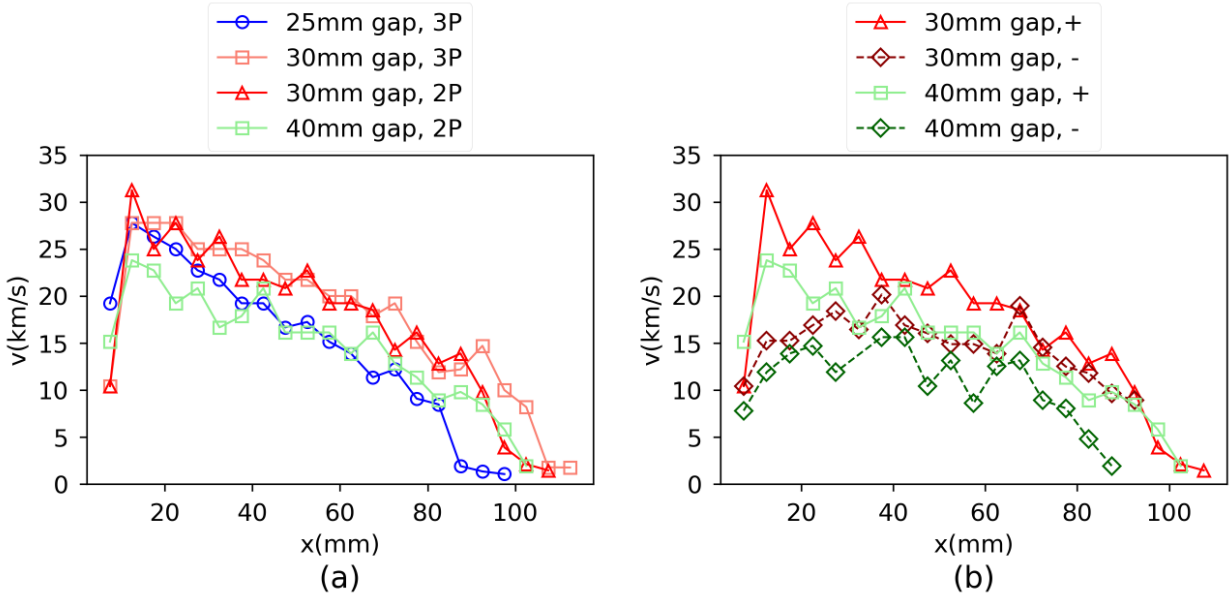

Figure 3.13. The propagation of the plasma bullet (the third discharge) a function of position. The driving frequency is fixed at 17 kHz. (a) shows the velocity of positive discharges with 25 mm, 30 mm, and 40 mm gap distances and in 2P and 3P period modes. (b) shows the velocity of positive and negative discharges with a gap distance of 30 mm and in 2P periodic mode

In multiperiodic modes, the velocities of the plasma bullets are similar in 2P and 3P modes. The velocity of the positive plasma bullets is about 60% higher than the negative plasma bullets.

3.4 Optical emission spectra

3.4.1 Time-integrated OES

The optical emission spectrum is acquired at 20 mm downstream of the ground electrode and the middle of the inter-electrode gap region. The results are shown in Figure 3.14(a) and (b), respectively. In Figure 3.14(a), the emission lines are identified. The main emission is the He I transition $3s^3S^1 \rightarrow 2p^3P^0$ at 706.5 nm and the 309 nm from the OH band ($A\ ^2\Sigma+ \rightarrow X\ ^2\Sigma$ transition). The emission from O I at 777 nm and H at 656.6 nm can also be observed. The line intensity at 706.5 nm and 309 nm are close. However, in the gap region, as shown in Figure 3.14(b), the line intensity of the OH band increased by a factor of ~30 compared to Figure 3.14(a) in the downstream region, while the light intensity of helium remained the same.

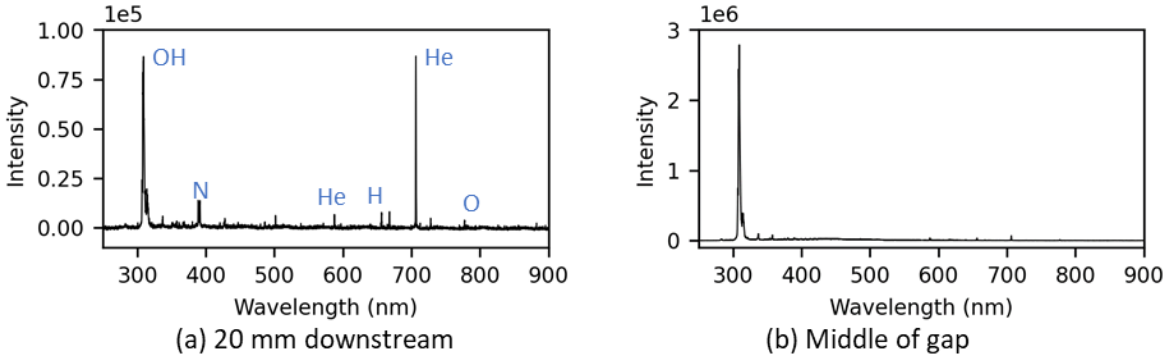

Figure 3.14. Optical emission spectrum of the plasma acquired at (a) 20 mm downstream of the ground electrode and (b) in the center of the gap region. The flow rate is 1 SLM; the driven voltage Vpp = 12 kV, 16 kHz.

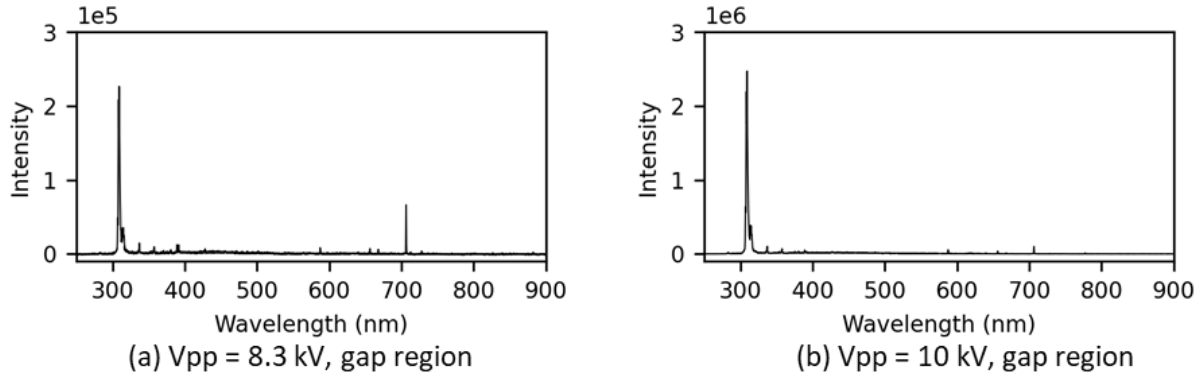

Figure 3.15. (a) Optical emission spectrum of the plasma acquired at the center of the gap region and the flow rate is 1 SLM; the frequency is 16 kHz. The applied peak-to-peak voltage is 8.3 kV for (a) and 10 kV for (b).

Figure 3.15 compares the optical emission spectrum of the plasma at the middle of the gap region with different applied voltages. When V_{pp} increased from 8.3 kV to 10 kV, the intensity of the OH band increased by a factor of ~10, while the intensity of the helium lines only increased by 40%. Similar measurements were performed by varying Vpp from 8.3 kV to 13 kV. The relative intensity is obtained by normalizing the line intensities to the line intensity of the He line at 706.5 nm with V_{pp}= 8.3 kV at the middle of the gap region. The result is plotted in Figure 3.16.

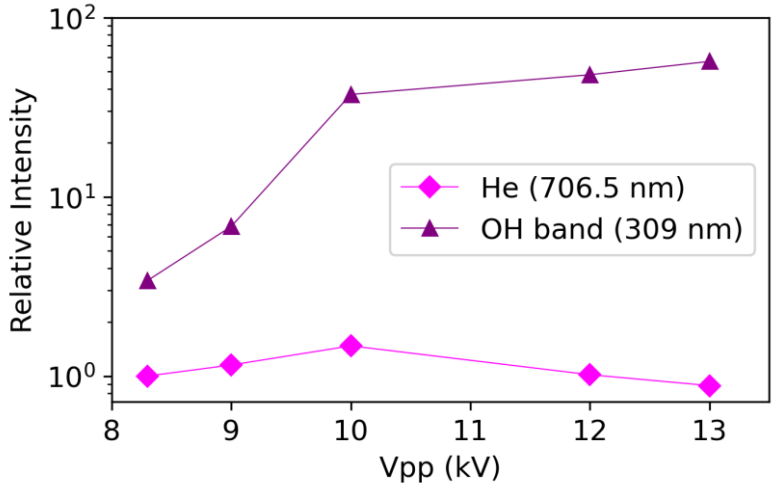

Figure 3.16 Relative intensity of the helium line at 706.5 nm and the OH band at 309 nm while V_{pp} increases from 8.3 kV to 13 kV. The spectra are acquired at the middle of the gap region.

Time-integrated OES show that the line intensity ratio of OH (309 nm)/ He(706 nm) is much higher in the gap region than in the downstream region, and can increase by a factor of 60 when the applied voltage increases by a factor of 50%.

3.4.2 Time-resolved OES

In the following, time-resolved OES is performed to study the emission of discharge in different periodic systems and different polarities.

OES in the gap region

As shown in Figure 3.7 and Figure 3.8, multiple ionization waves are observed during the process of forming a plasma bullet. Time-resolved OES is performed to compare the emission of the different ionization waves. Figure 3.17 shows the applied voltage and the light signal of a plasma bullet acquired at the middle of the gap region. The APPJ is operated in 2P mode. The first and the second light peak corresponds to the first and second gap discharges shown in Figure 3.8. The third light peak is the light emission in the gap region after the plasma bullet ignition which happens at the ground electrode. The gate width of the ICCD is set to 1 μs. The oscilloscope is triggered on the signal of a plasma bullet, and the spectrometer is delayed for about 125 μs (two AC cycles) so that the signal of the next plasma bullet is obtained by the spectrometer. The gates of the spectrometer are shown in Figure 3.17 with red dash lines. Each spectrum is accumulated 5000 times to increase the signal-to-noise ratio.

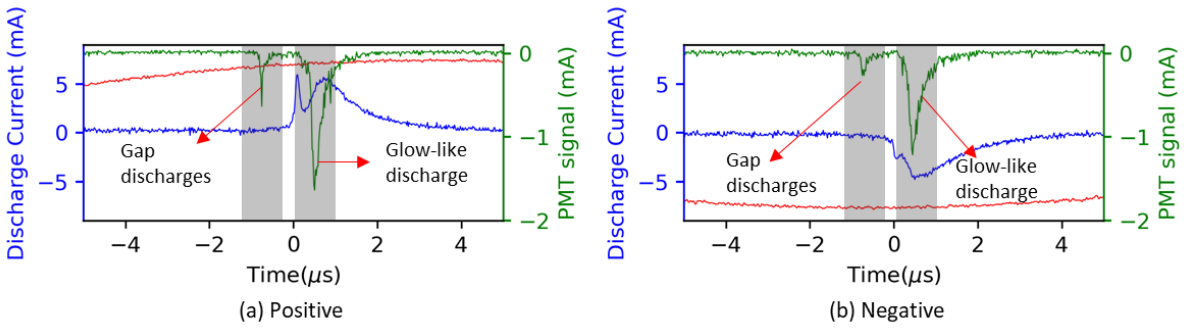

Figure 3.17. Applied voltage, discharge current, and the PMT signal of a positive plasma bullet operating in 2P mode. The 1 μs gates of the spectrometer are shown with the grey areas.

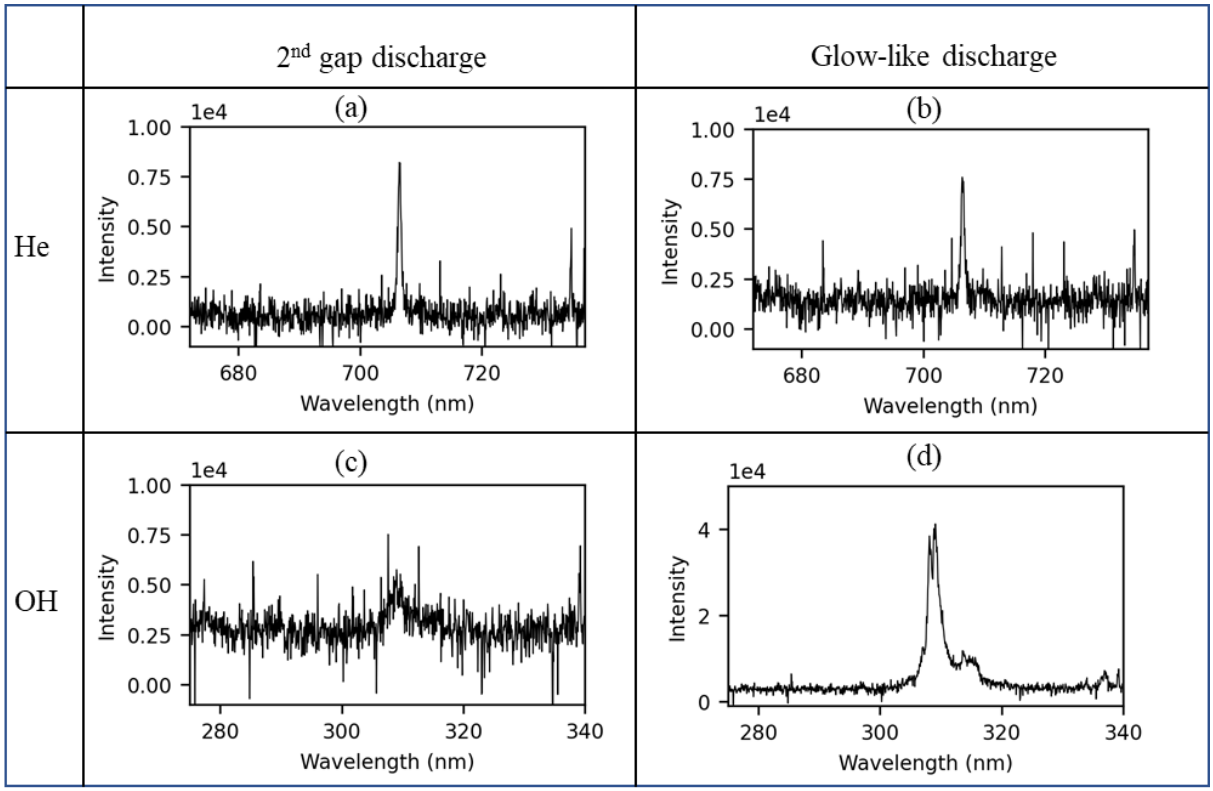

Figure 3.18. Spectrum of the 2nd positive discharge and the afterglow in the gap region near 706.5 nm of helium and 309 nm of OH band.

Due to the small exposure time of the spectrometer, only the emission line at 706.5 nm and 309 nm can be clearly detected. The spectra of the gap region ionization waves and the afterglow during the positive cycle are shown in Figure 3.18. The intensities of helium lines at 706.5 nm for the gap region ionization waves and the afterglow are similar, but the emission of the OH band in the afterglow is much higher than in the gap region ionization waves. Same measurements are performed for the negative cycles, and the relative intensities of He 706 nm and OH 309 nm are shown in Figure 3.19, where helium emission is shown with bars in pink and OH in purple. The relative line intensities are obtained by normalizing the line intensities to the intensity of He 706 nm of the positive gap region ionization wave.

As shown in Figure 3.19, for both positive and negative discharges, the emission intensity of the OH band is significantly enhanced by a factor of approximately 7. However, the emission intensity of He 706 nm remains similar for all discharges.

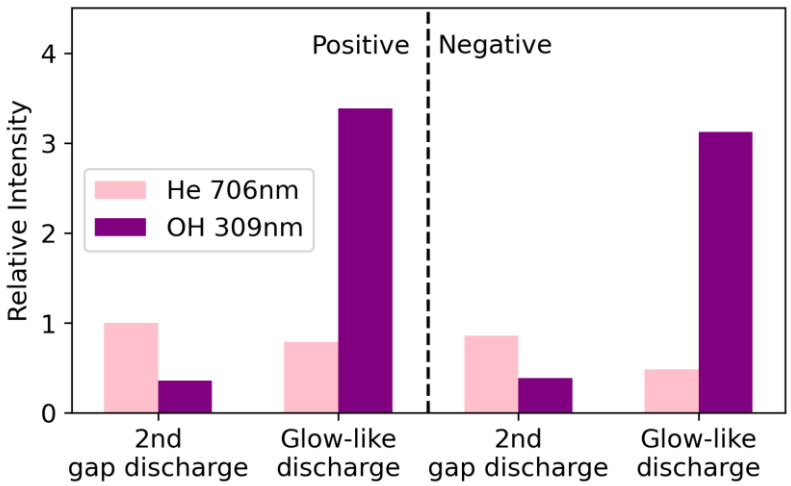

Figure 3.19. The relative optical emission intensity of helium 706 nm and OH 309 nm of positive (left side) and negative (right side) gap region ionization waves and the afterglow. The gap distance is 30 mm. The applied peal-to-peak voltage is 6 kV. The signal is acquired in the middle of the inter-electrode gap region. The intensity is the accumulation of 5000 plasma bullets and is normalized to the intensity of positive gap region ionization waves bullet in 3P mode at He 706 nm.

OES of bullets (outside the gap region)

Time-resolved OES of the plasma bullet is compared with different multiperiodic modes. Optical emission is acquired at 20 mm downstream of the ground electrode, where bullets velocity is maximum (Figure 3.13). The exposure time of the camera is set to 10 μs to ensure that each shot collects only the emission of one single discharge. Each spectrum is the accumulation of signal of 5000 discharges. We measure the peak value of the emission at the He 706.5 nm and OH 309 nm and normalized to the value of 706.5 nm in the positive discharge of 3P mode to 1. The results are shown in Figure 3.20. It is shown that compared to the positive bullets, the emission of negative bullets has a significantly smaller fraction of helium lines. This change in helium emission fraction is even more significant in 2P mode than in 3P mode.

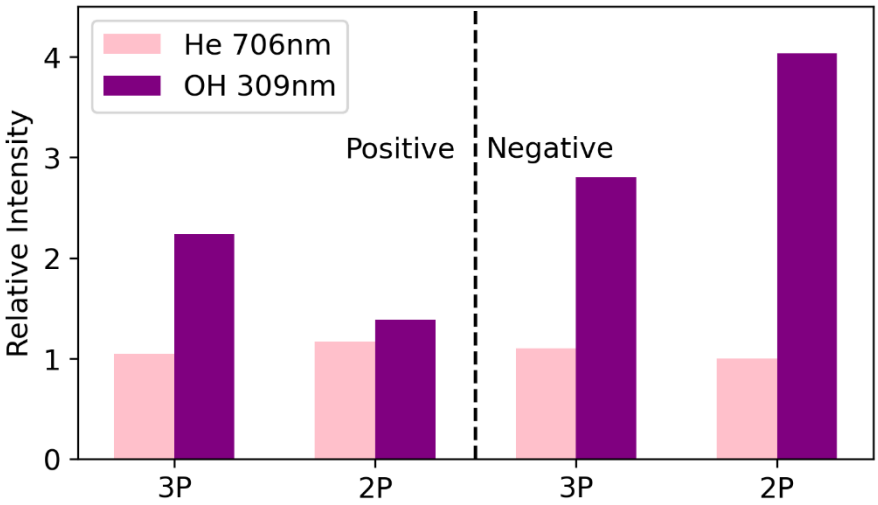

Figure 3.20. The relative optical emission intensity of helium 706 nm and OH 309 nm of positive (left side) and negative (right side) in 2P and 3P mode. The gap distance is 30 mm. The applied voltage is 5.88 kV for 3P mode and 6 kV for 2P mode. The signal is acquired at 20 mm downstream of the ground electrode. The intensity is the accumulation of 5000 plasma bullets and is normalized to the intensity of positive bullets in 3P mode at He 706 nm.

The different ratio of helium and OH emission has been reported in previous studies with He-APPJ driven by pulsed power supply [143] and compared to the positive cycle, the negative discharge tends to have a higher fraction of OH emission than helium emission.

3.4.3 Discussion

Impurities in the gas helium gas bottle is H_2O and O_2 at a concentration of 3 ppm and 2 ppm, respectively. Hence, in the plasma, H_2O as well as OH, H, and O radicals may be detected. Figure 3.14 show that apart from helium, the strongest OES peaks come from OH excited states. By changing the applied voltage, measurement position, and measurement time, the intensity of OH emission is significantly changed by a factor of at most 60 in this experiment, while the intensity of helium emission only changed at most 50%.

The kinetics in helium plasmas with humidy have been intensively studied [144–148].

The formation of OH(A) can be through electron dissociation of water:

$$H_2O + e^- \rightarrow OH(A) + H + e^- \quad (3.2)$$

Or through dissociative recombination of H_2O^+ or H_3O^+

$$H_2O^+ + e^- \rightarrow OH(A) + H \quad (3.3)$$

H_2O^+ can be formed from Penning ionization from helium metastables and charge transfer..

$$He^* + H_2O \rightarrow He + H_2O^+ + e^- \quad (3.4)$$

$$He_2^* + H_2O \rightarrow 2He + H_2O^+ + e^- \quad (3.5)$$

$$He^+ + H_2O \rightarrow He + H_2O^+ \quad (3.6)$$

$$He_2^+ + H_2O \rightarrow 2He + H_2O^+ \quad (3.7)$$

Helium metastables are created in the gap discharges:

$$e^- + He \rightarrow He^* + e^- \quad (3.8)$$

Or through dissociacive recombination:

$$He_2^+ + e^- \rightarrow He^* + He \quad (3.9)$$

Reaction (3.2) and (3.3) can also form OH(*X*). In case of sufficient amount of OH(*X*), OH(*A*) can also be formed by direct excitation:

$$OH(X) + e^- \rightarrow OH(A) + e^- \quad (3.10)$$

The most intensive helium line at 706 nm results from the de-excitation of excited helium He(3^3S):

$$He(3^3S) \rightarrow He(2^3P) + h\nu(706.5\ nm) \quad (3.11)$$

The excited helium results from inelastic electron collisions with helium atoms in the ground state[149,150]:

$$He(1^1S) + e^- \rightarrow He(3^3S) + e^- \quad (3.12)$$

Figure 3.19 shows that the OH emission measured in the gap region mainly comes from the glow-like discharge. Unfortunately we can't verify whether this is still true with increased voltages up to 13 kV, because time-resolved OES cannot be performed with higher voltages due to the random plasma ignition. However, we believe that it is reasonable to suppose the dominant source of the OH emission in the gap region is always the glow-like discharge regardless of the applied voltage.

Under this assumption, the explanation to the difference of spectra in the gap region and the downstream region shown in Figure 3.14 is trivial: the emission of glow-like discharges is not integrated in the spectrum of downsteam plasma bullets, thus the OH emission in the downstream plasma is much weaker than in the gap region. Also under this assumption, the increase of time-intergrated OH line intensities with the applied voltage as shown in Figure 3.16 should be mainly attributed to the increase of OH emission in the glow-like discharge.

Only a few studies have discussed the nature of the glow-like discharge in the gap region of APPJ [136]. However, similar phonomena have been observed in streamer discharges. Primary and secondary streamers have been reported, and it is shown that most of the reactive species including OH is mainly formed in the secondary streamer [151–154]. The glow-like discharge is ignited in the ionized channel with abundant helium metastables. When the applied voltage

increases, the density of electrons and metastables in the gap region increases, which enhances the formation of OH through electron dissociation and formation of H_2O^+. H_2O^+ can also form OH(A) through dissociative recombination. On the other hand, due to the high electron density in the ionized channel, the electric field and the electron energy is lower than the gap region ionization waves. However, the electron energy required for the formation of OH(A) is around 1~2 eV, which is much lower than for the excitation of helium. Thus, the reduced electron enegy should also result in a lower ratio of He/OH emission line intensities.

The OES measurements in this section show that the OH is possibly mainly produced during the glow-like discharges. The production of OH is enhanced due to the increased dissociation recombination of $H2O^+$ which is mainly produced by helium metastables through Penning ionizations.

3.5 Comparative study with a DC pulsed APPJ

In this section, experiments were performed by replacing the AC power supply with a DC pulsed power supply while the APPJ configuration remains the same. The propagation is compared with the results obtained with the AC power supply.

3.5.1 Electrical description of the discharge

Figure 3.21 shows the applied voltage pulse and the corresponding current measured at the ground electrode. The voltage has a rise time of ~ 50 μs and a fall time of ~300 μs. The plateau of the pulse is about 300 μs. The displacement current is subtracted. In an AC-driven APPJ, an afterglow(secondary discharge) is observed after the formation of plasma bullet and causes a slowly-rising current ~1 μs after the first current peak. In the DC-driven APPJ, the secondary discharge in the gap region is much less obvious. The amplitude of the current peak is 10~20 times higher than the AC-driven APPJ if driven by voltages with the same amplitude.

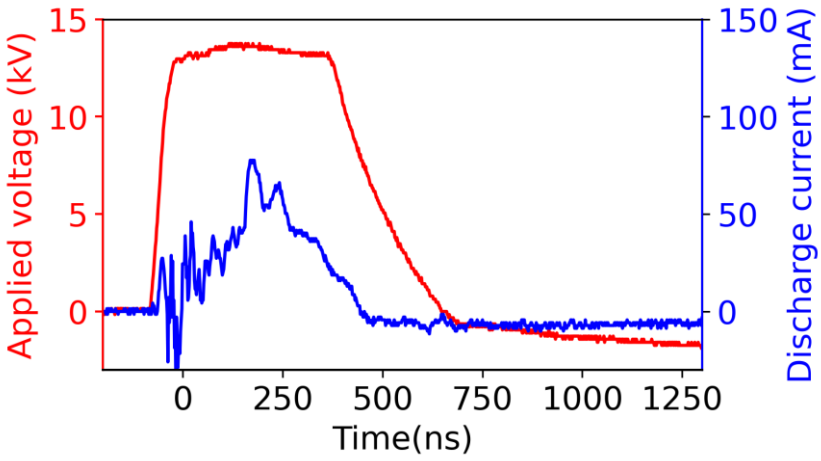

Figure 3.21. The applied voltage (red) of the pulsed power supply and the discharge current(blue) were measured at the ground electrode.The displacement current is subtracted. The frequency is 2 kHz. The voltage is 14.4 kV.

3.5.2 Propagation of the pulsed discharge

The propagation of the DC-driven plasma bullet is observed using the ICCD camera using the same methods as the AC-driven APPJ. The photos are shown in Figure 3.22. The gate width of the ICCD camera is 200 ns and each photo is accumulated 100 times. The voltage is 7 kV with a frequncy of 10 kHz. While multiple short gap discharges are observed before the plasma bullet formation in the AC-driven APPJ, only one discharge can be observed in Figure 3.22(a). The plasma bullet propagates with a nearly constant velocity. When an external ring-like ground electrode is used with a gap distance of 30 mm, the propagation is shown in Figure 3.22(b). The propagation velocity of the discharge increases when the discharge approaches

the ring-like ground electrode then slows down when it reaches it, and then restarts to accelerate after the ground electrode. A bright ionized channel is formed in the gap region with nearly homogeneous emission intensity. The light intensity of this glow-like discharge is smaller than the previous ionization wave. In contrast, the glow-like discharge in the AC driven APPJ shown in Figure 3.7 and Figure 3.8 has a light intensity stronger than the previous ionization wave.

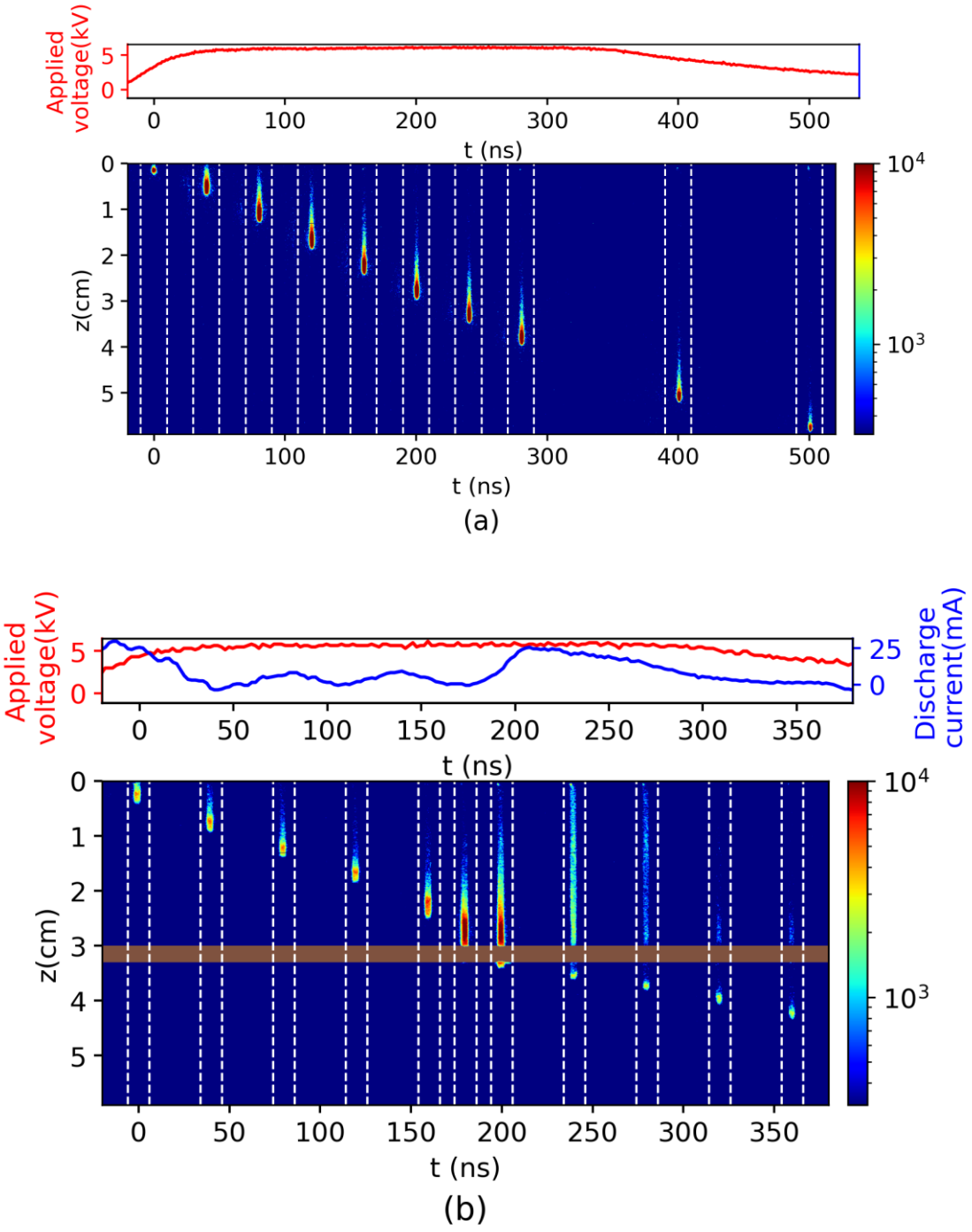

Figure 3.22. Propagation of a plasma jet driven by DC pulsed voltage. The applied voltage is 7 kV. The driven frequency is 10 kHz. The helium flow rate is 1 SLM. The gate width of the ICCD is 200 ns.

Each photo is accumulated 100 times. (a) shows the propagation without a ground electrode. (b) shows the propagation with a external ring-like ground electrode which is marked with the orange bar.

The velocity of the discharge propagation is calculated using the signals acquired by PMT signals at different positions and is plotted in Figure 3.23. Figure 3.23(a) shows the propagation velocity with a 5.5 kV pulse with or without the ground electrode. The ground electrode causes a significant increase in the velocity shortly upstream of it. The slowing down cannot be detected, possibly because it happens within a distance of less than 5 mm, as shown in Figure 3.22, which is shorter than the spatial resolution of the velocity measurement. By comparing the red and yellow curves in Figure 3.23(a), one can see that the final velocity with or without the ground electrode is close. Generally, the ground electrode only causes a velocity variation near it; and causes a propagation length extension of about 30%. No extra discharge is caused by the ground electrode. Figure 3.23(b) shows the propagation velocity of the discharge with different pulse amplitude without the ground electrode. A high voltage increases both the propagation velocities and the propagation lengths.

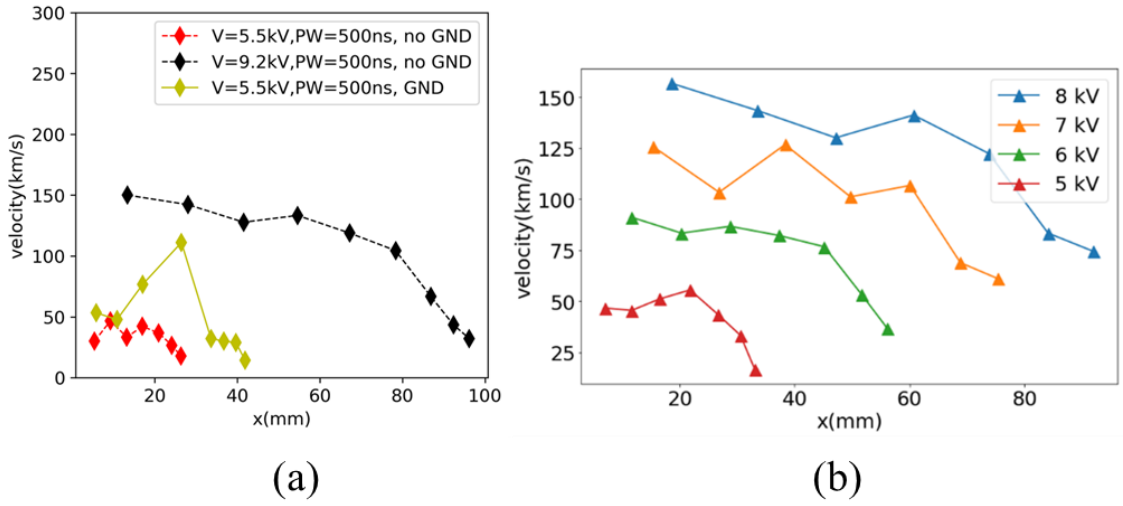

Figure 3.23. (a) compares the propagation velocity of the plasma bullet as a function of its position with a ground electrode (GND) or without the ground electrode (no GND). (b) shows the plasma bullet velocity with pulse amplitude from 5 kV to 8 kV without the ground electrode. The pulse repetition rate is 10 kHz.

3.5.3 Stability of the discharge

The discharge current, propagation dynamics, and velocity shown in section 3.5.1 and section 3.5.2 are also measured by varying the frequency from 0.1 kHz to 10 kHz. No significant difference is observed. For example, the propagation velocity of the plasma bullet without a ground electrode is shown in Figure 3.24. The propagation velocity only decreases by a factor of ~20% when the frequency decreases from 10 kHz to 0.1 kHz. Although the discharge remains periodic when varying the frequency, the discharge loses stability when the

frequency is below 70 Hz, i.e. sometimes the discharge cannot be ignited and the propagation length and velocity are random. This is possibly associated with the lifetime of surface residual charges. The plasma ignition is due to the electric field generated between the powered electrode and the surface charges deposited on the capillary wall surrounding the powered electrode. With higher frequency, the charge deposition and recombination reach a steady state. With a frequency below 70 Hz, the recombination of surface charges increases, possibly causing a random surface charge distribution before the voltage pulses. Thus, the lifetime of surface deposited charges can be estimated to be ~10 ms.

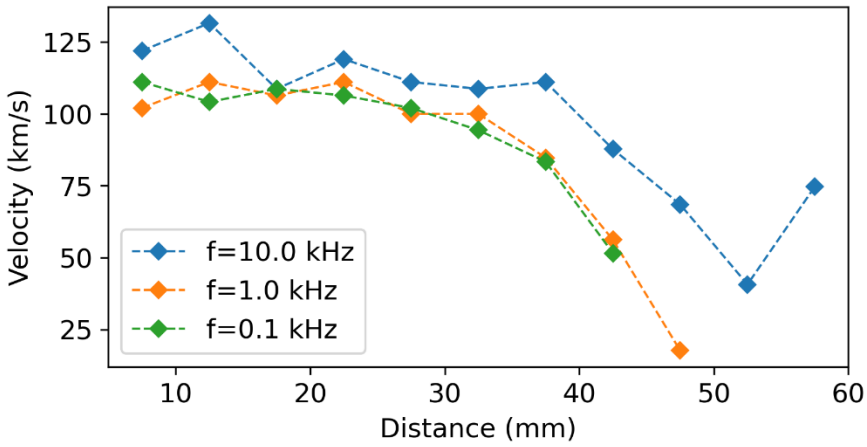

Figure 3.24. The propagation velocity of the plasma bullets with a pulse repetition rate of 0.1 kHz, 1 kHz, and 10 kHz. The pulse amplitude is 6 kV. There is no ground electrode.

3.5.4 Comparison to AC-driven APPJ

The propagation of DC driven APPJ is significantly different from the AC-driven APPJ. First, in a DC-driven APPJ, the plasma is ignited during every pulse with similar characteristics like the discharge current, light intensity, and velocity; multi-periodic mode cannot be found. Second, the ground electrode only influences the velocity near it; it does not cause multiple gap discharges before the plasma bullet ignition.

Such difference is possibly due to two reasons. First, in the AC-driven plasma jet, the ignition voltage is influenced by the applied voltage and the surface charges near the powered electrode, and the discharge propagation length is influenced by the voltage during the propagation; thus ignition at different time of the AC phase leads to different propagation length. In the DC driven plasma jet, the applied voltage increase to the maximum value within 50 ns, which is much smaller than the propagation time of the plasma. Thus, every discharge propagates with the same applied voltage, which leads to identical plasma characteristics.

Second, in the AC-driven plasma, the reverse of voltage polarities plays an important role. For example, the positive discharge first compensates the negative surface residual charges beneath the ground electrode, then charges the ground electrode region and re-ignites the plasma bullets;

in the DC-driven plasma jet, due to the lack of negative surface charges, the discharge can propagate through the ground electrode; the positive surface charge accumulation beneath the ground electrode causes the plasma to accelerate after the ground electrode as shown in Figure 3.22, but only one light peak can be observed.

The velocity of DC pulsed plasma bullets are higher than the AC-driven plasma bullets. However, it is likely to be due to the different instantaneous voltage. When V= 5.5 kV in the pulsed APPJ, the velocity is about 50 km/s. While for the AC-driven APPJ, the veocity is about 25 km/s for a plasma bullet ignited when V ≈ 3 kV. It seems that the instantaneous voltage is the most important factor to the plasma bullet velocity for both AC and DC pulsed APPJ.

The comparative study with the DC driven plasma jet shows that the propagation velocity is mainly related to the applied voltage. The charge accumulation at the ground electrode contributes to about 30% of the propagation length.

3.6 Conclusion

In this chapter, an experimental study on a helium Atmospheric Pressure Plasma Jet driven by a 15-18 kHz AC power supply is performed by fast imaging and Optical Emission Spectroscopy. Some results are compared with a DC pulsed APPJ.

The discharge exhibits multi-periodic behavior and random behavior depending on the driving voltage, driving frequency, and gap distance. The multi-periodic mode is self-triggered generating ionization waves— bullets —with a jitter of less than 100 ns, similar to the pulsed mode condition. In multi-periodic mode, negative and positive plasma bullets are initiated every 2, 3, or more periods depending upon working conditions. Negative bullets always immediately precede positive ones. Such multi-periodic bullets are observed only when a ground electrode is located 20 mm away or more from the HV pin electrode.

It is remarkable that during cycles when no bullets are ignited, positive and negative gap discharges can be detected using fast ICCD imaging. The gap discharges are similar to self-triggered DBD discharges. It is assumed that such gap discharges build-up a surface charge accumulation in the gap region, particularly in the vicinity of the ground electrode. This charge accumulation at the inner surface of the capillary surrounded by the ground electrode leads to an electric field enhancement near the ground electrode and the generation of a fast-traveling bullet. However, the evolution of surface charges discussed in section 3.2.3 does not apply to the situation when a short plasma is periodically ignited in every AC cycle (1P mode), which requires further investigation.

Bullets of different periodic modes show small differences in terms of velocity, propagation length, and optical emissions.

Optical emission spectra at different locations, voltages, and measurement time show that the variation of operating conditions significantly changes the ratio between the helium emission and the OH(A-X) emission. Most of the OH emission comes from the glow-like discharge in the gap region after the plasma bullet formation.

The comparative study with the DC driven plasma jet shows that the propagation velocity is mainly related to the instantaneous applied voltage for both AC and DC driven APPJ. The charge accumulation at the ground electrode contributes to about 30% of the propagation length.

Chapter 4: Random plasma jet

In chapter 3, we have characterized the APPJ in multi-periodic modes. We mentioned that when the applied voltage V_{pp} is high enough, multiple plasma bullets are generated in one AC cycle, and the ignition time and discharge current amplitude are random (section 3.2.1, Figure 3.3(d)).

To generate multiple random plasma bullets, the gap distance is reduced to 5 mm in this chapter to produce a higher electric field in the gap region. The discharge process is mainly influenced by the electric field which can be approximately expressed as V/d. Instead of increasing V, the gap distance d is decreased to increase the electric field and generate multiple random plasma bullets. Except for the gap distance, the plasma jet is the same as the one used for chapter 3, and is shown in Figure 4.1.

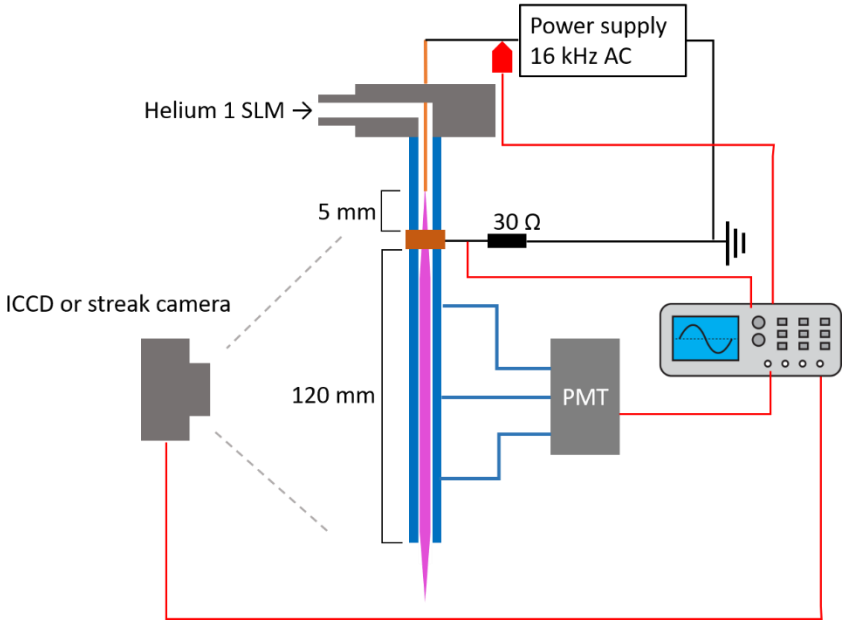

Figure 4.1 Experimental setup of the APPJ used in this chapter. The distance between the pin and the ring-like ground electrode is 5 mm. The distance from the pin to the capillary outlet is 12.5 cm. The helium flow rate is 1000 sccm. A PMT and an ICCD camera and a streak camera are combined for the optical diagnostics of the plasma.

The structure of this chapter is described below:

Section 4.1 describes the multiple random plasma bullets in the positive half-cycles. The ignition of slow periodic bullets and fast random bullets is revealed. The propagation length and ignition time jitter of the slow bullets and fast bullets are compared

Section 4.2 shows the propagation of the consecutive slow bullets and fast bullets observed by the streak camera and the ICCD camera. The velocity of the slow bullets and the fast bullets are compared.

Section 4.3 discuss the role of surface charges and volumetric charges in the propagation of consecutive plasma bullets. The random ignition of fast bullets is considered due to the high electron density, which is caused by the continuous plasma in the gap region.

Section 4.4 makes a general conclusion of this chapter.

4.1 Description of discharge

4.1.1 Plasma power

By connecting a capacitor to the ring ground electrode and measuring the voltage on the capacitor, the power of plasma can be calculated using the method introduced in section 2.1.2. The result is plotted in Figure 4.2 as a function of the applied voltage.

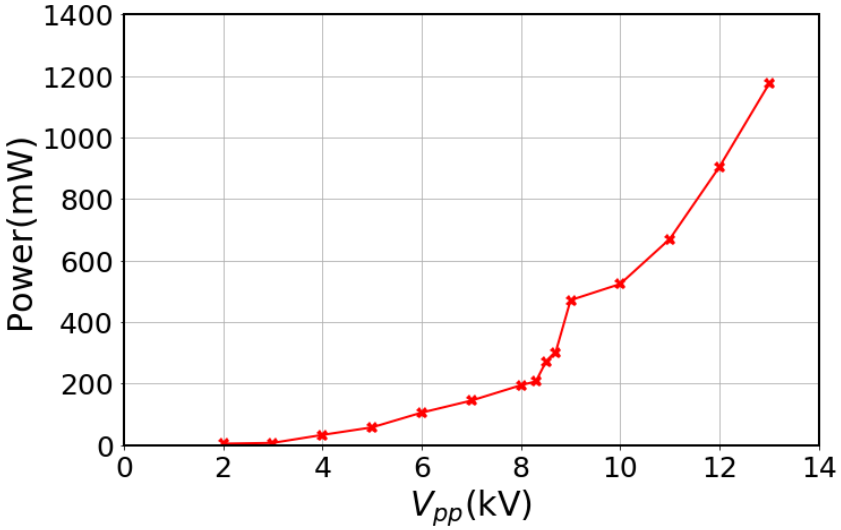

Figure 4.2 the power transferred to the plasma system as a function of the applied voltage (V_{pp}). The flow rate is 1 SLM. The gap distance is 5 mm.

As shown in Figure 4.2, the power increases with applied voltage. It is worth noting that at ~8 kV, $\frac{dP}{dV_{pp}}$ increases abruptly, which implies that the discharge process changes.

4.1.2 Multiple plasma bullet ignition

The typical waveform of the PMT signal and the discharge current is shown in figure 4.3. The applied voltage V_{pp} equals 7.5 kV. The discharge current (blue curve) is measured at the ground electrode, and the PMT signal (green curve) is measured about 3 mm downstream of the ring grounded electrode. To increase the signal-to-noise ratio, the high-frequency noise is filtered numerically. 4 discharges can be identified by the PMT signal. The first plasma bullets are observed in every cycle and their light intensity is reproducible from one cycle to another. In

the following, these bullets shall be called “slow bullets” due to their characteristics, which will be described in the following sections. The fourth bullet, which shows a significantly larger amplitude, is not observed when the applied voltage is below 7.5 kV. When V_{pp} is higher than 7.5 kV, as the applied voltage increases, the probability of observing this fourth bullet increases, and bullets of higher rank may be also ignited. They will be called “fast bullets” in the following. The start of ignition of fast bullets at about 7.5 kV causes an increase in plasma power as shown in Figure 4.2 at about 8 kV. The number of current peaks is more than the number of PMT signal peaks. These current peaks are probably the current of some micro DBDs due to the high electric field and do not form a plasma that propagates inside the tube.

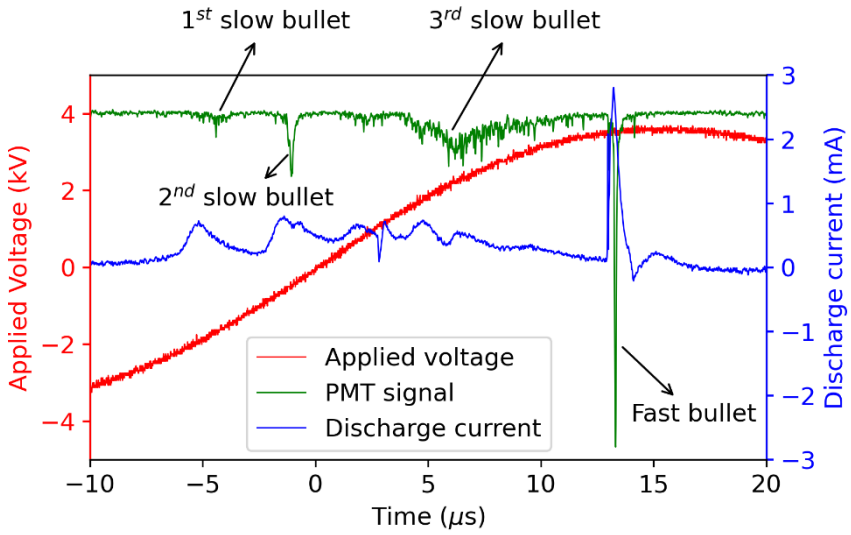

Figure 4.3 Example of the waveforms of the PMT signal (green curve) and discharge current (blue curve). The applied voltage is presented in red and V_{pp} = 7.5 kV

4.1.3 Propagation length of multiple plasma bullet

The propagation length of each discharge is different and is measured with the ICCD camera. The result is plotted in figure 4.4 as a function of the applied voltage. The gate width is set to 3 μs to cover the propagation time of the plasma bullet. The periodic slow plasma bullets were measured with the accumulation mode of the ICCD camera. The length of fast plasma bullets is random, so the length is measured with single shot mode and is averaged over 50 measurements and the standard deviation is shown with error bars.

As shown in figure 4.4, each slow bullet propagates slightly further than the previous one, typically 5, 11, and 17 mm for slow bullets number 1, 2, and 3 respectively. Similar results are reported by Mussard et al. using a helium APPJ powered by a 600Hz AC voltage[37].

The propagation length of the fast bullets of the same order can vary by a factor of 2 from one cycle to another. Figure 4.4 shows with red solid the average length of the fast bullets following the initial 3 bullets. The number of fast bullets varies from 1 to 3 typically depending upon

each cycle and on the applied voltage. Contrary to the slow bullets, the average propagation length of such fast bullets increases fast with the applied voltage. The error bar of the average propagation length can be up to 2 cm, showing that the fast plasma bullet lengths distribute in a wide range. The red dashed line in Figure 4.4 shows the max of the bullet extension over ~10^3 cycles, which is also the plasma length that can be observed by eyes in a dark room.

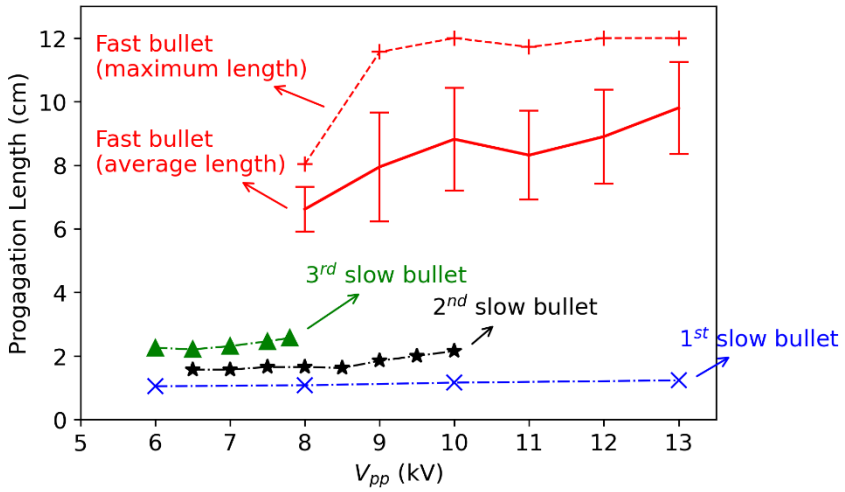

Figure 4.4 Average propagation length of the consecutive bullets. The blue, black, and green curves represent the lengths of slow bullets which are measured with the accumulation mode of ICCD because they are stable. The red solid line represents the averaged lengths of 50 fast bullets, and for each voltage and the error bar is shown. The red dashed line represents the maximum length of fast bullets, which is also the plasma jet length visible by naked eyes in a dark room.

With a 5 mm gap distance, multiple discharges are observed in the positive half cycle. Fast discharges start to ignite when V_{pp} exceeds 8 kV. These fast bullets are ignited after 3 slow bullets and have propagation lengths that are at least threes time longer.

4.1.4 Number of plasma bullets per ac cycle

In each positive cycle, 3 slow bullets are systematically ignited. On the opposite, the number of fast bullets varies for each positive cycle from 0 to 3 under the investigated conditions. In order to statistically measure the number of fast bullets as a function of the applied voltage, one optical fiber is placed 4 cm away from the ground electrode. This distance is too far to be reached by short/slow bullets and is only accessible to long/fast bullets, according to the result shown in figure 4.4. The peaks of the PMT signal in the positive cycle can be detected and its number can be counted by the oscilloscope. The measurement is repeated 2500 times for each voltage. The results are presented in figure 4.5. When V_{pp} equals 8 kV, the ignition of fast bullets is less than 4%; in 96% of the positive cycles, only slow bullets are ignited. As the voltage increases, the probability of fast bullets ignition increases, and the ignition of a second and even third fast bullet is also observed. When V_{pp} equals 13 kV, fast plasma bullets can be

generated in 50% of positive cycles, and the chance of generating a second fast bullet increases to 5%.

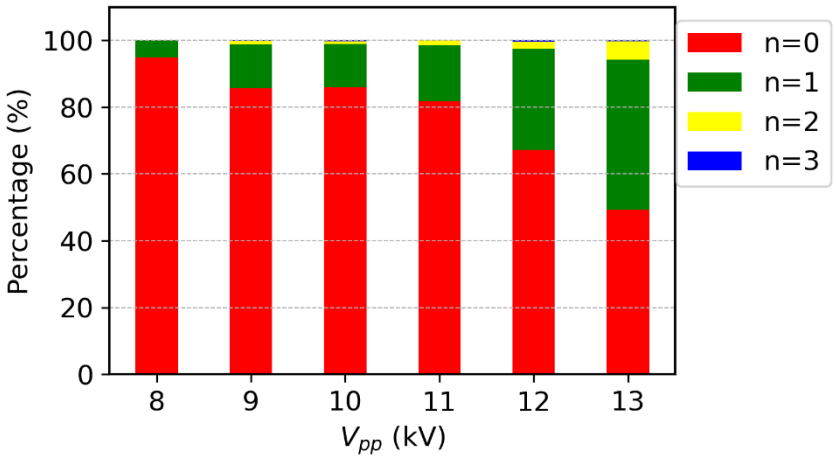

Figure 4.5 Number of fast bullets (n) ignited per positive cycle. For each of the recorded voltages, the number of slow bullets (not shown) equals 3.

4.1.5 Time jitter of plasma bullet ignition

As mentioned in section 4.1.2, the ignition of the slow bullets and the fast bullets have significantly different jitter of time. The slow bullets and generated periodically, and seem to be self-triggered. On the contrary, the generation of fast bullets is random. The delay of the ignition of the second slow bullet and the first fast bullet are measured.

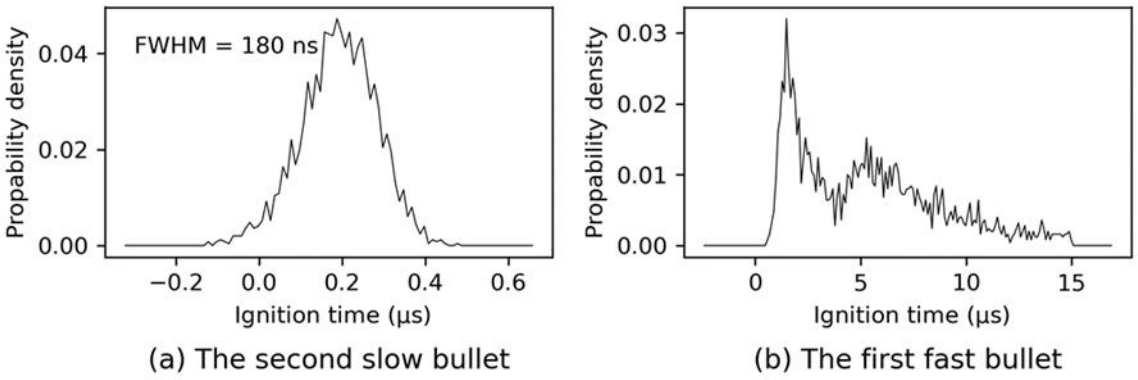

Figure 4.6 Distribution of the ignition time (ignition time jitter) of (a) the second slow bullet and (b) the first fast bullet

According to figure 4.3, the second slow bullet is generated when the applied voltage is about -600 V. So the oscilloscope is triggered with a double condition: it is triggered by the falling slope of PMT signal at 3 mm downstream the ground electrode when the applied voltage is higher than -600 V. The ignition delay is defined as the time interval between the triggering(PMT signal peak) and the time of $V_{pp} = 0$ during the positive slope. With the same

methods, the ignition delay of the first fast bullet is measured by triggering the oscilloscope when the applied voltage is higher than 4 kV. The distribution of ignition delay of the second slow bullet and the first fast bullet is plotted in figure 4.6(a) and (b), respectively.

For the slow bullets, the distribution has a standard deviation of ~90 ns, which is small compared to the period of the AC voltage (62.5 μs) and the time difference between the ignition of two bullets (usually ~5 μs); on the other hand, the distribution of the fast bullets ignition time is bimodal, with the first peak at 1.5 μs and another one at 5.5 μs. This ignition delay time is much longer than the one of slow bullets and is also comparable with the propagation time of fast bullets along the capillary.

Increasing the applied voltage increases the number of fast bullets. The ignition time jitter of the fast bullets can be 50 time larger than the slow bullets.

4.2 Propagation of consecutive plasma bullets

4.2.1 Propagation of slow bullets

As the generation of slow bullets is periodic, their propagation can be observed by the ICCD camera in accumulation mode with the method used in chapter 3. Figure 4.7 shows the photo of bullets taken at different delays. The exposure time is 200 ns and each photo is the accumulation of 50 bullets. The second slow bullet started at ~ 0.5 μs and has an initial velocity of ~4 km/s. It propagates at a nearly constant velocity over 1 μs, i.e. 4 mm, and slows down. However, the ionization front can keep emitting light for up to 8 μs although its position barely moves.

At 8 μs, the third slow bullet shows an initial speed of ~8 km/s, and the initial light intensity is lower than the first bullet. It propagates with almost constant velocity for about 3 μs. This corresponds to the re-ignition and re-excitation of the ionized channel left by the previous second bullet which stopped at 5.5 μs. At 11 μs in Figure 4.7, a remarkable phenomenon can be noticed: the third slow bullet reaches the maximum extension of the second bullet and starts propagating in a non-ionized media: The intensity of the plasma bullet significantly increases due to an increase of the electric field but the propagation velocity decrease to 2 km/s. This is very similar to the succession of bullets reported by Mussart *et al.* in a 600 Hz plasma jet.

The gap region was not observed in Figure 4.7. The ICCD photo in figure 4.8 includes the plasma in the gap region. A continuous DBD is observed in the gap region, which sustains between two plasma bullet ignitions and continues emitting light after the ignition of the third slow bullet. After the ignition of the third slow bullet, the inter-electrode plasma extends, which enlarges the pulse width of the PMT signal acquired after the ground electrode, like the PMT signal of the third bullet shown in Figure 4.3. The extended inter-electrode plasma can be also seen in Figure 4.7, from 8 μs to 10 μs.

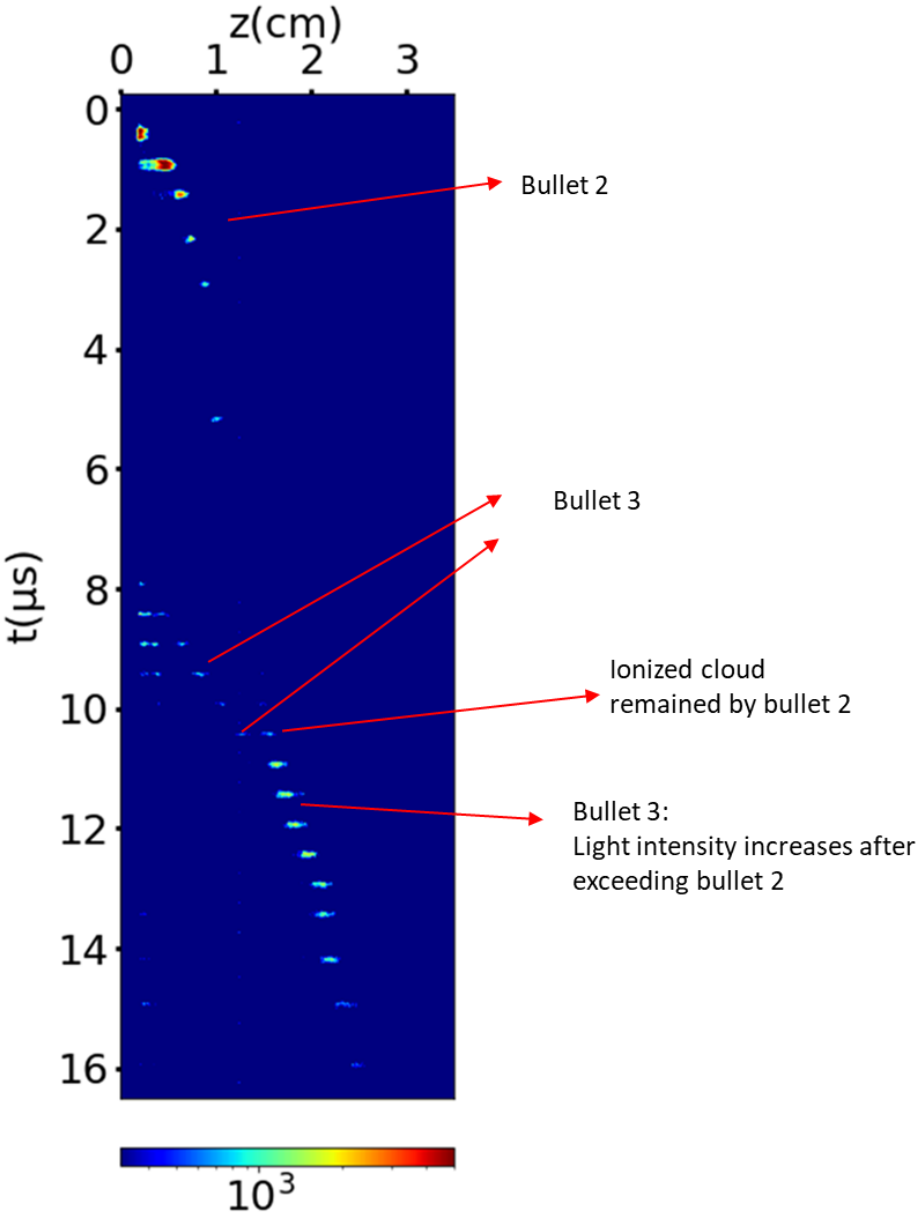

Figure 4.7 ICCD photos of the propagation of the second and the third slow bullet. The applied voltage V_{pp} is 7.5 kV. The frequency is 16 kHz. The gate width for each photo is 200 ns. Each photo is accumulated 100 times. 0 cm on the X axis corresponds to the position of the ground electrode: only the propagation after the ground electrode is observed by the ICCD camera.

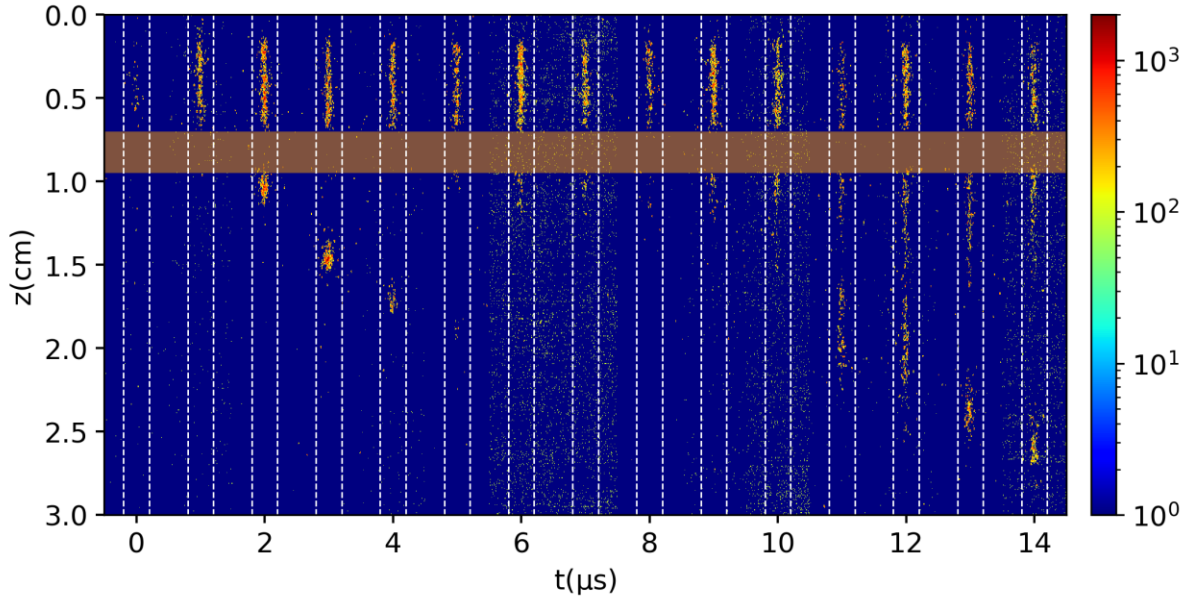

Figure 4.8 Propagation of the second and the third slow bullets. The orange bar represents the ring-like ground electrode; the white dashed lines represent the outer surface of the capillary. Each photo is accumulated 50 times with 1 μs ICCD gate width for each exposure. V_{pp} = 7.5 kV, f = 16 kHz.

Using the ICCD camera, we see that a slow bullet can catch up with the previous slow bullet and show an increase in the light emission and in the propagation velocity. A continous plasma in the gap region can be observed after the second slow plasma bullet.

4.2.2 Propagation of fast bullets

Due to the random ignition and random propagation velocity of the fast plasma bullets, their propagation cannot be traced with an ICCD camera. Alternatively, the propagation of the fast bullets is observed with a streak camera (Hamamatsu S20). This experiment is performed in collaboration with Professor Julien Fuchs, LULI, Ecole Polytechnique.

The streak camera imaging is combined with electrical signal measurements with antennas. Figure 4.9 is a schematic drawing of the experiment setup. The antenna is a ring copper tape wrapped around a 3d-printed tube. The distance from the 4 antennas to the ground electrode is 2 cm, 4 cm, 6 cm, and 8 cm, respectively. A 1 nF capacitor is connected to each antenna, and the voltage on the capacitor is measured. A one-centimeter wide slit is cut along the axis of the tube, so the streak camera can observe the plasma jet through this slit. The range of the streak camera observation is 6 cm.

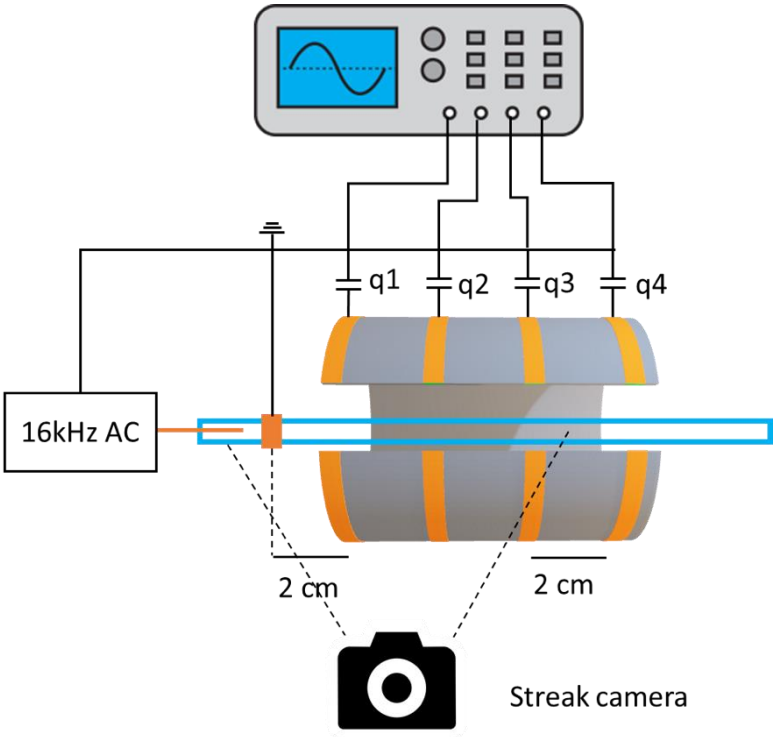

Figure 4.9 Schematic of the experiment setup of streak camera imaging. The antennas are ring copper tapes wrapped around a 3d-printed tube. The streak camera observes the plasma jet through a 1 cm wide longitudinal slit on the tube. The distance from the 4 antennas to the ground electrode is 2 cm, 4 cm, 6 cm, and 8 cm, respectively.

Figure 4.10 shows a typical streak image of the third slow plasma bullet and the corresponding signal measured on the antenna. Figure 4.10(a) shows the amount of charges measured on the 4 antennas in the voltage rising phase. The signal caused by the displacement current has been subtracted. The grey area represents the 10 μs time interval in which the gate of the streak camera is open. When a discharge propagates through an antenna at about 17 μs and 22 μs, a step of about 1 nC charges is detected. The rise time of an antenna signal is about 1 μs for a fast bullet, but the step for the slow bullet is not obvious due to the short propagation length and the continuous current. The signal detected by the antenna decreases as the plasma bullet propagates further. It is worth noting that the charges detected by the first antenna increase continuously between plasma bullets ignition from 14 μs to 22 μs. The continuous charging of the first antenna shows the existence of a continuous current between plasma ignitions. This continuous current significantly charges the ground electrode region and the tube's inner wall along the plasma propagation. It should be noted that the time resolution of antenna signals are two poor to derive the velocity of the plasma bullets.

The streak image of the plasma propagation in the 10 μs time interval is shown in figure 4.10(a). The propagation of the bullet 3 seems discontinuous, as the first 1 cm of the propagation can be barely observed. This is because the sensitivity of the streak camera is lower than the sensitivity of the ICCD camera, and the light intensity of the first one centimeter of the third

slow bullet propagation is relatively weak. A significant light increase is observed at about 2 μs, which corresponds to the intensity increase at 11 μs in figure 4.7 when the third slow bullet meets the plasma left by the second slow bullet. The velocity of the bright part of the third plasma bullet is 5~8 km/s.

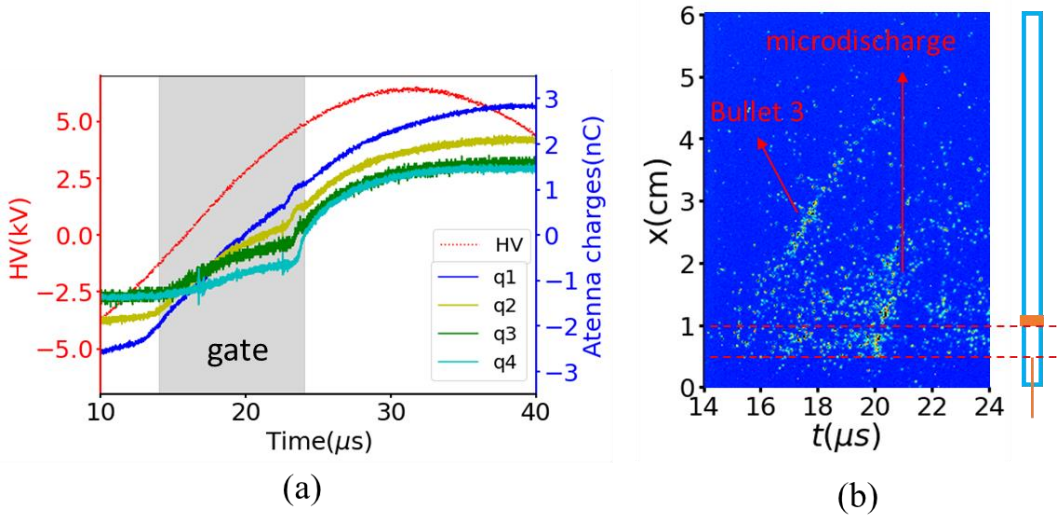

Figure 4.10 The antenna signal waveform and the corresponding streak camera image of a slow bullet. (a) shows the waveform of the applied voltage (red curve) and the amount of charges measured on the 4 antennas (q1 ~ q4). The grey area which covers 10 μs shows the time during which the gate of the streak camera is open. The streak image of this 10 μs is shown in figure(b). The horizontal axis is the time evolution, and the vertical axis is the length in centimeters. The inter-electrode gap is in the region between the two red dash lines.

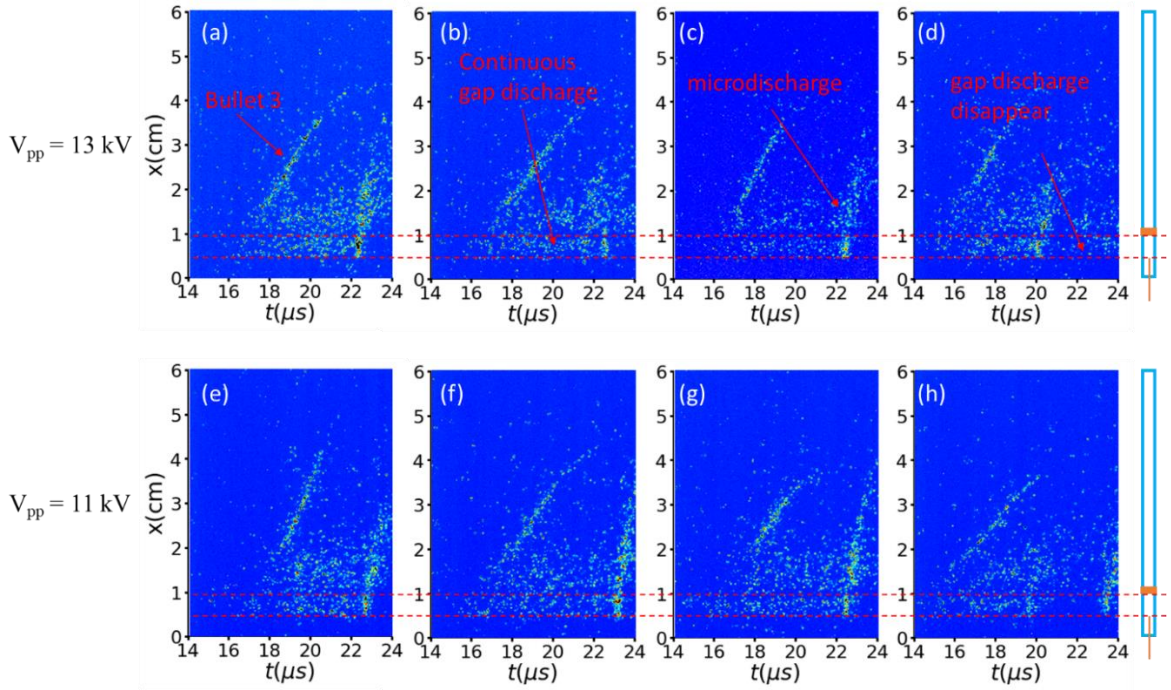

Figure 4.11 Some streak images of the propagation of the third slow bullet. The horizontal axis is the time evolution, and the vertical axis is the length in centimeters. The inter-electrode gap is in the region

between the two red dash lines. The first row(a-d) shows the images of discharges with 13 kV peak-to-peak voltage, and the second row shows the images of discharges with 11 kV peak-to-peak voltage.

This experiment is done with an applied voltage of 11 kV and 13 kV. Part of the results is shown in figure 4.11. The difference in propagation with 11 kV and 13 kV voltage is very small. The velocity of the slow bullets is not significantly influenced by the applied voltage.

A continuous plasma near the gap region is observed after the slow bullet, and a discharge with a length of typically 1 cm is observed. This discharge happens 4~5 μs after the third slow bullet and is not observed in the discharge current waveform, possibly due to the continuous current in the gap region. The continuous gap discharge disappears after this microdischarge. The nature of this discharge is little known due to the low signal-to-noise ratio caused by the continous plasma before it. More observation with streak camera in a smaller scale is required to help understanding its propagation dynamics.

By changing the delay of the streak camera, we can observe the propagation of the fast bullets which are typically ignited 2~10 μs later than the slow bullets.

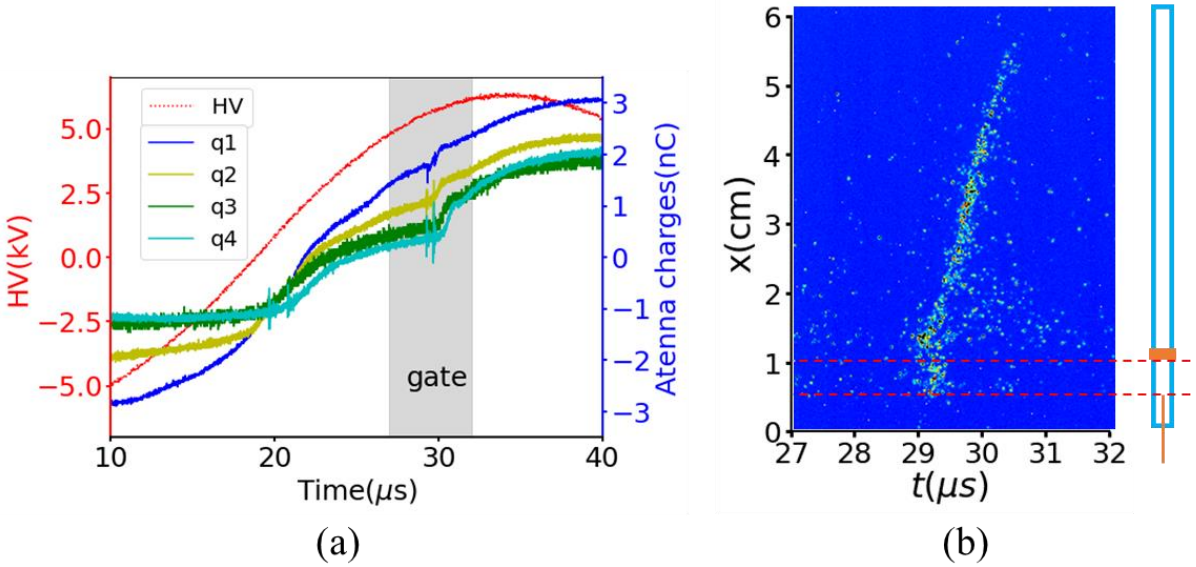

Figure 4.12 The antenna signal waveform and the corresponding streak camera image of a fast bullet. (a) shows the waveform of the applied voltage (red curve) and the amount of charges measured on the 4 antennas (q1 ~ q4). The grey area which covers 5 μs shows the time during which the gate of the streak camera is open. The streak image of this 5 μs is shown in figure(b). The horizontal axis is the time, and the vertical axis is the length in centimeters. The inter-electrode gap is in the region between the two red dashed lines

As shown in Figure 4.12(b), the light emission of the fast bullet does not seem to start from the pin electrode. Instead, the light emission starts downstream of the ground electrode; the ionization in the gap region starts about 0.2 μs after the downstream ionization.

Figure 4.13 compares some streak images of fast bullet propagation with applied peak-to-peak voltages of 11 and 13 kV. Unlike slow bullets, the propagation of fast bullets is significantly

influenced by the applied voltage amplitude. Generally, the light intensities of the fast bullets with 13 kV voltage are higher than the light intensities with 11 kV. The velocity of fast bullets with 11 kV ranges from 20 km/s to 40 km/s, while the velocity of fast bullets with 13 kV ranges from 35 km/s to 60 km/s.

It is also worth noting that continuous plasma in the gap region is observed after the slow bullet shown in Figure 4.11, but is not observed before the ignition of the fast bullet shown in Figure 4.13. It seems that the disappearance of the gap region plasma is essential for the ignition of fast bullets.

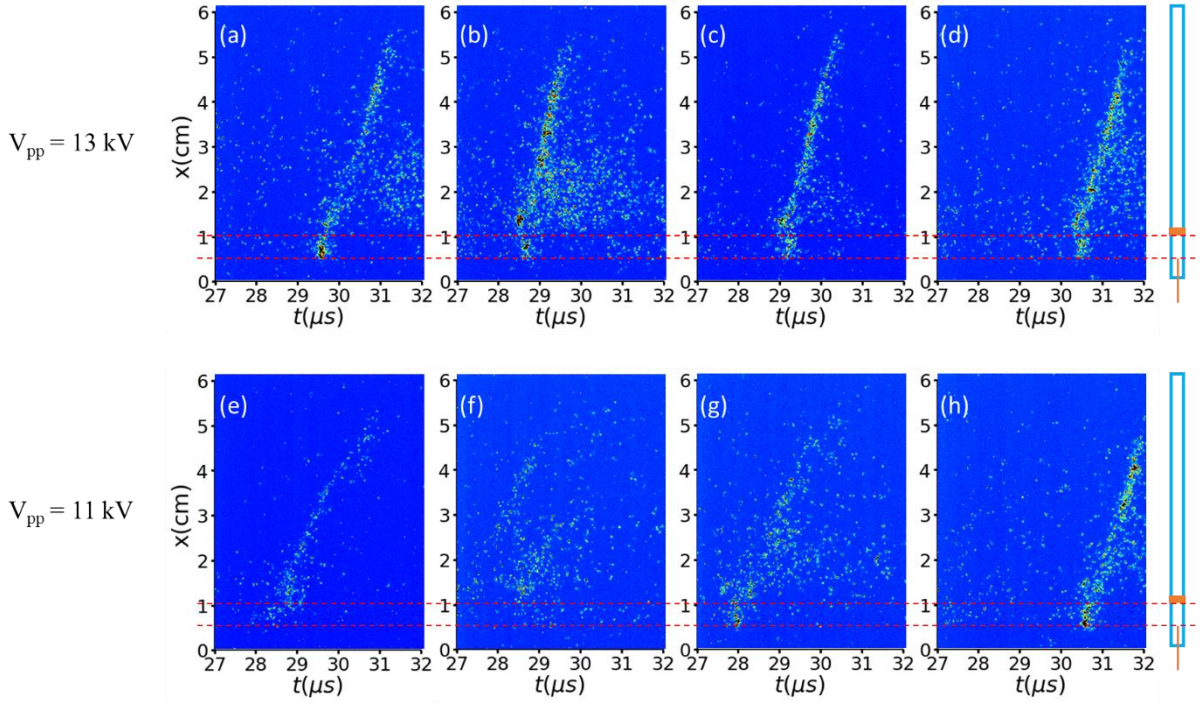

Figure 4.13 Some streak images of the propagation of the fast bullets. The horizontal axis is the time evolution, and the vertical axis is the length in centimeters. The inter-electrode gap is in the region between the two red dash lines. The first row(a-d) shows the images of discharges with 13 kV peak-to-peak voltage, and the second row shows the images of discharges with 11 kV peak-to-peak voltage.

Streak camera imaging shows a 4-6 μs "continuous"gap discharge start with the third slow bullet, and end with a microdischarge. Fast bullets are ignited more than 2 μs after the extinguishment of the continuous gap discharge.

4.2.3 Statistical study of the fast bullets' velocity

Due to the randomness of the ignition time of the fast bullets, it was not possible to measure their velocity using an ICCD camera, and the streak camera imaging shows that the fast bullets' velocity is 20 ~ 60 km/s, but it only gives limited samples of the propagation. In this subsection, the velocity of fast bullets is measured using two different methods: i) in the first method, the

propagation of one bullet is monitored using 5 optical fibers located along the capillary; ii) in the second method, at each distance, the velocity distribution is measured using two optical fibers distant from 2 cm.

Method 1: the velocity of fast bullets is measured using PMT signals at different positions. The PMT signals are acquired by 5 optical fibers at 5 locations which are 2 cm, 4 cm, 6cm, 8 cm, and 10 cm downstream of the ground electrode. The average velocity between two optical fiber locations is calculated by $\Delta d/\Delta t$, where Δd is 2 cm and Δt is the time interval between the peaks of the PMT signal at these two locations. This average velocity is considered to be the bullet velocity at the middle of the two optical fiber locations. In the case of bullet velocity at 1 cm, Δt is the time difference between the current peak measured at the ground electrode and the PMT signal at 2 cm. The velocities of 40 fast bullets are measured during their propagation. These bullets are grouped according to their maximum propagation length, and the evolution of the average velocities of each group is shown in figure 4.14 as a function of the position. Figure 4.14(a) and (b) display results when V_{pp} equals 11 kV and 13 kV, respectively.

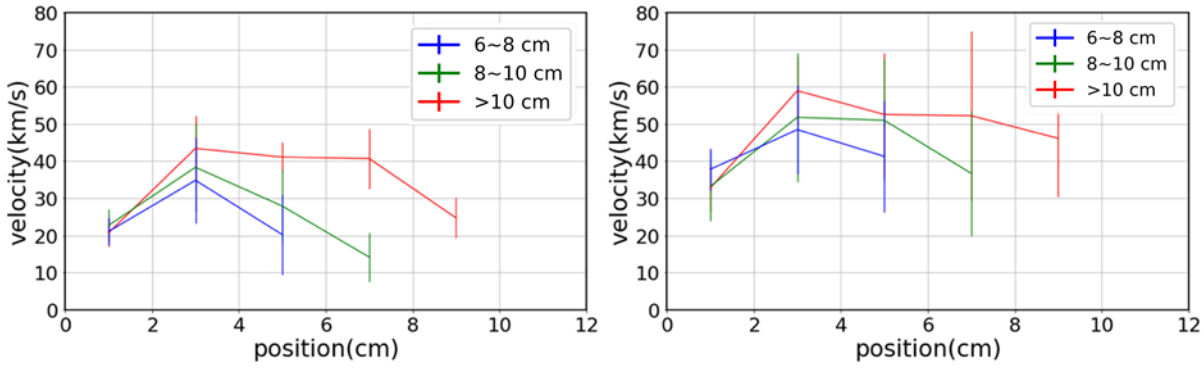

Figure 4.14 Velocity of 40 fast bullets at different positions when (a)V_{pp}=11 kV (b) V_{pp}=13 kV

Table 4.1 Percentage of fast bullets with different propagation lengths when V_{pp}=9 kV, 11 kV, and 13 kV

Maximum propagation length	3~4cm	4~6cm	6~8cm	8~10cm	>10cm
9 kV	10.6%	55.9%	31.2%	2.3%	0%
11 kV	32.4%	33.5%	4.4%	13.2%	16.5%
13 kV	25.1%	12.4%	6.3%	7.1%	49.1%

In all cases, bullets first accelerate at the early stage of their propagation(1~3 cm). The highest velocity is measured at 3 cm, regardless of the total propagation length. Generally, plasma bullets with higher maximum velocity can propagate longer. The propagation slows down after 3 cm. The velocity at the end of the propagation is about 20 km/s when V_{pp}=11 kV and 40 km/s when V_{pp}=13 kV, regardless of the total propagation length.

The increase in applied voltage amplitude has a small influence on the average propagation length. However, the increase of applied voltage amplitude can significantly increase the probability of igniting a long plasma bullet. Table 4.1 shows the probability of the bullet length falling in different ranges. When the applied peak-to-peak voltage increases from 9 kV to 13 kV, the probability that the propagation length of a fast bullet is longer than 10 cm increases from 0 to 49%.

Method 2 measures the distribution of bullet velocities at a certain position. To measure the velocity at x cm downstream of the ring ground electrode, two optical fibers are placed at x-1 and x+1 cm, respectively. The waveform of the PMT signal is monitored on the oscilloscope. For each waveform, the oscilloscope detects the first two peaks and calculates their time difference. In order to eliminate false measurements resulting from the noise, only reasonable values are accepted (50 ns~2 μs, corresponding to velocity 10 km/s ~ 400 km/s). The velocity distributions at different positions using an applied voltage of 11 kV and 13 kV are shown in figure 4.15 (a) and (b), respectively. The velocity of bullets at 3~9 cm exhibits a quasi-Gaussian distribution. The velocity varies in the range of 10~100 km/s. At 3 cm, the velocity is the maximum, and centers at 40~50 km/s, which is consistent with figure 4.14(b). From 3 cm to 8 cm, the velocity gradually decreases, due to the loss of energy, which has been reported in many articles [25,37]. It was observed in the present work that at the end of the propagation, velocity decreases abruptly with a fraction of mm.

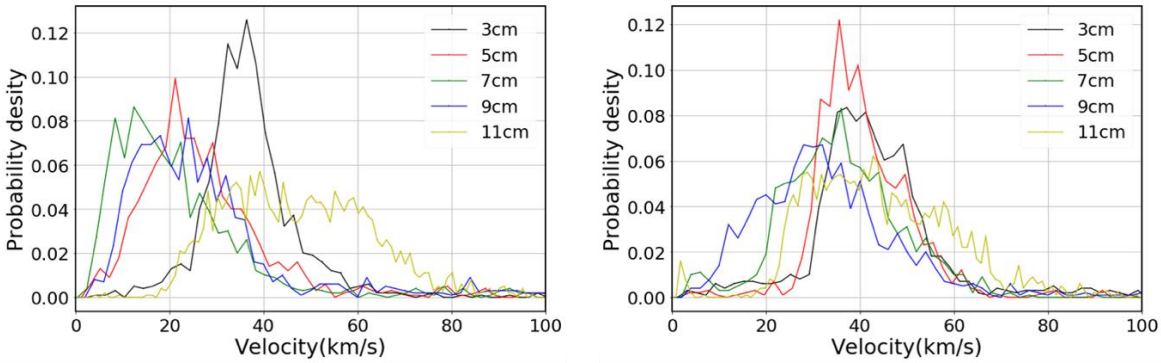

Figure 4.15 The distribution of bullet velocity at different positions. At each position, the average velocity at a distance of 2 cm is measured. (a)V_{pp}=11 kV, (b) V_{pp}=13 kV flowrate =1 SLM

At 11cm, the velocity slightly increases, which can be explained by two reasons:

1) When close to the exit of the capillary, the impurity of gas increases, which has been reported to accelerate the propagation of helium plasma bullets [155]. It has been reported that even a small fraction of N_2 can significantly change the ion composition in noble gas plasma [156].

2) The plasma bullets, which have enough energy to reach the end of the capillary may have a higher initial velocity.

In this section, the velocity of the fast bullets is obtained in 3 methods methods: 1) tracing the velocity of 50 fast bullets, 2) distribution of velocity at different locations and 3) the streak camera. The typical velocity of fast bullets measured with different methods is sumarized in Table 4.2. The results are in similar ranges, thus they can be considered consistent.

Table 4.2 The typical velocities of plasma bullets measured by 3 methods with V_{pp}=11 kV or V_{pp}= 13 kV. Method 1 is tracing the velocity of 50 fast bullets, method 2 is the distribution of velocity at different locations, method 3 is the streak camera.

	Method 1	Method 2	Method 3
V_{pp}=11 kV	35 ~ 45 km/s	25 ~ 50 km/s	20 ~ 40 km/s
V_{pp}=13 kV	50 ~ 60 km/s	35 ~ 55 km/s	35 ~ 60 km/s

Measurement with the PMT show that the fast bullets have a velocity of 15~50 km/s and a length of 3~12 cm. High velocity is linked to a longer propagation length. A small increase in the velocity is observed close to the outlet of the capillary. Velocities of fast bullets measured by 3 methods are consistent.

4.3 Discussion

4.3.1 Propagation velocity depends on the instantaneous voltage

In this chapter, we have studied the plasma bullet propagation when the applied voltage exceeds the range for multi-periodic modes. In this condition, multiple positive plasma bullets are observed in the voltage-rising phase, while the ignition of negative plasma bullets is much less frequent. The chance of igniting a negative plasma bullet is about 10% every cycle.

For positive bullets, we have evidenced the presence of the so-called slow bullets, which can be distinguished from the normal long bullets because they seem to have different properties. Slow bullets have a velocity of ~4.5 km/s; they can only propagate over short distances; they are stable and repeatable under a 16 kHz AC excitation. On the other hand, fast bullets are non-repeatable; their velocity is 5~20 times faster than the slow bullets and they propagate at least three times further than the slow bullets. Most importantly, the transition from slow bullets to fast bullets is not a continuous process: the propagation length is almost constant when the voltage is below 8 kV (slow bullets only), but it dramatically increases when the voltage increases from 7 kV to 8 kV when fast bullets are generated.

The velocity of plasma bullets in helium APPJ is reported to be in the range of 1~10^3 km/s. It is governed by many parameters. The velocity of bullets is positively related to the applied voltage [34,59]. The effect of the wall material on the bullet velocity has also been much reported, and the importance of the permittivity of the capillary wall has been addressed [26,33,155,157]. The velocity of bullets is reported to be maximum when the capillary has a certain inner diameter [33,158]. In this chapter, the velocities of slow bullets and fast bullets are significantly different and are measured separately.

The slow bullets have been reported in published articles. Ning *et al.* reported bullet velocities of 7 km/s in a helium APPJ driven by 10 kHz AC voltage when V_{pp} = 9 kV, which is close to our results [39]. It is also mentioned that the discharge starts to behave randomly when $V_{pp} > 9.\,\mathrm{kV}$. Mussard *et al.* did similar experiments using a 500 Hz frequency AC power supply to generate plasma in a helium jet, and reported bullet velocity of 5~20 km/s when $V_{pp} = 24\ \mathrm{kV}$. They discovered that the propagation length of two consecutive bullets increases linearly with the effective instantaneous voltage, which is defined as the difference between the instantaneous voltage and the voltage when the first positive discharge occurs [37]. A similar tendency is observed in this chapter, but only for the slow bullets. For pulsed APPJ, one bullet is usually ignited in one pulse, but multiple bullets in one rising edge have also been reported [159]. As shown in figure 3.21, The velocity of DC pulsed APPJ obtained in chapter 3 is in the range of 50~150 km/s depending on the applied voltage. and is much higher than the slow bullets in this chapter. For the fast bullets in the present chapter and plasma bullets in multiperiodic modes in chapter 3, the velocities are both 40~50 km/s if the instantaneous voltage is about 3 kV.

4.3.2 Role of surface charges

The difference between the ignition and/or propagation mechanisms of the slow bullets and the fast bullets is not fully understood. In the present chapter a short gap of 5 mm leads to a series of plasma bullet ignition during positive half cycles; each bullet modifies the volume and surface electrical properties of the capillary.

In chapter 3, surface residual charges are considered as the main factor that influences plasma ignition. In this chapter, the slow bullets should also be mainly influenced by the surface residual charges. During the positive cycle, the negative surface residual charges enable breakdown with low applied voltage. The first positive discharge in a 5 mm gap is brought forward compared to the 30 mm gap, i.e. it is ignited with even lower instantaneous applied voltage, because the shorter distance between the powered tip and the ground electrode increases the electric field. Also due to the short gap distance, the increase in the electric field in the gap region is more sensitive to the increase in the applied voltage, so several breakdowns were enabled during the rising phase of applied voltage. However, as mentioned in chapter 3, the propagation velocities and lengths are small due to the low instantaneous applied voltage.

The velocity of slow bullets is close to the velocity of short gap discharges in multi-periodic modes shown in Figure 3.7 and Figure 3.8, which is 5~10 km/s when $V \approx 0$.

The surface charges not only influence the breakdown in the gap region but also influence the propagation of discharge in the downstream region. In this work, each of the consecutive positive discharges deposits surface charges along the capillary wall that it propagates. The first positive discharges propagate along a capillary wall with negative surface charges; the following successive positive discharges first propagate along a capillary wall that is positively charged by previous short discharges; then enter the zone that is negatively charged in the previous cycle. In the transition zone between positively and negatively charged walls, the electric field is higher than in other areas, which may be the cause of the bullets acceleration shown in Figure 4.7. The different polarities of surface charges can explain the phenomenon shown in Figure 4.7: the third discharge is weak in the beginning, but becomes much brighter when it exceeds the previous discharge. The increase in light intensity may be due to increased recombination with negative charges on the capillary wall. Similar behavior has been reported by Mussard *et al.* [37], who reported acceleration and light increase in the transition region.

4.3.3 Role of volumetric charges

The role of residual volume charges is worth discussing in multiple consecutive discharges.

When the gap region is 20~40 mm like the multi-periodic modes discussed in Chapter 3, the time intervals between discharges are more than 20 μs, and the plasma light emission disappears between two discharges ; hence, the plasma density is expected to decrease to a low level before every breakdown, so the volumetric charges should not play a major role. However, in the random mode shown in this chapter, as shown in figure 4.7, continuous plasma is observed in the source region. This plasma may provide a high pre-ionization level with a seed electron density close to the plasma bullet, which is reported to be 10^{13}~10^{14} cm^{-3} for a typical atmospheric helium plasma jet[160]. Thus, the discharges ignited from this continuous plasma have higher seed electron density than discharges in multiperiodic modes.

In our experiment, the first slow bullet is ignited about 20 μs after the last discharge in the previous negative cycle; it is shown that in this time scale the electron density decays by a factor of 100~1000 [44,48]. After the slow bullets, continuous plasmas are observed in the gap region as shown in Figure 4.8 and Figure 4.10 Figure 4.13, which indicates a high initial plasma density possibly in the range of 10^{12} cm^{-3}. Moreover, some microdischarges are observed in the gap region after the slow bullets as shown by the streak camera.

The role of pre-ionization on bullet propagation has been reported in the literature. It has been reported that the preionization has a minor influence on the velocity and jet length. The discharge frequency influences the preionization level before the discharges. Several articles show that the frequency has a negligible influence on the bullet velocity and jet length from

100 Hz to 10 kHz using a pulsed power supply [161–163]. Xiong et *al.* showed that in a pulsed helium APPJ, the plasma reached the end of the tube earlier when the frequency increased, but the frequency has a minor influence on the propagation velocity out of the tube. Jánský *et al.* showed by simulation and experiments that the seeding electron density below 10^{10} cm^{-3} has a minor influence on the bullet velocity in a helium APPJ [164]. On contrary, Likhanskii *et al.* reported that initial electrons play an important role in enhancing the streamer propagation speeds in surface discharges [165]. Chen *et al.* reported that the propagation length of a helium jet increase with the frequency of the driven AC voltage in the range of kHz[166]. The frequency directly influences the seeding electron density before a bullet is launched. More importantly, many studies show that the seeding electron density influences the stability of discharge ignition[51,167–169]. Wu *et al.* show that the minimum seed electron density for repeatable discharge ignition in helium gases is about 10^{9} cm^{-3} [169].

However, the effect of relatively high electron density on the plasma ignition remains unclear un requires further investigation. In section 4.2.2, we can see that the fast bullets are ignited with relatively low seed electron density, as there is no plasma in the gap region before the fast bullet as shown in Figure 4.13. Thus, the ignition time of the fast bullets is possibly related to the time needed for extinguishment of continuous gap region plasmas, and the plasma bullets that are ignited later with high instantaneous voltage propagate longer. However, the decay of electron density after the slow bullet is influenced by the microdischarges shown in Figure 4.11. It is unclear why the decay of continuous gap discharge is random.

4.3.4 Comparison with multi-periodic mode.

In this chapter, the velocity of plasma bullets is similar to the velocity measured in chapter 3: 5 ~ 10 km/s with an instantaneous voltage close to 0, and 20~60 km/s with an instantaneous voltage of 2~4 kV.

With a gap distance of 30 mm, short gap discharges that can not reach the ground electrode can be observed. In this chapter, due to the short gap distance, every discharge can exceed the ground electrode. That, the propagation dynamics of every discharge are similar despite the different velocities. Discharge reflection in the gap region cannot be observed.

Also due to the short gap distance, the electric field in the gap region is more sensitive to changes in the applied voltage. Thus, more discharges are ignited during the voltage rising phase. Multiple discharges create a high continuous ionization level near the gap region, which possibly results in the random ignition of the fast bullets.

The slow bullets in this chapter have similarities to the gap discharges in chapter 3. They are ignited with an instantaneous voltage close to 0 V and have a typical velocity of 5 ~ 10 km/s. The total lengths are also similar(< 3 cm). In both cases, a bright ionization front can be observed. The main différence is that the 20-30 mm slow bullets are not confined to the 5 mm

gap, contrary to the gap discharges of Chapter 3. The propagation dynamics of the slow bullets in the 5 mm gap distance is unclear due to the limite of spatial resolution, so it is difficult to conclude whether they are the same phenomenon.

Finally, with a 20 ~ 40 mm gap distance, we observed in chapter 3 an equal number of negative plasma bullets. In contrast, the ignition of negative plasma bullet is rare(<10%) with a 5 mm gap distance. In chapter 3, we hypothesize that the backward propagating gap discharge is essential for the negative plasma bullet ignition, and this phenomenon is not observed in this chapter.

4.4 Conclusion

In this chapter, the ignition and propagation properties of the plasma Atmospheric Plasma Jets (APPJs) in helium are studied using a 16 kHz AC power supply and a small gap distance (5 mm) Two kinds of propagation modes have been evidenced. The slow bullets are stable and repeatable. They propagate with a velocity of ~4 km/s and decelerate strongly near the end of their length. 3 slow bullets are ignited in each positive cycle, and their propagation range increase consecutively. Although they are not confined to the gap, they show similarities (length, velocities, periodicity) with the gap discharges studied in Chapter 3. On the other hand, the fast bullets propagate much faster and further. They show randomness in many parameters, which is attributed to multiple random small discharges in the source region, but they are still statistically predictable. Generally, the number of fast bullets increases with the applied voltage. They are not repeatable, as the time of the fast bullet's ignition has a large deviation of 3.4 μs. The propagation ranges of fast bullets also vary but are at least twice longer (4~10 cm) than the longest of the slow bullets in our condition. The velocity of fast bullets is 2~20 times faster (10~100km/s) than the slow bullets and decreases significantly during their propagation.

The results in this chapter are compared with chapter 3. It is again confirmed that the propagation velocity and length of each discharge are strongly dependent on the instantaneous applied voltage, while the ignition is also strongly influenced by the surface residual charges.

ICCD imaging and streak camera imaging reveal light intensity increases during propagation. This is attributed to the transition between a positively charged surface and a negatively charged surface.

The continuous plasma in the gap region implies higher volumetric charge density before the ignition of fast bullets than slow bullets. The role of volumetric charges is discussed. However, it is unclear due to the lack of literature.

Chapter 5. Plasma liquid interaction

When the APPJ is used for medical applications, the interaction between plasma and target influences the discharge propagation and modifies the characteristics of the target. As the living tissues at least consist of 70% water, much attention has been paid to the interaction between APPJ and water target [170]. For safety reasons, plasma jets for treating living tissues usually use an external ring-like powered electrode.

In this chapter, the interaction between an APPJ and a liquid target is studied; an APPJ with an external ring-like powered electrode is used. The APPJ used in this chapter is shown in Figure 5.1. The powered electrode is a copper tape with a width of 20 mm and is powered by a 16 kHz sinusoidal voltage. In some cases, a 3 mm wide ground electrode is used. For water treatment, 15 mL of distilled water is put in a plastic petri dish with a diameter of 55 mm. An aluminum electrode at the bottom of the petri dish is connected to a 10 nF capacitor to measure the plasma power with the method introduced in section 2.1.2. This work aims to understand the influence of a liquid target on the propagation of plasma and the long-life RONS production by plasma inside the water.

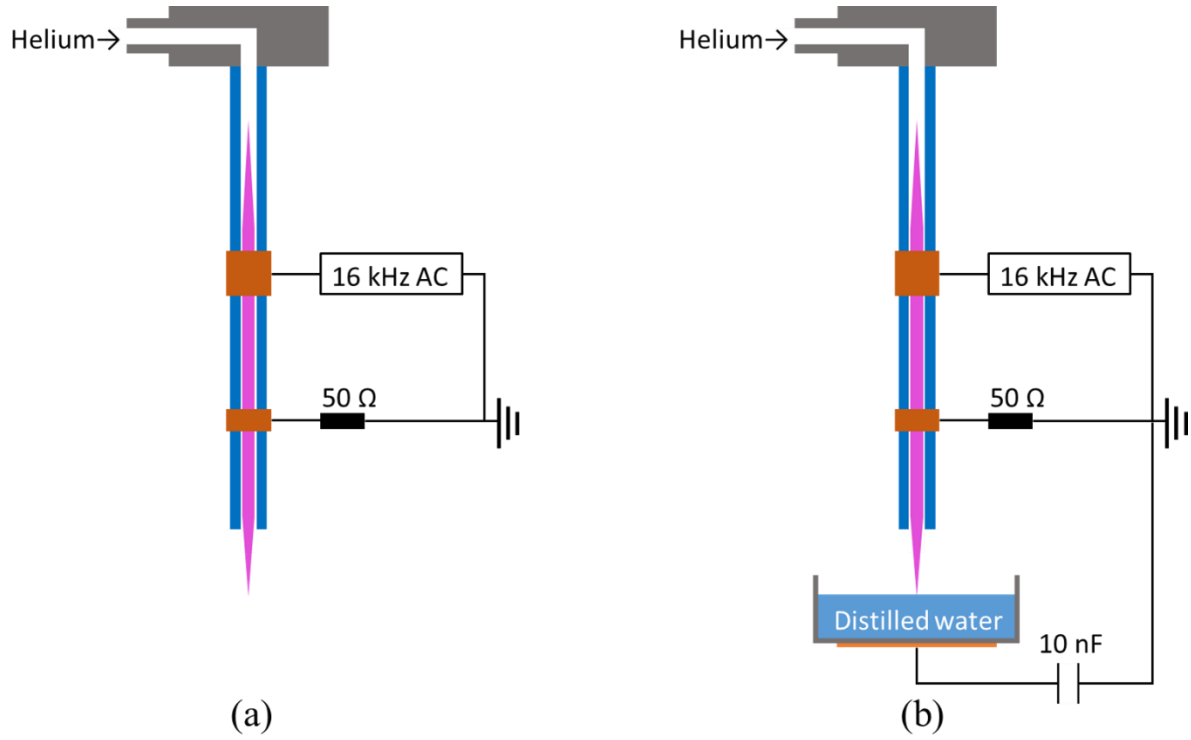

Figure 5.1 Schematic drawing of the plasma jet used in this chapter. (a) shows the plasma jet with two ring electrodes. The width of the powered electrode is 10 mm, and the width of the ring ground electrode is 3 mm. The gap distance is 20 ~ 40 mm depending on the configuration. (b) shows this plasma jet treating 15 mL of distilled water inside a plastic petri dish with a diameter of 55 mm. The depth of the water is 6.3 mm. An aluminum tape is attached to the bottom of the petri dish and is connected to the ground via a 10 nF capacitor for power measurement.

In section Chapter 5:, the propagation of plasma in the APPJ shown in Figure 5.1(a) is discussed.

In section 5.2, the propagation of the APPJ near a water target is shown.

In section 5.3, the H2O2 concentration in the PAW(Plasma activated water) is investigated by varying the applied voltage, the gas flow rate and the target distance (distance between the jet outlet and the water surface).

In section 5.4, the origin of the H_2O_2 formation is discussed combining experiments and literature reviews.

Section 5.5 makes a general conclusion of this chapter.

5.1 Propagation of plasma jet with a ring electrode

5.1.1 Multi-periodic mode with an external ring-like powered electrode without a target

Periodic and random mode is also observed in APPJ with an external ring-like powered electrode. The discharge current is shown in figure 5.2. In figure 5.2(a), while V_{pp} = 7.8 kV, positive and negative plasma bullets are ignited once every AC cycle, and the discharge current amplitudes are the same in every cycle. While V_{pp} = 8.8 kV as in figure 5.2(b), the discharge current exhibits a 2P mode: for both positive and negative discharges, a strong current peak and a weak current peak are observed alternatively. With frequencies from 10 kHz to 17 kHz, nP mode with n≥3 is not observed. Figure 5.2(c) shows the discharge current when V_{pp} = 9.3 kV, and the discharge current amplitude is random.

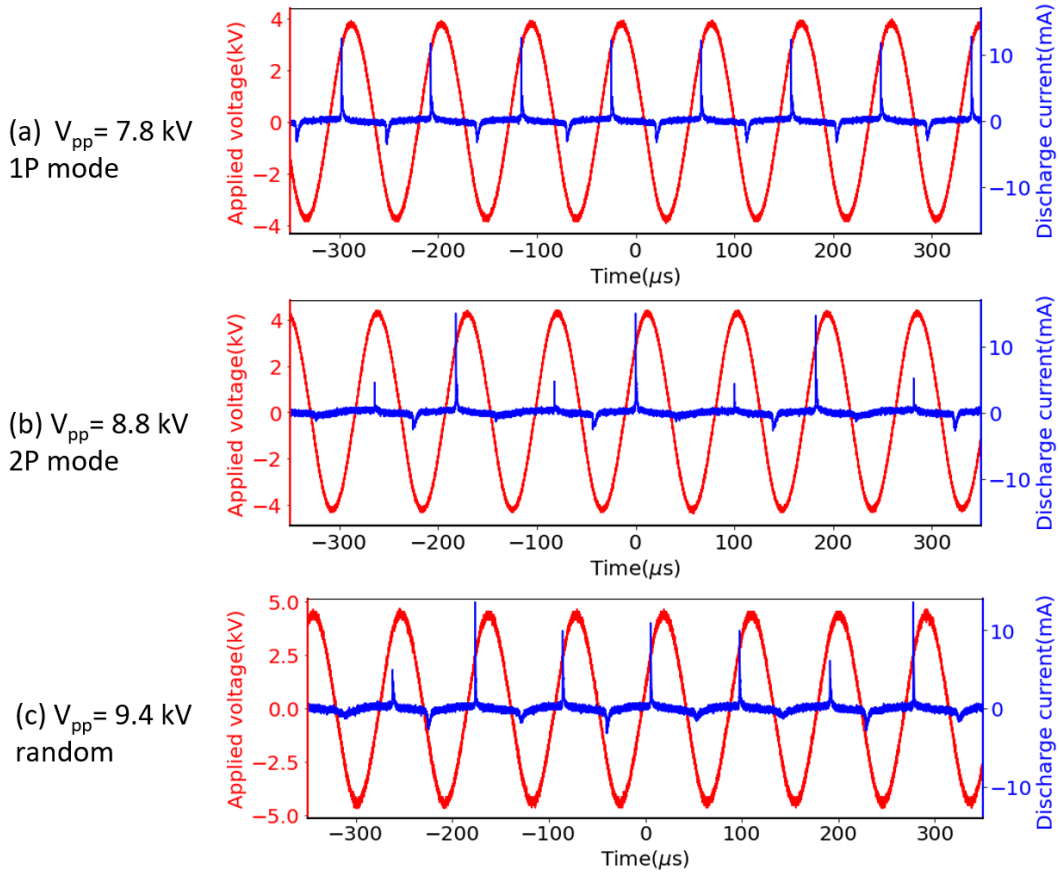

Figure 5.2 Discharge current (blue curve) of the APPJ with 40 mm gap distance. The applied voltage has a frequency of 11 kHz and is shown with the red curve. The helium flow rate is 1 SLM. (a) V_{pp}= 7.8 kV and a plasma bullet are formed every cycle. (b) V_{pp}= 8.8 kV, and a strong current peak and a weak current peak are detected alternatively. (c) V_{pp}= 9.4 kV, and the plasma bullet formation is random.

5.1.2 Influence of upstream plasma

In a pin-to-ring APPJ shown in chapter 3, the plasma propagation length has a trend of increasing as the applied voltage increases, despite the dramatic decrease at several voltage points. The maximum propagation length of the ring-to-ring APPJ is shown in figure 5.3 as a function of the peak-to-peak voltage. With a ring-like powered electrode, the breakdown voltage, also called the burning voltage, is 7.3 kV as shown in Figure 5.3 when the gap distance is 30 mm, which is much higher than the burning voltage with a pin electrode with a gap distance of 30 mm (3 kV as shown in Figure 3.4). A propagation length of 6.5 centimeters is observed once the voltage is high enough for the breakdown. A drastic decrease in propagation length happens when V_{pp} exceeds 9.3 kV, and a global trend of decrease is observed while V_{pp} continues to increase. In the meantime, the upstream propagation length shows a drastic increase when V_{pp} exceeds 9.3 kV, and continues to increase while V_{pp} increases. The total propagation has an overall trend of increasing with V_{pp}.

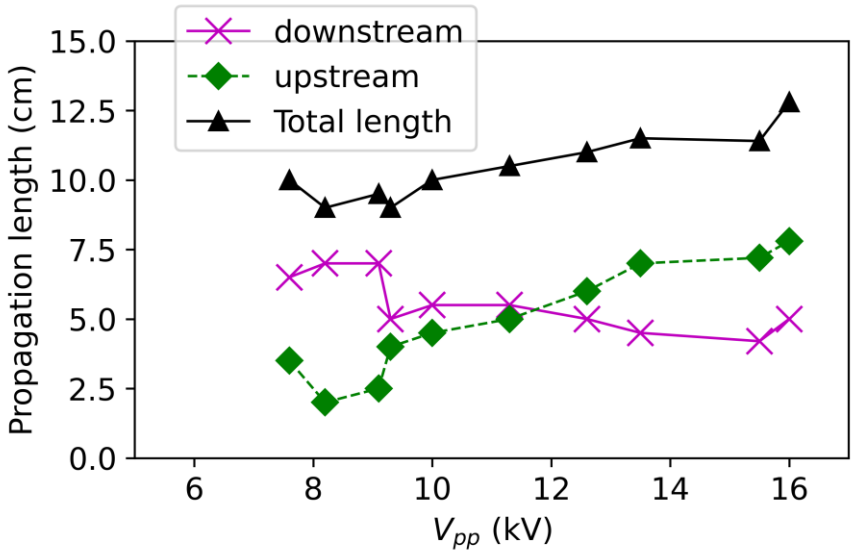

Figure 5.3 Downstream, upstream and total propagation lengths of the plasma jet as a function of the peak-to-peak applied voltage.

The variation of the upstream and downstream propagation length shown in Figure 5.3 indicates an interaction between the upstream and downstream plasma.

The propagation of the plasma in the upstream, downstream, and gap regions is observed with the method introduced in section 2.1.3. The chosen operation conditions are the same as the condition of figure 5.2(b) in 2P mode when the applied peak-to-peak voltage is 8.8 kV and the gap distance is 4 cm. The propagation of plasma bullet (strong discharge current shown in figure 5.2(b)) with 1 μs and 200 ns gate width are shown in figure 5.4 (a) and (b), respectively. The corresponding waveforms of the applied voltage and the discharge current that flows through the ground electrode are also shown, and the time axis for the waveform and the ICCD photos are aligned.

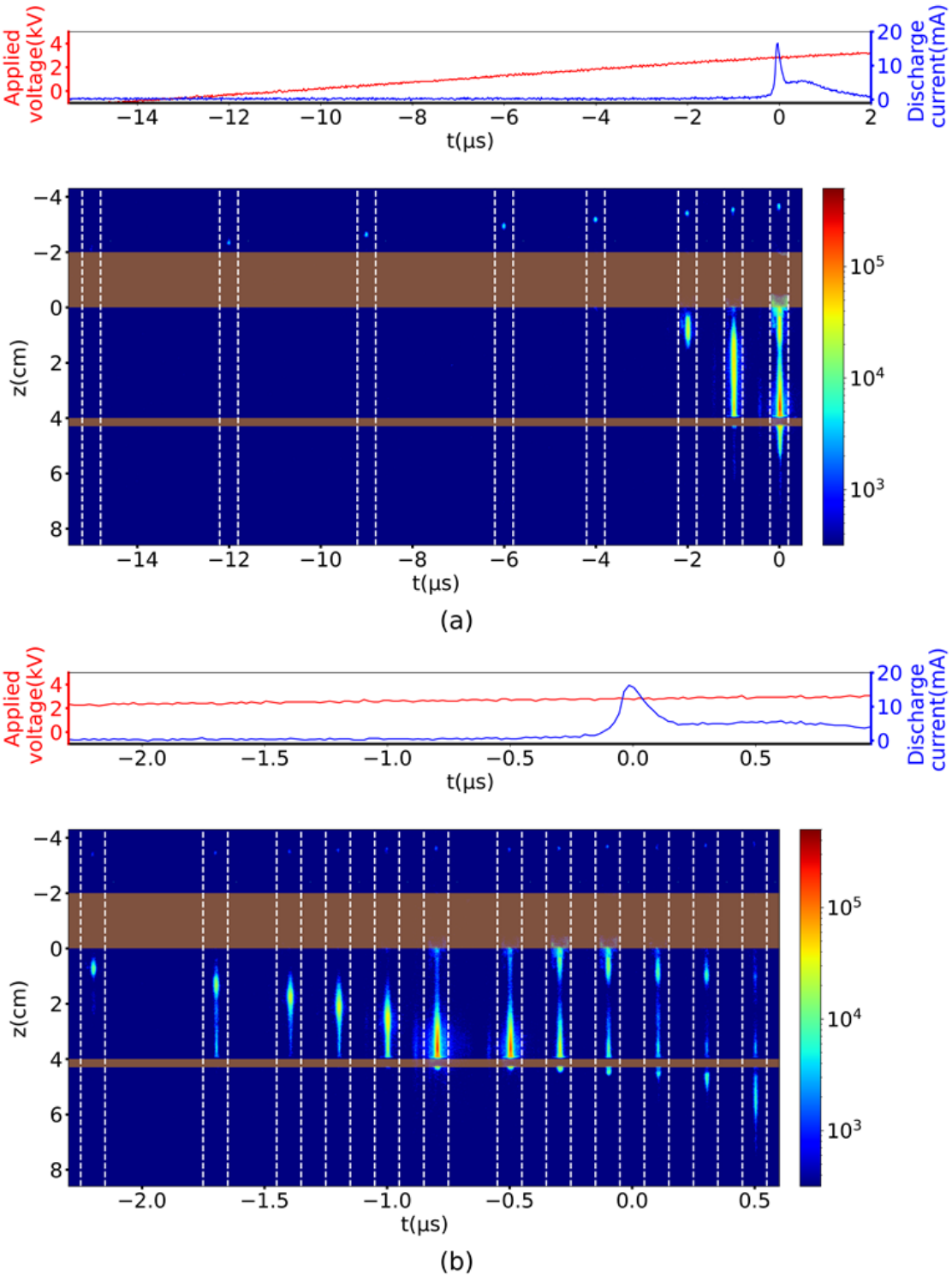

Figure 5.4 Early propagation of the positive long plasma bullet in 2P mode of the ring-to-ring plasma jet (lower figure) and the corresponding waveforms of applied voltage and discharge current (upper figure). Time zero of the waveform is defined as the time of discharge current peak. Each photo is accumulated 100 times with a gate width of 1 μs for (a) and 200 ns for (b). The gap distance is 40 mm. The applied voltage is 8.8 kV. The driving frequency is 11 kHz. The upper and the lower orange bars represent the positions of the 2 cm wide powered electrode and the 3 mm wide ground electrode,

respectively. The white dashed lines represent the inner walls of the capillary. Light intensity is shown in log scale.

As shown in figure 5.4, two breakdowns are observed. The first breakdown happens at the upstream edge of the powered electrode when the voltage is about -1 kV. A weak ionization wave is formed and propagates upstream with an average velocity of 1.5 km/s. The second breakdown happens at the downstream edge of the powered electrode when the voltage is about 2.2 kV. An ionization wave with about 5 times higher intensity than the first breakdown is formed and propagates toward the ground electrode. The average velocity in the gap region is about 26 km/s. The velocity of this ionization wave decreases at the ground electrode region when it reaches the ground electrode at -0.7 μs as shown in 5.4(b). The velocity increases again at 0.2 μs, and the plasma bullet that propagates in the downstream region is formed. This stop-and-go process is similar to the phenomenon shown in Figure 3.11.

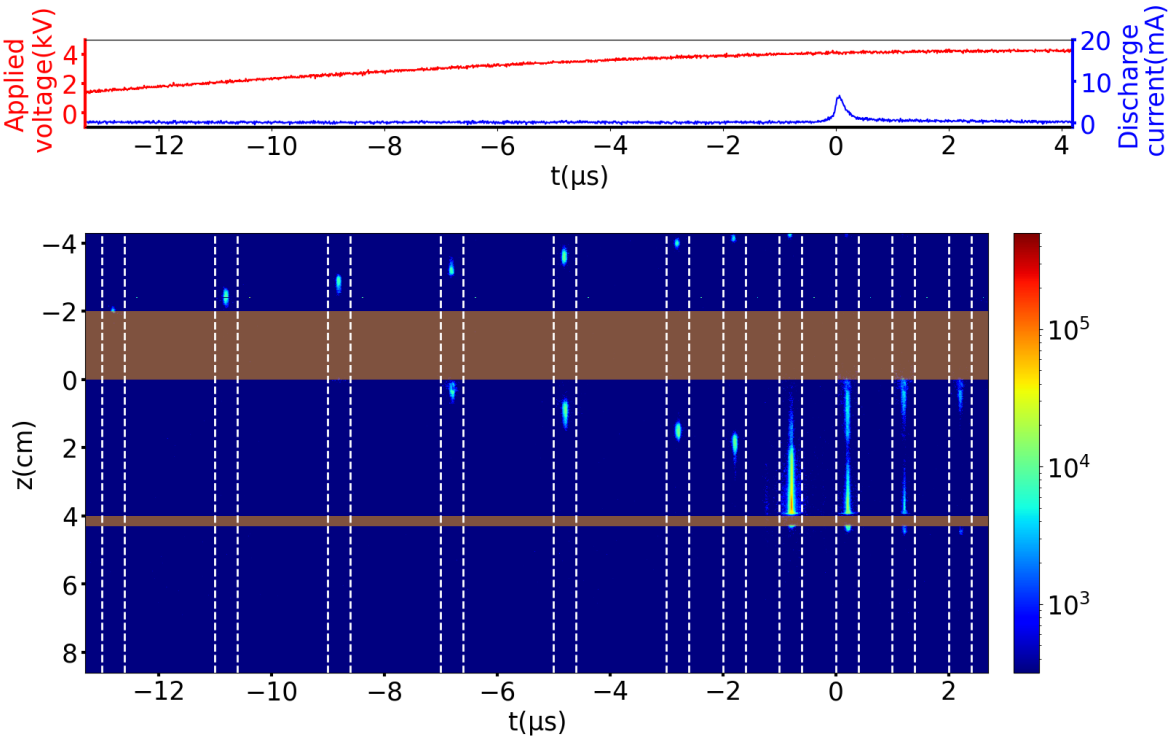

Figure 5.5 Early propagation of the positive gap discharges (with weak discharge current in figure 5.2(b)) in 2P mode of the ring-to-ring plasma jet (lower figure) and the corresponding waveforms of applied voltage and discharge current (upper figure). Time zero of the waveform is defined as the time of discharge current peak. Each photo is accumulated 100 times with a gate width of 1 μs. The gap distance is 40 mm. The applied voltage is 8.8 kV. The driving frequency is 11 kHz. The upper and the lower orange bars represent the positions of the 2 cm wide powered electrode and the 3 mm wide ground electrode, respectively. The white dashed lines represent the inner walls of the capillary. Light intensity is shown in log scale.

Similarly, the dynamics of positive gap discharge without plasma bullet are shown in Figure 5.5. Upstream and downstream breakdowns are observed. The upstream breakdown happens when the voltage is about 1.7 kV. The upstream ionization wave has a similar velocity as the

upstream ionization wave in Figure 5.4(a). The downstream breakdown happens when the voltage is about 3 kV. The downstream ionization wave has an average velocity of 6.7 km/s in the gap region, which is only 1/4 of the gap region velocity in Figure 5.4(b). The downstream ionization wave reaches the ground electrode region and forms a current peak with a maximum current of 8 A. However, the plasma bullet is not formed in the downstream region.

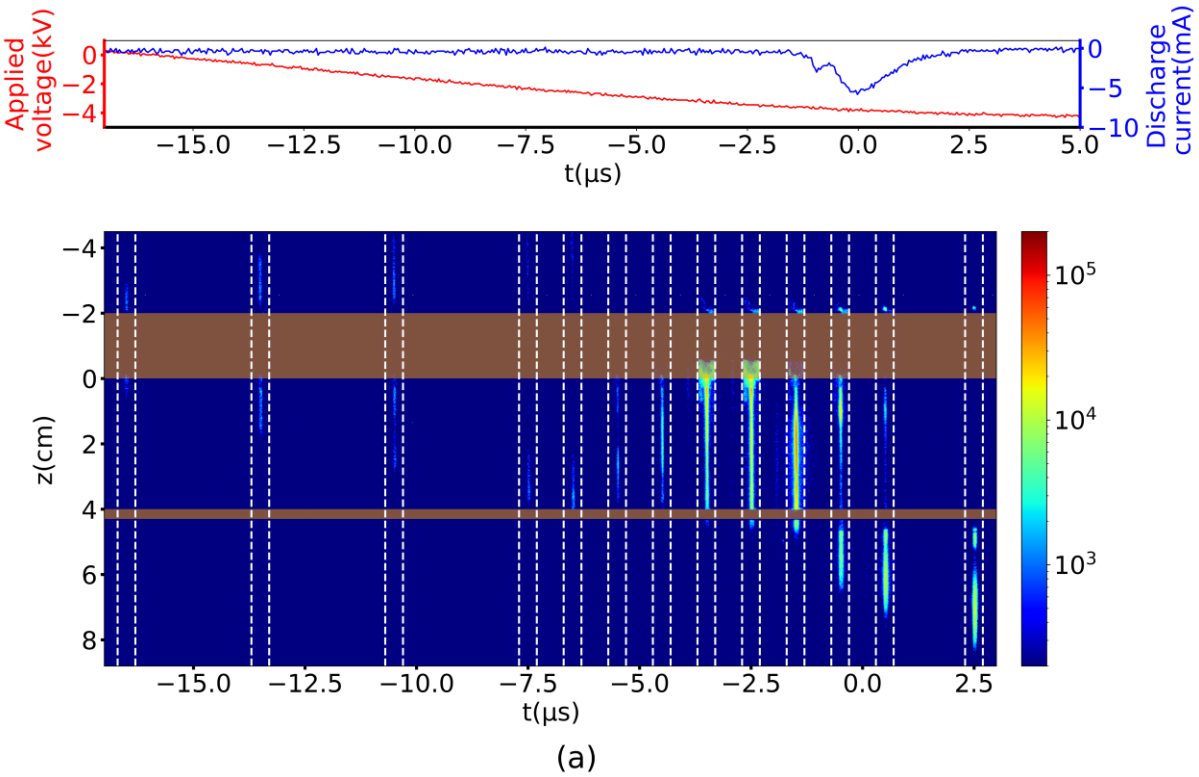

Figure 5.6 Early propagation of the negative plasma bullet in 2P mode of the ring-to-ring plasma jet (lower figure) and the corresponding waveforms of applied voltage and discharge current (upper figure). Time zero of the waveform is defined as the time of discharge current peak. Each photo is accumulated 100 times with a gate width of 1 μs. The gap distance is 40 mm. The applied voltage is 8.8 kV. The driving frequency is 11 kHz. The upper and the lower orange bars represent the positions of the 2 cm wide powered electrode and the 3 mm wide ground electrode, respectively. The white dashed lines represent the outer walls of the capillary. Light intensity is shown in log scale. The light in the powered electrode region is possible due to the diffraction of the glass wall.

The propagation of the negative plasma bullet is shown in Figure 5.6. The upstream ionization and downstream ionization started almost simultaneously at about -17 μs. These plasmas have a homogeneous light intensity through the ionized channel. The downstream ionization plasma is first reflected when it reaches the ground electrode, and reflected again when it propagates back to the powered electrode. The twice-reflected ionization wave forms the downstream-propagating negative plasma bullet at about −1 μs. In the meantime, an ionization wave is observed in the gap region and propagates upstream toward the powered electrode (−1 ~ 0.2 μs).

With a ring-like external powered electrode and ground electrode, multiperiodic modes are also observed. The discharges propagates both upstream and downstream. If a strong upstream discharges occurs, the downstream discharges are weaken. In multi-periodic modes, a weak upstream discharge is observed before the downstream discharge.

5.2 Influence of a water target on the propagation

5.2.1 Plasma power transferred to the water target

As discussed in chapter 3 and section 5.1, the charge deposition at the surface of the capillary is influenced by the ground electrode, resulting in periodic or random plasma ignition. When putting a grounded water target near the plasma jet outlet, the target shows a similar effect on the plasma ignition. The power transferred to the water target by the plasma jet is measured in different conditions are shown in Figure 5.7.

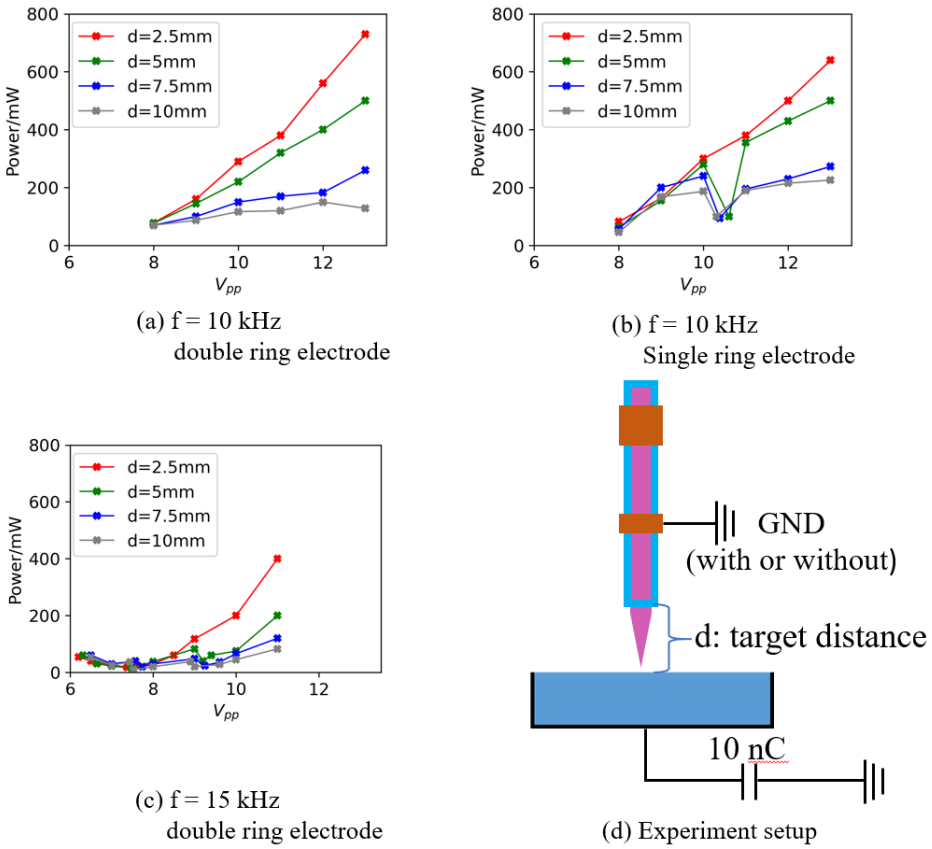

Figure 5.7. The average power deposited on the water target as a function of the applied peak-to-peak voltage in different conditions. (a) The voltage frequency is 10 kHz, and a ring grounded electrode is placed 35 mm downstream of the powered electrode. (b) The voltage frequency is 10 kHz, and the ring ground electrode is removed. (c) The electrode configuration is the same as (a), but the frequency is 15 kHz. The different line colors represent the power with different distances d between the outlet of the

plasma jet and the water surface. (d) The plasma jet configuration of (a-c). The power is measured with the 10 nC capacitor connected to the petri dish.

With 10 kHz frequency and double ring electrode configuration as shown in figure 5.7(a), the plasma ignition is always random regardless the variation of V_{pp} and the target distance. In this case, the plasma power increases monotonically with V_{pp}. If the ring ground electrode is removed, as shown in figure 5.7(b), the power decreases when V_{pp} increases to 10.5 kV with a target distance of 5~10 mm. Such decreases are caused by the transfer between periodic and random plasma ignition that results from the influence of the water target. For example, when the frequency is increased to 15 kHz and the ring ground electrode is present, as shown in figure 5.7(c), a decrease in power is observed at the voltage of 7.5 kV and 9 kV. This is due to a transition from multi-periodic modes to the random mode.

5.2.2 Charge deposited to the water target

The amount of charges deposited to the target surface is also measured. Due to the possible jitter of plasma bullets, the amount of charges of each plasma bullet may also be random: a statistic approach is performed to measure the charge distribution. A python program is used to analyze the waveform of voltage measured on the target and detect the start and end point of the step caused by a plasma bullet so that the amount of charges can be calculated. For each condition, the amounts of charges of 150 plasma bullets are measured, and the distributions of amounts of charges are plotted in Figure 5.8. The distance of inter-electrode gap regions is 45 mm; the distance between the ring ground electrode and the jet outlet is 35 mm; the distance between the jet outlet and the water surface is 5 mm, and the voltage frequency is 15 kV.

When V_{pp} = 9.6 kV and 12 kV, the plasma ignition is in 1P periodic mode with an ignition time jitter of < 100 ns, and the charges detected on the target show a narrow peak, with a relative standard deviation of typically 10%. In random mode (V_{pp} = 10 kV and 13 kV), the relative standard deviation can be up to 60%. The maximum value of the amount of charges is achieved with 10 kV peak-to-peak voltage. Increasing voltage beyond 10 kV causes shorter propagation length downstream and longer propagation length upstream, resulting in less charge transferred to the water target. As shown in Figure 5.8(d) and (d′), the distributions show two peaks for both positive and negative plasma bullets with 13 kV peak-to-peak voltage.

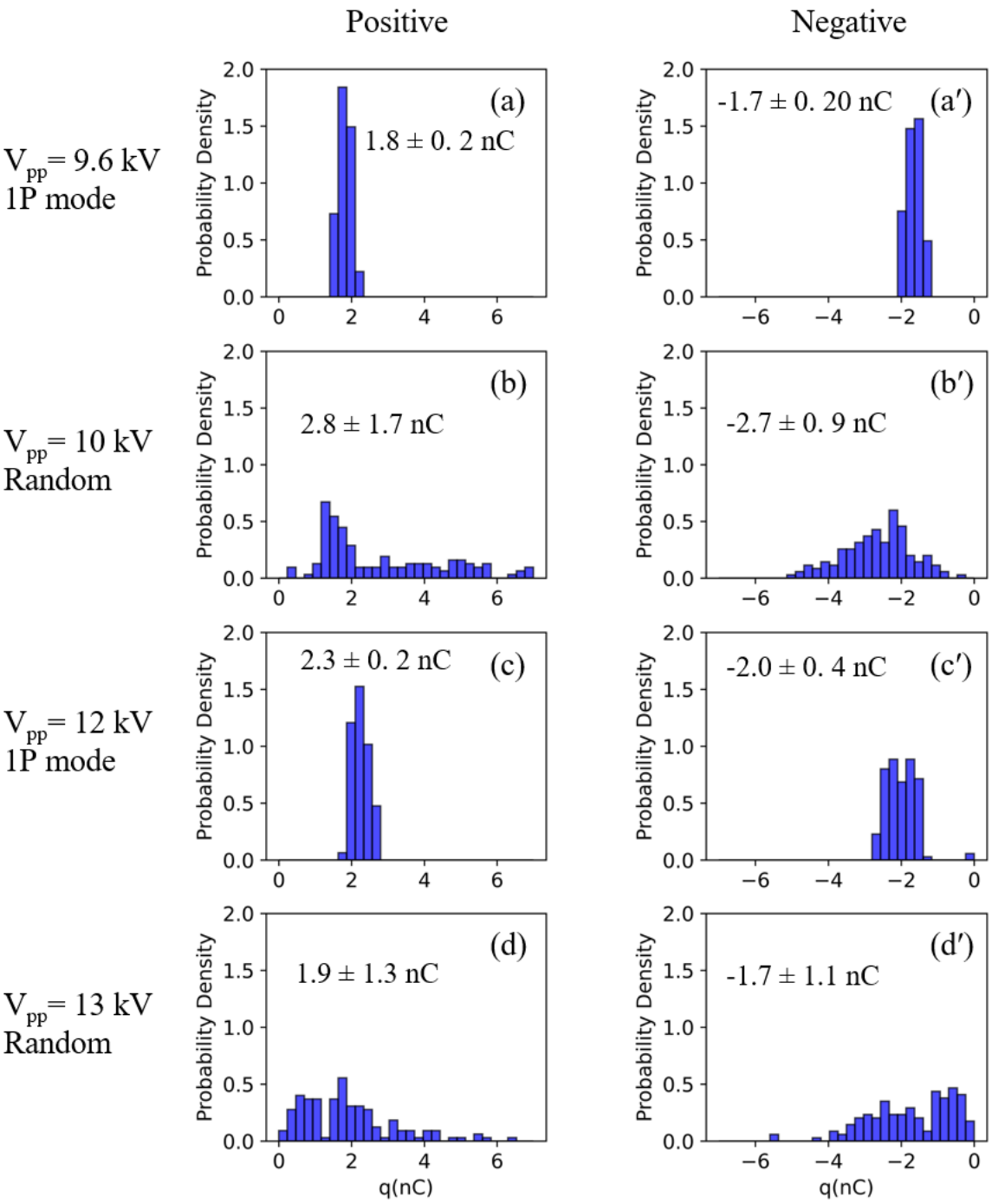

Figure 5.8. The distributions of amounts of charges deposited to the water target by 150 plasma bullets for each condition. The distributions are normalized and the probability densities are shown. The numbers in the figures show the mean value ± the standard deviation of the amount of charges. The distance of inter-electrode gap regions is 45 mm; the distance between the ring ground electrode and the jet outlet is 35 mm; the distance between the jet outlet and the water surface is 5 mm, and the voltage frequency is 15 kHz.

5.2.3 Fast imaging of the propagation near the water surface

The propagation of the plasma bullets in 1P mode near the water surface is observed by the ICCD camera. The photos of propagation for positive and negative plasma bullets are shown in Figure 5.9 and Figure 5.10, respectively. The operation conditions are the same as in Figure 5.8(c) and (c′).

As shown in Figure 5.9, the light emission intensity of the positive ionization front increases significantly when it propagates out of the capillary. A bright plasma plume is formed between the jet outlet and the water surface. The plasma in the region between the nozzle and water emits light for about 1.5 μs. At 3.3 μs, a backward propagating ionization front is observed inside the tube and has a weak light intensity. The backward propagation lasts for about 10 mm maximum, counting from the water surface. This backward ionization wave is induced by the water surface, and has been decribed in literature [171].

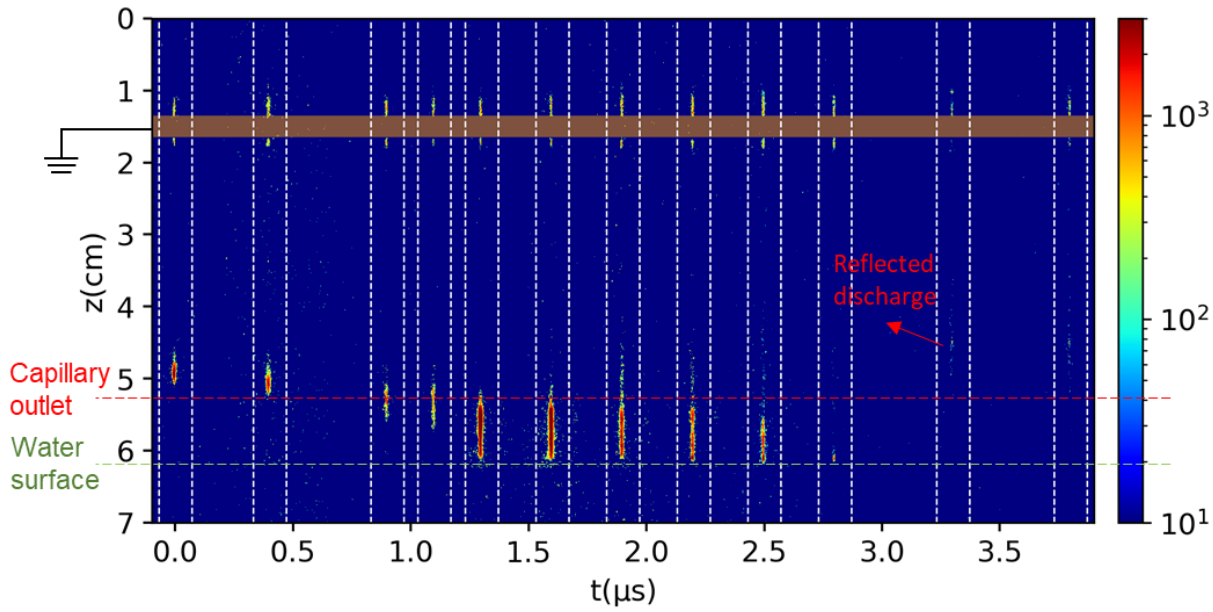

Figure 5.9. Propagation of the positive plasma bullet near the water surface. The orange bar represents the ring ground electrode; the red dash line represents the outlet of the capillary; the green dash line represents the water surface; the white dashed lines represent the outer surface of the capillary. Each photo is accumulated 100 times with 200 ns ICCD gate width for each exposure.

As shown in Figure 5.10, the negative plasma bullet has a lower light intensity but a longer bright area, which is consistent with the observation in Chapter 3. Similar to the positive plasma bullets, the negative plasma bullets are also reflected, and propagate backward from the water surface for about 10 mm.

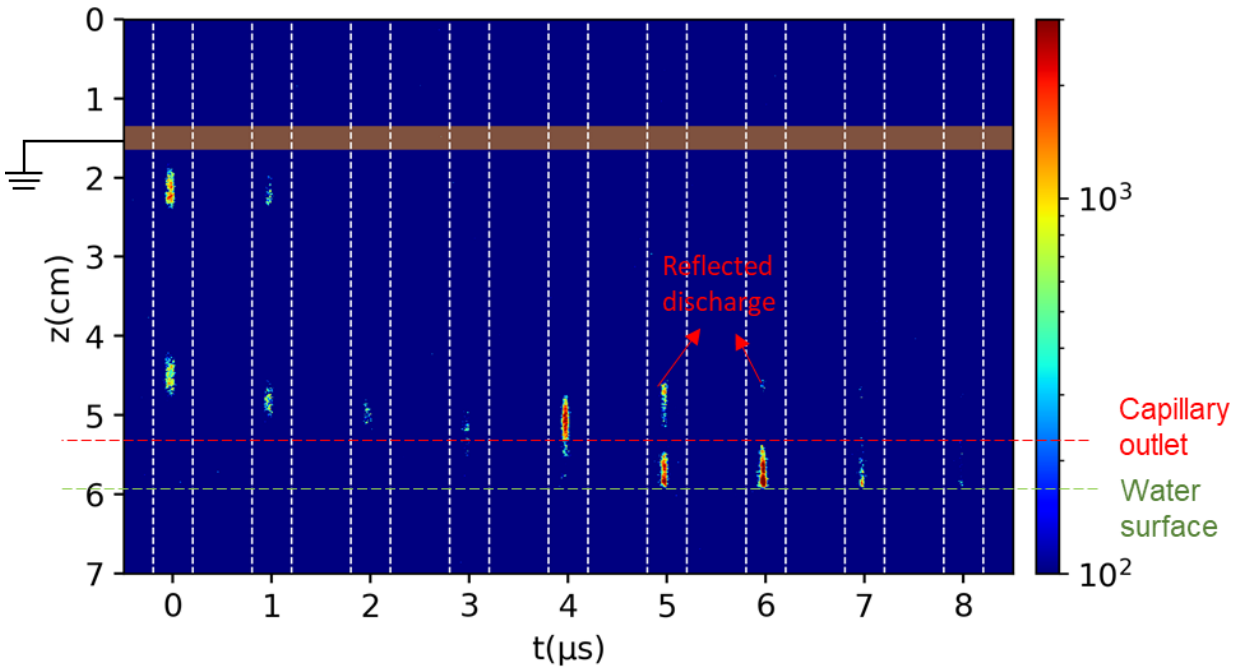

Figure 5.10. Propagation of the negative plasma bullet near the water surface. The orange bar represents the ring ground electrode; the red dash line represents the outlet of the capillary; the blue dash line represents the water surface. Each photo is accumulated 200 times with 1 μs ICCD gate width for each exposure.

A grounded water target, like another ground electrode, can change the multiperiodic modes of the plasma ignition; this influence the power and the amount of charges transferred to the water target. In random mode, the amount of charges deposited to the water can vary randomly by a factor of 10, while it vary by a factor of 20% in multi-periodic modes. Discharges can remain bright on the water surface for up to 2 μs. A weak backward discharge is observed after plasma interacting with the water surface.

5.3 Parametric study of long-live RONS production

In this section, the main long-live RONS produced by the plasma jet in water are measured in different operation conditions. The applied voltage, gas flow rate, and target distance are varied. The concentrations of H_2O_2 are measured and the production rate in nmol/min is evaluated.

5.3.1 Effect of voltage

As shown in Figure 5.3, the propagation length is influenced by the applied voltage. Thus, changing the applied voltage caused different plasma-liquid contact conditions and plasma air-contact conditions. Three possibilities of plasma-liquid/air contact conditions are shown schematically in Figure 5.11. In Figure 5.11(a), the water surface is close to the plasma jet

outlet, so the plasma plume directly contacts the water surface and can interact with liquid phase water. In Figure 5.11(b), the distance between the water surface and the APPJ outlet is increased compared to (a); although no visible plasma can reach the water surface and the plasma plume cannot interact with the liquid phase water, the plasma can still interact with water molecules that come from ambient air and water evaporation of target. In Figure 5.11(c), the plasma propagation is short and limited inside the capillary, so chemical reactions only happen among the molecules of the fed gas. The ICCD photos of the plasma plume with long exposure time (2 ms gate width) in plasma-liquid contact conditions and plasma-air contact conditions are shown in Figure 5.12.

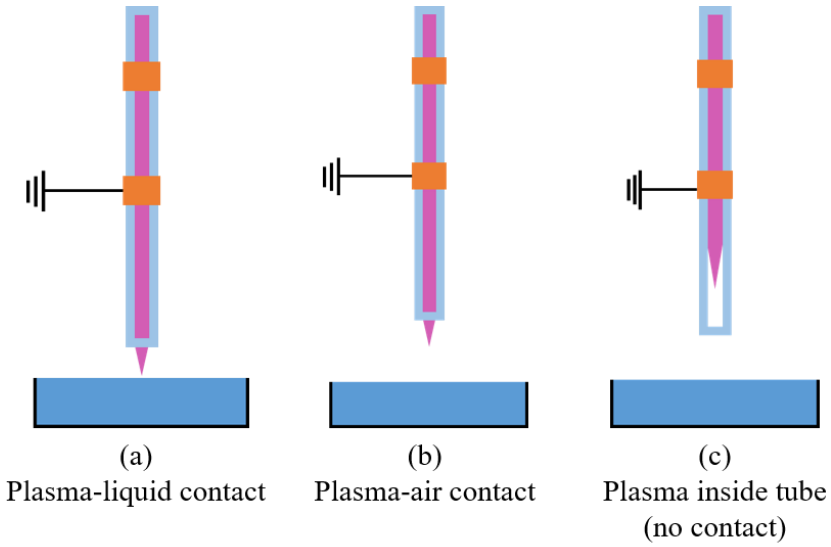

Figure 5.11. Schematic drawing of three possibilities of plasma liquid/air contact conditions. (a) The plasma plume is in direct contact with the water surface. (b) The plasma propagates outside of the capillary, but cannot reach the water surface. (c) No visible plasma light emission is observed outside of the capillary.

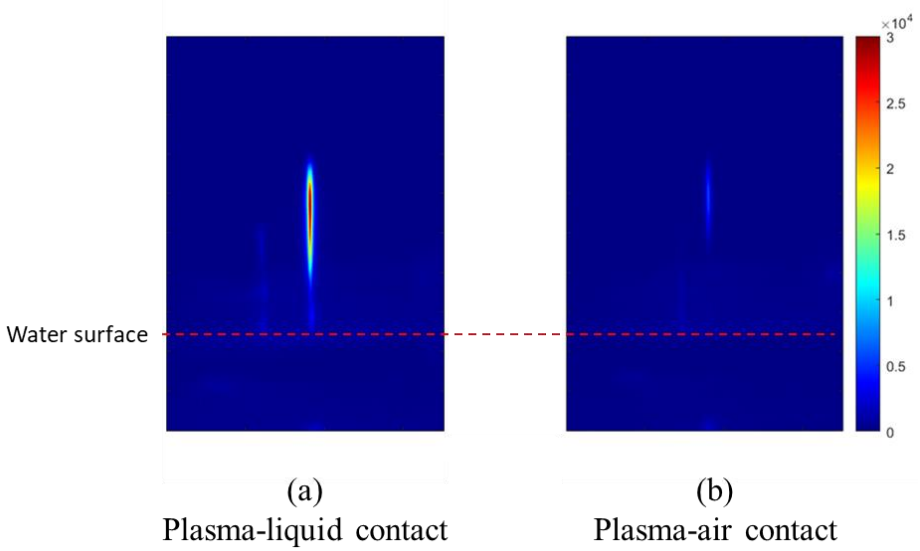

Figure 5.12. Long-exposure time (2 ms gate width) ICCD photo of the plasma plume between the APPJ outlet and the water target. (a) corresponds to plasma-liquid direct contact conditions in Figure 5.11(a). (b) corresponds to plasma-air contact conditions in Figure 5.11(b), and no plasma is observed to reach the water surface.

15 mL of water is treated by the APPJ for 10 min. The helium flow rate is 1 SLM and the target distance is 10 mm. V_{pp} is varied from 8 kV to 14.5 kV, with a fixed frequency of 10 kHz. The plasma power is measured during the treatment and the concentration of H_2O_2 is measured using the method introduced in section 2.2.2. The results are plotted in Figure 5.13.

As shown in Figure 5.13, the power transferred to the target is significantly influenced by the applied voltage. For example, the plasma power is 1.05 W when Vpp is 8 kV, and the plasma plume can reach the water. When Vpp is 8.5 kV, the power decreases to 0.32 W drastically, because in this condition the plasma mainly propagates upstream, which tends to weaken the downstream plasma, as introduced in section 5.1.2. In spite of the change of power, the H_2O_2 production rate is barely influenced by the variation in voltage. A slight decrease in production rate is observed at 8.5 kV.

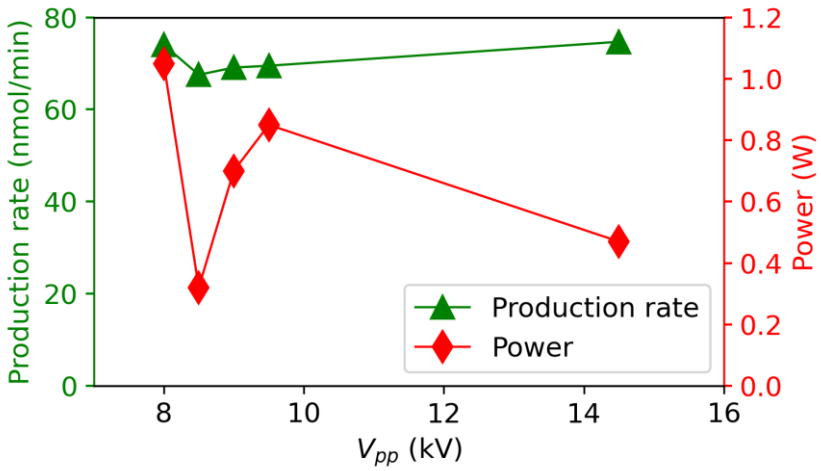

Figure 5.13. H_2O_2 production rate and plasma power transferred to the water as a function of the peak-to-peak applied voltage. The flow rate is 1 SLM. The distance between the water and the jet outlet is 10 mm.

5.3.2 Effect of helium flow rate

To study the effect of helium flow rate on H_2O_2 production, 15 mL of water is treated by the APPJ for 10 min with a target distance of 10 mm. Vpp is 10.5 kV, with a fixed frequency of 10 kHz. The flow rate is varied from 400 to 1000 sccm. The results are plotted in Figure 5.14.

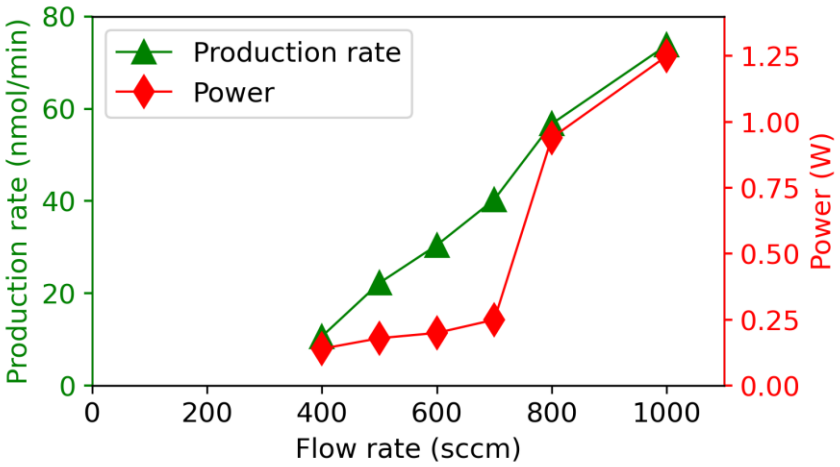

Figure 5.14 H_2O_2 production rate and plasma power as a function of the helium flow rate. The distance between the water and the jet outlet is 10 mm. The applied peak-to-peak voltage is 10.5 kV.

As shown in Figure 5.14, the production rate increases linearly with the flow rate from 400 to 1000 sccm. However, the plasma power does not increase linearly with the flow rate. Note that a drastic increase in power happens when the flow rate increases to 800 sccm, because the inside tube plasma changes to a plasma touching the liquid surface. The comparison between the H_2O_2 production rate with a flow rate of less than 700 sccm and more than 800 sccm indicates that the plasma-liquid contact and the plasma-air contact has a minor influence on the H_2O_2 production.

5.3.3 Effect of target distance

To study the effect of target distance (distance between the outlet of APPJ and the water surface) on the H_2O_2 production, 15 mL distilled water is treated by the APPJ for 10 min with 1000 sccm helium flow rate. Vpp is 10.5 kV, with a fixed frequency of 10 kHz. The gap distance is varied from 5 mm to 82 mm. According to ICCD imaging, in the operation condition mentioned above, the plasma plume is in direct contact with the water surface if the target distance is less than 22 mm. The obtained H_2O_2 production rate and treatment power are plotted in Figure 5.15.

As shown in Figure 5.15, a significant decrease in plasma power is observed when the target distance increases in plasma-liquid contact mode (1~22 mm). The power when the target distance is greater than 30 mm is about 0.4 W and only slightly decreases due to increasing target distance. A maximum production rate of 74 nmol/min is achieved with a 30 mm target distance, and a graduate decrease in production rate is shown when the target distance increases. With a target distance of 82 mm, which is much further compared to the target-treating distance used in most studies involving APPJ, a production rate of 51 nmol/min is still obtained. This is 70% of the maximum production rate. Also surprisingly, the drastic decrease in power does not influence the production rate. In general, no direct link is found between the target distance (within 80 mm) and H_2O_2 production.

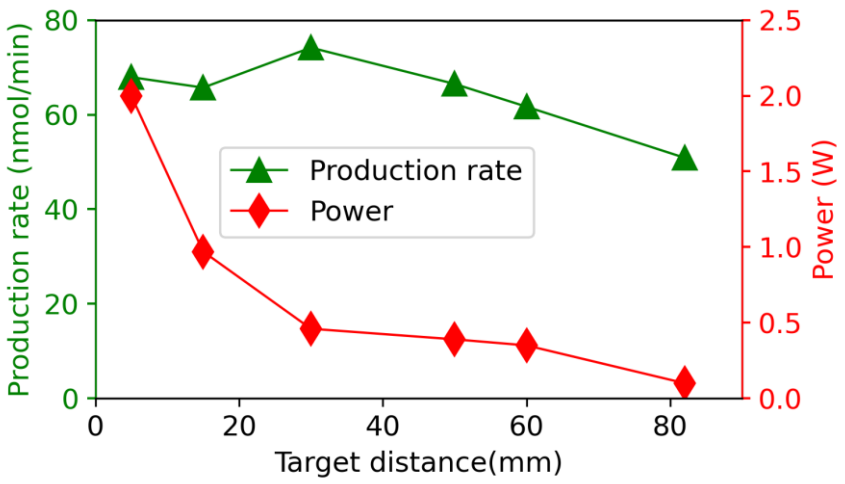

Figure 5.15. H_2O_2 production rate and plasma power as a function of the distance between the jet outlet and the water surface. The helium flow rate is 1 SLM. The applied peak-to-peak voltage is 9 kV.

The production rate of H_2O_2 in Plasma Activated Water is mainly influenced by the flow rate, while the gap distance and the applied voltage have a minor influence. Whether the plasma plume contacts the water surface the the ambient air does not significantly influence the production rate.

5.4 Source of H_2O_2 production

5.4.1 H_2O_2 is mainly produced inside the tube

As introduced in chapter 1, section 1.3.3, H_2O_2 can be formed in several pathways in plasma-liquid interaction. Although some literature suggests H_2O_2 is mainly formed in gas phase and diffuses to bulk water, some studies conclude that H_2O_2 is mainly formed in plasma-water surface through the recombination of OH• radical. To satisfy the potential need of manipulating H_2O_2 production for medical applications, it is interesting to clarify the origin of H_2O_2 formed in water by plasma treatment.

In this report, the distance between the APPJ outlet and the water target has a minor influence on the production rate of H_2O_2 in water, as shown in Figure 5.15. The maximum production rate is obtained with a 30 mm gap distance. In this condition, there is no direct contact between the plasma plume and the water surface, which indicates that H_2O_2 is not mainly produced in plasma-liquid interface. This is consistent with the result obtained by Oh *et al*, who found the highest RONS generation efficiency with a 22 mm target distance [89]. A significant amount of H_2O_2 is obtained with an 80 mm gap distance, showing that most of the H_2O_2 molecules are already produced in gas phase.

It is proposed that the recombination of OH• radicals can form liquid phase H_2O_2 [95]. The formation of OH• radicals in plasma has been intensively investigated [93,97,172–176]. The production of OH• depends on the gas temperature, the electron temperature, the ionization degree, the gas composition, etc [172]. The liquid phase OH• can be formed by water dissociated by electrons, and combination of H atoms and O atoms [173], or by UV photolysis of water [97]. However, direct formation of OH radicals in liquid phase should not be the main source of OH• radicals in this work when the plasma plume does not directly contact the water surface.

OH• radicals can also be formed in gas phase and transferred to the water surface[175,176]. The OH radicals have a lifetime of typically 100 μs in helium-water plasma[73]. The velocity of the gas effluent in the tube with a flow rate of 1 SLM and a tube diameter of 1 mm is 21.23 m/s, so the molecule in plasma can travel 2.1 mm maximum within the lifetime of OH• radicals. Therefore, if the plasma plume does not directly contact the water surface, the OH• radicals are unlikely to recombine on the water surface and form H_2O_2. The 30% loss of H_2O_2 concentration compared to the maximum value is highly likely to be due to diffusion from post-discharge gas into the ambient air. The H_2O_2 is more likely to be formed mainly from the recombination of OH radicals in gas phase:

$$2OH + He \rightarrow H_2O_2 + He \qquad (5.1)$$

Having concluded that H_2O_2 is not mainly formed by the direct interaction between plasma plume and liquid phase water, it is interesting to clarify whether it is formed in the plasma plume by interacting with water vapor from ambient air and evaporation of water target, or it is formed inside the plasma, by chemical reactions of fed gas impurities.

When an APPJ fed by dry helium gas is treating a water target, the water content in the plasma plume is significantly influenced by the target distance and the flow rate. The dry helium flow pushes away the water vapor evaporating from the wet surface. Therefore, increasing the helium flow rate or decreasing the target distance leads to less gas-phase water content in the plasma plume. Yagi *et al.* measured the humidity and OH• radical density in a helium plasma interacting with a water target with a 5 mm target distance. The result shows that the relative humidity along the central axis of the gas flow near the water surface is 20% with a 0.3 SLM flow rate, and about 2% with a 1 SLM flow rate[88]. The OH• radical density with a 0.05 SLM flow rate is typically twice more than the density with a 0.3 SLM flow rate.

Similarly, as H_2O_2 can only be formed by the water molecules in plasma, the H_2O_2 production in the plasma plume should be strongly influenced by the water content in the plasma plume. To study whether the gas mixing between the plasma effluent and the ambient air has an influence on the formation of H_2O_2, the H_2O_2 production rate in water is measured in four conditions. For all four conditions, gas the flow rate is 1 SLM, the applied voltage is 10.5 kV

and the frequency is 10.5 kHz. 15 mL of water is treated for 10 min. The position of the jet outlet is varied, and is schematically demonstrated in Figure 5.16.

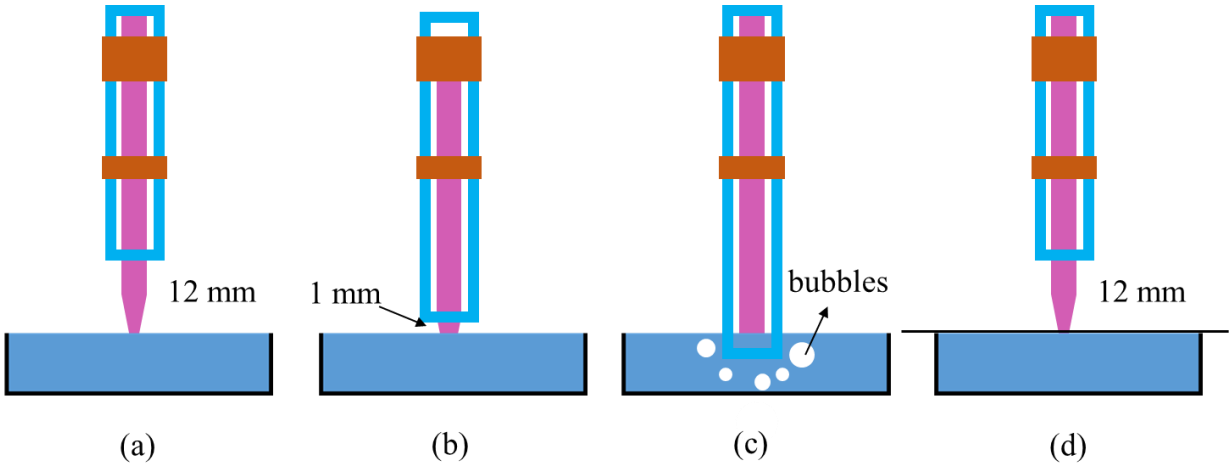

Figure 5.16 Plasma jet treating water with three different target positions. (a) The water surface is 12 mm away from the jet outlet. (b) The water surface is as close to the jet outlet as possible (< 1 mm). (c) The jet outlet is inserted into the water, 2 mm below the water surface. (d) The water surface is covered by a polyethylene film. The plasma plume is in contact with the film.

a) The distance between the water target and the jet outlet is 12 mm. In this condition, the plasma plume can mix with the water vapor evaporated from the water surface.

b) The jet outlet is placed as close to the water surface as possible. The gas flow pushes the water surface away and the distance between the jet outlet and the water surface is estimated to be 1 mm. In this condition, the water content is much lower than in the condition A.

c) The jet is immersed 2 mm below the water surface, forming helium gas bubbles in the water. In this condition, interacting with ambient air is not possible.

d) The water surface is covered by a thin Polyethylene film. The distance between the target and the jet outlet is 12 mm. In this condition, the species and charged particles connot contact the water surface, but the current can flow through the water.

The obtained plasma power and H_2O_2 production rate are shown in Table 5.1.

Table 5.1 The plasma power and production rate of H_2O_2 in three conditions. (a) 12 cm target distance. (b) 1 mm target distance. (c) The jet outlet is immersed in water. (d) The water surface is covered by a PE film.

condition	(a)	(b)	(c)	(d)
Power (W)	0.7	1.55	2.1	0.7
Production rate(nmol/min)	77	61	50	Non-detectable

In condition (d), no H_2O_2 is detected in the water. Thus, the water electrolysis cause by the discharge current does not contribute to the formation of H_2O_2 in PAW.

In condition (a), a production rate of 77 nmol/min is obtained, which is close to the value that we obtained in Figure 5.13 ~ Figure 5.15. When the jet outlet is moved closer to the water, the plasma power is increased by a factor of 3. The H_2O_2 production rate is only decreased by a factor of 30%.

On the other hand, as shown in Figure 5.15, for a larger target distance such as 80 mm, humidity in the plasma plume due to water evaporation is probably less than for a a short target distance; howaver, a significant amount of H_2O_2 is still obtained. Therefore, in the conditions of this work, the main source of H_2O_2 production is likely the plasma inside the tube. The H_2O_2 mainly comes from the water impurities inside the plasma.

Results of a comparison study suggest that the H_2O_2 is mainy produced in the plasma inside the capillary. The interaction with the water surface or air has a small contribution to the H_2O_2 production.

5.4.2 Impurities caused by the molecule desorption from the gas tube inner wall

In all the experiments shown in this chapter, 80 nmol H_2O_2 maximum is transferred to water per liter of helium flown through the tube. According to the label of the helium gas bottle, H_2O impurities are less than 3 ppm or less than 134 nmol H_2O per liter of helium. By assuming that H_2O_2 production does not come from the water vapor of the target and that all the H_2O_2 produced in plasma is dissolved in water, we find that 60% of H_2O impurities are transformed into H_2O_2 through reactions. However, it has been shown that a large fraction the OH radicals recombine to form H_2O instead of H_2O_2 [146]. To confirm the conclusion that we draw in the previous section, the humidity in the discharge gas is evaluated.

The impurities in the gas are identified by optical emission spectroscopy. The plasma jet is driven by 12 kV, 10 kHz voltage and propagates to ambient air. The optical emission is measured with a spectrometer (Ocean Optics Maya Pro 2000) with the configuration shown in section 2.1.3. For each location, the spectrum is accumulated 1000 times with a gate width of 1 ms for each acquisition. The spectrum is measured at 3 locations shown in Figure 5.17(d). The optical emission spectra at locations a, b, and c are shown in Figure 5.17(a-c). Note that the emissions at 900 nm and 280 nm are caused by damaged pixels of the spectrometer, and is marked with red "×" in Figure 5.17(b).

As shown in Figure 5.17(a), in the middle of the gap where the light intensity is the highest, the main optical emission from impurities is the OH band at 309 nm. The signal from the excitation of N_2 bands is relatively weak. The emission lines of OH, He, O, and H are marked in Figure 5.17(a). The OES inside the tube close to the outlet is shown in Figure 5.17(b). At 2

mm before the jet outlet, the emission from N2 bands is barely detectable, showing that the diffusion of molecules from the ambient air into the tube is negligible. When the plasma plume propagates out of the tube, as shown in Figure 5.17(c), the emission from N2 bands significantly increases.

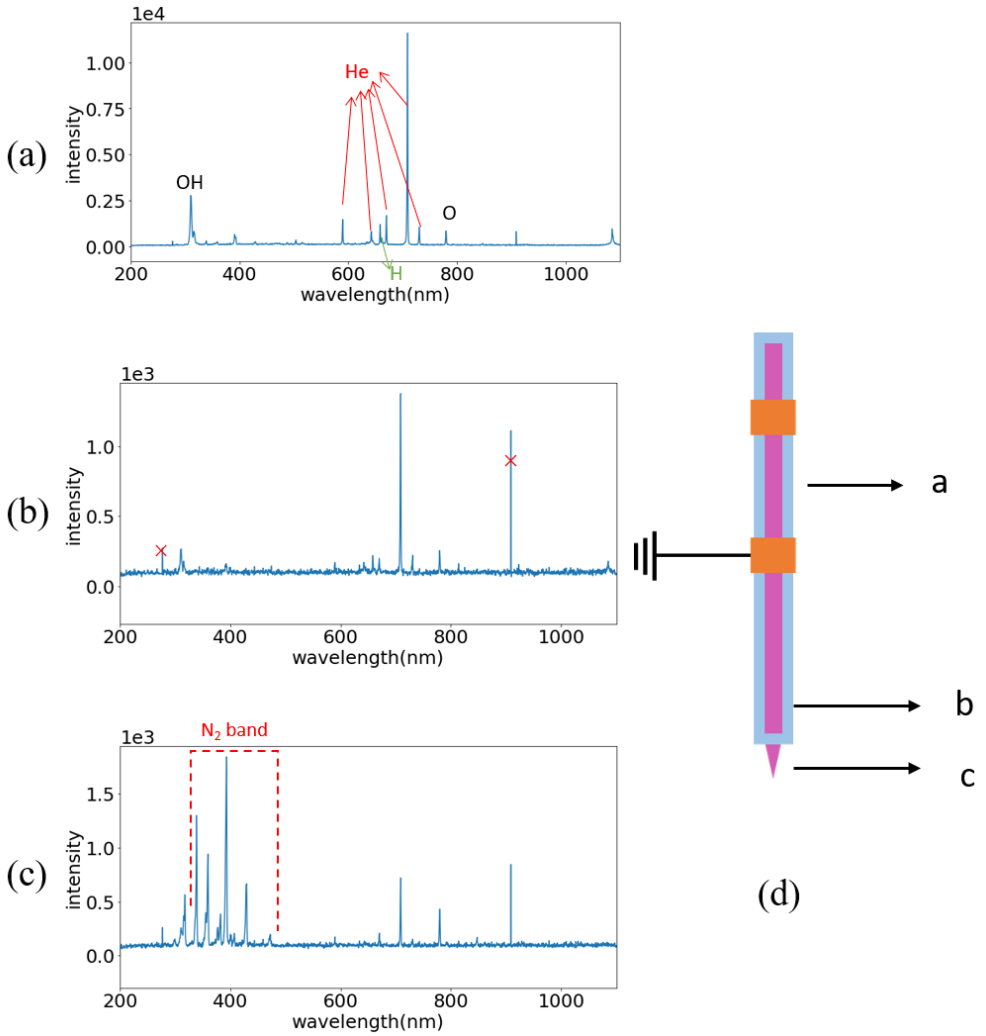

Figure 5.17 Optical emission spectrum of the plasma acquired at three locations (shown in (d)). (a) shows the spectrum in the middle of the inter-electrode gap. (b) shows the spectrum acquired at 2 mm upstream of the jet outlet. (c) shows the spectrum acquired at 2 mm downstream of the jet outlet in the open air. Operation condition: f = 10 kHz, Vpp=10 kV, flow rate= 1 SLM.

The OES test shows that the main impurities inside the tube are H_2O and O_2, which is in agreement with the label of the gas bottle (H_2O < 2 ppm and O_2 < 2 ppm). The leakage from ambient air is negligible. The source of nitrogen is mainly the ambient air when the plasma propagates into the open air. However, OES cannot measure the amount of impuries. Therefore, the amount of impurities in the gas flow is measured with a mass spectrometer. The result has been shown in section 2.3. The humidity in the discharge gas after flushing the gas tube with helium is about 250 ppm.

The formation pathways of the H_2O_2 in PAW have been intensively investigated, and different conclusions were drawn. As OH• recombination is an important pathway to form liquid phase H_2O_2, the formation of OH• radicals will be also discussed hereafter.

OES measurements and mass spectra show that the impurities in the discharge gas is much higher than the gas impuritities indicated on the helium gas bottle, and is mainly caused by disorption of molecules from the tube inner wall.

5.4.3 H_2O_2 origin depends on the electron energy and gas humidity

The different origins (in gas phase or plasma-liquid interface) of H_2O_2 and OH• radical are probably because of the different experiment configurations. In the experiments conducted by He *et al.* [95], Chen *et al.* [96] and Ghimire *et al.* [91], although the term "plasma jet" is used, the distance between the metal electrode and the water target is less than 5 mm, and there is no dielectric layer between the metal electrode and the water surface. Thus, such discharge configurations are more like a needle-plate discharge; no plasma bullet is formed or propagates along the tube's inner surface.

In the experiments conducted by Gorbanev *et al.* [93], Yonemori et *al.* [175], Winter et *al.* [176], and Uchida *et al.* [90], the configuration is more similar to the configuration in this work: the plasmas propagate for a distance of at least several centimeters, or a dielectric layer exists between the powered metal electrode and the plasma. Gorbanev *et al.* used hydrogen and oxygen isotopic labeling to measure the reactive species produced by an APPJ driven by a 24.9 kHz AC voltage. It is concluded that H_2O_2 is mainly formed in the plasma tube [93]. Srivastava and Wang *et al.* showed that varying water addition can change the OH• number densities in a microwave APPJ [177]. Yonemori *et al.* measured the time-averaged OH• density in an 8.4 kHz pulsed APPJ using laser-induced fluorescence (LIF); the result shows that OH• is in mainly formed in the center of the plasma plume, and a smaller number density of OH• is found on the plasma-air interface.

The characteristics of a needle-plate DBD and the plasma bullets are different. In a needle-to-dielectric-plate configuration, discharge forms an ionized channel between the cathode and the anode, which is similar to the gap region discharge shown in this report. The characteristics of plasma are relatively uniform throughout the whole ionized channel. In the APPJ used in this report, as discussed in chapter 3, section 3, OH emission is mainly visible during the glow-like discharge in the gap region. This is probably linked to a production of OH radicals. Thus, in the downstream area where there is no glow-like discharges, the OH production is much less. Furthermore, when the plasma bullets propagate downstream of the ground electrode, the ionization becomes weaker. It has been reported that the OH denisty significantly decreases during the propagation downstream of the ground electrode [147]. For example, Förster *et al.* showed that the electron temperature of a plasma jet decreased from 1 eV to 0.7 eV in 15 mm

propagation [178]. Sretenović *et al*. showed that after 20 mm propagation, the electric field and electron density in a helium APPJ decrease by 60% and 70%, respectively[25]. The decrease in the density of electrons and helium metastables[179] further leads to the decrease in the reaction rate of dissociative recombination which is the dominant OH formation processas reported in a similar APPJ configuration [147]:

$$2OH + He \rightarrow H_2O_2 + He \qquad (5.2)$$

However, even when the OH• and H_2O_2 are measured or transferred to water at a short distance to the powered electrode, contradictory experiments are obtained. For example. Pei *et al.* measured the time-resolved OH• density by LIF imaging, and found that the OH• formation has a donut shape during and shortly after the voltage pulse, i.e. the OH• LIF signal is much stronger on the plasma-air interface [180]. This is different from the result of Yonemori *et al* [175]. Such discrepancy may result from the underestimation of gas humidity. Winter *et al.* measured the H_2O_2 production in water when controlling the feed gas humidity with a hygrometer. It is found that the feed gas humidity is possibly widely underestimated. A 3 m long PUR gas tube results in more than 1000 ppm initial humidity and 70 ppm after 3 h flushing, and the humidity caused by metal tubing is about 30% of polymeric tubing. Winter *et al.* also pointed out that the ambient humidity can be neglected when the feed gas is humid, but become more important if the feed gas is dry [176]. In most of the publications mentioned above, the tubing material and the time of flushing before the discharge are not mentioned, and the gas humidity is not monitored. Thus, the H_2O_2 production in the center of the tube is possibly caused by water desorption from the tube walls, and different experiment results can be obtained due to different tubing materials and lengths.

In the present work, few hundreds ppm of H_2O is detected in Helium flow gas; this explains why H_2O_2 is mainly formed in the capillary tube and then transferred to water target; while in a dry helium gas, H_2O_2 is mainly formed in the plasma-air interface.

5.5 Conclusion

In this chapter, an AC-driven APPJ is used to treat a water target. External ring-like electrodes are used for both the powered electrode and the ground electrode.

- With the presence of a ground electrode, multi-periodic modes similar to those reported in chapter 3 are observed. An upstream plasma is observed before the ignition of the downstream plasma jet. The downstream propagation length decreases when the upstream propagation length extends.

- A water target slightly changes the voltage range of the multi-periodic modes. The amount of charges deposited to the water target is in the range of 1.5 ~ 3 nC.

- The production rate of H_2O_2 in the PAW (plasma-activated water) by the APPJ is measured in different conditions. Comparative studies indicate that H_2O_2 is mainly produced by plasma inside the tube. This is in agreement with the OES measurement in section 3 of chapter 3, which shows that the OH emission is most from the glow-like discharge in the inter-electrode gap region after plasma bullet formation.

Chapter 6. Plasma skin interaction

As introduced in Chapter 1, NTP (Non-Thermal Plasma) has great potential for application in the field of dermatology. NTP treatment at low power helps the healing of skin wounds such as burns and clinical wounds. At higher power, NTP treatment can induce cell death, which can be used for tumor treatment or blood coagulation. Some of those effects are associated with the modification of skin's microstructure. The cause of the microstructural modification of skin is attributed to the Reactive Oxygen and Nitrogen Species (RONS, like H_2O_2 measured in Chapter 5) and/or to the thermal effects of NTP.

In this chapter, we use an APPJ to generate NTP to treat inert defrost pig skin samples. For the first time, Mueller Polametric Imaging (MPI, introduced in Chapter 1) is used to evaluate the modification to the skin microstructure caused by NTP treatment. This chapter aims to show that full-field Mueller Polarimetric Imaging is suitable for fast and without-contact detection of skin microstructure modifications induced by plasma treatment, and to clarify which component of plasma (RONS or heat) is the predominant cause of changes in the tissue microstructure observed over a short time scale.

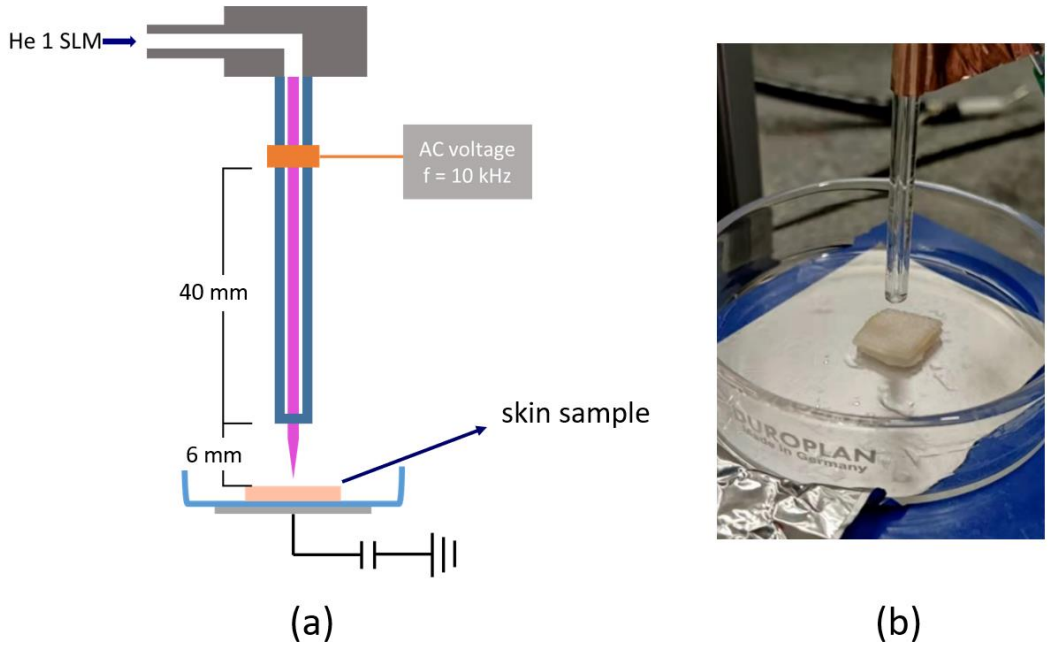

Figure 6.1 (a) shows the schematics of the APPJ treating a pig skin sample. The APPJ is powered by a 10 kHz AC voltage. The discharge gas is helium with a flow rate of 1 SLM. (b) shows a photo of the APPJ device and the pig skin sample.

A 0.3~1.4 W APPJ is used as an NTP source to treat defrosted pig skin samples. The APPJ is shown in Figure 6.1. It is powered by a 10 kHz AC voltage with an external ring-like electrode. The discharge gas is helium with a flow rate of 1 SLM. For all the APPJ treatments in this chapter, the distance between the target and the APPJ outlet is 6 mm. The plasma power transferred to the target is measured by a capacitor connected to an aluminum ground electrode

on the bottom of the container. Changes in tissue microstructure were detected and quantified by means of MPI immediately after plasma treatment. The linear retardance LR and total depolarization Δ are quantified. These two parameters LR and Δ are decomposed from the obtained Mueller Matrix and are related to the birefringence characteristics and the scattering characteristics of the skin samples, respectively.

The structure of this chapter is described below.

Section 6.1 introduces the different treatment protocols for the 8 groups.

Section 6.2 shows the results of the preliminary experiments which prove that the water loss during the experiment does not have significant influence on the results.

Section 6.3 shows the change of Mueller matrix parameters caused by plasma treatments of different power.

Section 6.4 shows the change of Mueller matrix parameters caused by plasma treatments for variable treatment time.

Section 6.5 compares the effect of plasma treatment and the effect of heating by a beam of light to the same temperature on LR and Δ.

Section 6.6 compares the effect of plasma treatment with the effect of the H_2O_2 solution.

Section 6.7 makes a general conclusion of this chapter.

6.1 Introduction to experiment protocols, groups

The treatment and measurement protocol is summarized in Figure 6.2. The experiments were performed between February 2021 and March 2022. First, each skin sample was taken out of the refrigerator and its mass m_0 was measured using an analytical balance with a precision of 0.1 mg. Right after, the "dry" sample was imaged using MPI. Then, it was soaked in Phosphate Buffered Saline solution (PBS 1×) for 30 minutes to set its temperature and moisture. Measurement of the mass m_s and MPI of each soaked sample were performed immediately afterward.

All analyzed samples were divided into eight groups, indicated by letters from A to H. Each sample was treated in a maximum of four different locations. After all treatments, mass measurements and MPI were performed again. For all plasma treatments mentioned below, the distance of the capillary outlet from the skin surface is 6 mm and the helium flow rate is 1 SLM.

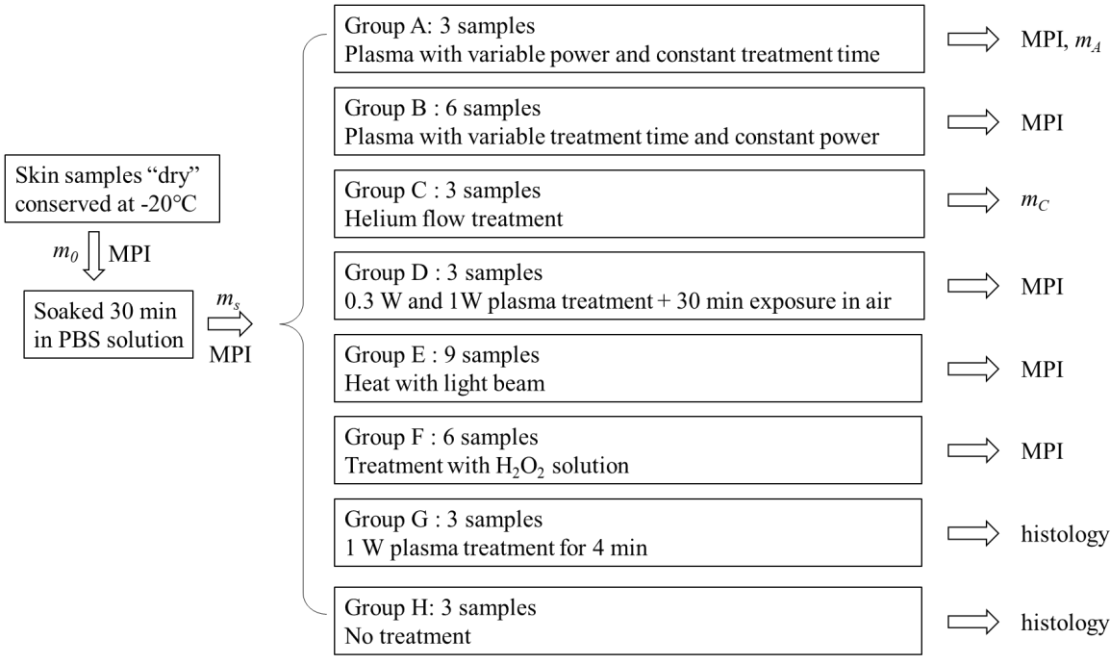

Figure 6.2 Summary of the experimental protocol, including plasma treatment, mass measurements, and Mueller Polarimetric Imaging (MPI).

The samples in Group A ($n = 3$) were treated with plasma at variable power and constant treatment time. On each sample, four different locations were irradiated for 4 minutes at 0.5, 0.8, 1, and 1.4 W, respectively.

The samples in Group B ($n = 6$) were treated with plasma at constant power and variable treatment time. In particular, 3 samples were treated with 1 W plasma jet for 0.5, 1 and 1.5 min in three different locations. In the same way, the other 3 samples were treated with 1 W plasma jet for 2, 4, and 6 min in three different locations.

The effect of the gas flow alone was investigated for the samples of Group C ($n = 3$). These samples were placed under the capillary with 1.0 SLM helium flow without any applied voltage. In these conditions, no plasma was formed. The exposure time (4 min) and the distance between the capillary and the skin (6 mm) were similar to those used for the experiments performed on the samples of Group A. Group C permits to control the water loss in the samples and determine the polarimetric effects it could induce.

In Group D ($n = 3$), each sample was treated in two different locations at 0.3 and 1 W, respectively, for 4 min. Skin modifications were investigated 5 and 30 minutes after irradiation to determine whether a delayed or progressive treatment effect occurred.

The effect of heating was explored in Group E ($n = 9$). The samples were illuminated with light from a halogen lamp (Olympus CLH-CS) for 4 minutes. Two convex lenses were used for focusing the light beam on the sample surface in order to illuminate a circular area of 2 mm in diameter, close to that irradiated by the plasma jet. The focused beam increased the local temperature to 43, 56, and 65 °C, depending on the chosen intensity of the light source. Thus, the maximum skin temperatures obtained in Group E are close to those induced by plasma-skin interaction under the different conditions considered.

The effect of H_2O_2 exposure was investigated only for samples within Group F ($n = 6$). Indeed, H_2O_2 is the one of the main reactive species produced by the plasma discharge. To determine the amount of H_2O_2 produced by the plasma during the treatment time, 5 mL of distilled water was exposed to a 1 W plasma jet for 4 min. The capillary exit was placed at a distance of 6 mm from the irradiated surface of the liquid sample. The total amount of H_2O_2 measured was about 280 nmol, according to the photometric method described hereafter. A reagent containing copper(II) ions (Sigma-Aldrich 1.18789) was added to the liquid sample, in which the H_2O_2 reduces the copper(II) ions to copper(I) ions and forms an orange colored complex. The absorption was measured at 433 nm with a photometer (Secomam Uviline 9100). In Groupe F, a 5.0 µL droplet of 0.2%v H_2O_2 solution was deposited on the pig skin using a micropipette. The droplet on the surface of the sample covers a circular area with approximately 2 mm diameter. The total amount of H_2O_2 in the droplet was 293 nmol, similar to that produced by the plasma jet. Three samples were exposed for 4 min and three others samples for 1 hour in only one location.

The samples in Group G ($n = 3$) were treated in the central zone with 1 W plasma jet for 4 min. The histological analysis of the irradiated area was performed for each sample after treatment. The protocol implemented for the histological analysis is described in detail below.

The samples in Group H ($n = 3$) underwent no treatment. The histological analysis of these samples was performed directly after soaking.

Histological sections of 5 µm thickness were cut from fixed paraffin-embedded porcine tissue. Then, they were deparaffinized in two changes of xylene and re-hydrated in two changes of

absolute alcohol, after which they were transferred into 70% (vol./vol.) and 30% (vol./vol.) alcohol. The sections were brought to water and stained with Masson's trichrome using Leica Bond III (Leica Biosystems, Nanterre, France). Bright field microscopy was performed using a Leica TCS SP5 confocal microscope.

6.2 Validation of experiment methods

6.2.1 Water loss and uptake during experiments

Since *ex-vivo* skin samples can dry out very quickly, it was essential to quantify the water loss during the experiments and assess its effect on the measurement of LR and Δ. First, let us see how we decide to soak the sample for 30 min before the treatment via a preliminary experiment (not shown in Figure 6.2). The mass of the skin sample is measured as a function of time. The skin samples are soaked in 1×PBS solution. After a certain amount of time, the skin sample is taken out of the solution. The water on the sample surface is gently removed with filter paper and the mass of the skin is measured. The relative mass increase with respect to the initial mass is plotted in Figure 6.3. The water uptake of the skin increase with soaking time until about 30 min, then remains stable. Therefore, the soaking time of the sample preparation is set to 30 min.

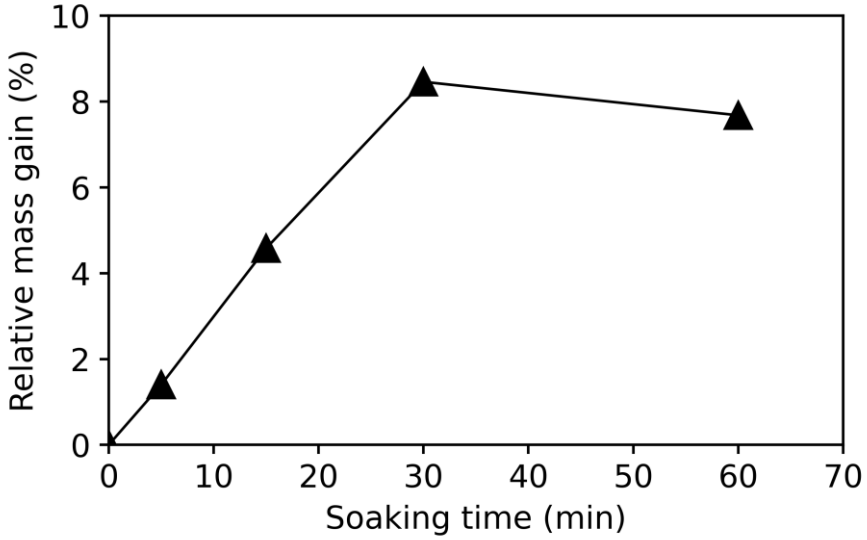

Figure 6.3 The percentage of defrost skin sample mass gain due to soaking in PBS solution as a function of the soaking time.

The samples in group A and group C (6 samples in total) are used to study the effect of soaking and plasma effect on the water uptake of skin. First, the mass is measured when the skin is taken out of the refrigerator. The mass of these "dry" samples taken out of the refrigerator is indicated as m_0. Then, the samples are soaked for 30 min and the mass is measured after

soaking. The mass of a sample after soaking is denoted as m_s. Then each of the 3 samples in group A is treated with plasma at four different locations for 4 minutes at 0.5 W, 0.8 W, 1 W, and 1.4 W, respectively. The samples in group C are treated with 1.0 SLM helium flow for the same time as group A without any applied voltage. The mass of a sample after treatment is denoted as m_A for group A and as m_C for group C. As a reminder, while as explained above. Figure 6.4 shows the measured value for mass compared between different groups. In particular, m_s, m_A, and m_C are normalized to m_0 for each sample.

The mass of the soaked samples increased on average by about 10% compared to that of dry samples ($p < 0.001$). The comparison between the group of soaked samples and Group C shows that about 3% of the mass loss is due to drying caused by the helium flow alone ($p < 0.05$), which is always present during plasma treatment. Furthermore, the comparison between Group C and Group A shows that plasma treatment alone contributes to an additional 3% mass loss ($p < 0.01$).

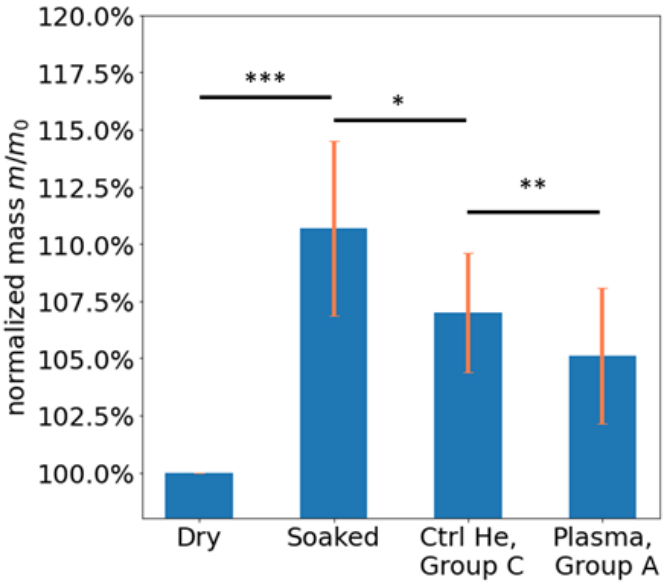

Figure 6.4 Normalized mass of dry, soaked, group C (control, treated by helium flow only for 16 min after soaking), and group A (plasma treatment after soaking with power of 0.5 W, 0.8 W, 1 W, and 1.4 W for 4 min each). The mass was normalized to the initial mass of the sample m_0 (dried).

6.2.2 Effect of water content of skin on linear retardance and total depolarization

MPI is performed before and after soaking. The intensity image (element M11 of the Mueller Matrix), lieanre ratardance (LR), and total depolarization (Δ) of one sample is shown in Figure 6.5. Not that it is not possible to compare pixel by pixel the images before and after plasma treatment or soaking, etc., because the samples have slight deformation due to treatment or water loss/gain. However, we can correlate the images before and after treatment according to the shape of the sample and the pattern of the sample surface. We can see visually that the

linear retardance slightly decreases due to the water uptake, while the total depolarization seems to decrease. However, the effect needs to be quantified.

In this research, the Mueller Matrix parameters are quantified in a selected ROI (region of interest). In the first step, the linear phase retardance LR and the total depolarization Δ were averaged over all pixels in a region of interest (ROI) selected for each sample. Then, the mean and the standard deviation of the mean values obtained for LR and Δ in the first step, within the ROI selected for each sample, were calculated for all samples treated under the same conditions.

Figure 6.5 compares, as an example, the unpolarized intensity images (I – II), as well as the LR (III – IV) and Δ (V – VI) images, for a representative skin sample before and after soaking. The ROI selected in the central area of the skin sample is marked by a white circle in Fig. 3(a)I. The edges of the skin sample were excluded from the ROI as they undergo accelerated drying compared to the central area.

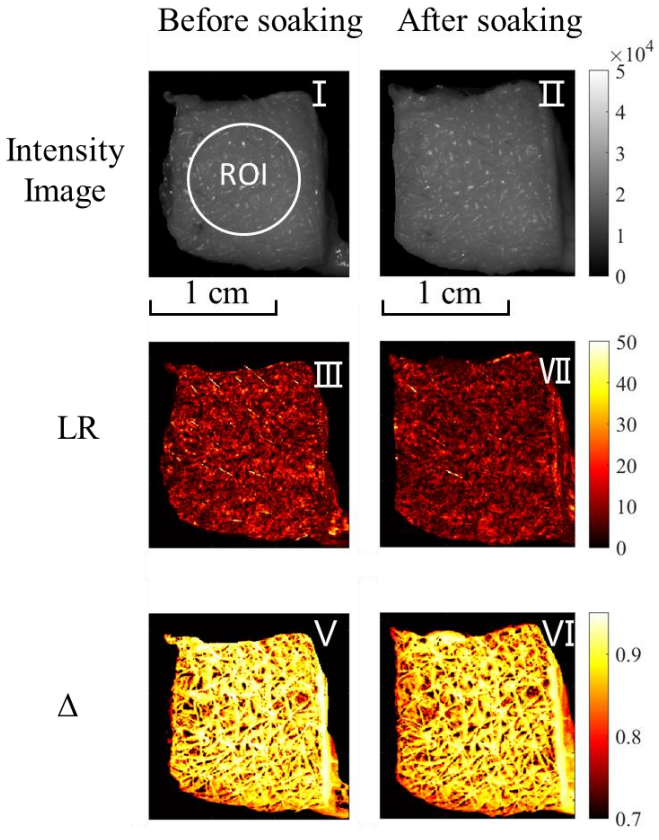

Figure 6.5 Image of non-normalized intensity (corresponding to the M11 coefficient of the measured Mueller matrix) in the first line, LR image in the second line, and Δ image in the third line for a skin sample before and after soaking in 1×PBS solution for 30 min, respectively.

Figure 6.6 shows the statistical comparison of LR between the group of dry skin samples and the group of soaked skin samples. Soaking significantly decreased LR ($p < 0.05$) by about 16%. The change in total depolarization Δ caused by soaking is not shown because it is non-significant ($p > 0.05$).

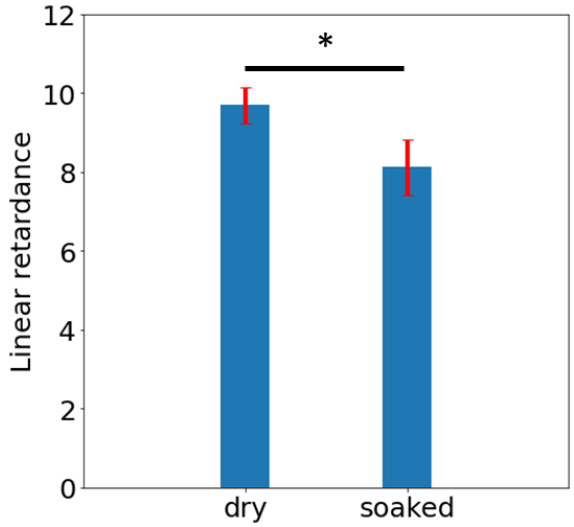

Figure 6.6 The average linear retardance in ROI (region of interest) of 3 pig skin samples (Group D) before and after soaking.

6.2.3 Increased skin temperature due to plasma treatment

The plasma treatment heats the skin. The temperature in the central area of 3 skin samples treated with 1.0 W plasma jet was monitored for 2 min, as shown in Figure 6.7. The temperature increased rapidly during the first 20 seconds and became stable after about 40 seconds for all samples. The temperature difference between the 3 samples was less than 2°C after 2 minutes. The final steady-state temperature was found to be dependent on the plasma power. Indeed, it reached 45°C, 55°C, 63°C, and 73°C with 0.5 W, 0.8 W, 1.0 W, and 1.4 W plasma jet, respectively (not shown).

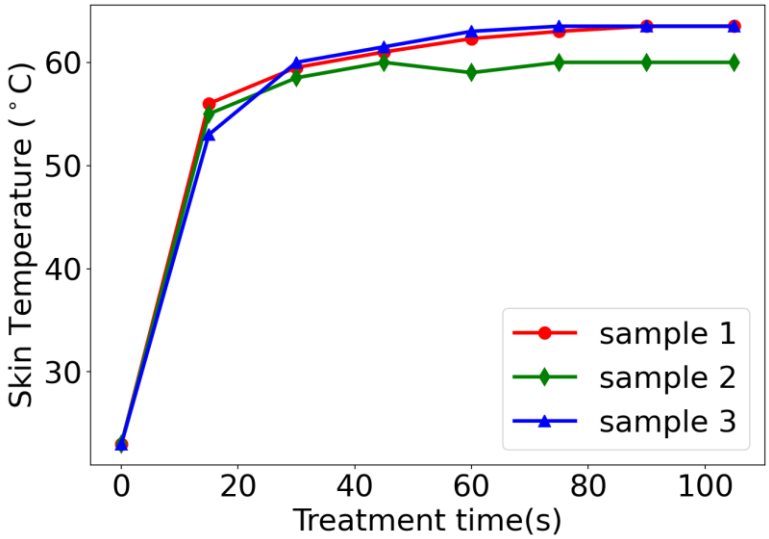

Figure 6.7 Maximum skin temperature in the area of 3 samples treated with plasma as a function of treatment time. The power of plasma is 1 W. Maximum skin temperature of the three samples in the plasma-treated surface with plasma as a function of treatment time, power $P = 1.0\,W$.

6.2.4 Modification of LR due to plasma treatment

After treatment, the skin is exposed to the ambient air during transport and measurement. Therefore, it is necessary to confirm that such exposure does not significantly affect the optical parameters of the skin samples.

Figure 6.8 shows the unpolarized intensity images (I – IV), as well as LR (V – VIII) and Δ (IX – XII) images of a skin sample treated for 4 min at locations A and B with a plasma jet of 0.3 W and 1 W, respectively (Group D). The treatment locations are marked with white circles in Figure 6.8-II. The maximum temperature, measured using the infrared camera, reached 35℃ and 63℃ in A and B locations, respectively. MPI was performed before the plasma treatment, then 5 min and 30 min afterward.

No notable changes were observed in the intensity-based images for both locations. In addition, no notable changes in LR and Δ were observed in A, treated with lower power plasma (0.3 W). In contrast, 1 W plasma treatment in B produced observable changes in LR and Δ within a circular area, as shown in Figure 6.8 VIII and XII, respectively.

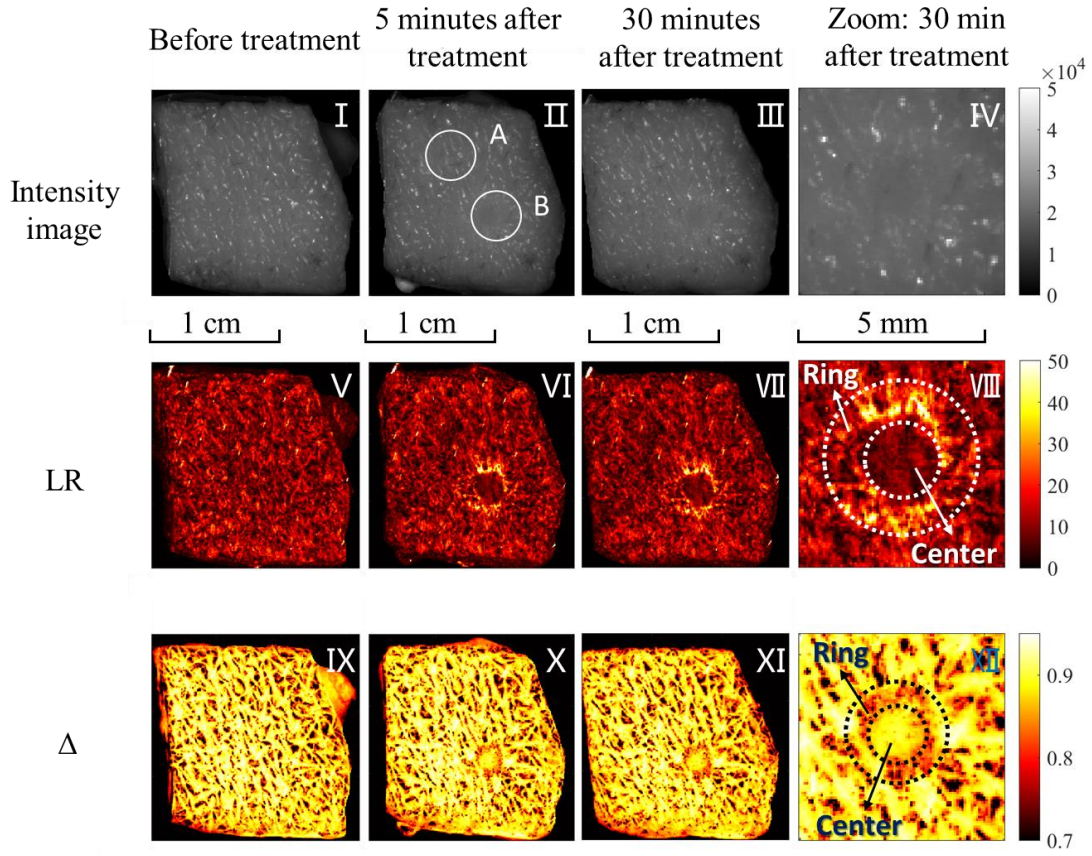

Figure 6.8 Intensity image, linear retardance (LR), and total depolarization (Δ) of a skin sample before treatment, 5 min and 30 min after treatment. Location A and B, marked as a white circle in II, were treated with 0.3 W and 1 W plasma for 4 min, respectively. The skin reached a maximum temperature of 35℃ and 63℃.

Two different zones, delimited by two concentric circles, can be clearly observed for LR and Δ parameters. In particular, the innermost circle enables to delimit the central area, which is different for both parameters compared to the surrounding ring area. As the spatial pattern produced by the plasma treatment was not perfectly identical for LR and Δ, the diameters of the concentric circles were selected independently for these two parameters, as shown in Table 6.1.

Table 6.1 Diameter of the circles delimiting the center and ring area for LR and Δ. Groupe D (n=3).

Diameter ± SD	Innermost circle	Outermost circle
LR	$1.8 \pm 0.9\ mm$	$3.7 \pm 0.7\ mm$
Δ	$1.2 \pm 0.6\ mm$	$2.3 \pm 0.8\ mm$

The diameter of the innermost circle is 44 % smaller for Δ than LR. Similarly, the diameter of the outermost circle is 48 % smaller for Δ than for LR.

The central circle selects an area where LR is significantly lower compared to the surrounding ring area after plasma treatment, as shown in Figure 6.8-VIII. On the other hand, the ring selects an area where LR after treatment is significantly higher compared to the untreated area. Figure 6.9(a) shows quantitatively that after plasma treatment, the LR in the ring area is significantly higher than the LR in the center area ($p < 0.001$).

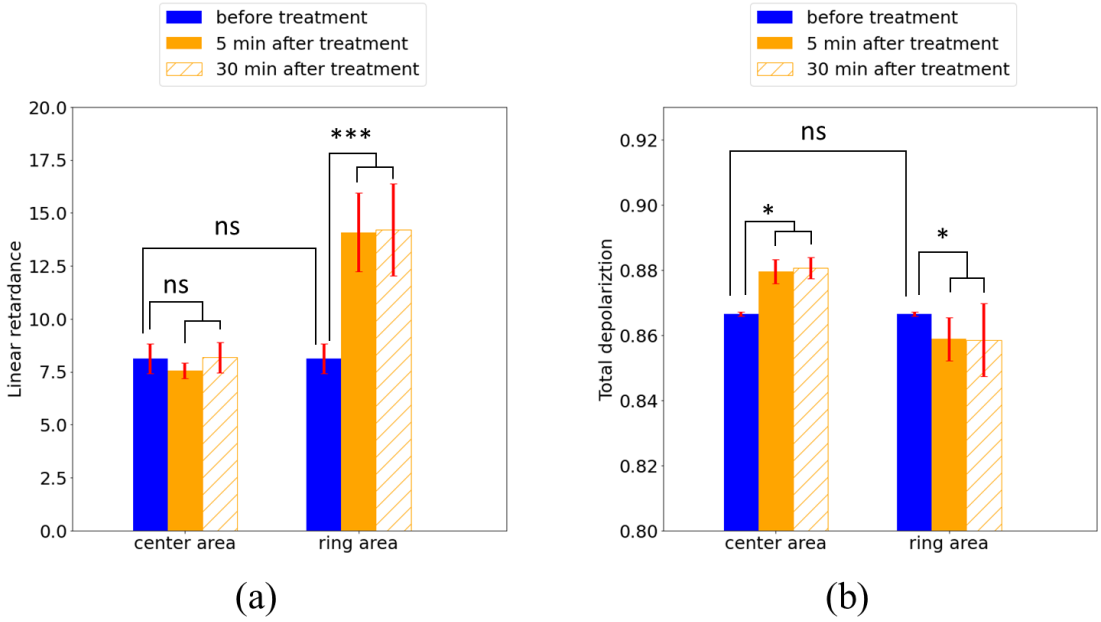

Figure 6.9 (a) The average linear retardance in the center and ring areas before and after treatment. (b) The average total depolarization in the center and ring areas before and after treatment. The values are measured in an ROI treated by 1 W plasma (63°C) for 4 min (location B shown in Figure 6.8).

The value of Δ decreases within the selected ring, compared to the untreated skin, as shown in Figure 6.8-XII. The central circle selects a region where Δ is more homogeneous than in untreated skin and higher than in the area contained within the surrounding ring. Figure 6.9(b) shows quantitatively that after plasma treatment, the Δ value in the selected ring area is significantly lower than the Δ in the center and untreated area $p < 0.05$).

For group D, Δ seems to slightly increase after plasma treatment compared to before treatment as shown in Figure 6.9(b). However, in this case, it is difficult to verify whether this difference is significant by having a *p*-value close to 0.05 ($p = 0.048$). Nevertheless, considering all 12 samples of groups A, B and D, it was observed that the increase of Δ in the central area due to plasma treatment is in most cases negligible compared to the untreated area ($p > 0.05$).

The LR and Δ images acquired 5 and 30 minutes after treatment did not show visible differences, as can be seen in Figure 6.8. The average value of LR and Δ was calculated for the ring and the central area in location B. Between 5 min and 30 min, the difference in LR and Δ is non-significant ($p > 0.05$) for both the center area and ring area, as shown in Figure 6.9. These results prove that all the modifications observable with MPI occur instantly after

treatment. In particular, the slight drying of the skin or possible delayed/gradual effects of plasma treatment do not contribute to the changes in polarimetric properties.

Finally, it should be noted that the changes in linear phase retardance previously described for soaking is minor compared to those caused by plasma treatment.

With a plasma power of 0.3 W (35 ℃) no modifications of MPI parameters are detected. At 1 W (63℃), the plasma treatment induces a ring-shape pattern on LR (linear retardance) and Δ (total depolarization). In the edge of the treated area ("ring" area), LR increases after treatment. In the center of treated area, LR decreases, Δ becomes more homogeneous. The water loss caused by the NTP treatment is small, and causes a negligible effect on LR and Δ. The values of LR and Δ remain stable after the treatment.

6.2.5 Histology of the skin sample

The effect of plasma treatment was visualized using histology of the skin sample and the results are shown in Figure 6.10. The samples shown in Figure 6.10(a-c) are three non-treated pig skin samples. The samples shown in Figure 6.10(d-f) are treated by the plasma for 4 min with a plasma power of 1 W, heating the skin surface up to 63°C. The stratum corneum, epidermis, and dermis are visualized and marked in Figure 6.10. After treatment, collagen fibers (stained in green) are rearranged in a more compact way, possibly due to shrinkage of skin tissue. The collagen fibers also show greenish discoloration caused by the treatment. Red staining is observed in the treated sample in the dermis layer, and is possibly due to collagen denaturation. The change in collagen fibers is similar to the collagen change in *ex vivo* porcine skin model or human skin model caused by moderate burn reported in previous studies [181–185]. Note that the defrost skin samples used in this experiment are not in culture media, and that the time laps between the NTP treatment and MPI analysis is less than 30 min. Hence, no metabolism is expected to take place in the experiment and the greenish discoloration cannot be interpreted as new collagen production.

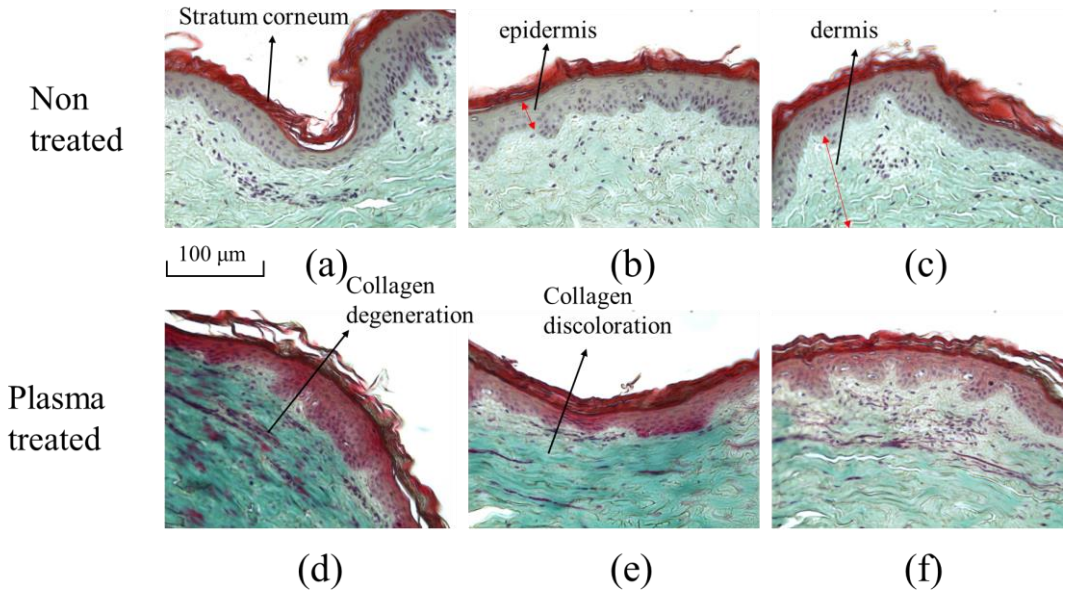

Figure 6.10 Histology of the skin samples. (a-c) non-treated (group H) and (d-f) treated by plasma in the center of the treated area with a power of 1 W (63°C) for 4 min (group G). The size of each photo is 305 μm × 230 μm.

6.3 Effect of plasma power on LR and *Δ*

To evaluate the effect of plasma power on the variation of linear retardance and total depolarization, samples are treated with power ranging from 0.5 W to 1.4 W.

Figure 6.11 shows the MPI of a pig skin sample treated in locations A, B, C, and D (white circle shown in Figure 6.11 II) at 0.5 W, 0.8 W, 1 W, and 1.4 W, respectively, for 4 minutes each (group A). The effect of plasma treatment was barely observable in the unpolarized intensity images for all plasma powers, as shown in Figure 6.11 (I – II). Moreover, the 0.5 W plasma treatment produced no noticeable changes in LR and Δ images, as shown in Figure 6.11 (III – IV) and Figure 6.11 (V – VI), respectively. In contrast, MPI showed that the plasma effect became more evident and affected a larger area with increasing the treatment power.

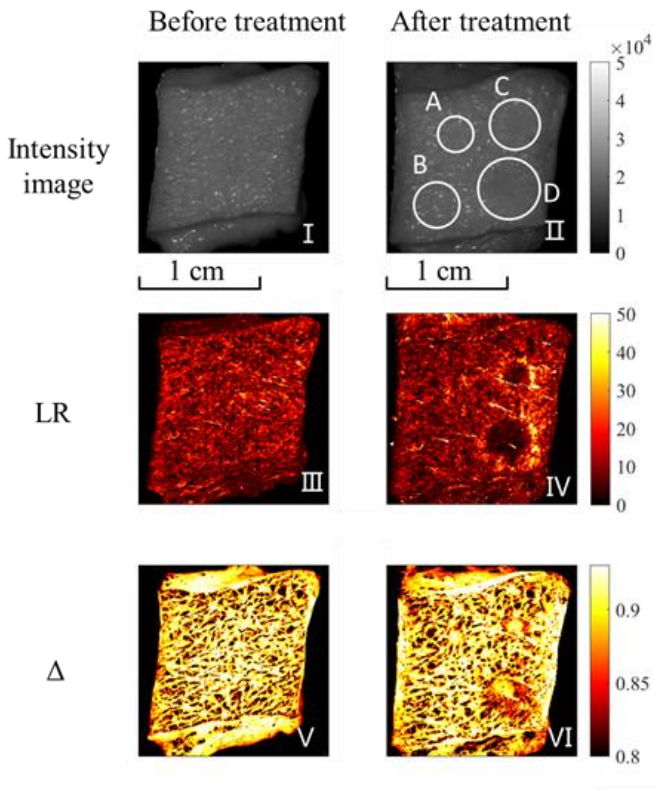

Figure 6.11 : Variable plasma power and constant treatment time (Group A). Intensity-based image, linear retardance (LR), total depolarization(Δ) of a representative skin sample before and after plasma treatment. The plasma power was 0.5 W, 0.8 W, 1 W, and 1.4 W for locations A, B, C, and D, respectively. The treatment time was 4 min.

Figure 6.12(a) shows the area bounded by the central circle for LR as a function of plasma power. In particular, the plasma power is expressed as a function of the maximum temperature reached by the skin in the treated zone. Indeed, the maximum temperatures of 45°C, 55°C, 63°C and 73°C, correspond to power levels of 0.5 W, 0.8 W, 1 W and 1.4 W, respectively.

As the plasma power increases, the central area in which LR decreases, with respect to the surrounding ring area, becomes larger. Figure 6.12(b) shows the evolution of the mean value (μ_{LR}) of LR as a function of temperature in the central and annular region. The "control" curve is the mean value of LR for the untreated skin.

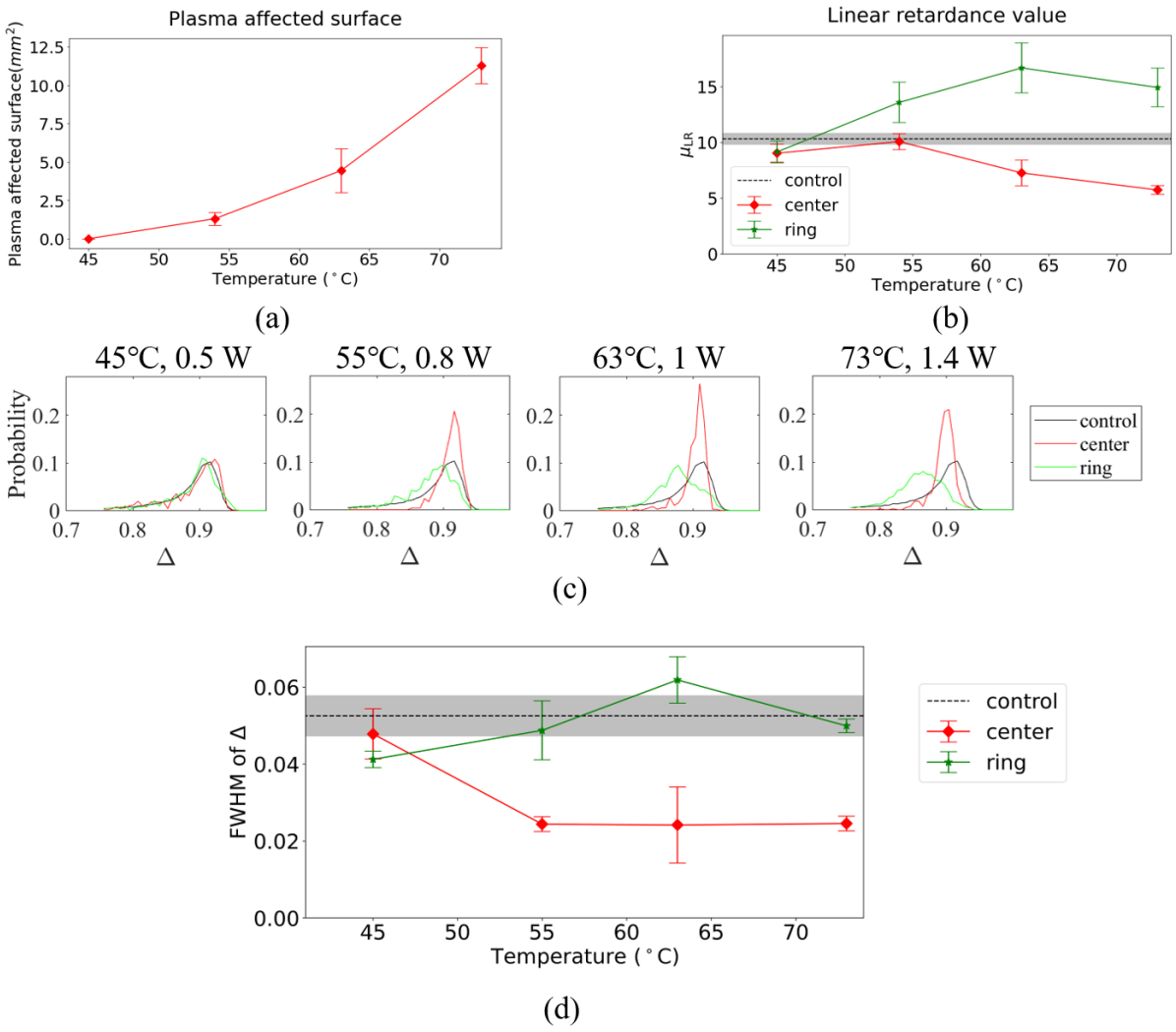

Figure 6.12 Variable plasma power and constant treatment time (Group A). Treatment time: 4 min. The plasma power was 0.5 W, 0.8 W, 1.0 W, and 1.4 W leading to the maximum final temperature of 45°C, 55°C, 63°C, and 73 °C. (a) Area of the "center area" for LR in mm². (b) Average LR in the center, ring, and control area (untreated skin). (c) Probability distribution of the pixels according to Δ for a representative skin sample. (d) Average FWHM of the Δ probability distribution as a function of the maximum temperature reached. The error bars are the standard deviation on all the samples treated with a given power ($n = 3$). The value of the control is measured before the treatment and is indicated with black dash line. The standard deviation is shown with the gray area.

The value of LR significantly decreased in the central area compared to untreated skin as the power was increased from 0.5 W (45°C) to 1.0 W (73°C). Similarly, LR significantly increased in the ring area with increasing power. The ANOVA test shows that the decrease in LR with power is statistically significant ($p < 0.01$) in the central area. Similarly, the increase in LR with power is also statistically significant ($p < 0.0001$) in the ring area.

The variation in the mean value of Δ with increasing plasma treatment power was non-significant ($p > 0.05$) for the central and ring areas (not shown). However, the probability distribution shape of Δ changed significantly between central and ring areas, as well as between

them and the untreated skin, as shown in Figure 6.12(c). Indeed, the distribution of Δ in the central area becomes narrower with increasing plasma power. On the contrary, it slightly varies in the ring area. Figure 6.12 (d) shows the evolution of the full width at half maximum (FWHM) for the probability distribution of Δ as a function of maximum temperature after plasma treatment both for the central area and the ring surrounding area. In the central area, the FWHM decreases significantly ($p < 0.001$), showing that Δ becomes more spatially homogeneous. On the contrary, the variation of the FWHM within the annular zone is non-significant ($p > 0.05$).

6.4 Effect of plasma treatment time on LR and Δ

The dose of plasma treatment also depends on the treatment time. In this section, we study the effect of plasma treatment time on the variation of linear retardance and total depolarization. Accroding to figure 6.7, the skin temperature is stable after 20 s treatment, so the treatment time range in this study is 30 seconds to 6 min. The plasma power is 1 W, and the skin surface is heated to 63°C during the treatment. 6 samples are used in this experiment (Group B). For 3 of the samples, 3 location on the samples is treated for 0.5 min, 1 min and 1.5 min, respectively. For the other 3 samples, 3 location on the samples is treated for 2 min, 4 min and 6 min, respectively. Mueller matrix is measured before and after treatment.

Figure 6.13 shows the unpolarized intensity images (I – II), as well as the LR (III – IV) and Δ (V – VI) images of a representative sample treated for 2, 4, and 6 min in the areas indicated as A, B, and C, respectively. As before, the unpolarized intensity images barely visualize the treated locations. In contrast, the LR and Δ images show that the extension of the area modified by the irradiation becomes more prominent with increasing treatment time.

Figure 6.14(a) shows that the area contained in the central circle becomes larger with increasing treatment time. In particular, it is observed that it increases monotonously with treatment time. Moreover, it can be larger than the area effectively in contact with the plasma jet (about 3.1 mm^2).

Figure 6.14(b) shows that the the mean value (μ_{LR}) of LR increases for the ring and decreases for the central circle with increasing treatment time. However, the greater change in LR occurs before 2 min. Indeed, the LR remains quite stable after 2 min, within the limits of the error bars. The ANOVA test showed that the effect of treatment time on LR is statistically significant both for the central area ($p < 0.05$) and for the ring area ($p < 0.001$).

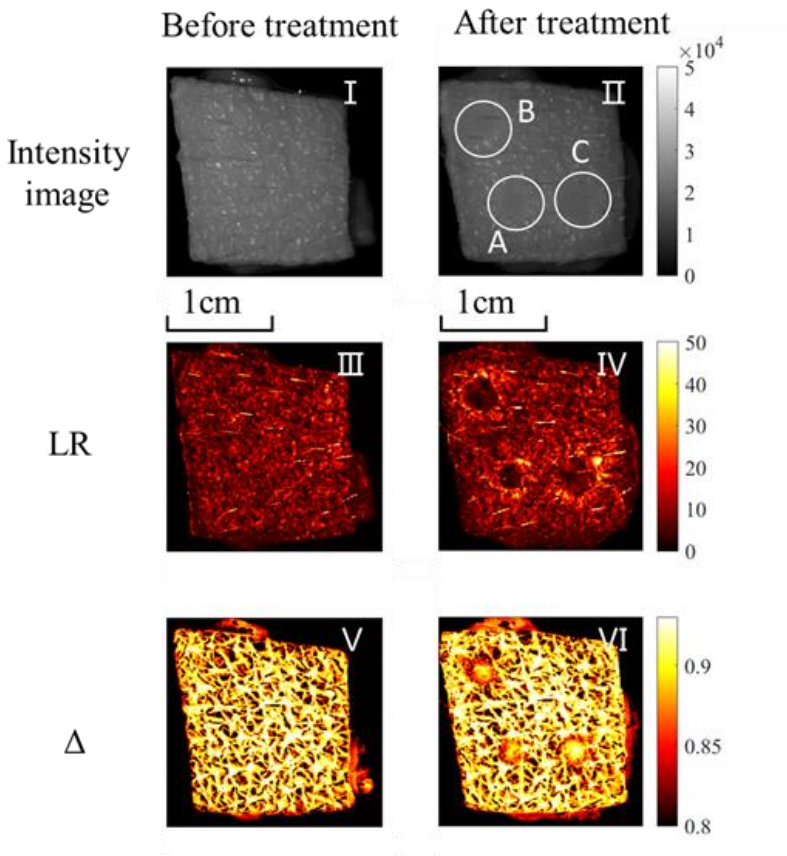

Figure 6.13. Variable plasma treatment time for constant power (Group B). Intensity-based image, linear retardance (LR), total depolarization(Δ) of a skin sample before and after treatment. The treatment time was 2 min, 4 min, and 6 min for A, B, and C, respectively. The plasma power was 1 W. The surface reached a maximum temperature of 63°C at each location.

The change in the mean value of Δ was non-significant ($p > 0.05$) for the central and ring area (not shown). However, also in this case, the probability distribution shape of Δ changed significantly between central and ring areas, as well as between them and the untreated skin. Figure 6.14(c) shows that the distribution of Δ in the central zone becomes narrower with increasing treatment time. On the contrary, it seems to slightly change in the ring area.

Figure 6.14(d) shows the evolution of the FWHM for the probability distribution of Δ as a function of treatment time both for the central area and the ring surrounding area. In the central area, the FWHM decreases significantly ($p < 0.05$), showing that Δ becomes more spatially homogeneous. In particular, the FWHM strongly decreases up 2 min, whereas it remains relatively constant over a longer treatment time. On the contrary, the modification of the FWHM in the ring area is non-significant ($p > 0.05$).

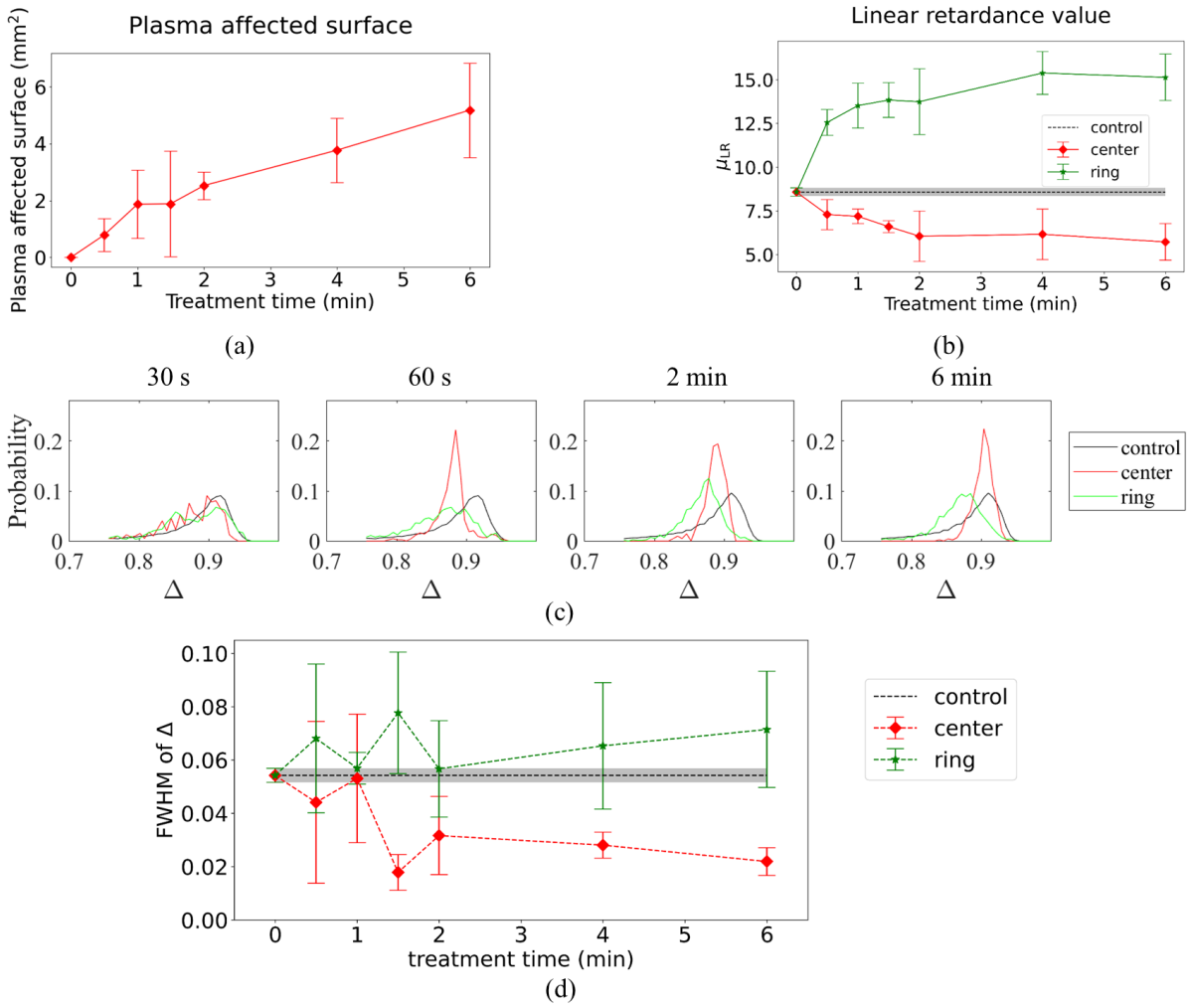

Figure 6.14 Variable plasma treatment time for constant power (Group B). (a) area of the "center area" for LR. (b) Average value of LR in the center, ring, and control area (untreated skin) as a function of the treatment time. (c) Probability distribution of the pixels according to Δ for a representative skin sample. (d) Average FWHM of the Δ probability distribution as a function of the treatment time. The error bars are the standard deviation on all the samples treated for a given time ($n = 3$). The plasma power was 1 W. The surface reached a maximum temperature of 63°C at each location. The value of the control is measured before the treatment and is indicated with black dash line. The standard deviation is shown with the gray area.

It has been shown that, depending on the power conditions ranging from 0.3 W to 1.4 W, the temperature of the treated skin varied from 35°C to 73°C after 4 min treatment. Plasma irradiation significantly increased the local temperature of the treated area compared to the room temperature. The increase in temperature is known to lead to dehydration of skin tissue. However, the exposure of the skin to the air revealed that the water loss due to the evaporation at room temperature is very small, as shown in Figure 6.4. This small water loss only results in a slight overall increase of LR as shown in Figure 6.5 and Figure 6.6. Meanwhile, increasing the power of plasma jet and treatment time significantly decrease the LR in the center of the

treated area. Thus, although the plasma effect is primarily caused by the heating, it is unlikely that it is due to the water loss of skin tissue.

A substantial increase in tissue anisotropy is observed not only in the directly irradiated part, but also over a larger area as the NTP dose increases. The widening of central area for LR suggests that the reduction of this parameter is likely heat-induced, as the part of the skin exposed to damaging temperature increase due to heat transfer. The heated area may show a reorganization of fibrous structures, such as collagen fibers, on a microscopic scale, as shown in Figure 6.10. The increase in LR in the annular zone can be caused by the presence of fibrous microstructures reorganized by the mechanical stresses produced by the treatment. More specifically, the heated area may shrink. Thus, the fibrous structures of the skin located at the edges of the heated area may be pulled towards the center.

As we increase the plasma power and treatment time, the NTP effect on LR(linear retardance) and Δ (total depolarization) increases. A maximum effect on LR and Δ can be achieved when the plasma power exceeds 1 W (63°C) and when the treatment time exceeds 2 min.

6.5 Heating is the main contribution to the observed changes in MPI compared to H_2O_2 local effect.

The mechanism of plasma influence on living tissues have been widely investigated in different types of medical applications. The interaction between plasma and skin includes the heating effect, production of reactive oxygen and nitrogen species, energetic electrons and ions, electric field, etc. In this study, experiments are designed to study the effect of heating and RONS separately. In this section we will show the effect of heating.

Two experiments were performed to elucidate the effect of temperature and H_2O_2 on the polarimetric properties of pig skin. Indeed, the exposure to plasma irradiation generates heat and H_2O_2 on the skin.

The pig skin samples were heated by a light beam for 4 min to investigate the temperature role on the tissue modifications (Group E). The focused light beam increased the local temperature to 43, 56, and 65 °C, reproducing the thermal conditions observed in Group A (variable power and constant treatment time) using 0.8, 1.0, and 1.4 W plasma jet, respectively. The FWHM of the light distribution (about 2 mm) was close to the diameter of the plasma-treated surface.

Figure 6.15 shows the unpolarized intensity images (I – II), as well as the LR (III – IV) and Δ (V – VI) images of a representative skin sample before and after being heated to 65°C. As before, the unpolarized intensity images barely visualize the treated locations. In contrast, the focused light beam produced observable changes in LR and Δ within a circular area, as shown in Figure 6.15 IV and VI, respectively.

In particular, the spatial patterns in LR and Δ images produced by the focused light beam are similar to those produced by the plasma treatment in different conditions. Indeed, also in this case, two different zones, delimited by two concentric circles, were clearly observed in LR and Δ images.

The average values of LR were measured in the central area and in the surrounding ring area. Figure 6.16 shows the evolution of the mean value (μ_{LR}) of LR as a function of temperature for the light-treated (dotted lines) and plasma-treated (solid lines) skin. No significant difference was observed for these two groups ($p > 0.05$) both for central and surrounding ring area. This result suggests that the thermal component of the 1.0 W plasma treatment plays a predominant role in modifying the polarimetric properties of pig skin.

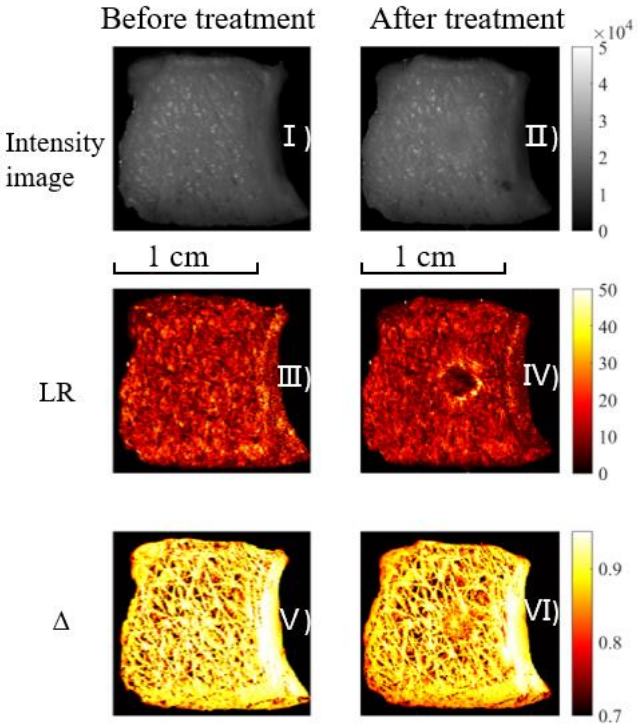

Figure 6.15: The intensity image, LR and Δ of a skin sample before and after treatment. It is treated in the center by the focused light beam for 4 min, which heats the surface to 63°C.

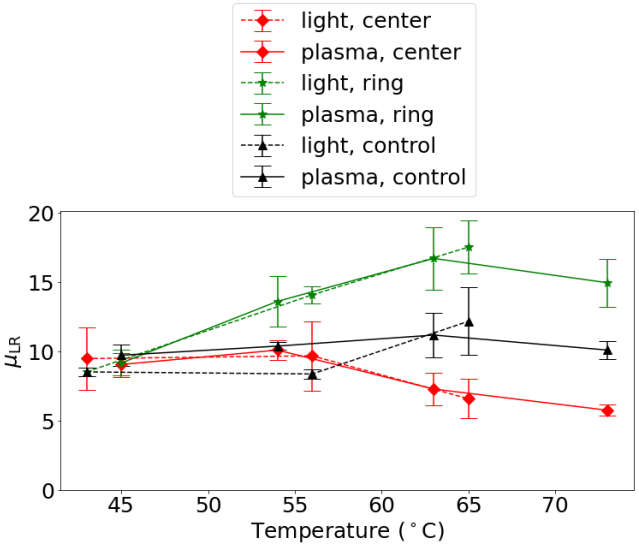

Figure 6.16: The curve of LR mean value in the center(red) and ring area(green) of skin samples treated by light (dash lines) or by plasma (solid lines) for 4 min. The black curves represent the LR of corresponding area before treatment.

6.6 Effect of H_2O_2 is negligible

Reactive oxygen species(ROS) are considered to have significant effects on the metabolism of living tissues. In order to address the effect of ROS on pig skin, the pig skin samples were exposed to H_2O_2 (0.02%v) droplets for 4 min and 1 h (Groupe F). This experiment was conducted to determine whether the one of the main RONS produced by the plasma, in particular H_2O_2, could also affect the polarimetric properties of the skin. The MPI revealed that no noticeable effects can be observed, as shown in Figure 6.17. Thus, the amount of H_2O_2 produced by the plasma jet does not affect the polarimetric properties of the skin. This lack of effects is observed on non-living tissues on a timescale of 30 min time scale. In the present work, the skin samples are defrosted and not placed in culture medium. Hence, the obtained results do not contradict the numerous previous publications showing that the RONS produced by plasma have many biological effects *in-vivo* and *in-vitro.* Moreover, the concentration of H_2O_2 in the droplets is small and corresponds to the amount of H_2O_2 molecules produced by an equivalent plasma treatment on a liquid surface. It is possible that a higher concentration of H_2O_2 would lead to skin modifications.

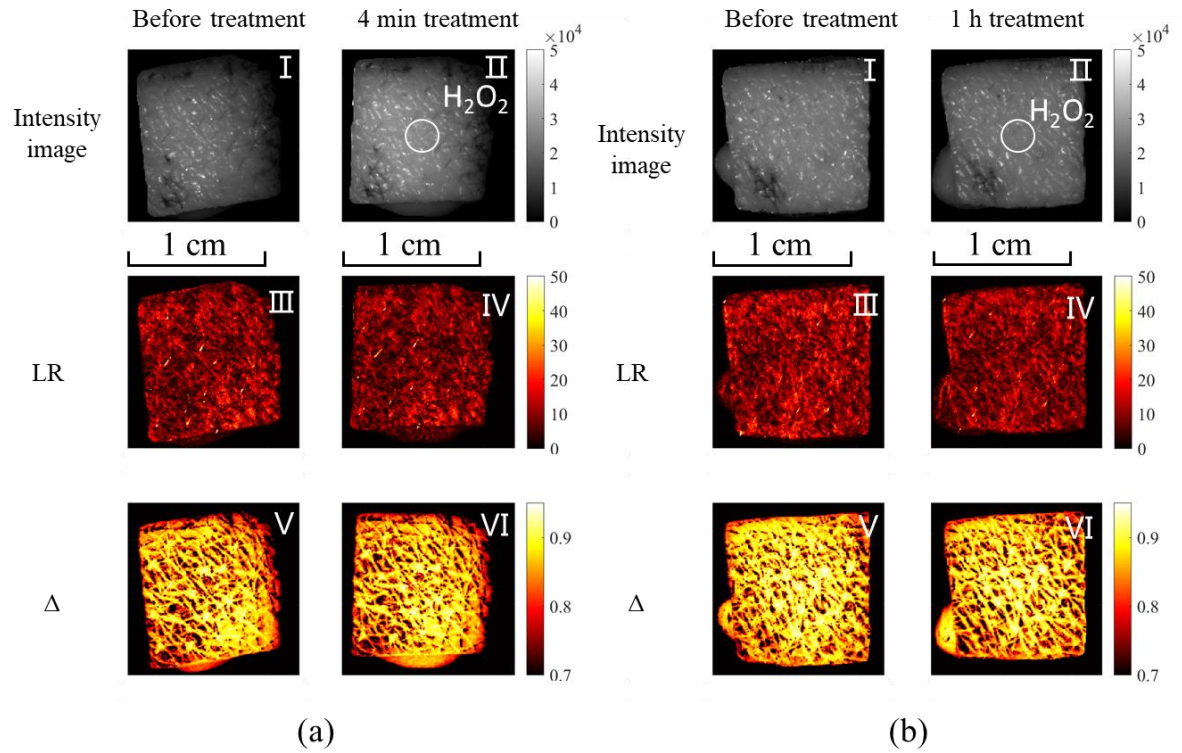

Figure 6.17: MPI of two representative skin samples exposed to H_2O_2 (Group F). Intensity-based image, linear retardance (LR), and total depolarization (Δ) of skin samples before and after treatment with 0.2% H_2O_2, 5 µL droplet. The exposure time was 4 min (a) and 1 h (b).

Thermal treatment and plasma treatment show similar effect on on the linear retardance and the total depolarization. On defrost inert skin, H_2O_2 produced by the plasma does not seem to modify the microstructure of the pig skin, possibly due to the lack of cell metabolism . Hence the short time effect effect of plasma treatment of the inert skin sample is mostly due to thermal effects and no effect is detected at 0.3 W / 35 C.

6.7 Conclusion

In this chapter, Mueller Polarimetric Imaging is used to analyzed effects of Non-Thermal Plasma 10~30 min after treatment of defrost pig skin samples. The aim is to show how MPI can be used to evidence skin microstructure modifications caused by NTP treatment. NTP power and treatment durations have been varied. In addition, heat treatment and H_2O_2 treatment have been performed to identify key parameters responsible of skin microstructure modifications.

1) MPI parameters such as Linear Retardance and Depolarization of the treated skin area are modified depending upon the plasma power. Under mild NTP conditions and temperature of 35°C which is often required for wound healing, no MPI parameters are not modified.

Modifications appear from 45°C (0.5 W) and increase continuously up to 73°C (1.5 W). Such high-power NTP is often used to induce tumor death.

2) Part of these modifications may be attributed to the heating of the skin sample and denaturation of collagen fibers.

3) Conversely, chemical treatment using H_2O_2, does not show any effect on polarimetric properties. On inert skin sample, such a small quantity of chemical species does not likely induce any change in the skin microstructure.

Mueller polarimetric imaging could be a breakthrough technology for the non-invasive and real-time investigation of the structural modifications of the skin occurring in the development and treatment of pathologies such as skin cancers, blood coagulation wounds, and burns. RONS are considered to play an essential role in many biomedical processes such as the production extracellular matrix or angiogenesis. As a next step, instead of defrost inert skin, MPI could also be used to monitor the effect of NTP treatments on tissue metabolism and production of collagen in living tissues in *in-vivo* or *ex-vivo* studies.

General conclusions

In recent years, numerous researchers focused on Atmospheric Pressure Plasma Jet (APPJ) due to its great potential for applications in biomedical fields. It has been used for wound healing, dermatology, cancer treatment, etc. The objective of the thesis is to study the physics of propagation of APPJs which are typically designed for medical applications, and their interaction with liquid or skin targets.

The APPJ used in this thesis has a glass capillary with an inner diameter of 1 mm. A needle-like internal powered electrode or ring-like external powered electrode are used for different purposes. The plasma is mostly generated with an AC voltage of 10~18 kHz. Electrical and optical diagnostic methods are combined to study the physics of propagation. The production of H_2O_2 in plasma-activated water (PAW) is measured under different conditions. The microstructural modifications to the skin caused by APPJ treatment are evaluated with Mueller Polarimetric Imaging. The main results are summarized below.

In chapter 3, random vs multi-periodic plasma bullets have been studied in order to address the dynamic of formation of such multiperiodic mode. An helium APPJ with a needle-like powered electrode driven by 15~18 kHz sinusoidal voltage, the discharge exhibits multi-periodic behavior and random behavior depending on the driving voltage, driving frequency, and gap distance. The multi-periodic mode is a self-triggered mode that generates ionization waves—bullets —with a jitter of less than 100 ns, similar to the pulsed mode condition. In multi-periodic mode, negative and positive plasma bullets are initiated every 2, 3, or more periods depending upon working conditions. Negative bullets always immediately precede positive ones. Such multi-periodic bullets are observed only when a ground electrode is located 20 mm away or more from the HV pin electrode.

During cycles when no bullets are ignited, positive and negative gap discharges are observed. The gap discharges are similar to self-triggered dielectric barrier discharges. It is assumed that such gap discharges result in a surface charge accumulation in the gap region, particularly in the vicinity of the ground electrode. This local charge accumulation leads to an electric field enhancement near the ground electrode and the generation of a fast-traveling bullet. Bullets of different periodic modes show small differences in terms of velocity, propagation length, and optical emissions. Our results are consistent with the literature where the surface residual charges or volumetric residual charges are considered to be the main factor that influences the periodicity of plasma ignition in DBDs.

It is proposed that in multi-periodic modes, the backward propagating ionization waves during the negative cycle trigger the discharge sequences that finally lead to the ignition of plasma bullets. Yet, the mechanism of this backward discharge is not fully understood and requires more experimental or numerical research.

The comparative study with a DC-pulsed APPJ shows that the propagation velocity is mainly related to the instantaneous applied voltage for both AC and DC driven APPJ. The charge accumulation at the ground electrode contributes to about 30% of the propagation length. Unfortunately, the pulsed DC generator was acquired near the end of my Ph.D. and some more investigations in order to compare AC / pulsed DC would provide fruitful information.

Time-resolved optical emission spectra at different locations and voltages show that the variation of operating conditions significantly changes the ratio between the helium emission and the OH(A-X) emission. Most of the OH emission comes from the glow-like discharge in the gap region after the plasma bullet formation. The increase of OH emission in the glow-like discharge is attributed to the enhanced Penning ionization.

The time-resolved optical emission spectroscopy shows that the plasma bullets and the following glow-like discharges have significantly different spectrums. However, in AC mode such time-resolved OES (optical emission spectroscopy) is only possible in the limited stability domain of multiperiodic regime. Studying the glow-like discharge with a pulsed power supply is a possible approach even though the glow-like discharge seems weaker than in an APPJ powered by an AC power supply. On the other hand, a simulation of the chemical kinetics during the glow-like discharge may help in understanding the formation of OH radicals and H_2O_2.

In Chapter 4, in order to study the plasma ignition with a higher electric field, an inter-electrode gap distance of 5 mm is used, and the APPJ exhibits mostly random mode. Two kinds of propagation modes have been evidenced: i) slow bullets, which are stable and repeatable; 3 slow bullets are ignited in each positive cycle with consecutively increased length. ii) On the other hand, fast bullets propagate about 10 times faster and 3 times further. They show randomness in many parameters including the velocity, length, and ignition time, which is attributed to multiple random small discharges in the source region, but they are still statistically predictable. Generally, the number of fast bullets increases with the applied voltage. The randomness of the fast bullets may be due to the higher volumetric charge density before the ignition of fast bullets than slow bullets. However, it is unclear due to the lack of literature. Surface charges also have a significant influence on the propagation of a random plasma jet. ICCD (intensified charge-coupled device) imaging and streak camera imaging reveal light intensity increases during propagation. This is attributed to the transition between a positively charged surface and a negatively charged surface.

The slow bullets have similarities to the gap discharges shown in chapter 3 in terms of velocity and length. However, due to the short gap distance and the limit of spatial resolution, the propagation of slow bullets in the 5 mm gap region was not observed. More observation with the streak camera could be performed while focusing on the propagation of plasma in the 5 mm gap region.

In chapter 5, we focused on a plasma/water target interaction using a slightly different jet with a ring-like powered electrode instead of a pin electrode; multi-periodic modes are observed under some conditions similar to what has been described in Chapter 3. An upstream plasma is observed before the ignition of the downstream plasma jet. The downstream propagation length decreases when the upstream propagation length extends. A water target slightly changes the voltage range of the multi-periodic modes. The amount of charges deposited to the water target is in the range of 1.5 ~ 3 nC. Comparative studies indicate that H_2O_2 in the PAW (plasma-activated water) is mainly produced by plasma inside the tube, which is in agreement with the OES measurement in APPJ with a need-like powered electrode.

Knowing that the H_2O_2 mainly comes from the impurities inside the tube, it should be possible to adjust the H_2O_2 production rate by mixing water vapor with the helium gas and this is a promising approach for biological applications.

In Chapter 6, we focused on the plasma-skin interaction with an APPJ with an external -ring-like powered electrode and evaluated the effect on the skin microstructure using Mueller Polarimetric Imaging (MPI). The originality of our approach is to focus on the short-term (30 min) physical-chemistry effect of a plasma treatment rather than on a biological effect. For this an inert defrost pig skin sample is treated by an APPJ driven by a 10 kHz sinusoidal voltage, MPI parameters such as Linear Retardance and Total Depolarization of the treated skin area are modified depending on the plasma power. Under mild NTP conditions and a temperature of 35°C which is often required for wound healing, no MPI parameters are modified. Modifications appear from 45°C (0.5 W) and increase continuously up to 73°C (1.5 W). Such high-power NTP is often used to induce tumor death. Using a parametric approach where skin samples are treated by heat only or H_2O_2 only, we could attribute part of these modifications to the heating of the skin sample and the denaturation of collagen fibers. Conversely, chemical treatment using H_2O_2 does not show any effect on polarimetric properties. On inert skin samples, such a small quantity of chemical species does not likely induce any change in the skin microstructure.

As a perspective, it will be interesting to treat *in-vivo* or *in-vitro* skin samples with NTP to observe if NTP can induce a microstructural modification that can be observed by MPI. Because in such conditions, the cell metabolism process is maintained and RONS can play a role.

References

[1] Hippler R, Pfau S, Schmidt M, Schoenbach KH. Low Temperature Plasma Physics: Fundamental Aspects and Applications. 2001.

[2] Kakiuchi H, Ohmi H, Yasutake K. Atmospheric-pressure low-temperature plasma processes for thin film deposition. Journal of Vacuum Science & Technology A: Vacuum, Surfaces, and Films 2014;32:030801.

[3] Kim H-H. Nonthermal plasma processing for air-pollution control: a historical review, current issues, and future prospects. Plasma Processes and Polymers 2004;1:91–110.

[4] Attri P, Ishikawa K, Okumura T, Koga K, Shiratani M. Plasma agriculture from laboratory to farm: A review. Processes 2020;8:1002.

[5] Fridman A. Plasma chemistry. Cambridge university press; 2008.

[6] Laroussi M. Plasma Medicine: A Brief Introduction. Plasma 2018;1:47–60. https://doi.org/10.3390/plasma1010005.

[7] Laroussi M. Sterilization of contaminated matter with an atmospheric pressure plasma. IEEE Transactions on Plasma Science 1996;24:1188–91.

[8] Alkawareek MY, Algwari QT, Laverty G, Gorman SP, Graham WG, O'Connell D, et al. Eradication of Pseudomonas aeruginosa biofilms by atmospheric pressure non-thermal plasma 2012.

[9] Matthes R, Bender C, Schlüter R, Koban I, Bussiahn R, Reuter S, et al. Antimicrobial efficacy of two surface barrier discharges with air plasma against in vitro biofilms. PloS One 2013;8:e70462.

[10] Høiby N, Bjarnsholt T, Givskov M, Molin S, Ciofu O. Antibiotic resistance of bacterial biofilms. International Journal of Antimicrobial Agents 2010;35:322–32.

[11] Shintani H, Sakudo A, Burke P, McDonnell G. Gas plasma sterilization of microorganisms and mechanisms of action. Experimental and Therapeutic Medicine 2010;1:731–8.

[12] Lerouge S, Wertheimer MR, Marchand R, Tabrizian M, Yahia L. Effect of gas composition on spore mortality and etching during low-pressure plasma sterilization. Journal of Biomedical Materials Research: An Official Journal of The Society for Biomaterials, The Japanese Society for Biomaterials, and The Australian Society for Biomaterials and the Korean Society for Biomaterials 2000;51:128–35.

[13] Gan L, Zhang S, Poorun D, Liu D, Lu X, He M, et al. Medical applications of nonthermal atmospheric pressure plasma in dermatology. JDDG: Journal Der Deutschen Dermatologischen Gesellschaft 2018;16:7–13.

[14] Brehmer F, Haenssle HA, Daeschlein G, Ahmed R, Pfeiffer S, Görlitz A, et al. Alleviation of chronic venous leg ulcers with a hand-held dielectric barrier discharge plasma generator (PlasmaDerm® VU-2010): results of a monocentric, two-armed, open, prospective, randomized and controlled trial (NCT 01415622). Journal of the European Academy of Dermatology and Venereology 2015;29:148–55.

[15] Reuter S, Von Woedtke T, Weltmann K-D. The kINPen—A review on physics and chemistry of the atmospheric pressure plasma jet and its applications. Journal of Physics D: Applied Physics 2018;51:233001.

[16] Arjunan KP, Friedman G, Fridman A, Clyne AM. Non-thermal dielectric barrier discharge plasma induces angiogenesis through reactive oxygen species. Journal of the Royal Society Interface 2012;9:147–57.

[17] Duchesne C, Banzet S, Lataillade J-J, Rousseau A, Frescaline N. Cold atmospheric plasma modulates endothelial nitric oxide synthase signalling and enhances burn wound neovascularisation. The Journal of Pathology 2019;249:368–80.

[18] Duchesne C, Frescaline N, Blaise O, Lataillade J-J, Banzet S, Dussurget O, et al. Cold Atmospheric Plasma Promotes Killing of Staphylococcus aureus by Macrophages. MSphere 2021;6:e00217-21.

[19] Keidar M. Plasma for cancer treatment. Plasma Sources Science and Technology 2015;24:033001.
[20] Brullé L, Vandamme M, Riès D, Martel E, Robert E, Lerondel S, et al. Effects of a Non Thermal Plasma Treatment Alone or in Combination with Gemcitabine in a MIA PaCa2-luc Orthotopic Pancreatic Carcinoma Model. PLOS ONE 2012;7:e52653. https://doi.org/10.1371/journal.pone.0052653.
[21] Honnorat B. Application of cold plasma in oncology, multidisciplinary experiments, physical, chemical and biological modeling. PhD Thesis. Sorbonne université, 2018.
[22] Teschke M, Kedzierski J, Finantu-Dinu EG, Korzec D, Engemann J. High-speed photographs of a dielectric barrier atmospheric pressure plasma jet. IEEE Transactions on Plasma Science 2005;33:310–1.
[23] Lu X, Laroussi M, Puech V. On atmospheric-pressure non-equilibrium plasma jets and plasma bullets. Plasma Sources Science and Technology 2012;21:034005.
[24] Shashurin A, Shneider MN, Keidar M. Measurements of streamer head potential and conductivity of streamer column in cold nonequilibrium atmospheric plasmas. Plasma Sources Science and Technology 2012;21:034006.
[25] Sretenović GB, Guaitella O, Sobota A, Krstić IB, Kovačević VV, Obradović BM, et al. Electric field measurement in the dielectric tube of helium atmospheric pressure plasma jet. Journal of Applied Physics 2017;121:123304.
[26] Mericam-Bourdet N, Laroussi M, Begum A, Karakas E. Experimental investigations of plasma bullets. J Phys D: Appl Phys 2009;42:055207. https://doi.org/10.1088/0022-3727/42/5/055207.
[27] Jarrige J, Laroussi M, Karakas E. Formation and dynamics of plasma bullets in a non-thermal plasma jet: influence of the high-voltage parameters on the plume characteristics. Plasma Sources Science and Technology 2010;19:065005.
[28] Puač N, Maletić D, Lazović S, Malović G, \DJor\djević A, Petrović ZL. Time resolved optical emission images of an atmospheric pressure plasma jet with transparent electrodes. Applied Physics Letters 2012;101:024103.
[29] Park HS, Kim SJ, Joh HM, Chung TH, Bae SH, Leem SH. Optical and electrical characterization of an atmospheric pressure microplasma jet with a capillary electrode. Physics of Plasmas 2010;17:033502.
[30] Naidis GV, Babaeva NY. Electric field distributions along helium plasma jets. High Voltage 2020;5:650–3.
[31] Naidis GV. Simulation of streamers propagating along helium jets in ambient air: Polarity-induced effects. Applied Physics Letters 2011;98:141501.
[32] Naidis GV. Modelling of streamer propagation in atmospheric-pressure helium plasma jets. J Phys D: Appl Phys 2010;43:402001. https://doi.org/10.1088/0022-3727/43/40/402001.
[33] Jánskỳ J, Tholin F, Bonaventura Z, Bourdon A. Simulation of the discharge propagation in a capillary tube in air at atmospheric pressure. Journal of Physics D: Applied Physics 2010;43:395201.
[34] Jánský J, Delliou PL, Tholin F, Tardiveau P, Bourdon A, Pasquiers S. Experimental and numerical study of the propagation of a discharge in a capillary tube in air at atmospheric pressure. J Phys D: Appl Phys 2011;44:335201. https://doi.org/10.1088/0022-3727/44/33/335201.
[35] Stoffels E, Kieft IE, Sladek REJ. Superficial treatment of mammalian cells using plasma needle. Journal of Physics D: Applied Physics 2003;36:2908.
[36] Brandenburg R, Navrátil Z, Jánskỳ J, St'Ahel P, Trunec D, Wagner H-E. The transition between different modes of barrier discharges at atmospheric pressure. Journal of Physics D: Applied Physics 2009;42:085208.

[37] Mussard MDVS, Guaitella O, Rousseau A. Propagation of plasma bullets in helium within a dielectric capillary—influence of the interaction with surfaces. Journal of Physics D: Applied Physics 2013;46:302001.
[38] Walsh JL, Iza F, Janson NB, Kong MG. Chaos in atmospheric-pressure plasma jets. Plasma Sources Science and Technology 2012;21:034008.
[39] Ning W, Wang L, Wu C, Jia S. Influence of voltage magnitude on the dynamic behavior of a stable helium atmospheric pressure plasma jet. Journal of Applied Physics 2014;116:073301.
[40] Liu JJ, Kong MG. Sub-60 C atmospheric helium–water plasma jets: modes, electron heating and downstream reaction chemistry. Journal of Physics D: Applied Physics 2011;44:345203.
[41] Qi B, Huang J-J, Zhang Z-H, Wang D-Z. FUNDAMENTAL AREAS OF PHENOMENOLOGY (INCLUDING APPLICATIONS): Observation of Periodic Multiplication and Chaotic Phenomena in Atmospheric Cold Plasma Jets. Chinese Physics Letters 2008;25:3323–5.
[42] Kim H-J, Kim JY, Kim JH, Kim DH, Lee D-S, Park C-S, et al. Improvement of stability of sinusoidally driven atmospheric pressure plasma jet using auxiliary bias voltage. AIP Advances 2015;5:127141.
[43] Schweigert IV, Alexandrov AL, Zakrevsky DE. Self-organization of touching-target current with ac voltage in atmospheric pressure plasma jet for medical application parameters. Plasma Sources Science and Technology 2020;29:12LT02.
[44] Van Der Schans M, Platier B, Koelman P, Van De Wetering F, Van Dijk J, Beckers J, et al. Decay of the electron density and the electron collision frequency between successive discharges of a pulsed plasma jet in N2. Plasma Sources Science and Technology 2019;28:035020.
[45] Shashurin A, Shneider MN, Dogariu A, Miles RB, Keidar M. Temporary-resolved measurement of electron density in small atmospheric plasmas. Appl Phys Lett 2010;96:171502. https://doi.org/10.1063/1.3389496.
[46] Wu F, Li J, Xian Y, Tan X, Lu X. Investigation on the electron density and temperature in a nanosecond pulsed helium plasma jet with Thomson scattering. Plasma Processes and Polymers 2021;18:2100033.
[47] Pancheshnyi S. Role of electronegative gas admixtures in streamer start, propagation and branching phenomena. Plasma Sources Science and Technology 2005;14:645.
[48] Wu S, Lu X, Pan Y. Effects of seed electrons on the plasma bullet propagation. Current Applied Physics 2013;13:S1–5. https://doi.org/10.1016/j.cap.2012.12.004.
[49] Nijdam S, Takahashi E, Markosyan AH, Ebert U. Investigation of positive streamers by double-pulse experiments, effects of repetition rate and gas mixture. Plasma Sources Science and Technology 2014;23:025008.
[50] Babaeva NY, Naidis GV. Modeling of streamer interaction with localized plasma regions. Plasma Sources Science and Technology 2018;27:075018.
[51] Nie L, Chang L, Xian Y, Lu X. The effect of seed electrons on the repeatability of atmospheric pressure plasma plume propagation: I. Experiment. Physics of Plasmas 2016;23:093518.
[52] Nijdam S, Wormeester G, Van Veldhuizen EM, Ebert U. Probing background ionization: positive streamers with varying pulse repetition rate and with a radioactive admixture. Journal of Physics D: Applied Physics 2011;44:455201.
[53] Jánskỳ J, Bourdon A. Simulation of helium discharge ignition and dynamics in thin tubes at atmospheric pressure. Applied Physics Letters 2011;99:161504.
[54] Yousfi M, Eichwald O, Merbahi N, Jomaa N. Analysis of ionization wave dynamics in low-temperature plasma jets from fluid modeling supported by experimental investigations. Plasma Sources Science and Technology 2012;21:045003.
[55] Breden D, Miki K, Raja LL. Self-consistent two-dimensional modeling of cold atmospheric-pressure plasma jets/bullets. Plasma Sources Science and Technology 2012;21:034011.

[56] Becker MM, Hoder T, Brandenburg R, Loffhagen D. Analysis of microdischarges in asymmetric dielectric barrier discharges in argon. J Phys D: Appl Phys 2013;46:355203. https://doi.org/10.1088/0022-3727/46/35/355203.
[57] Kogelschatz U. Dielectric-barrier discharges: their history, discharge physics, and industrial applications. Plasma Chemistry and Plasma Processing 2003;23:1–46.
[58] Huang B, Zhang C, Adamovich I, Akishev Y, Shao T. Surface ionization wave propagation in the nanosecond pulsed surface dielectric barrier discharge: the influence of dielectric material and pulse repetition rate. Plasma Sources Sci Technol 2020;29:044001. https://doi.org/10.1088/1361-6595/ab7854.
[59] Robert E, Barbosa E, Dozias S, Vandamme M, Cachoncinlle C, Viladrosa R, et al. Experimental study of a compact nanosecond plasma gun. Plasma Processes and Polymers 2009;6:795–802.
[60] OUYANG J, LI B, HE F, DAI D. Nonlinear phenomena in dielectric barrier discharges: pattern, striation and chaos. Plasma Sci Technol 2018;20:103002. https://doi.org/10.1088/2058-6272/aad325.
[61] Boeuf JP, Bernecker B, Callegari T, Blanco S, Fournier R. Generation, annihilation, dynamics and self-organized patterns of filaments in dielectric barrier discharge plasmas. Applied Physics Letters 2012;100:244108.
[62] Morabit Y, Hasan MI, Whalley RD, Robert E, Modic M, Walsh JL. A review of the gas and liquid phase interactions in low-temperature plasma jets used for biomedical applications. Eur Phys J D 2021;75:32. https://doi.org/10.1140/epjd/s10053-020-00004-4.
[63] Bing Q, Jian-Jun H, Zhe-Huang Z, De-Zhen W. Observation of periodic multiplication and chaotic phenomena in atmospheric cold plasma jets. Chinese Physics Letters 2008;25:3323.
[64] Bernecker B, Callegari T, Blanco S, Fournier R, Boeuf J-P. Hexagonal and honeycomb structures in dielectric barrier discharges. The European Physical Journal-Applied Physics 2009;47.
[65] Célestin S, Canes-Boussard G, Guaitella O, Bourdon A, Rousseau A. Influence of the charges deposition on the spatio-temporal self-organization of streamers in a DBD. Journal of Physics D: Applied Physics 2008;41:205214.
[66] Chirokov A, Gutsol A, Fridman A, Sieber KD, Grace JM, Robinson KS. Analysis of two-dimensional microdischarge distribution in dielectric-barrier discharges. Plasma Sources Science and Technology 2004;13:623.
[67] Hoder T, Höft H, Kettlitz M, Weltmann K-D, Brandenburg R. Barrier discharges driven by sub-microsecond pulses at atmospheric pressure: Breakdown manipulation by pulse width. Physics of Plasmas 2012;19:070701.
[68] Cheung PY, Wong AY. Chaotic behavior and period doubling in plasmas. Physical Review Letters 1987;59:551.
[69] Wang YH, Zhang YT, Wang DZ, Kong MG. Period multiplication and chaotic phenomena in atmospheric dielectric-barrier glow discharges. Applied Physics Letters 2007;90:071501.
[70] Zhang J, Wang Y, Wang D. Numerical study of period multiplication and chaotic phenomena in an atmospheric radio-frequency discharge. Physics of Plasmas 2010;17:043507.
[71] Shi H, Wang Y, Wang D. Nonlinear behavior in the time domain in argon atmospheric dielectric-barrier discharges. Physics of Plasmas 2008;15:122306.
[72] Dai D, Zhao X, Wang Q. Inverse period-doubling bifurcation in an atmospheric helium dielectric barrier discharge. EPL (Europhysics Letters) 2014;107:15002.
[73] Nakagawa Y, Ono R, Oda T. Effect of discharge polarity on OH density and temperature in coaxial-cylinder barrier discharge under atmospheric pressure humid air. Jpn J Appl Phys 2018;57:096103. https://doi.org/10.7567/JJAP.57.096103.
[74] Girard P-M, Arbabian A, Fleury M, Bauville G, Puech V, Dutreix M, et al. Synergistic effect of H2O2 and NO2 in cell death induced by cold atmospheric He plasma. Scientific Reports 2016;6:1–17.

[75] Oktyabrsky ON, Smirnova GV. Redox regulation of cellular functions. Biochemistry (Moscow) 2007;72:132–45.
[76] Niethammer P, Grabher C, Look AT, Mitchison TJ. A tissue-scale gradient of hydrogen peroxide mediates rapid wound detection in zebrafish. Nature 2009;459:996–9.
[77] Duchesne C, Frescaline N, Lataillade J-J, Rousseau A. Comparative Study between Direct and Indirect Treatment with Cold Atmospheric Plasma on *In Vitro* and *In Vivo* Models of Wound Healing. PMED 2018;8. https://doi.org/10.1615/PlasmaMed.2019028659.
[78] Paal JV der, Verlackt CC, Yusupov M, Neyts EC, Bogaerts A. Structural modification of the skin barrier by OH radicals: a reactive molecular dynamics study for plasma medicine. J Phys D: Appl Phys 2015;48:155202. https://doi.org/10.1088/0022-3727/48/15/155202.
[79] Pan J, Sun P, Tian Y, Zhou H, Wu H, Bai N, et al. A novel method of tooth whitening using cold plasma microjet driven by direct current in atmospheric-pressure air. IEEE Transactions on Plasma Science 2010;38:3143–51.
[80] Kapila V, Sellke FW, Suuronen EJ, Mesana TG, Ruel M. Nitric oxide and the angiogenic response: can we improve the results of therapeutic angiogenesis? Expert Opinion on Investigational Drugs 2005;14:37–44.
[81] Nichols SP, Storm WL, Koh A, Schoenfisch MH. Local delivery of nitric oxide: targeted delivery of therapeutics to bone and connective tissues. Advanced Drug Delivery Reviews 2012;64:1177–88.
[82] Del Rosso JQ, Kircik LH. Spotlight on the use of nitric oxide in dermatology: what is it? What does it do? Can it become an important addition to the therapeutic armamentarium for skin disease? Journal of Drugs in Dermatology: JDD 2017;16:s4–10.
[83] Kevil CG, Kolluru GK, Pattillo CB, Giordano T. Inorganic nitrite therapy: historical perspective and future directions. Free Radical Biology and Medicine 2011;51:576–93.
[84] Lundberg JO, Weitzberg E, Gladwin MT. The nitrate–nitrite–nitric oxide pathway in physiology and therapeutics. Nature Reviews Drug Discovery 2008;7:156–67.
[85] Uchida G, Takenaka K, Takeda K, Ishikawa K, Hori M, Setsuhara Y. Selective production of reactive oxygen and nitrogen species in the plasma-treated water by using a nonthermal high-frequency plasma jet. Jpn J Appl Phys 2018;57:0102B4. https://doi.org/10.7567/JJAP.57.0102B4.
[86] Baek EJ, Joh HM, Kim SJ, Chung TH. Effects of the electrical parameters and gas flow rate on the generation of reactive species in liquids exposed to atmospheric pressure plasma jets. Physics of Plasmas 2016;23:073515. https://doi.org/10.1063/1.4959174.
[87] Omran AV, Busco G, Ridou L, Dozias S, Grillon C, Pouvesle J-M, et al. Cold atmospheric single plasma jet for RONS delivery on large biological surfaces. Plasma Sources Sci Technol 2020;29:105002. https://doi.org/10.1088/1361-6595/abaffd.
[88] Yagi I, Ono R, Oda T, Takaki K. Two-dimensional LIF measurements of humidity and OH density resulting from evaporated water from a wet surface in plasma for medical use. Plasma Sources Sci Technol 2014;24:015002. https://doi.org/10.1088/0963-0252/24/1/015002.
[89] Oh J-S, Kakuta M, Furuta H, Akatsuka H, Hatta A. Effect of plasma jet diameter on the efficiency of reactive oxygen and nitrogen species generation in water. Jpn J Appl Phys 2016;55:06HD01. https://doi.org/10.7567/JJAP.55.06HD01.
[90] Uchida G, Nakajima A, Ito T, Takenaka K, Kawasaki T, Koga K, et al. Effects of nonthermal plasma jet irradiation on the selective production of H_2O_2 and NO_2^- in liquid water. Journal of Applied Physics 2016;120:203302. https://doi.org/10.1063/1.4968568.
[91] Ghimire B, Sornsakdanuphap J, Hong YJ, Uhm HS, Weltmann K-D, Choi EH. The effect of the gap distance between an atmospheric-pressure plasma jet nozzle and liquid surface on OH and N_2 species concentrations. Physics of Plasmas 2017;24:073502. https://doi.org/10.1063/1.4989735.
[92] Li J, Wu F, Nie L, Lu X, Ostrikov K. The Production Efficiency of Reactive Oxygen and Nitrogen Species (RONS) of AC and Pulse-DC Plasma Jet. IEEE Transactions on Plasma Science 2020;48:4204–14. https://doi.org/10.1109/TPS.2020.3030985.

[93] Gorbanev Y, O'Connell D, Chechik V. Non-thermal plasma in contact with water: The origin of species. Chemistry–A European Journal 2016;22:3496–505.
[94] Hefny MM, Pattyn C, Lukes P, Benedikt J. Atmospheric plasma generates oxygen atoms as oxidizing species in aqueous solutions. J Phys D: Appl Phys 2016;49:404002. https://doi.org/10.1088/0022-3727/49/40/404002.
[95] He X, Lin J, He B, Xu L, Li J, Chen Q, et al. The formation pathways of aqueous hydrogen peroxide in a plasma-liquid system with liquid as the cathode. Plasma Sources Sci Technol 2018;27:085010. https://doi.org/10.1088/1361-6595/aad66d.
[96] Chen Z, Liu D, Chen C, Xu D, Liu Z, Xia W, et al. Analysis of the production mechanism of H2O2 in water treated by helium DC plasma jets. Journal of Physics D: Applied Physics 2018;51:325201.
[97] Attri P, Kim YH, Park DH, Park JH, Hong YJ, Uhm HS, et al. Generation mechanism of hydroxyl radical species and its lifetime prediction during the plasma-initiated ultraviolet (UV) photolysis. Scientific Reports 2015;5:1–8.
[98] Lu S-Y, Chipman RA. Interpretation of Mueller matrices based on polar decomposition. J Opt Soc Am A, JOSAA 1996;13:1106–13. https://doi.org/10.1364/JOSAA.13.001106.
[99] Ghosh N, Wood MFG, Vitkin IA. Mueller matrix decomposition for extraction of individual polarization parameters from complex turbid media exhibiting multiple scattering, optical activity, and linear birefringence. JBO 2008;13:044036. https://doi.org/10.1117/1.2960934.
[100] Haertel B, von Woedtke T, Weltmann K-D, Lindequist U. Non-Thermal Atmospheric-Pressure Plasma Possible Application in Wound Healing. Biomol Ther (Seoul) 2014;22:477–90. https://doi.org/10.4062/biomolther.2014.105.
[101] Wende K, Straßenburg S, Haertel B, Harms M, Holtz S, Barton A, et al. Atmospheric pressure plasma jet treatment evokes transient oxidative stress in HaCaT keratinocytes and influences cell physiology. Cell Biology International 2014;38:412–25. https://doi.org/10.1002/cbin.10200.
[102] Heinlin J, Isbary G, Stolz W, Morfill G, Landthaler M, Shimizu T, et al. Plasma applications in medicine with a special focus on dermatology. Journal of the European Academy of Dermatology and Venereology 2011;25:1–11. https://doi.org/10.1111/j.1468-3083.2010.03702.x.
[103] Choi J-H, Song Y-S, Lee H-J, Hong J-W, Kim G-C. Inhibition of inflammatory reactions in 2,4-Dinitrochlorobenzene induced Nc/Nga atopic dermatitis mice by non-thermal plasma. Sci Rep 2016;6:27376. https://doi.org/10.1038/srep27376.
[104] Isbary G, Heinlin J, Shimizu T, Zimmermann J l., Morfill G, Schmidt H-U, et al. Successful and safe use of 2 min cold atmospheric argon plasma in chronic wounds: results of a randomized controlled trial. British Journal of Dermatology 2012;167:404–10. https://doi.org/10.1111/j.1365-2133.2012.10923.x.
[105] Schmidt A, Bekeschus S, Wende K, Vollmar B, von Woedtke T. A cold plasma jet accelerates wound healing in a murine model of full-thickness skin wounds. Experimental Dermatology 2017;26:156–62. https://doi.org/10.1111/exd.13156.
[106] Arndt S, Unger P, Berneburg M, Bosserhoff A-K, Karrer S. Cold atmospheric plasma (CAP) activates angiogenesis-related molecules in skin keratinocytes, fibroblasts and endothelial cells and improves wound angiogenesis in an autocrine and paracrine mode. Journal of Dermatological Science 2018;89:181–90. https://doi.org/10.1016/j.jdermsci.2017.11.008.
[107] Mashayekh S, Rajaee H, Akhlaghi M, Shokri B, Hassan ZM. Atmospheric-pressure plasma jet characterization and applications on melanoma cancer treatment (B/16-F10). Physics of Plasmas 2015;22:093508. https://doi.org/10.1063/1.4930536.
[108] Dezest M, Chavatte L, Bourdens M, Quinton D, Camus M, Garrigues L, et al. Mechanistic insights into the impact of Cold Atmospheric Pressure Plasma on human epithelial cell lines. Sci Rep 2017;7:41163. https://doi.org/10.1038/srep41163.

[109] Lin C-J, Chen T-L, Tseng Y-Y, Wu G-J, Hsieh M-H, Lin Y-W, et al. Honokiol induces autophagic cell death in malignant glioma through reactive oxygen species-mediated regulation of the p53/PI3K/Akt/mTOR signaling pathway. Toxicology and Applied Pharmacology 2016;304:59–69. https://doi.org/10.1016/j.taap.2016.05.018.
[110] Fridman G, Peddinghaus M, Balasubramanian M, Ayan H, Fridman A, Gutsol A, et al. Blood Coagulation and Living Tissue Sterilization by Floating-Electrode Dielectric Barrier Discharge in Air. Plasma Chem Plasma Process 2006;26:425–42. https://doi.org/10.1007/s11090-006-9024-4.
[111] Masi GD, Gareri C, Cordaro L, Fassina A, Brun P, Zaniol B, et al. Plasma Coagulation Controller: A Low- Power Atmospheric Plasma Source for Accelerated Blood Coagulation. PMED 2018;8. https://doi.org/10.1615/PlasmaMed.2018028202.
[112] Duval A, Marinov I, Bousquet G, Gapihan G, Starikovskaia SM, Rousseau A, et al. Cell Death Induced on Cell Cultures and Nude Mouse Skin by Non-Thermal, Nanosecond-Pulsed Generated Plasma. PLOS ONE 2013;8:e83001. https://doi.org/10.1371/journal.pone.0083001.
[113] Cordaro L, De Masi G, Fassina A, Mancini D, Cavazzana R, Desideri D, et al. On the Electrical and Optical Features of the Plasma Coagulation Controller Low Temperature Atmospheric Plasma Jet. Plasma 2019;2:156–67. https://doi.org/10.3390/plasma2020012.
[114] Chernets N, Zhang J, Steinbeck MJ, Kurpad DS, Koyama E, Friedman G, et al. Nonthermal Atmospheric Pressure Plasma Enhances Mouse Limb Bud Survival, Growth, and Elongation. Tissue Engineering Part A 2015;21:300–9. https://doi.org/10.1089/ten.tea.2014.0039.
[115] Mora-Núñez A, Martínez-Ponce G, García-Torales G, Beltrán-González AB. Texture analysis applied to polarimetric images of healthy in vivo murine skin. OE 2018;57:054106. https://doi.org/10.1117/1.OE.57.5.054106.
[116] Pierangelo A, Manhas S, Benali A, Fallet C, Antonelli M-R, Novikova T, et al. Ex vivo photometric and polarimetric multilayer characterization of human healthy colon by multispectral Mueller imaging. JBO 2012;17:066009. https://doi.org/10.1117/1.JBO.17.6.066009.
[117] Pierangelo A, Nazac A, Benali A, Validire P, Cohen H, Novikova T, et al. Polarimetric imaging of uterine cervix: a case study. Opt Express, OE 2013;21:14120–30. https://doi.org/10.1364/OE.21.014120.
[118] Rehbinder J, Haddad H, Deby S, Teig B, Nazac A, Novikova T, et al. Ex vivo Mueller polarimetric imaging of the uterine cervix: a first statistical evaluation. JBO 2016;21:071113. https://doi.org/10.1117/1.JBO.21.7.071113.
[119] Vizet J, Rehbinder J, Deby S, Roussel S, Nazac A, Soufan R, et al. In vivo imaging of uterine cervix with a Mueller polarimetric colposcope. Sci Rep 2017;7:2471. https://doi.org/10.1038/s41598-017-02645-9.
[120] Kupinski M, Boffety M, Goudail F, Ossikovski R, Pierangelo A, Rehbinder J, et al. Polarimetric measurement utility for pre-cancer detection from uterine cervix specimens. Biomed Opt Express, BOE 2018;9:5691–702. https://doi.org/10.1364/BOE.9.005691.
[121] Heinrich C, Rehbinder J, Nazac A, Teig B, Pierangelo A, Zallat J. Mueller polarimetric imaging of biological tissues: classification in a decision-theoretic framework. J Opt Soc Am A, JOSAA 2018;35:2046–57. https://doi.org/10.1364/JOSAA.35.002046.
[122] Novikova T, Pierangelo A, De Martino A, Benali A, Validire P. Polarimetric Imaging for Cancer Diagnosis and Staging. Optics & Photonics News 2012;23:26. https://doi.org/10.1364/OPN.23.10.000026.
[123] Pierangelo A, Benali A, Antonelli M-R, Novikova T, Validire P, Gayet B, et al. Ex-vivo characterization of human colon cancer by Mueller polarimetric imaging. Opt Express, OE 2011;19:1582–93. https://doi.org/10.1364/OE.19.001582.
[124] Antonelli M-R, Pierangelo A, Novikova T, Validire P, Benali A, Gayet B, et al. Mueller matrix imaging of human colon tissue for cancer diagnostics: how Monte Carlo modeling can help in

the interpretation of experimental data. Opt Express, OE 2010;18:10200–8. https://doi.org/10.1364/OE.18.010200.
[125] Pierangelo A, Manhas S, Benali A, Fallet C, Totobenazara J-L, Antonelli MR, et al. Multispectral Mueller polarimetric imaging detecting residual cancer and cancer regression after neoadjuvant treatment for colorectal carcinomas. JBO 2013;18:046014. https://doi.org/10.1117/1.JBO.18.4.046014.
[126] Wang W, Lim LG, Srivastava S, Bok-Yan So J, Shabbir A, Liu Q. Investigation on the potential of Mueller matrix imaging for digital staining. Journal of Biophotonics 2016;9:364–75. https://doi.org/10.1002/jbio.201500006.
[127] Smith MH, Burke PD, Lompado A, Tanner EA, Hillman LW. Mueller matrix imaging polarimetry in dermatology. Biomedical Diagnostic, Guidance, and Surgical-Assist Systems II, vol. 3911, SPIE; 2000, p. 210–6. https://doi.org/10.1117/12.384904.
[128] Smith MH. Interpreting Mueller matrix images of tissues. Laser-Tissue Interaction XII: Photochemical, Photothermal, and Photomechanical, vol. 4257, SPIE; 2001, p. 82–9. https://doi.org/10.1117/12.434690.
[129] Dong Y, He H, Sheng W, Wu J, Ma H. A quantitative and non-contact technique to characterise microstructural variations of skin tissues during photo-damaging process based on Mueller matrix polarimetry. Sci Rep 2017;7:14702. https://doi.org/10.1038/s41598-017-14804-z.
[130] Vizet J, Manhas S, Tran J, Validire P, Benali A, Garcia-Caurel E, et al. Optical fiber-based full Mueller polarimeter for endoscopic imaging using a two-wavelength simultaneous measurement method. JBO 2016;21:071106. https://doi.org/10.1117/1.JBO.21.7.071106.
[131] Fade J, Alouini M. Depolarization Remote Sensing by Orthogonality Breaking. Phys Rev Lett 2012;109:043901. https://doi.org/10.1103/PhysRevLett.109.043901.
[132] Lindberg A, Vizet J, Rehbinder J, Gennet C, Vanel J-C, Pierangelo A. Innovative integrated numerical-experimental method for high-performance multispectral Mueller polarimeters based on ferroelectric liquid crystals. Applied Optics 2019;58:5187–99.
[133] Lindberg A, Vizet J, Rehbinder J, Gennet C, Vanel J-C, Pierangelo A. Innovative and high-performance instrumentation for biomedical Mueller polarimetric imaging in vivo. Optical Biopsy XVII: Toward Real-Time Spectroscopic Imaging and Diagnosis, vol. 10873, SPIE; 2019, p. 28–35. https://doi.org/10.1117/12.2510232.
[134] Rehbinder J, Deby S, Haddad H, Teig B, Nazac A, Pierangelo A, et al. Diagnosis of uterine cervix cancer using Müller polarimetry: a comparison with histopathology. In: Amelink A, Vitkin IA, editors., Munich, Germany: 2015, p. 95400W. https://doi.org/10.1117/12.2192423.
[135] Compain E, Poirier S, Drevillon B. General and self-consistent method for the calibration of polarization modulators, polarimeters, and Mueller-matrix ellipsometers. Appl Opt, AO 1999;38:3490–502. https://doi.org/10.1364/AO.38.003490.
[136] Chen S, Chen X, Wen J, Yao C, Xu G, Li Y, et al. Primary and secondary discharges in an atmospheric pressure plasma jet fed with helium and tetrafluoromethane mixtures. Physics of Plasmas 2019;26:010703.
[137] Oh SY, Uhm HS, Kang H, Lee IW, Suk H. Temporal evolution of electron density and temperature in capillary discharge plasmas. Journal of Applied Physics 2010;107:103309. https://doi.org/10.1063/1.3415553.
[138] Jiang N, Ji A, Cao Z. Atmospheric pressure plasma jet: Effect of electrode configuration, discharge behavior, and its formation mechanism. Journal of Applied Physics 2009;106:013308.
[139] Jiang N, Ji A, Cao Z. Atmospheric pressure plasma jets beyond ground electrode as charge overflow in a dielectric barrier discharge setup. Journal of Applied Physics 2010;108:033302.
[140] Liu C-T, Wu C-J, Yang Y-W, Lin Z-H, Wu J-S, Hsiao S-C, et al. Atomic oxygen and hydroxyl radical generation in round helium-based atmospheric-pressure plasma jets by various electrode

arrangements and its application in sterilizing Streptococcus mutans. IEEE Transactions on Plasma Science 2014;42:3830–6.
[141] Jánskỳ J, Bourdon A. Surface charge deposition inside a capillary glass tube by an atmospheric pressure discharge in air. The European Physical Journal-Applied Physics 2011;55.
[142] Jiang C, Chen MT, Gundersen MA. Polarity-induced asymmetric effects of nanosecond pulsed plasma jets. Journal of Physics D: Applied Physics 2009;42:232002.
[143] Xiong Z, Lu X, Xian Y, Jiang Z, Pan Y. On the velocity variation in atmospheric pressure plasma plumes driven by positive and negative pulses. Journal of Applied Physics 2010;108:103303.
[144] Mladenović Ž, Gocić S. Influence of air and water vapor on EEDF, plasma parameters, and the main RONS in atmospheric pressure low temperature helium plasmas: Global model approach. Physics of Plasmas 2022;29:103504. https://doi.org/10.1063/5.0110151.
[145] Lin L, Lyu Y, Trink B, Canady J, Keidar M. Cold atmospheric helium plasma jet in humid air environment. Journal of Applied Physics 2019;125:153301. https://doi.org/10.1063/1.5086177.
[146] Schröter S, Wijaikhum A, Gibson AR, West A, Davies HL, Minesi N, et al. Chemical kinetics in an atmospheric pressure helium plasma containing humidity. Phys Chem Chem Phys 2018;20:24263–86. https://doi.org/10.1039/C8CP02473A.
[147] Ono R, Tokuhiro M. Spatiotemporal measurement of OH density from upstream to downstream in humid helium atmospheric-pressure plasma jet. Plasma Sources Sci Technol 2020;29:035021. https://doi.org/10.1088/1361-6595/ab3c75.
[148] Bruggeman P, Iza F, Guns P, Lauwers D, Kong MG, Gonzalvo YA, et al. Electronic quenching of OH(A) by water in atmospheric pressure plasmas and its influence on the gas temperature determination by OH(A–X) emission. Plasma Sources Sci Technol 2009;19:015016. https://doi.org/10.1088/0963-0252/19/1/015016.
[149] Ricard A, Décomps Ph, Massines F. Kinetics of radiative species in helium pulsed discharge at atmospheric pressure. Surface and Coatings Technology 1999;112:1–4. https://doi.org/10.1016/S0257-8972(98)00797-X.
[150] Bogaczyk M, Sretenović GB, Wagner H-E. Influence of the applied voltage shape on the barrier discharge operation modes in helium. Eur Phys J D 2013;67:212. https://doi.org/10.1140/epjd/e2013-40279-x.
[151] Komuro A, Ono R, Oda T. Effects of pulse voltage rise rate on velocity, diameter and radical production of an atmospheric-pressure streamer discharge. Plasma Sources Sci Technol 2013;22:045002. https://doi.org/10.1088/0963-0252/22/4/045002.
[152] Komuro A, Takahashi K, Ando A. Numerical simulation for the production of chemically active species in primary and secondary streamers in atmospheric-pressure dry air. J Phys D: Appl Phys 2015;48:215203. https://doi.org/10.1088/0022-3727/48/21/215203.
[153] Ono R, Oda T. Formation and structure of primary and secondary streamers in positive pulsed corona discharge—effect of oxygen concentration and applied voltage. J Phys D: Appl Phys 2003;36:1952. https://doi.org/10.1088/0022-3727/36/16/306.
[154] Ono R, Oda T. Nitrogen oxide γ-band emission from primary and secondary streamers in pulsed positive corona discharge. Journal of Applied Physics 2005;97:013302. https://doi.org/10.1063/1.1829371.
[155] Wu S, Lu X, Pan Y. On the mechanism of acceleration behavior of plasma bullet. Physics of Plasmas 2014;21:073509.
[156] Martens T, Bogaerts A, Brok WJM, Dijk JV. The dominant role of impurities in the composition of high pressure noble gas plasmas. Appl Phys Lett 2008;92:041504. https://doi.org/10.1063/1.2839613.
[157] Xiong Z, Babaeva NY, Tian W, Kushner M, Arbor A. Interaction of high pressure plasmas with their boundaries: channels, tubes, liquids and tissue. Proc. 30th Int. Conf. Phenomena Ionized Gases, Citeseer; 2011, p. 1–4.

[158] Le Delliou P, Tardiveau P, Jeanney P, Bauville G, Pasquiers S. Development of pulsed discharges inside narrow cavities and their interaction with dielectric surfaces. Proceedings of the 30th International Conference on Phenomena in Ionized Gases (ICPIG), Belfast, Northern Ireland, UK, vol. 28, Citeseer; 2011, p. C10.
[159] Xian Y, Lu X, Liu J, Wu S, Liu D, Pan Y. Multiple plasma bullet behavior of an atmospheric-pressure plasma plume driven by a pulsed dc voltage. Plasma Sources Sci Technol 2012;21:034013. https://doi.org/10.1088/0963-0252/21/3/034013.
[160] Qian M, Ren C, Wang D, Zhang J, Wei G. Stark broadening measurement of the electron density in an atmospheric pressure argon plasma jet with double-power electrodes. Journal of Applied Physics 2010;107:063303. https://doi.org/10.1063/1.3330717.
[161] Robert E, Sarron V, Riès D, Dozias S, Vandamme M, Pouvesle J-M. Characterization of pulsed atmospheric-pressure plasma streams (PAPS) generated by a plasma gun. Plasma Sources Sci Technol 2012;21:034017. https://doi.org/10.1088/0963-0252/21/3/034017.
[162] Xiong Q, Lu X, Xian Y, Liu J, Zou C, Xiong Z, et al. Experimental investigations on the propagation of the plasma jet in the open air. Journal of Applied Physics 2010;107:073302. https://doi.org/10.1063/1.3369538.
[163] Xiong Q, Lu X, Ostrikov K, Xiong Z, Xian Y, Zhou F, et al. Length control of He atmospheric plasma jet plumes: Effects of discharge parameters and ambient air. Physics of Plasmas 2009;16:043505.
[164] Jansky J, Pechereau F, Bourdon A. Simulation of the dynamics of a helium discharge in a thin dielectric tube at atmospheric pressure. Bulletin of the American Physical Society 2011;56.
[165] Likhanskii AV, Shneider MN, Macheret SO, Miles RB. Modeling of dielectric barrier discharge plasma actuators driven by repetitive nanosecond pulses. Physics of Plasmas 2007;14:073501. https://doi.org/10.1063/1.2744227.
[166] Chen L, Zhao P, Shu X, Shen J, Meng Y. On the mechanism of atmospheric pressure plasma plume. Physics of Plasmas 2010;17:083502. https://doi.org/10.1063/1.3465665.
[167] Poolcharuansin P, Liebig B, Bradley J. Plasma Parameters in a Pre-Ionized HiPIMS Discharge Operating at Low Pressure. IEEE Transactions on Plasma Science 2010;38:3007–15. https://doi.org/10.1109/TPS.2010.2069572.
[168] Lu X, Ostrikov K (Ken). Guided ionization waves: The physics of repeatability. Applied Physics Reviews 2018;5:031102. https://doi.org/10.1063/1.5031445.
[169] Wu S, Lu X. The role of residual charges in the repeatability of the dynamics of atmospheric pressure room temperature plasma plume. Physics of Plasmas 2014;21:123509. https://doi.org/10.1063/1.4904369.
[170] Bruggeman PJ, Bogaerts A, Pouvesle JM, Robert E, Szili EJ. Plasma–liquid interactions. Journal of Applied Physics 2021;130:200401. https://doi.org/10.1063/5.0078076.
[171] Kovačević VV, Sretenović GB, Slikboer E, Guaitella O, Sobota A, Kuraica MM. The effect of liquid target on a nonthermal plasma jet—imaging, electric fields, visualization of gas flow and optical emission spectroscopy. J Phys D: Appl Phys 2018;51:065202. https://doi.org/10.1088/1361-6463/aaa288.
[172] Bruggeman P, Schram DC. On OH production in water containing atmospheric pressure plasmas. Plasma Sources Sci Technol 2010;19:045025. https://doi.org/10.1088/0963-0252/19/4/045025.
[173] Luo Y, Lietz AM, Yatom S, Kushner MJ, Bruggeman PJ. Plasma kinetics in a nanosecond pulsed filamentary discharge sustained in Ar–H2O and H2O. J Phys D: Appl Phys 2018;52:044003. https://doi.org/10.1088/1361-6463/aaeb14.
[174] Elg DT, Yang I-W, Graves DB. Production of TEMPO by O atoms in atmospheric pressure non-thermal plasma–liquid interactions. J Phys D: Appl Phys 2017;50:475201. https://doi.org/10.1088/1361-6463/aa8f8c.

[175] Yonemori S, Nakagawa Y, Ono R, Oda T. Measurement of OH density and air–helium mixture ratio in an atmospheric-pressure helium plasma jet. J Phys D: Appl Phys 2012;45:225202. https://doi.org/10.1088/0022-3727/45/22/225202.
[176] Winter J, Wende K, Masur K, Iseni S, Dünnbier M, Hammer MU, et al. Feed gas humidity: a vital parameter affecting a cold atmospheric-pressure plasma jet and plasma-treated human skin cells. J Phys D: Appl Phys 2013;46:295401. https://doi.org/10.1088/0022-3727/46/29/295401.
[177] Srivastava N, Wang C. Effects of water addition on OH radical generation and plasma properties in an atmospheric argon microwave plasma jet. Journal of Applied Physics 2011;110:053304. https://doi.org/10.1063/1.3632970.
[178] Förster S, Mohr C, Viöl W. Investigations of an atmospheric pressure plasma jet by optical emission spectroscopy. Surface and Coatings Technology 2005;200:827–30. https://doi.org/10.1016/j.surfcoat.2005.02.217.
[179] Douat C, Kacem I, Sadeghi N, Bauville G, Fleury M, Puech V. Space-time resolved density of helium metastable atoms in a nanosecond pulsed plasma jet: influence of high voltage and pulse frequency. J Phys D: Appl Phys 2016;49:285204. https://doi.org/10.1088/0022-3727/49/28/285204.
[180] Pei X, Lu Y, Wu S, Xiong Q, Lu X. A study on the temporally and spatially resolved OH radical distribution of a room-temperature atmospheric-pressure plasma jet by laser-induced fluorescence imaging. Plasma Sources Sci Technol 2013;22:025023. https://doi.org/10.1088/0963-0252/22/2/025023.
[181] Liu A, Ocotl E, Karim A, Wolf JJ, Cox BL, Eliceiri KW, et al. Modeling early thermal injury using an ex vivo human skin model of contact burns. Burns 2021;47:611–20. https://doi.org/10.1016/j.burns.2020.08.011.
[182] Singh M, Nuutila K, Minasian R, Kruse C, Eriksson E. Development of a precise experimental burn model. Burns 2016;42:1507–12. https://doi.org/10.1016/j.burns.2016.02.019.
[183] Papp A, Kiraly K, Härmä M, Lahtinen T, Uusaro A, Alhava E. The progression of burn depth in experimental burns: a histological and methodological study. Burns 2004;30:684–90. https://doi.org/10.1016/j.burns.2004.03.021.
[184] Hirth DA, Singer AJ, Clark RAF, McClain SA. Histopathologic staining of low temperature cutaneous burns: Comparing biomarkers of epithelial and vascular injury reveals utility of HMGB1 and hematoxylin phloxine saffron. Wound Repair and Regeneration 2012;20:918–27. https://doi.org/10.1111/j.1524-475X.2012.00847.x.
[185] Singer AJ, Berruti L, Thode Jr. HC, McClain SA. Standardized Burn Model Using a Multiparametric Histologic Analysis of Burn Depth. Academic Emergency Medicine 2000;7:1–6. https://doi.org/10.1111/j.1553-2712.2000.tb01881.x.

ECOLE DOCTORALE

Titre : Modes multi-périodiques et aléatoires des jets de plasma à pression atmosphérique et leurs interactions avec des cibles liquides et biologiques

Mots clés : APPJ, plasma multi-périodique, auto-déclenchement, RONS, MPI, plasma médecine

Résumé : Dans cette thèse, trois caractéristiques principales de l'APPJ sont étudiées : i) les modes de propagation multi-périodiques et aléatoires ainsi que le rôle des charges de surface ; ii) l'interaction entre l'APPJ et les cibles liquides ; iii) la modification d'échantillons de peau inerte après traitement au plasma.

Un APPJ à l'hélium alimenté par une tension sinusoïdale de 15 ~ 18 kHz opère en mode auto-déclenché multi-périodique ou en mode aléatoire selon la tension, la fréquence, ou de la distance entre les électrodes. La plupart des ondes multi-périodiques observées se déclenchent toutes les 2 ou 3 périodes sinusoïdales. De telles ondes présentent des similitudes avec le mode de fonctionnement pulsé, ayant un retard aléatoire <100 ns. La présence d'une électrode de masse en forme d'anneau est un paramètre clé permettant l'allumage de ce type de plasmas multi-périodiques. Lors de l'interaction avec une cible d'eau, la propagation de cet APPJ montre des modes multi-périodiques et des modes aléatoires similaires. Le taux de production de H_2O_2 dans l'eau est mesuré et il est conclu que le H_2O_2 est principalement produit à l'intérieur du tube capillaire à partir des impuretés désorbées de la paroi interne du tube à gaz.

De la peau de porc décongelée et inerte est traitée par l'APPJ et analysée par imagerie polarimétrique Mueller plein champ (MPI). Il est démontré que le traitement plasma peut modifier le retard de phase linéaire et la dépolarisation totale selon la puissance du plasma et/ou la durée du traitement. Selon les groupes témoins, les altérations tissulaires sont principalement causées par le chauffage local concomitant à l'interaction plasma-peau au-dessus de 0,5 W.

Title : Multi-periodic and random mode of Atmospheric Pressure Plasma Jets and their interactions with liquid and biological target

Keywords : APPJ, multi-periodic plasma, self-trigger, RONS, MPI, plasma medicine

Abstract : In this thesis, three main features of Atmospheric Pressure Plasma Jets (APPJ) are investigated: i) multi-periodic and random modes of propagation and the role of surface charges; ii) the interaction between the APPJ and liquid targets; iii) the modification of inert skin samples after plasma treatment.

A helium APPJ driven by 15~18 kHz sinusoidal voltage ignites multi-periodic mode or random mode depending on the voltage, frequency, and inter-electrode gap distance. Most of the observed multi-periodic bullets operate every 2 or 3 sinusoidal periods and have a jitter of <100 ns. The presence of an outer grounded electrode ring is a key parameter permitting the ignition of multiperiodic bullets. Fast imaging reveals that 2-3 self-triggered discharges occur in the gap region before the ignition of bullets in both positive or negative polarities. When interacting with a water target, the propagation of this APPJ shows similar multi-periodic and random modes. The H_2O_2 production rate is measured and it is concluded that the H_2O_2 is mostly produced inside the APPJ from the impurities desorbed from the gas tube's inner wall.

Defrost pig skin is treated by the APPJ and analyzed by full-field Mueller polarimetric imaging (MPI). It is shown to modify the linear phase retardance and the total depolarization for higher plasma power and/or longer treatment duration. According to control groups, tissue alterations are primarily caused by the local heating concomitant to plasma-skin interaction above 0.5W/45 °C. This study aims to show that full-field MPI is suitable for fast and without-contact detection of skin microstructure modifications induced by plasma treatment.